TECHNISCHE UNIVERSITÄT MÜNCHEN

Lehrstuhl für Numerische Mechanik

Multiphysics Coupled Computational Modeling in Cardiac Electromechanics

Julia Maria Hörmann

Vollständiger Abdruck der von der Fakultät für Maschinenwesen der Technischen Universität München zur Erlangung des akademischen Grades eines

Doktor-Ingenieurs (Dr.-Ing.)

genehmigten Dissertation.

Vorsitzender: Priv.-Doz. Dr.-Ing. habil. Christian Krempaszky

Prüfer der Dissertation:

1. Prof. Dr.-Ing. Wolfgang A. Wall
2. Prof. Dr. rer. nat. Björn H. Menze

Die Dissertation wurde am 24.09.2018 bei der Technischen Universität München eingereicht und durch die Fakultät für Maschinenwesen am 01.03.2019 angenommen.

Abstract

The heart is the central organ of the body and its condition determines life and death. A healthy heart is thus fundamental and medicine is further developing its potential towards highly personalized health care. Computer simulations are becoming an important aspect of modern medicine and play an increasing role in identifying the cause of disease and support clinicians in deciding for the most promising treatment. Fast growing knowledge and precise equipment together with simulations can provide a powerful tool to improve the therapy of heart diseases, e.g. cardiac arrhythmia. Our goal is to compute realistic simulations of healthy and pathological hearts to better understand cardiac functions and to improve the performance of surgery.

The aim of this thesis is to build a computational model to simulate patient-specific cardiac performance in healthy and pathological cases. Cardiac function is determined by three main physiological aspects, namely electrical propagation, active tissue contraction, and hemodynamical feedback. In this thesis a framework for a coupled electro-mechano-hemodynamic model based on biophysical principles is build to simulate realistic cardiac contraction.

The clinical importance of this model is demonstrated for the treatment of atrial fibrillation, which is the most common cardiac arrhythmia. Radiofrequency ablation is applied to the standard ablation sides without considering the loss on contraction ability. With the model, the impact of standard ablation concepts on the mechanical performance of the atria are investigated. This provides new insights, as different ablation combinations cannot be applied in practice to the same patient. The computational model is able to detect the differences in atrial contraction and ejection fractions for various electrical activation sequences resulting from different ablation combinations. This thesis shows that multiphysics modeling has the potential to quantify cardiac performance, which could be used as additional pre-operative clinical information.

However, in order to make cardiac computations more valuable for clinical application their computational demand needs to be drastically reduced. Electrophysiological simulations are especially numerically challenging due to the propagation of a steep electrochemical wave front. Using standard continuous Galerkin methods discretizations with small mesh sizes would be required to obtain accurate results. Therefore, the numerical framework is improved by implementing the Hybridizable Discontinuous Galerkin method. This method allows a straight forward implementation of high-order discretizations. In this thesis, a p-adaptive strategy to accurately track the wave front is presented, using the advantage of the discontinuous function space. It is shown that the high-order p-adaptive Hybridizable Discontinuous Galerkin method is an efficient way of computing the electrophysiological problem.

The patient-specific geometrical model is important for improving simulations, especially knowledge about the fiber direction is a necessary step. An accurate shape of the patient's cardiac muscle can be obtained from medical imaging devices. However, until now in-vivo measurements of the fibers, i.e. the alignment myocytes, are difficult in the ventricle and not possible in the atria. In this thesis, a method is presented which defines the fiber architecture in arbitrarily shaped atria using image registration and reorientation methods based on atlas atria with fibers predefined from detailed histological observations. With this method, it is possible to generate detailed fiber families in every new patient-specific geometry in an automated, time-efficient process.

Using the methods presented in this thesis, realistic simulations of cardiac contraction can be performed. The geometry is equipped with physiological fiber orientations in an automated way. Electrophysiological computations are performed with a high-order p-adaptive Hybridizable Discontinuous Galerkin method and, thus, represent correct electrical propagation. Additionally, mechanical contraction, which is coupled to the electrical signal, can be computed together with the hemodynamical influence of the blood pressure. Thus, the framework presented in this thesis allows the computation of efficient patient-specific healthy and pathological hearts in order to investigate treatment options and support clinicians.

Zusammenfassung

Das Herz ist das zentrale Organ des Menschen und sein Zustand bestimmt über Leben und Tod. Ein gesundes Herz ist daher grundlegend für ein normales Leben. Deswegen suchen Wissenschaftler in der Medizin ständig nach besseren und erfolgversprechenderen Therapien um den Patienten zu helfen. Bereits heute stellen Computersimulationen einem wichtigen Faktor der modernen Medizin dar und in Zukunft werden sie eine essenzielle Rolle in der Identifizierung der Krankheitsursache und in der Entscheidung für die vielversprechendste Behandlung übernehmen. Schnell wachsendes Wissen und präzises Equipment bilden zusammen mit Simulationen ein mächtiges Instrument um die Therapie von Herzerkrankungen zu verbessern. Durch realistische Simulationen von gesunden und pathologischen Herzen nähert man sich dem Ziel, die einzelnen Funktionen des Herzens genau zu verstehen und die Erfolge der klinischen Eingriffe zu vergrößern.

Das Bestreben dieser Arbeit ist es, ein Modell zu bauen, um in gesunden und pathologischen Fällen patientenspezifische Simulationen der Herzleistung zu erstellen. Die erfolgreiche Aktivität des Herzens wird bestimmt durch drei Hauptaspekte nämlich die elektrische Ausbreitung, die Gewebekontraktion und die Hämodynamik. Im Laufe dieser Arbeit wurde ein System für ein gekoppeltes elektro-mechano-hämodynamisches Modell entwickelt, das auf biophysikalischen Prinzipien basiert, um eine möglichst realitätsnahe Kontraktion des Herzmuskels zu simulieren. Für klinische Fragestellungen ist dieses Modell von großer Bedeutung. Am Beispiel der Therapie von Vorhofflimmern, das die häufigste Art von Herzrhythmusstörungen ist, wird das Simulationsmodell angewendet und dadurch erfolgreich gezeigt, welches Potential das Modell für die klinische Anwendung bietet. Angewendet auf Vorhöfe von Ablationspatienten erlaubt das Modell Untersuchungen des Einflusses von Ablationskonzepten auf die mechanische Leistung der Vorhöfe. Diese Untersuchungen führen zu neuen Erkenntnissen, da verschiedene Linienkombinationen in der Praxis nicht an einem einzelnen Patienten verglichen werden können. Das Computermodell ist in der Lage Unterschiede in der Vorhofskontraktion und der Auswurfleistung zwischen verschiedenen elektrischen Anregungen aufzuzeigen, die von unterschiedlichen Ablationslinienkombinationen herrühren. Durch die vorliegende Arbeit wird gezeigt, dass Mehrphysikmodelle das Potential haben die Herzleistung unter verschiedensten Bedingungen zu quantifizieren, was als zusätzliche präoperative Information in der Klinik verwendet werden kann.

Um Herzsimulationen für die klinische Anwendung noch wertvoller zu machen, müssen sie in Sinne der Effizienz verbessert werden. Vor allem Elektrophysiologiesimulationen stellen numerisch eine große Herausforderung dar, da sich der Impuls mit einer sehr steilen elektrochemischen Wellenfront ausbreitet. Um genaue Ergebnisse zu erzielen sind Diskretisierungen mit sehr kleinen Netzgrößen notwendig. Um dies zu vermeiden wurde die numerische Berechnung durch die Implementierung der Hybridizable Discontinuous Galerkin Methode verbessert, da diese Methode eine effiziente Implementierung von Ansatzfunktionen mit höheren Ordnungen erlaubt und somit gröbere Diskretisierungen ermöglicht. Zusätzlich wird in der vorliegenden Arbeit eine p-adaptive Strategie präsentiert, die die Wellenfront genau verfolgt und durch Ausnutzen der Vorteile des diskontinuierlichen Funktionenraumes sich zu einer sehr effizienten Methode entwickelt. Es wird gezeigt, dass die höhergradige p-adaptive Hybridizable Discontinuous Galerkin Methode einen effizienten Weg darstellt um das elektrophysiologische Problem zu berechnen.

In der Verbesserung und Optimierung von Simulationen für individuelle Patienten spielt der geometrische Aspekt auch eine sehr wichtige Rolle. Eine genaue Form des Herzmuskels und seiner Zu- und Abflüsse des Patienten kann durch die Verwendung von medizinischen bildgebenden Verfahren erzeugt werden. Bis heute jedoch ist es schwer in-vivo Messungen der Muskelfaserrichtungen, d.h. die Ausrichtung der Myozyten, in den Herzkammern durchzuführen und nahezu unmöglich in den Vorhöfen. Dennoch ist für Elektrophysiologie- und Kontraktionssimulationen das Wissen über die Faserrichtung ein essenzieller Faktor. In dieser Arbeit wird deswegen eine Methode vorgestellt, welche die Faserarchitektur für beliebig geformte Vorhöfe bestimmt. Dies erfolgt durch die Verwendung von Bildregistrierungs- und Reorientierungsmethoden basierend auf einer Atlasvorhofsgeometrie, die mit vordefinierten Fasern aus detaillierten histologischen Untersuchungen ausgestattet ist. Mithilfe des in dieser Arbeit entwickelten Prozesses ist es möglich automatisiert und zeit-effizient detaillierte Faserfamilien in jeder neuen patientenspezifischen Geometrie zu erzeugen.

Unter Verwendung der in dieser Arbeit vorgestellten Methoden können realistische Simulationen der Herzkontraktion erstellt werden. Die Geometrie wird in einem automatisierten Verfahren mit physiologisch sinnvollen Faserorientierungen ausgestattet. Die Elektrophysiologiesimulationen werden mit einer höhergradigen p-adaptiven Hybridizable Discontinuous Galerkin Methode durchgeführt und bilden so die korrekte elektrische Ausbreitung ab. Die mechanische Kontraktion, welche mit der Elektrophysiologie gekoppelt ist, kann zusammen mit dem hämodynamischen Einfluss des Blutdruckes berechnet werden. Die gesamten präsimulativen Prozesse und das vollständige numerisch und biophysikalische Modell, die in dieser Arbeit vorgestellt werden, erlauben eine effiziente Berechnung von patientenspezifischen gesunden und pathologischen Herzen, um verschiedene Therapiemöglichkeiten und postoperative Szenarios zu untersuchen und mit diesen Informationen die Ärzte zu unterstützen.

Acknowledgment

First, I would like to thank Professor Wolfgang A. Wall for giving me the opportunity to work on this very interesting topic.

I am deeply grateful to Professor Cristóbal Bertoglio for being my mentor throughout the thesis and for guiding me through my work, giving me important advice, and always being there to help. I would like to thank Andreas Nagler who first as supervisor and later as colleague was always trying to help if any problems arose. My sincere gratitude goes to Martin Pfaller, my officemate, who always took the time to answer my questions in a very helpful way, to discuss results and future steps, and to give feedback and advice. I was very happy to work at this research group with many inspiring people, who accompanied me as friends through almost four years of research work. Special thanks goes to Rui Fang and Anh-Tu Vuong for introducing me to the code and for all our discussions regarding implementations. Thanks also to my colleagues and friends Martin Pfaller, Martin Kronbichler, Christoph Ager, Sebastian Brandstäter, Simon Hörmann, Clara Bah, and Alexander Woitalka, for reviewing this thesis. I would also like to express my gratefulness to all the people with whom I had the possibility to write publications together.

Lastly I would like to thank my family including, my parents and my aunt for always supporting me, my brothers for believing in me and encouraging me to reach for higher limits. I would especially like to thank my husband Alexander for his love and help throughout all our years together.

Contents

Nomenclature

Mathematical Operators

$\frac{\partial \cdot}{\partial t}, \partial_t \cdot$	partial time derivative
$\frac{\partial \cdot}{\partial x}$	partial derivative with respect to the quantity x
$\frac{\mathrm{d} \cdot}{\mathrm{d} x}$	total derivative with respect to the quantity x
$\dot{f}, \ddot{f}$	first, second time derivative of f
$\int_\Omega$	integral over the domain Ω
$\det$	determinant
$\lceil \cdot \rceil$	ceiling function
$\ln(\cdot)$	natural logarithm
$\exp(\cdot)$	exponential function
const	constant function
∇	gradient operator
$\nabla \cdot$	divergence operator
Δ	Laplace operator
$\times$	operator for the product of spaces
α	multi-index $\alpha = (\alpha_1, \alpha_2, ..., \alpha_n)$ for derivatives
$D^\alpha \cdot$	high-order partial derivative
tr	trace operator
$\lim$	limit
$\arg\min$	argument of the minimum
$\{\{\cdot\}\}$	operator for the mean value of discontinuous functions at the interface
$[\![\cdot]\!]$	operator for the jump of discontinuous functions at the interface
$\cdot\vert_K$	function restricted to the domain K
α_l, q_l	quadrature weights, quadrature points
$H(\cdot)$	Heaviside step function
$\tanh$	hyperbolic tangent
$\mathbb{1}$	indicator function
$SO(d)$	group of all rotations in $\mathbb{R}^d$
$\otimes, \cdot$	outer, inner product between tensors
R^2	correlation coefficient

Physics

μ_k	chemical potential for the substance k
$\tilde{\mu}_k$	electrochemical potential for the substance k
G	Gibbs energy
G_k	molar Gibbs energy for the pure substance k
x_k	mole fraction of substance k
n_k	amount of substance k
R	molar gas constant ($8.314\,47\,\mathrm{J\,mol^{-1}\,K^{-1}}$)
T	temperature
p	pressure
z, z_k	charge number, charge number of substance k
F	Faraday constant
c_k	concentration of substance k
f_k	production density for substance k
$\boldsymbol{J}_k$	flux density for substance k
φ	electrical potential
κ	conductivity
$\boldsymbol{D}_k$	diffusivity tensor for substance k
$[\cdot]$	concentration of a substance
I, I^k	current density, current density for substance k
C	capacitance
Q	charge

Electrophysiology

i	index for intracellular domain
e	index for extracellular domain
Φ_i	interior, exterior electrical potential
Φ_e	exterior electrical potential
Φ	electrical potential difference
Φ_{N}	Nernst potential
Φ_{GHK}	Goldman-Hodgkin-Katz potential
σ	diffusion coefficient
$\boldsymbol{D}$	diffusivity tensor
ψ_k	current-voltage relationship for substance k
$g_k, \overline{g}_k$	membrane permeability, maximal conductance of substance k
m_p	state of the channel p
$\alpha(\cdot), \beta(\cdot)$	voltage dependent rate constants
χ	ratio of membrane area per tissue volume
C_m	membrane capacitance
$I_{\mathrm{cap}}, I_m, I_{\mathrm{ion}}, I_{\mathrm{stim}}$	capacitive, membrane, ionic, and stimulus current density
$u(\boldsymbol{x}, t)$	action potential (transmembrane potential)
$\boldsymbol{w}(\boldsymbol{x}, t)$	gating variables $\boldsymbol{w} = (w_1(\boldsymbol{x}, t), w_2(\boldsymbol{x}, t), ..., w_n(\boldsymbol{x}, t))$

Domains and Boundaries

Ω	domain
Ω_0	domain in reference configuration
d	spatial dimension of the domain
$\partial\Omega$	boundary of domain Ω
Γ_i	subdomain of $\Gamma_i \subset \partial\Omega$
Γ_0	boundary of domain Ω_0 in reference configuration

Function Spaces and Weak Forms

$W^{k,p}$	Sobolev space up to order k based on $L^p(U)$ semi-norms on U
H^m	standard Sobolev space of order $m \in \mathbb{R}$ in U
L^2	Sobolev space of order $m = 0$ in U
$\|\| \cdot \|\|_{L^2(U)}$	norm associated with $L^2(U)$
p	maximal degree of polynomials
m_i	dimension of the space i
$\mathcal{P}^p(U)$	set of polynomials of maximal degree p
φ, φ_h	test function, finite dimensional test function
$\boldsymbol{\psi}$	finite dimensional test function $\boldsymbol{\psi} = (\psi_1, \psi_2, ..., \psi_d)$
V, V_h, V_h^p	test function space, finite dimensional test function space, finite dimensional test function space of polynomial up to degree p
$W_h^p, [W_h^p]^d, M_h^p$	finite dimensional test function spaces

Time and Space Discretization

$\mathcal{T}$	time interval
t, T	time, final time
$\boldsymbol{x}$	space
$\lambda_h, \hat{q}_h$	numerical traces
$(\cdot)_h$	index indicating the discretized version
Δt	time step length
h	element size
τ	stabilization parameter

Mesh and other Geometry

$\mathcal{T}_h$	finite element mesh
K	a finite element
ε_h	set of interior and boundary faces
γ	a face of an element
A_γ	surface area of the face γ
$\boldsymbol{n}$	outward pointing unit normal vector

Continuum Mechanics

R	real numbers
φ	mapping from reference configuration to current configuration
$u, w, \boldsymbol{u}, \boldsymbol{w}$	scalar quantities, vector valued quantities
$\boldsymbol{X}$	position of a point in reference configuration
$\boldsymbol{x}$	position of a point in current configuration
$\boldsymbol{d}$	displacement field between reference and current configuration
$\boldsymbol{F}$	deformation gradient tensor
$\nabla_{\boldsymbol{X}}$	gradient operator with respect to reference configuration
$\nabla_{\boldsymbol{x}}$	gradient operator with respect to current configuration
$\mathrm{d}\boldsymbol{x}, \mathrm{d}\boldsymbol{X}$	infinitesimal long line element in reference, current configuration
$\boldsymbol{I}$	second order identity tensor
$\boldsymbol{R}, \boldsymbol{U}$	rigid body rotation, stretch from the polar decomposition of $\boldsymbol{F}$
$\boldsymbol{C}$	right Cauchy-Green tensor
$\boldsymbol{E}$	Green-Lagrange strain
$\boldsymbol{e}$	Euler-Almansi strain
$\boldsymbol{t}$	traction vector
$\boldsymbol{N}, \boldsymbol{n}$	normal vector in reference, current configuration
σ	Cauchy stress tensor
$\boldsymbol{S}$	second Piola-Kirchhoff stress tensor
ρ_0, ρ	mass density in reference, current configuration
$\mathcal{B}_0, \mathcal{B}$	domain in reference, current configuration
$m(\mathcal{B}, t)$	mass of domain $\mathcal{B}$ at time t
$\boldsymbol{b}$	body forces
$\boldsymbol{J}$	determinant of the deformation gradient $\boldsymbol{F}$
$\boldsymbol{S}_p, \boldsymbol{S}_\tau$	passive, active stress component
Ψ_{elast}	hyperelastic potential
Ψ_{visco}	viscous pseudo-potential
Ψ_{vol}	volume penalty term
$\boldsymbol{I}_1, \boldsymbol{I}_2, \overline{\boldsymbol{I}}_1, \overline{\boldsymbol{I}}_2$	invariants, modified invariants of the Cauchy-Green tensor
$\tau(t)$	time depending stress
$\boldsymbol{f}_0$	fiber direction in reference configuration
$z(t)$	control variable for the transmembrane potential
p_A	blood pressure acting on the endocardium
$\boldsymbol{P}$	first Piola-Krichhoff stress tensor

Hemodynamics

$q(t)$	current density
$p(t)$	pressure
R, R_1, R_2	resistances
C	compliance

Registration

S, T	set of landmarks in source, target image
s_i, t_i	landmark positions in source, target image
n_i	number of points or nodes
$\tilde{\boldsymbol{n}}, \boldsymbol{n}^{\mathrm{rt}}, \boldsymbol{n}$	original mesh nodes, nodes after rigid transformation, nodes after rigid and affine transformation
$\boldsymbol{R}, \boldsymbol{b}$	rigid body rotation, translation
$\boldsymbol{x}_i, \boldsymbol{y}_i$	translated landmark points (centroid of geometry to origin)
$\overline{\boldsymbol{s}}, \overline{\boldsymbol{t}}$	weighted mean of all landmark points (weighted centroid)
$\boldsymbol{S}$	covariance matrix form the matrices of the landmarks and weights
$\boldsymbol{U}, \Sigma, \boldsymbol{V}$	orthogonal and scaling matrices of the singular value decomposition of $\boldsymbol{S}$
I_0, I_k	initial source image, image at iteration step k
$\boldsymbol{p}$	transformation and rotation parameters
$f(\boldsymbol{p})$	objective function depending on parameters $\boldsymbol{p}$
$A(\boldsymbol{p}), s(\boldsymbol{p})$	functions for the transformation and translation depending on the parameters $\boldsymbol{p}$
$\boldsymbol{A}, \boldsymbol{s}$	transformation matrix, translation vector
I_s, I_t	binary voxel representation of the source, target geometry
I_a, I_p	binary voxel representation of the atlas, patient geometry
$\boldsymbol{\varphi}$	transformation of the source image
$\boldsymbol{u}, \boldsymbol{u}^h, \boldsymbol{u}^*$	displacement field, discretized displacement field, optimal displacement field
$\mathcal{D}, \boldsymbol{D}$	distance measure, discretized distance measure
$\mathcal{S}, \boldsymbol{S}^h$	regularization, discretized regularization
$\mathcal{B}$	differential operator
$\mathcal{J}, \boldsymbol{J}^h$	objective function, discretized objective function
α	regularization parameter
λ, μ	Lamé constants
$\nabla^h, \nabla^h \cdot, \Delta^h$	discretized gradient, divergence operator, Laplace operator
$\boldsymbol{B}$	Navier-Lamé operator
$\boldsymbol{H}$	Hessian matrix
$\boldsymbol{F}$	deformation gradient
$\mathcal{R}, \mathcal{U}$	rotational component, scaling component of $\boldsymbol{F}$
$\boldsymbol{f}, \boldsymbol{f}'$	source fiber orientation, transformed source fiber orientation
$\tilde{\boldsymbol{f}}$ target fiber orientation	
$\tilde{\boldsymbol{f}}_{\tan}$	target fiber orientation projected onto the tangential plane
$\boldsymbol{g}, \tilde{\boldsymbol{g}}$	target fiber field, normalized target fiber field

Abbreviations

AF	atrial fibrillation
AL	anterior line
ATP	adenosine triphosphate
BL	posterior box lesion
Ca^{2+}	calcium
CFAE	complex fractionated atrial electrograms on both sites
CFAE-ant	CFAE on the anterior site
CFAE-post	CFAE on the posterior site
CG	Continuous Galerkin
Cl^{-}	chloride
CT	computed tomography
CRT	cardiac resyncronization therapy
cv	conduction velocity
EF	ejection fraction
FS	finite strain
HDG	Hybridizable Discontinuous Galerkin
hex	hexahedral element
ICP	Iterative Clostest Point
IVC	inferior vena cava
K^{+}	potassium
LA	left atrium
LAA	left atrial appendage
L-BFGS	limited memory Broyden–Fletcher–Goldfarb–Shanno algorithm
LBBB	left bundle branch block
LDG	Local Discontinuous Galerkin
L-type Ca^{2+} channel	long lasting or high voltage activated calcium channel
Mg^{2+}	magnesium
MIL	Mitral isthmus line
MRI	magnetic resonance imaging
Na^{+}	sodium
ndof	number of degrees of freedom
nnz	number of non-zeros in system matrix
PPD	preservation of principal directions
PV	pulmonary vein
PVI	PV isolation
RL	roofline
SSD	sum of squared differences
SVC	superior vena cava
tet	tetrahedral element
t-tubules	transverse tubules
T-type Ca^{2+} channel	transient or low voltage activated calcium channel
WACA	wide area circumferential ablation

1 Introduction

The hearts ability to pump blood through the body determines life and death. Thus, knowledge of the cardiac function is of utmost importance for surgical interventions. Computer simulations can be a valuable tool to increase the understanding and the investigation of individual heart functions before surgery, in order to determine the optimal intervention with reduced impacts and side effects.

1.1 Motivation

The main function of the heart is to provide a blood flow through the body. This occurs at a macroscopic level, but the processes responsible for, and those which enable contractions to take place, occur at a nanoscopic level: ion fluxes through the cell membrane allow the excitation of myocardial cells, a surplus of calcium ions in excited cells promotes a molecule conformation change, which in turn enables macromolecules to shorten the cell. Events at nanoscopic scale lead to occurrences at microscopic scale, which in turn lead to actions on the macroscopic scale. Due to this complexity, it is not possible to foresee the influence of an action taking place at nanoscopic scale on the macroscopic scale. However, mathematical modeling can solve this issue. Using multiscale models, it is possible to describe nanoscopic events using physical principles and investigate the macroscopic consequences. Furthermore, models provide additional insights and allow a deeper understanding of the system to be gained. To improve therapy, simulations enable comparisons between different treatment options under the same conditions. The long term goal of simulations in the medical sector is to help clinicians by providing additional information. Models are adapted so that they agree with patient-specific assumptions and different treatment options are simulated. The result is then a comparison between these options for each individual patient.

To model the periodic contraction of the heart and maintenance of the blood flow different fields have to be investigated. The functional interaction of three major components enables the processes that occur during a heartbeat. The *electrophysiology* describes the activation and conduction of the electrical signal through cardiac myocytes. *Mechanical contraction* is defined as the contraction of the cardiac chambers: when triggered by an electrical signal, the myocardial cell contracts. This can be described as a shortening of the myocyte along the long axis. The synchronized contraction of the myocytes results in a decreasing of the cardiac volume, and thus, an ejection of intercardiac blood. This process maintains the blood flow through the body. *Hemodynamic* is the term used for the interaction of the blood flow and the contraction of the heart. These three domains are the major ingredients for mathematical modeling. However, an additional input for the model is necessary and should not be underestimated: the *geometry* of the heart. For patient-specific simulation, the geometry of the patient's heart is the first step, since the shape of the geometry can always be acquired without surgery. The three domains for the simulation can be described and simulated separately, but only the interaction of all of them allows a realistic simulation of the heart. However, it must be noted that computational cost increases with increasing complexity. Because of the reasons state thus far, numerical methods that facilitate accuracy at low computational cost and time are necessary. Additionally, automaticity during patient-specific model quantities and geometry adaption is unavoidable for usage under clinical conditions. With accurate, fast and automatic computations, simulations can be used for diagnostic purposes before and during clinical surgeries.

1.2 Background

Simulations and computational modeling are becoming promising tools for medical investigations and treatments in the clinic [65]. In the last few years, cardiac modeling has made a huge progress, from simple cell models describing electrical activation in a single cell to coupled three dimensional whole heart simulations, incorporating various physical phenomena. This was also enabled by increased computational resources. However, the research questions remains the key factor when developing a new computational model. Because many possibilities exist to compute action potential, the electrical propagation and the mechanical deformation, including different material formulations, a careful decision has to be made to choose the best model in accordance with the research interest.

Cardiac modeling can be divided into three main topics: electrophysiology, contraction, and blood flow. Under electrophysiology, we include all topics describing the electrochemical reaction on micro- and macroscopic scales. Contraction includes the continuum mechanical description of the deformation of the heart muscle, which contains the constitutive equations, describing the material properties, and external tractions, describing the surrounding tissue. The blood flow and blood pressure can be described with fluid mechanical principles or in a lumped version with a windkessel model. Now a more detailed description of each topic is given.

The first electrophysiology model, developed from Hodgkin and Huxley, described the action potential of the single nerve cell of a squid [165]. The development of more detailed models went hand in hand with experimental work, and together led to a deeper understanding of the physical principles [255]. Throughout the years, many improvements to the Hodgkin and Huxley model have been made [120, 252, 253]. With the development of better experiments, new ion currents were detected [62, 95, 178, 256, 257, 296], which led to an improvement of the cardiac cell models [28, 99, 222–224, 229]. A detailed review on the development of experiments and ventricular cell models from 1960 to 2001 can be found in [255]. Atrial cell models were first presented for rabbit [106, 154, 215] and canine [293]. The first human atrial cell model was published in 1998 by Courtemanche [91] and Nygren [262]. A comparison between these two models can be found in [72, 76, 263]. Later, improvements of these atrial models were published [133, 134, 200] and models of the sinoatrial node were developed [19, 316]. In [365] a comprehensive comparison between the atrial cell models in healthy and remolded state is presented. All these models try to describe the action potential based on electrochemical principles, e.g. ion flow due to an electrochemical gradient, varying membrane permeability depending on the transmembrane potential etc. However, depending on the purpose of a simulation it may not be necessary to describe single ion type fluxes and specific channels explicitly. Phenomenological models describe the action potential correctly, without describing the interactions of single ions types, i.e. the variables of the phenomenological models represent multiple channel properties. A prominent example hereof is the FitzHugh-Nagumo model [121, 242]. In 2008, Bueno-Orovio developed a phenomenological model for the human ventricular action potential [52]. An adaption of this model was done by Lenk et al. [212] to describe the action potential of atrial cells. These models are only some examples of cardiac cell models, many more are available and are continuously being improved to describe additional effects, e.g., metabolic activity [69], excitation-contraction coupling [297], drug-receptor interactions [258], genetic modifications [146], instabilities in action potential duration [334, 335], influence of special currents [117, 134] and other latest findings [266].

Single cell models are fundamental when investigating alternations in channel properties. However, to simulate the excitation wave traveling over cardiac muscle tissue, thousands of cells have to be modeled side by side. Only this facilitates to model macroscopic phenomena like disturbed excitation such as re-entrant waves. First, phenomenological models are used to simulate propagation in multi-dimensional tissue [138, 170, 277, 277, 350] and later more complex models [41, 59, 367, 377]. Furthermore, electrophysiology was then computed at individual patient-specific heart geometries [19, 207, 230, 287, 294, 345]. A summary of the nonlinear and stochastic dynamics of the heart can be found in [290].

First models describing the mechanical properties of the heart used simple geometries, like cylinders or spheres, which were symmetric [98, 371]. Later, more complex linear elastic Finite Element models were used to study stress and strain distribution in cardiac walls [132], which were then replaced by non-linear models [183]. Streeter et al. investigated myocardial fiber orientation in the ventricular wall [331, 332]. In 1991 the first model with detailed fiber orientations in the ventricle was computed [250], which was then improved [89, 177]. Many models were developed which provide new insight into cardiac tissue mechanics [136, 137, 139, 176, 249, 274, 353].

On pathological functions such as arrhythmia many studies were carried out. First studies on whole heart simulations were performed [135, 275, 276] and later with reconstructed real heart geometries [366, 368]. Further simulation on arrhythmia were addressing various fields, such as the role of a complex geometry [373], presence of cardiac micro-structure [348], wave and rotor dynamics [23, 81, 310, 344] and also real human hearts [333, 343]. All these simulations make an important contribution to understanding cardiac arrhythmia [33, 73, 108, 127, 191, 192].

A detailed review of the beginning of cardiac modeling development in both electrophysiology and mechanics, can be found in [199], a review of cardiac mechanical modeling in [260], whole heart modeling in [339], electromechanical modeling in [340] and atrial computational models in [101].

To calculate blood flow and pressure in the cardiovascular system, either a full fluid mechanical simulation has to be performed, or a lumped version of blood flow such as a windkessel model can be used. In 1899 Frank developed the first lumped model for blood flow [123], which was then improved by Westerhof [361]. Adding additional resistances and compliances many new windkessel models were developed. The most important ones are the three-element windkessel [286, 362] and the four-element windkessel models [55, 209, 327]. A review about fluid mechanical simulation in the ventricle can be found in [260].

The numerical method plays an important role for the computation of the electrophysiological problem, since this happens to be numerically challenging [248]. Thus, different spatial discretizations have been reported to solve the electrical propagation problem, in particular Finite

Difference Method (FDM) [53, 114, 243, 299, 309, 342, 379], Finite Volume Method (FVM) [32, 90, 147, 181, 282, 341], and Finite Element Method (FEM) [86, 119, 131, 203, 218, 280, 355]. The FDM is intuitive and easy to implement, but becomes very unhandy when using complex geometries and unstructured grids, which are favorable in the reaction-diffusion electrophysiology equations. The FVM is able to calculate complex geometries for low order approximations, but lacks the feature when using higher order elements. However, in the FVM the definition of the flux has a physical significance. From these discretization methods only FEM allows a simple usage of complex geometries and high order approximations. The time discretization in the electrophysiology problem can be done implicitly, explicitly or semi-implicitly. Since the implementation of explicit methods is comparatively easy, they are used often (see [80] and references therein). However, to guarantee stability explicit approaches require the usage of very small time steps, which compensates the benefit of the fast computations of each time step. Implicit methods are also stable with larger time steps [237]. However, with implicit methods it is necessary to solve a nonlinear system in each time step. Semi-implicit approaches avoid to solve a non-linear system through a different treatment of linear and nonlinear terms. Nonlinear terms are treated explicitly, while linear terms are solved implicitly. This improves the stability for larger time steps and is therefore popular for electrophysiology computations [80, 113, 190].

1.3 Research Objective

The purpose of this thesis was to develop a realistic computational model to describe cardiac contraction. The model needs to be applied to clinical relevant aspects regarding cardiac diseases. For research purpose an accurate model is of high priority, however, for clinical relevance additionally efficiency and automaticity are very important.

1.3.1 Why Modeling Atrial Performance?

Until now, the main focus of cardiac computations was on ventricular actions, since ventricles are life determining. Despite the minor role of the atria, their impact on the quality of life should therefore not be underestimated. Atrial fibrillation is the most common cardiac arrhythmia and roughly estimated of around $0.5\,\%$ of human population are suffering from this disease with a rising trend [78, 126].

Atrial fibrillation is the most common sustained cardiac arrhythmia and a leading cause of thromboembolic cerebral insults [148]. In general, atrial fibrillation is described by chaotic electrical waves traveling along myocardial tissue, preventing a regular contraction of the atrium [145]. Patients suffering from atrial fibrillation are additionally exposed to an increased risk of stroke, cardiac failure, and mortality [370]. Due to the limited success rate of drug therapy [60] interventional treatments in terms of radiofrequency catheter ablation are the methods of choice.

Pulmonary vein isolation is the standard ablation approach of paroxysmal atrial fibrillation [15]. However, in the case of persistent atrial fibrillation, several additional ablation concepts are established, comprising ablation of complex fractionated atrial electrograms, ablation of atrial lines [352] or rotor-ablation [144, 318]. By now the effect of these ablation concepts on atrial contractility and atrial ejection fraction remains unclear.

Atrial contribution to ventricular filling is known to be as 10–40 % and increases with age [6]. Hence, choosing the most suitable ablation concept also considering the hemodynamic performance of the left atrium after the procedure may improve the postoperative cardiac performance, especially in older patients [202].

In clinical studies, the effect of different ablation strategies can hardly be examined without having patient-dependent conditions. Moreover, in clinical trials only a single ablation concept can be applied in one patient and thus a direct comparison is not possible.

In the last decade various simulation approaches were reported examining the impact of different ablation techniques on the excitation sequence and during fibrillation in atrial models [206, 295, 302] in order to investigate whether atrial fibrillation terminates under the setup of different atrial fibrillation initiation [295] and incomplete ablation lines [302]. To the best of our knowledge, the only work considering electromechanical coupling (without hemodynamic effects) in the atria is the one of [2].

However, none of these works analyzed the impact of the ablation concepts on the atrial mechanics and its contribution to ventricular filling, since the mechanics of the tissue and the fluid were not taking into account. Hence, the aim of the present study is to fill this gap and to assess the ablation approaches with regard not only to the electrical activation sequence of the atria but in particular to the activation triggered contraction and hemodynamic performance.

For this purpose, we present a computational model bridging all three main physical phenomena: the electrophysiological wave propagation, myocardial contraction and blood pressure development. We simulated the atrial function for two different patient-specific geometries, non-pathological, and dilated, to investigate the influence of the different ablation concepts on the activation sequences and mechanical performance in terms of ejection fraction.

1.3.2 Efficiency

Biophysical and computational modeling of the heart has been pursued as a tool for accelerating cardiovascular research. Translation to clinic to personalize the care is very promising [65]. One of the challenges modelers have to face is the high cost of the computations, in particular when moving towards whole heart modeling and coupling different physics and scales. To develop methods that reduce the computing time while keeping numerical accuracy is essential for speeding-up fundamental research but most importantly the translation of modeling into clinical practice.

Cardiac electrophysiology simulations are classically based on monodomain or bidomain reaction-diffusion equations for the transmembrane electrical potential, which are coupled to a model for the gating dynamics of the ionic channels on the cell membrane. Due to the fast upstroke of the action potential, which is caused by voltage-dependent sodium channels, a numerically robust calculation of the propagation of the wave across the tissue is well known to be computationally challenging. This rapid increase of the transmembrane potential in one cell over a few milliseconds results also in a steep wave front in space [290], requiring high resolution temporal and spatial discretizations [248].

Galerkin methods are popular in cardiac electrophysiology due to their simple applicability to complex geometries and higher-order discretizations [86, 119, 131, 203, 218, 279, 280, 284, 355]. Attempts have been made to improve the performance of the numerical method by using h-adaptivity in space [31, 217, 338], adaptivity in time [86, 149, 291] and in both space and time [74, 75, 96, 124, 364]. Adaptivity in space based on low order elements requires remeshing during the calculation, which involves a considerable computational effort. Furthermore, this approach has to couple the numerical solver with a mesh generator. Therefore, studies about efficient simulations with high-order elements and high-order p-adaptive elements were performed for continuous Galerkin (CG) in [16, 17]. High-order discretizations have been shown to be more efficient than low-order ones for a variety of contexts, i.e. they achieve better accuracy with fewer degrees of freedom and less computational cost [16, 317]. However, the adaption of the polynomial degree in CG faces additional challenges, e.g. for preserving continuity between the elements [130].

To our best knowledge, discontinuous Galerkin (DG) approaches have not received any attention yet for the electrophysiology problem. The discontinuous setting allows a straightforward implementation of global or local high-order discretizations and/or local mesh refinement.

The hybridizable discontinuous Galerkin (HDG) method [84] is a special case of the DG family of methods that allows a reduction of the degrees of freedom that appear in the final linear system by static condensation on the element to those defined on the faces between the elements. The goal of this work is to present a suitable HDG formulation for cardiac electrophysiology, study the numerical performance of HDG in this context and to compare it against standard CG approaches.

1.3.3 Automaticity

Patient-specific mathematical and computational models can contribute to understand the (patho-) physiological function of the heart. These models require not only an accurate geometrical representation of the heart, usually obtained from computed tomography (CT) or from magnetic resonance imaging (MRI), but also a description of the fiber directions. The term fiber is referred to myofiber bundles, which are similarly oriented myocytes running along a certain direction denoted as fiber direction. For a correct representation of the electrophysiological behavior knowledge about the fiber direction is necessary, since the electrical signal travels faster in fiber direction than perpendicular to it [82] and this anisotropy influences the electrical activation [378]. But a correct fiber representation is obviously also important from the mechanical point of view, e.g. studies of the left ventricle show that different fiber architecture lead to different results in the mechanical contraction due to active and passive anisotropy [110, 251].

The fiber architecture of the atria differs from the one of the ventricles. While in the ventricles the fibers are aligned in an almost regular way [109, 332], the fibers in the atria are aligned in individual bundles which run in different directions through the left and right atrial wall [160]. Due to individual fiber bundles running in different directions it is not straight-forward to use rule-based approaches, as it can be done in the ventricles [25, 372]. Besides rule-based methods, another promising approach to define the fiber direction in ventricles is to use diffusion tensor MRI (DTMRI), which is capable to measure non-invasively the fiber architecture of the left ventricular myocardium [174]. This technology is often used ex-vivo [150, 239, 283], since in-vivo measurements are challenging [322, 329] and only few slices can be acquired. Furthermore, it requires sophisticated reconstructions of the fibers for the whole ventricles [241, 337]. However, until now it is not possible to obtain in-vivo fiber directions in the atria since their thickness is smaller than current DTMRI voxel size. Precisely, the atrial wall is around $2\,\mathrm{mm}$ thick [29], while in comparison the left ventricle is around $8\,\mathrm{mm}$ thick [184]. Only recently, ex-vivo fiber orientation in eight different atria could be analyzed with submillimeter DTMRI [278], which could be used as additional information for fiber definitions in the future.

Until now, only few methods have been proposed to create fiber directions in patient-specific atria [151, 205, 308]. The approach in [205] is a first step towards realistic atrial models. The importance of fiber orientations for patient-specific simulations is demonstrated with different geometrical models, to which the semi-automatic method is applied and additional electrophysiological simulations are performed. The method uses voxel based atrial images and manually defined seed points to specify different fiber bundles using marching level sets methods. It is shown that this method works very robust and the results correspond well with reported literature. However, the semi-automatic approach is strongly depending on user input of the 22 seed points, which have to be set in an accurate way. Variation of the seed points can lead to different results. Strong shape variations, which are common in human atria, are difficult to handle with this algorithm, since it depends on shortest paths between seed and auxiliary points and subdivisions at fixed relations. For example to incorporate absent or additional pulmonary vein orifices an adaption of the algorithm is necessary. Additionally, these models are limited to the information about anatomical fiber orientations known at the time of the development of the methods. New information can be only incorporated into the model by changing the methodology, which in turn would lead to more user interaction by defining additional seed points.

To the authors' best knowledge until now image registration techniques are not yet used for fiber estimation in the atria. We propose a method to map atlas atria to a patient's atria using image registration techniques. Using the computed deformation map, the fiber directions are reoriented and then transferred to the patient's atria. The initial user input of seed point is reduced in comparison to rule-based models and is only needed for a first general alignment of the geometries. The influence of user variations is therefore greatly decreased. Additionally, the benefit of using registration methods is that the accuracy of the fiber orientation can be easily improved by adapting only the atlas model. More complex data and details have to be included only in the atlas model without changing the registration algorithm. Additionally, geometry variations as the number of pulmonary orifices, which is a challenge for the rule based models, can be handled by the usage of different atlas atria. Another benefit is the possibility of using ex-vivo measured DTMRI atria with fiber data as atlas atria, thus, improving the accuracy of the model. In [347] a method has been proposed to register an atlas ventricle to the patient's ventricle using large deformation diffeomorphic metric mapping. The goal is to propose an image registration and reorientation method for atrial geometries and fibers and to demonstrate its performance solving an electromechanical problem of patient-specific atria using our fiber definition.

1.4 Contribution of this Work

This thesis describes the developed computational model to simulate patient-specific cardiac performance. This coupled electro-mechano-hemodynamic model can be used to compute the function of the atria under different healthy and pathological conditions. To emphasize its importance in this thesis the computational model is used to investigate the treatment of atrial fibrillation, which is the most common cardiac arrhythmia. Different radiofrequency ablation sites are evaluated using results of the simulations, which are on one hand the electrical activation sequence and on the other hand the mechanical performance. Until now, in clinical purpose it was not possible to compare different ablation strategies for the same patient. With the coupled model it is done in a realistic way considering the three main pyhsiological aspects determining cardiac function, namely electrical propagation, active tissue contraction, and hemodynamical feedback. Furthermore, throughout this thesis the computational model is improved to meet the requirements for clinical application. For the first time high-order p-adaptive Hybridizable Discontinuous Galerkin methods are used to solve the electrophysiological problem. This is shown to be an efficient way to compute accurately the electrical propagation. Additionally, to further personalize the model it is necessary to use the patient-specific shape of the atria. Because in-vivo measurements of the fiber direction in the atria are not possible until now, an automated, time-efficient method is developed to define fiber orientation in arbitrarily shaped geometries. Using registration and reorientation techniques the fiber architecture is mapped from a highly accurate atlas model to the patient-specific geometry. Thus, the methods presented in this thesis allow automated, efficient and accurate computation of cardiac function that can be used as support for clinicians investigating treatment options.

1.5 Outline

The structure of the thesis is as follows. **Chapter 2** describes the biological theory behind the work in this thesis. There, the cardiac structure and functions are described. First a general overview of the anatomy and the morphology of the heart and the circulatory system is given. Then, the structure and the fiber architecture and the heart is explained, with the main focus on the atria. In more detail the conduction system is described. The processes are explained from the nanoscopic level until macroscopic level to provide a solid background on the actions happening during cardiac contraction. Indeed, it is the molecular action that enables the propagation of the electrical signal and the contraction of the cardiac muscle on macroscopic scale. Thus, also for the modeling purpose it is very important to have a good knowledge on the biology.

Chapter 3 describes the modeling. Here it is explained how the chemical and physical processes are translated into mathematical models. The main focus therefore lays on the electrophysiological processes, which describe the conduction and the action potential. First, some basic principles and the electrical properties of the membrane are shown. For that, two definition of the membrane potential are derived, which define the membrane potential in a single-ion system and a multi-ion system. Then the electrical circuit model of the cell membrane is explained and different modeling approaches of the ion transportation are shown. Last, the conduction equations, referred to as bi- and monodomain equations, for a three dimensional system are derived.

The next three chapters describe the development of the cardiac model and improvements in terms of efficiency and automaticity. These chapters are designed to be self-contained and describe different modeling aspects and improvements. **Chapter 4** describes the electro-mechano-hemodynamical model that we developed for human atria. To show the relevance of our simulation model to clinical practice, we used our model to simulate atrial activation. In particular, we compare the impact of atrial ablation strategies on the mechanical performance of the atria.

In **Chapter 5** we explain the improvements we made for computing efficiently electrophysiology. In this chapter the derivation of the numerical methods is shown, which are the Continuous Galerkin and Hybridizable Discontinuous Galerkin method. Additionally, the method for discretizing the ionic current are explained, which is very important when using high-order methods. Comparison between Continuous Galerkin and Hybridizable Discontinuous Galerkin are made and at last the performance of the high-order p-adaptive method is shown.

The next chapter, **Chapter 6**, describes the method to define the fiber architecture in atria. This is done using image registration and reorientation methods based on atlas atria with fibers predefined from detailed histological observations. Thus, first the registration theory is explained together with the reorientation methods. Second, the performance of our method is shown on different shaped atria and with electro-mechano-hemodynamical computations using the previously defined fiber models.

Finally, the last chapter summarizes the work done in this project and provides the perspective for future work.

2 Biological Basics of the Human Heart

The heart is a hollow muscular organ and its condition determines about life and death. The main function of the heart is to supply all body cells with oxygen and nutrients. This is guaranteed by a continuous flow of blood through different sized blood vessels in every part of the body. The flow, however, is maintained by continuous pumping of the heart. Throughout the whole life the heart contracts and relaxes in general once in each second.

The heart is located in the inferior part of the mediastinum, protected from the thoracic cage. It is bordered on both sides by the lung, the inferior boarder is defined by the diaphragm on which the heart partially rests (see Figure 2.2a). The sternum is located anterior and the organs of the mediastinum, primarily the esophagus, are located posterior to the heart. The size of an adult human heart is around the the size of a fist and its weight is around $280\,\mathrm{g}$ for a women and $320\,\mathrm{g}$ for a man, respectively [238, 360].

2.1 Fundamentals

2.1.1 Morphology

The heart consists of four hollow and distinct chambers: the left atrium and left ventricle and the right atrium and right ventricle. Th atria are the smaller chambers compared to the ventricles. All lumina are surrounded by muscular tissue with varying thickness. The lumen of the right heart (right atrium and ventricle) and the left heart (left atrium and ventricle) are distinct, i.e. there does not exist any direct interluminal connection between the left and the right heart. The left and right atrium are separated by the interatrial septum and the ventricles by the interventricular septum (see Figure 2.1a). At the atrio-ventricular junctions between the atrium and the ventricle the mitral and the tricuspid valve are located in the left and right heart, respectively (see Figure 2.1a). Between the atria and the ventricles is the cardiac skeleton located (see Figure 2.1b). The skeleton has different functions. It consists of a dense tissue which forms a connection between the atrial and the ventricular tissue. The skeleton forms a union of four rings to which the valves are attached. The skeleton supports the valves during contraction and high pressures. Additionally, the skeleton acts as an electrical insulator, which prohibits the electrical signal to travel from the atria to the ventricle. At the orifices of the ventricles the aortic and the pulmonary valves are situated, which separate the left and right ventricular volume from the aorta and the pulmonary artery, respectively. Two major veins are connected to the right atrium: the superior vena cava (SVC) and the inferior vena cava (IVC). A third inflow connection to the right atrium is the sinus coronarius, which is a conflux of different cardiac veins. Commonly there are four pulmonary veins (PV) which are connected to the left atrium: the left inferior, the left superior,

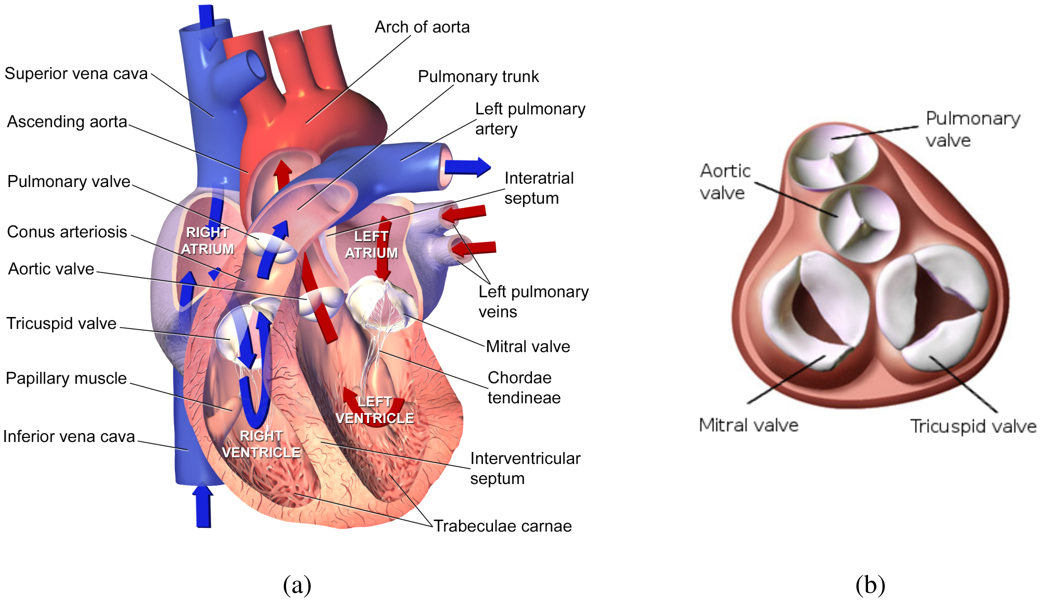

(a) (b)

Figure 2.1: (a) Anatomy of the heart (adapted from [43]). (b) Skeleton of the heart with valves (adapted from [43]).

the right inferior and the right superior pulmonary vein. Though, it often occurs that the number of PVs is unequal to four, depending if the veins join already before entering the left atrium. Thus, it is possible could be that there is one PV inlet less or one more [161]. No valves exist at the inlets of the veins to the atria .

2.1.2 Pericardium

The heart is surrounded by the pericardium, which on one hand protects the cardiac muscle and on the other hand keeps the heart in place and limits acute excessive dilation. Additionally the pericardium effects strongly the cardiac contraction process [326]. The pericardial fluid, which is produced by the pericardium, reduces friction during heart movements. The pericardium consists of two components: the visceral pericardium and the parietal pericardium (see Figure 2.3). Both parts build a continuous layer in which the pericardial fluid is enclosed. The visceral pericardium is attached to the heart surface while the parietal pericardium forms the outer boarder [298]. The parietal pericardium is attached anteriorly by ligaments to the sternum and more firmly to the diaphragm. Laterally, the pericardium is in contact with the covers lung. The visceral pericardium is sometimes referred also as epicardium and the parietal pericardium simply as the pericardium [326, 359].

2.1.3 Circulatory System

The flow of the blood through the body is driven by the periodic pumping of the heart. Taking a closer look on the heart, it actually consists of two pumps: one is the left heart and one the right heart, which maintain two closed loops of blood flow (see Figure 2.2b). The right heart pump

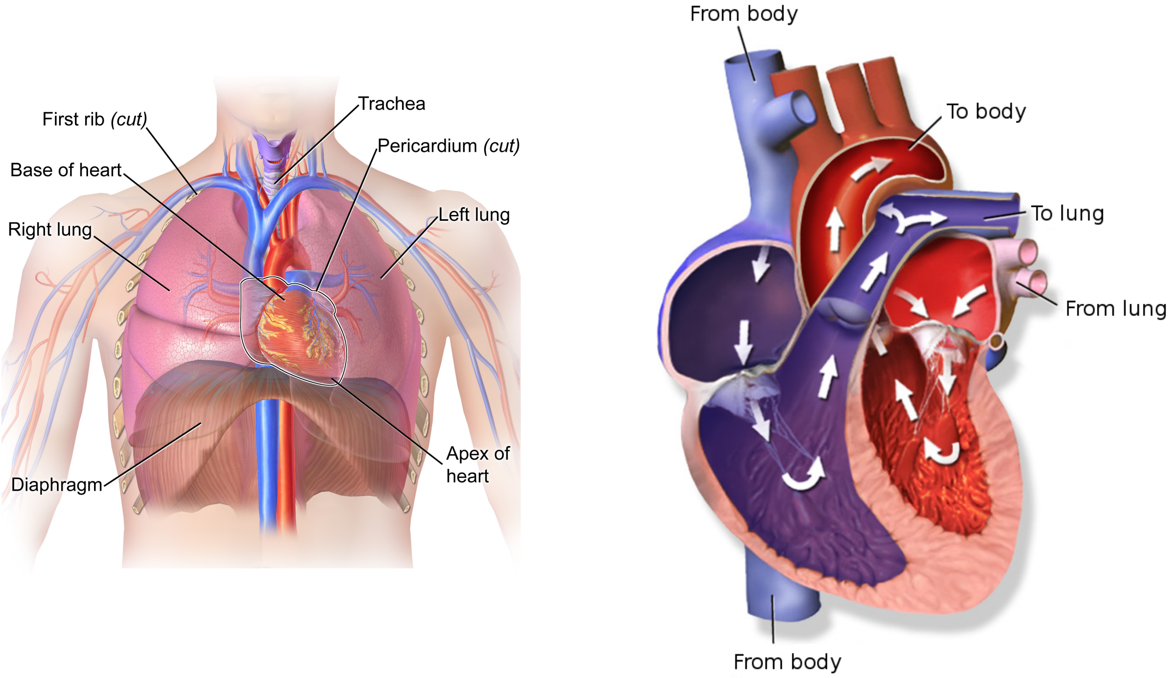

(a) (b)

Figure 2.2: (a) Blood flow thought the cardiac system (adapted from [43]). (b) Position of the heart in the thoracic cavity (adapted from [43]).

is responsible for the smaller pulmonary circulation, which runs through the lung. The blood enters the right atrium through the IVC and SVC. The tricuspid valve is closed. When the right atrium contracts at a certain point the pressure in the right atrium exceeds the pressure in the right ventricle and the valve opens and blood flows into the ventricle. When the right atrium relaxes the valve closes and the ventricle starts its contraction, which results in a higher ventricular pressure than pulmonary artery pressure. The pulmonary valve opens and the blood flows towards the lung. After carbon dioxide and oxygen exchange in the capillaries in the lung the oxygenated blood flows back to the left heart, entering the left atrium through the PVs. Contraction of the left atrium forces the blood to flow through the mitral valve into the left ventricle. Contraction of the left ventricle pumps the blood into the aortic artery through the aortic valve. Oxygenated blood is then distributed to all cells of the body. In the capillaries exchange in the blood takes place, now, oxygen for carbon dioxide. Afterwards the blood returns to the right atrium. This back flow to the right heart is enabled due to a very low pressure in the atria and valves in the veins, which prevent back flow. The pressure difference between right atrium and veins, which is necessary for the return of the oxygen-poor blood to the right heart, is increased due to two additional factors, besides the cardiac contraction. The first one is the contraction of skeletal muscles, which decreases the size of the veins and thus increases venous pressure (see Figure 2.4). The second one is due to respiratory activity, which helps decreasing the atrial pressure while increasing the volume of the thorax [195]. The cardiac cycle is divided into two phases, one

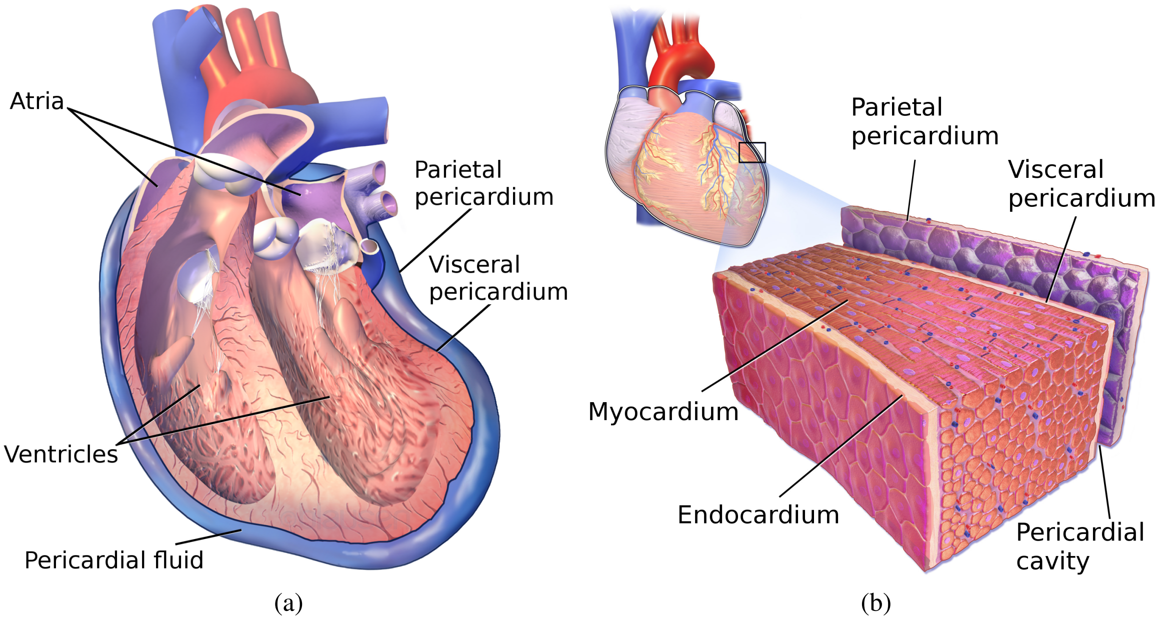

Figure 2.3: (a) Pericardial sac with visceral and parietal pericardium enclosing the pericardial fluid (adapted from [179]). (b) Section of the heart wall showing its three layers: endocardium, myocardium and epicardium (adapted from [43]).

is the contraction phase of the ventricles, the so called systole, and the second is the relaxation phase of the ventricle, the so called diastole (see Figure 2.5).

2.1.4 Functions of the Heart

Different components of the heart are responsible for different tasks. The two smaller chambers, the so called atria, have three main functions during the cardiac cycle. Firstly, they serve during systole as a reservoir. Secondly, during early diastole they act as a passive tube and allow the blood to flow through them into the ventricle. Thirdly, during late diastole the help filling the ventricle as they contract [236]. The ventricles have mainly one task, to pump the blood through the body and to the lung. The left ventricle is responsible for the systemic circulation, while

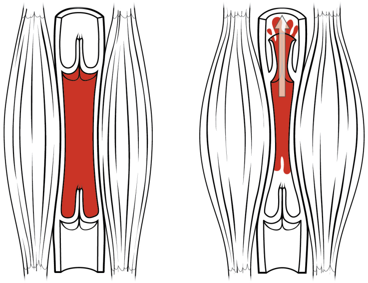

Figure 2.4: Pressure increase in the veins due to skeletal muscle contraction supports blood flow back to the heart [270]).

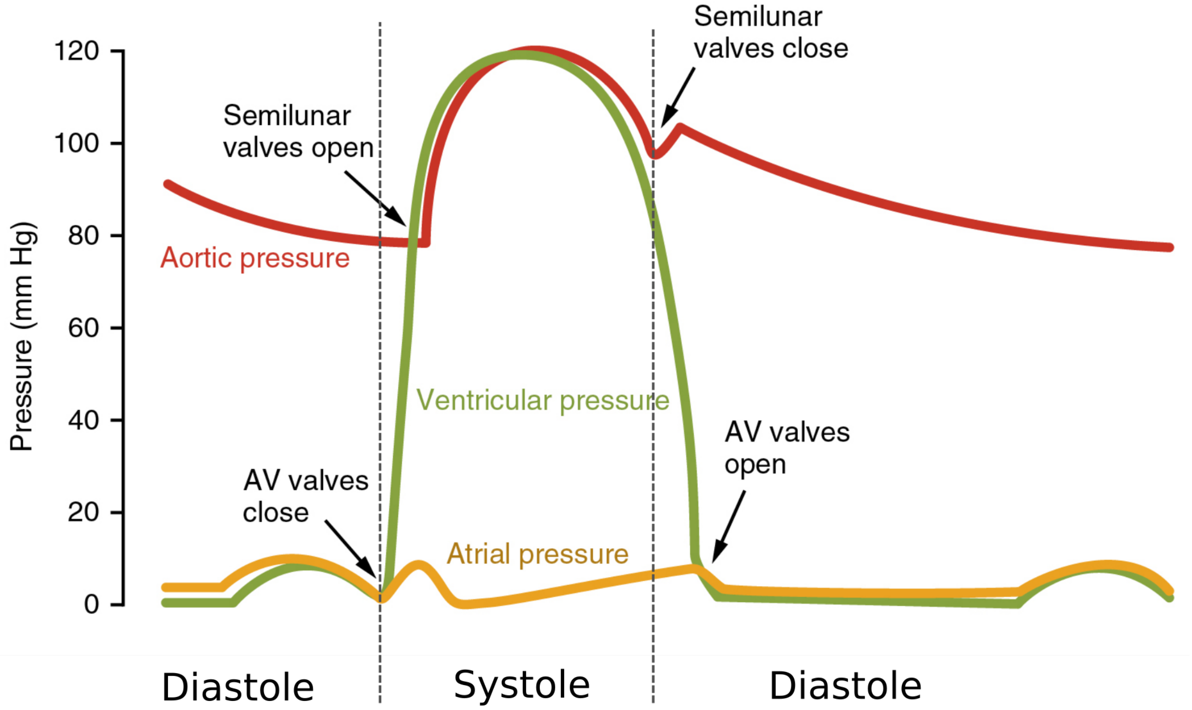

Figure 2.5: Pressure curves (adapted from [272]).

the right ventricle is responsible for the pulmonary circulation. Valves between the atria and the ventricle prevent the blood from flowing back to the atria during contraction of the ventricle. And the valves at the orifice of the ventricle prevent the blood from flowing back into the ventricle after ventricular contraction.

2.1.5 Internal Anatomy

The heart walls including the pericardium are composed of five different layers (see Figure 2.3b). The parietal pericardium is the outermost layer. The epicardium is the third layer and between the parietal pericardium and the epicardium is the pericardial cavity. These three layers belong to the pericardium. The epicardium is connected with the myocardium, which is the thickest layer. It contains the muscular tissue of the cardiac wall and it is responsible for the contraction. The innermost layer is the endocardium, which is the internal lining of the cardiac chambers (see Figure 2.3b) [104, 359]. The heart walls have a varying thickness depending on their muscular bulk. The thin walls of the atria have only a thickness of $2\,\mathrm{mm}$ [29], since they serve more as a reservoir and contribute only little to the filling of the ventricle. The right ventricle has a thickness between $2\,\mathrm{mm}$ and $7\,\mathrm{mm}$ [122] and the left ventricle is around $8\,\mathrm{mm}$ thick [184].

2.2 Gross Structure and Fiber Architecture of the Atria

The cavities of the right and the left atrium are positioned right of the ventricular chambers. When viewed from the front, the right atrium is anterior, and the left atrium posterior. The left atrium is slightly shifted leftward relative to the right atrium. The atrial septum is oblique to the sagittal plane at an angle of around 65° [156, 160]. The two atrial chambers differ in their morphology as well as in the fiber organization. However, both atria have the same basic components: a venous part, an appendage, a vestibule and a septum, which is shared by the two atria. Each chamber begins at the venoatrial junctions and ends at the vestibule and the valves, which mark the intersection between the ventricles. The venoatrial junctions are the entrances of the caval veins and the pulmonary veins in the right atrium and in the left atrium, respectively [156].

2.2.1 Right Atrium

The right atrium has three mayor components, which belong exclusively to the wall of the right atrium (see Figure 2.6). The fourth component, the atrial septum, is shared by both atria. One part of the right atrium is the venous component, which expands between the orifices of the superior and inferior caval vein. At the front it is separated from the rest of the atrium by the terminal groove outside, which equates to the terminal crest, or the crista terminalis inside. Dorsal the venous component boarders the atrial septum. The interior of the venous component is characterized by its smooth walls (see Figure 2.7) [156]. The terminal crest forms a discrete ridge on the endocardial surface and thus it is readily identifiable. It is the most prominent bundle in the right atrium. The crest curves in front of the superior vein almost in a C-shape inferiorly to the inferior caval vein (see Figure 2.7). After passing rightward to the inferior caval vein it ramifies and enters the posterior region of the inferior isthmus. In the terminal crest the myocytes tend to run longitudinally along the long axis of the muscle bundle [156, 160]. The sinus node is located in the terminal groove close to the orifice of the superior caval vein [160].

The dominant feature of the right atrium is its appendage (see Figures 2.6 and 2.7). The appendage is easily distinguished from the rest of the atrium because of its ridged walls (see Figure 2.7). These ridges are known as the pectine muscle bundles, which originate perpendicularly from the terminal crest and fan out over the entire wall of the appendage. Along the ridges of the pectine muscles the myocytes are arranged longitudinally [156]. The pectine muscles run nearly in a parallel fashion over the entire wall of the appendage. In most hearts fine muscular strands cross over the parallel arranged pectine muscles [311]. The space between the ridges is almost lacking in musculature. The pectine muscles along with the appendage form the entirety of the anterior wall of the chamber [160].

A prominent pectine muscle is the sagittal bundle. It originates in the terminal crest and runs along the edge of the appendage to the tip of the appendage (see Figure 2.6). This bundle divides the appendage into a anteromedial and posterolateral part [156]. On the tip of the appendage the muscle bundles are not arranged regularly. Most of them originating from the sagittal bundle run palm leave or frond like or are arranged in whorls [160, 311].

The vestibule forms the leftward margin of the right atrium. It is a smooth muscular rim, which surrounds the valvar tricuspid orifice to the right ventricle. The myocytes in the vestibule run circumferentially around the outlet, perpendicular to the pectine muscles. The vestibule thins out toward the valve [156, 160].

On the posterior atrial wall the triangle of Koch forms a portion of the vestibule (see Figure 2.8a). The inferior border of the triangle is the septal isthmus. The septal isthmus is located between orifice of the cornary sinus and the attachment of the septal leaflet of the tricuspid valve. The posterior boarder of the triangle consists of the tendron of Todaro. The tendron of Todaro is

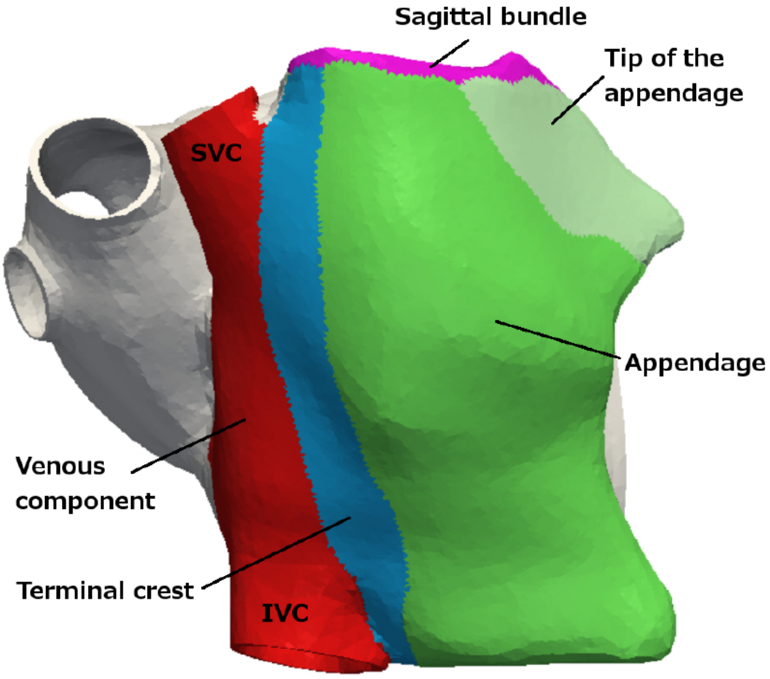

Figure 2.6: Diagrammatic representation of the right anterior oblique view of the right atrium with the mayor components: venous part (red), crista terminalis (blue), appendage (green) and sagittal bundle (purple). IVC inferior vena cava; SCV superior vena cava.

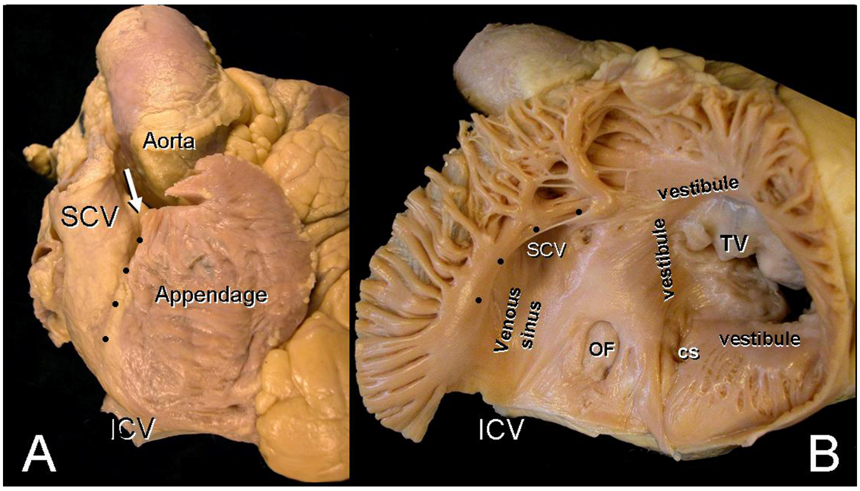

Figure 2.7: View of the right atrium. The points mark the terminal crest. On the left image the rough surface due to the pectine muscles is visible and the smooth surface between the superior and inferior caval vein. The oval fossa and the rim of the oval fossa are shown, together with the smooth surface of the vestibulum.The arrow points to the location of the sinoatrial node. IVC inferior vena cava; SCV superior vena cava; OF oval fossa; TV tricuspid valve; CS coronary sinus. (adapted form [159])

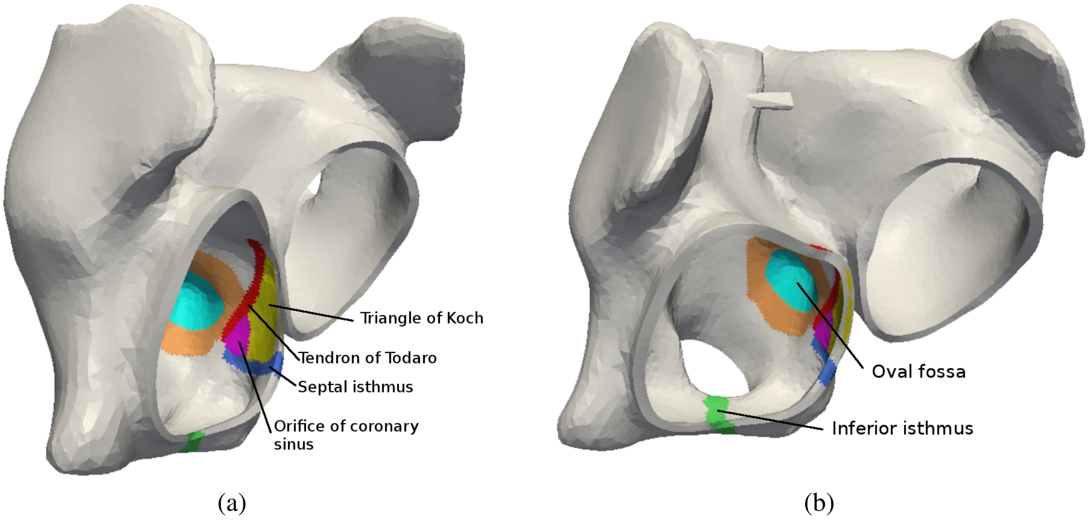

(a) (b)

Figure 2.8: Diagrammatic representation of the vestibule with the triangle of Koch: Tendron of Todaro (red), Septal isthmus (blue), inferior isthmus (green).

formed by a tendinous continuation of the Eustachian valve. The Eustachian valve is a variably developed remnant of the fetal circulation [314]. The triangle of Koch is the anatomical landmark for the location of the antrioventricular node. The node lies in the apex of the triangle. At this point exists the only electrical connection between atria and ventricles. The atrioventricular conduction system penetrates the insulation plane between the atria and the ventricles. The connecting bundle is called the bundle of His [160].

The second isthmus, known as the inferior isthmus, lies between the inferior caval vein and the tricuspid valve (see Figure 2.8b). It can be divided into three morphologic zones. The posterior part receives an array of finer bundles from the terminal crest and thus is, fibrous. The middle zone is trabeculated from extensions of the pectine muscles and the anterior zone is the smooth wall of the vestibule [156, 160, 311].

It is common to find sleeve like extensions of the myocardium on the superior and inferior caval vein. The fibers were arranged predominantly circulatory around the veins [193]. The posterior right atrial wall is dominated from the oval fossa, which belongs to the atrial septum (see Figure 2.9). The rim around the oval fossa is an important part in the atrial conduction system. Myocytes in the rim are arranged circumferentially around the fossa. The anterior rim joins with the triangle of Koch and the Eustachian ridge. The fibers of the rim extend superiorly towards the origin of the terminal crest and posterioly towards the intercaval region [12, 156, 160].

2.2.2 Left Atrium

The left atrium has the same basic components as the right atrium, but they differ in shape and morphology. The most important components are the appendage, the venous component and the vestibule (see Figure 2.10). The appendage of the left atrium is smaller than the right appendage, and thus, not highly dominant. It has a tubular shape with several bends so that it looks like little

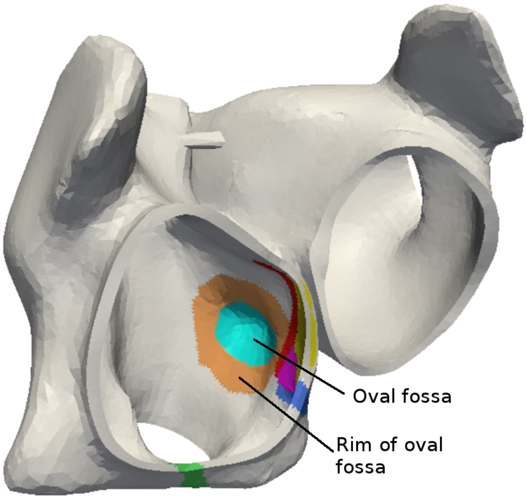

Figure 2.9: Diagrammatic representation of the oval fossa (turquoise) and the rim of the oval fossa (orange).

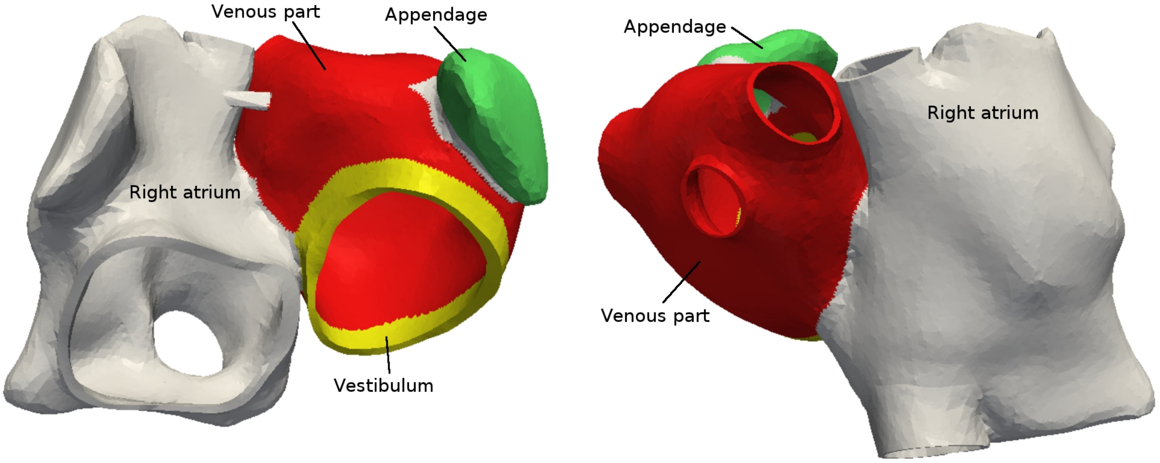

(a)

(b)

Figure 2.10: Diagrammatic representation of the anterior (left) and posterior (right) view of the left atrium with the major components: vestibulum (yellow), venous part (red) and appendage (green).

fingers. However, the morphology of the left atrial appendage varies significantly in size, shape and volume between different humans [3, 111, 330, 351]. Due to its tubular shape it has a well-defined junction with rest of the left atrium [156]. On the endocardial surface of the appendage the pectine muscles appear less extensive than they do in the right atrium. In contrast to pectine muscles in the right atrium, in the left atrium they are also not arranged regularly and could appear like whorls. Between the ridges the wall is very thin. The terminal crest is also missing in the left atrium. Instead, the division between the rough wall of the pectine muscles and the smooth wall of the venous component is around the mouth of the appendage [156, 160–162].

Like in the right atrium, the vestibule surrounds the outlet of the atrium. It is a smooth zone, with myocardium overlapping the atrial surfaces of the mitral leaflets [12, 156, 160, 161]. The venous component forms the posterior part of the left atrium, where the orifices of the pulmonary veins are located. It is directly confluent with the body of the left atrium. Commonly the venous component has four entrances for the left superior and left inferior and right superior and right inferior pulmonary vein. However there exist more variations in the number of venous entrances. It is possible that the left or right superior and inferior veins already join before entering the atrium [235]. The wall of the pulmonary venous component is mainly smooth. There are no clear distinctions between the veins and the atrium, especially if the vein has a funnel shape [156]. Atrial musculature extends over the walls of the pulmonary veins for various distances [12, 161, 164].

The walls of the left atrium are smooth. However, they are not uniform in thickness or myoarchitecture. They are composed of diverse layers with different oriented fibers. One to three (and sometimes even more) layers form the wall. Thus, regionally varying thickness of the the left atrial walls is common [160]. A layer is defined as bundles with the same gross orientation. Different layer describe overlapping bundles, but between the layers no separating fibrous tissue exists. Mainly the smooth part of the left atrium has different layers. The interatrial Bachmann bundle is the most important bundle on the epicardium (see Figure 2.11). It runs parallel with the circularly arranged left atrial fibers. They arise from the anterior margin of the atrial septum, then they go leftward, joining with the interatrial bundle. Before the appendage they bifurcate, encircle it and rejoin in the lateral wall and thereby form a broad band. This broad band in the inferior wall enters the septal raphe [160].

The septopulmonary bundle runs one layer below the circular fibers. This bundle arises obliquely from the antero-superior septal raphe. It then fans out and passes in front, between and behind the orifices of the pulmonary veins. The strands also join with the muscular sleeves around the veins. In the posterior wall the septopulmonary bundle in most hearts bifurcates into two oblique bundles. Then, the branches fuse with the circularly arranged fibers. In other hearts the septopulmonary bundle becomes an area of mixed fibers [160].

The subendocardium is mainly formed by the septoatrial bundle. The fibers arise in the anterior septal raphe. Running obliquely the bundle fans out into three major bundles. One broad bundle joins with the septopulmonary bundle and reaches between the left and right pulmonary veins the posterior wall. Another band turns laterally, joining with the leftward fibers of the septopulmonary bundle to run toward the insertions of the left pulmonary veins. Between the branches on the posterior wall there exist areas of mixed fibers. The third branch surrounds the mouth of the appendage and merge in the inferior wall with the circular fibers. Sometimes the fibers of the septoatrial bundle encircle the orifices of the pulmonary veins, running in the same direction as the muscular sleeves. However, in other hearts the fibers of the septoatrial bundle run perpendicular to the muscular sleeves, which makes the orifices a nonuniform anisotropic region, and thus, is maybe substrate for ectopic stimuli [156, 160].

2.2.3 The Atrial Septum

The atrial septum is limited to the oval fossa. The oval fossa is surrounded by an extensive muscular rim. Although the rim seems to be part of the septum, the main part is an infolding of the right and left atrial wall between the superior caval vein of the right atrium and the pulmonary

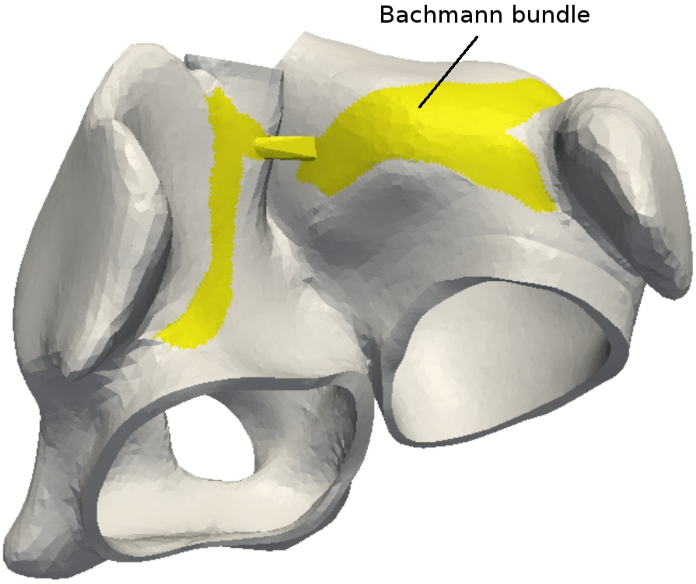

Figure 2.11: Diagrammatic view of the atria with the Bachmann bundle (yellow)

veins of the left atrium. The true septum is limited to the flap valve with its anchorage. The groove between the infoldings, which is also known as septal raphe, is filled with fat tissue [156, 160].

2.2.4 Interatrial Connections

One muscular connection between the right and left atrium is through the septum. More precisely, the muscular rim of the oval fossa connects the two atria. However, there are more connections, mostly in form of muscular bridges on the subepicardium. These bridges are composed of ordinary working myocardium [156]. They vary in thickness and width [160]. The most prominent muscle bundle is the interatrial bundle, which is also known as Bachmann bundle. It originates at the apex of the terminal crest close to the sinus node (see Figure 2.11). While the terminal crest descends inferiorly, the Bachmann bundle turns to the posterior wall of the right atrium (see Figure 2.11). It bifurcates on both atria. On the right atrium one branch runs to the sinus node and the other branch runs in the direction of the vestibule, so that the Bachmann bundle encircles the right appendage. In the left atrium the bifurcation of the Bachmann bundle encircles the left appendage. While crossing the septal raphe it is a discrete bundle. However, the Bachmann bundle is not a cable-like structure, but rather a flat band or several parallel bundles. On the walls of the atria the bundles joins with adjacent musculature. In the anterior left atrial wall the Bachmann bundle joins with the circular fibers of the subepicardium. Then they bifurcate to encircle the appendage and rejoin again and continue in the lateral and posteroinferior wall [156, 160]. There also exist other bridges posteriorly, establishing connections between the left atrium and intercaval area on the right atrium or between the left atrium and the region of the inferior caval vein. Muscular bridges between the muscular wall of the coronary sinus and the remnant of the vein of Marshall to the left atrium can also be found [68, 160, 161].

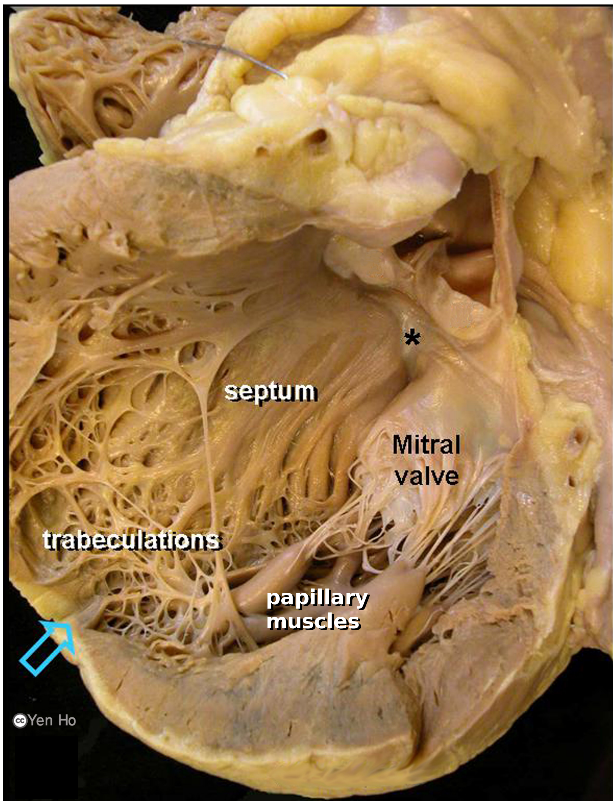

Figure 2.12: Dissection of the left ventricle. The asterix marks the atrioventricular conduction bundle at the membranous septum. The arrow points to the tip of the apex (adapted from [158]).

2.3 Gross Structure and Fiber Architecture of the Ventricle

The ventricle can be dividend into three main parts: the inlet portion, the outlet portion and the apical portion. The apical portion contains fine trabeculations, which are round muscular columns that are connected as an irregular network on the endocardial side of the ventricles (see Figure 2.12). The shape of the left ventricle can be seen roughly as a cone with the triangular shape of the right ventricle curving over it. Thus, the ventricular septum is convex, warping into the right ventricle. The walls of the ventricle have a varying thickness. The left ventricle is in general thicker than the right ventricle. However, the thickness of the left ventricular free wall varies. From base to apex the thickness decreases gradually. The maximal thickness of an adult heart is $12–15\,\mathrm{mm}$ [157]. Nevertheless, at the tip of the apex the muscular wall is only $1–2\,\mathrm{mm}$ [157] (see Figure 2.12). The wall of the right ventricle measures only $2–7\,\mathrm{mm}$ [122]. The outlet region of the septum is relatively smooth. The muscular trabeculations in the right ventricle are coarser than the trabeculations in the left ventricle, which are characterized by a crisscrossing pattern [157, 163].

While the fibers in the atria are aligned in individual bundles which run in different directions through the left and right atrial wall [160], in the ventricle the fibers are aligned in a almost regular way. Roughly, the left ventricular myoarchitecture is composed of three layers and the right ventricle of two layers. Superficially the fibers are arranged in the right ventricle mostly circumferentially. They turn slightly towards the apex and the base near the interventricular groove to continue with the left ventricular fibers. Towards the apex the fibers of the left and right ventricle run in spiral fashion. Since the wall of the right atrium is relatively thin compared to the wall of the left atrium the right atrium lacks a middle layer. The fibers of the middle layer of the left atrium are arranged in a circumferentially fashion parallel to the atrioventricular groove. There exist a continuity between the fiber orientation of the different layers. On the subendocardium in both ventricles the fibers are arranged longitudinally form apex to base. They join with the trabeculations, the papillary muscles and the valvar insertion [116, 157, 163]. However, the myoarchitecture in the ventricles is not completely understood until now and still under investigation. In a study the change of the fiber directions through the left ventricular wall is analyzed in more detail. The fiber angle between the subepicardium and the subendocardium changes smoothly, but the change is larger towards the endocardial and epicardial surfaces [332], which coincides with Ho et al. [157]. More recently a study in ovine hearts also showed the smooth transitions of the fiber angle through the wall of the left ventricle [109].

2.4 Conduction System

The process of the contraction is triggered by an electrical impulse, which travels through the heart and activates the muscle cells. A network of modified cardiac muscle cells together with the normal working myocardium initiate and transport the electrical signal throughout the heart (see Figure 2.13). The so called conduction system, which is composed of several specialized cell types, is located between the working myocardium and cannot be dissected easily. Thus, new findings about special conduction cells are still ongoing [13, 45].

The electrical signal is initiated from the sinoatrial node, which lies in the right atrium at the junction of the SVC with the atrium [13]. It is situated around $1\,\mathrm{mm}$ deep in the subepicardium and has a length between $10\,\mathrm{mm}$ to $20\,\mathrm{mm}$ and a thickness up to $5\,\mathrm{mm}$. It consists of spontaneous self depolarizing cells which have poorly developed contractile properties. Although the sinoatrial node is an autonomous pacemaker, i.e. it could depolarize without external stimuli, the frequency of the depolarization is influenced from innervation. Thereby the heart rhythm can be adapted to physical requirements [104]. The depolarization of the sinoatrial node cells results in a depolarization of neighboring cells of the right atrial myocardium. It was believed for a long time that special pathways exist in the atrial myocardium like they do in the ventricles. However, special insulated pathways are not found in the atria [11]. The signal is spread only over the normal working myocardium, but with the important property that propagation along fiber direction is faster than perpendicular to it [82]. Special alignment of the fiber bundles in the right atrium result in fast pathways from the sinoatrial node to the atrioventricular node. The main conducting pathways are the terminal crest and the rims of the oval fossa. From the right atrium to the left atrium the preferred conducting paths are muscular interatrial bridges, from which the most prominent one is the Bachmann bundle. The sinoatrial node lays near the origin of the terminal crest and the Bachmann bundle, and thus, perfectly located to rapidly activate them [11, 210]. When the electrical signal reaches the atrioventricular node it gets delayed. The purpose of this delay is to have a time difference between the contraction of the atria and the ventricles. This

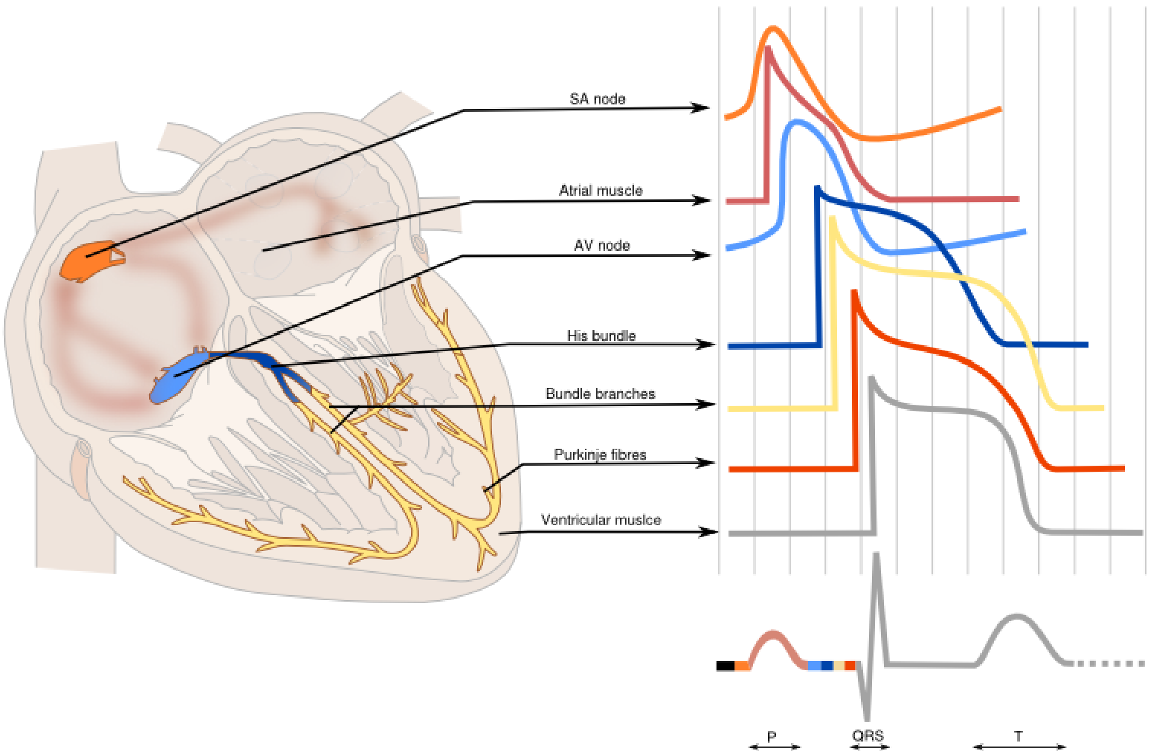

Figure 2.13: Conduction system and specialized cells types with the action potential curves of the heart. Additionally, also the action potential curves of the normal working myocardium of the atria and the ventricle are shown (adapted from [325]).

results in an efficient maximization of blood filling of the ventricle before systole due to a previous contraction of the atria. Additionally, the atrioventricular node has the property to protect the ventricle from rapid atrial arrhythmia and can act as a pacemaker if the sinoatrial node fails or the signal is blocked before reaching the atrioventricular node [24]. Although, the conduction is spread out over both atria, it does not reach the myocardial cells of the ventricle directly. This is due to the heart skeleton, which electrically separates the atria form the ventricles. The only electrical connection is the atrioventricular conduction axis, which consist of the atrioventricular node, the atrioventricular bundle and the bundle branches (see Figure 2.13). The atrioventricular bundle is also referred to as bundle of His [24, 104]. The atrioventricular bundle divides in the ventricular septum into left and right branch. The bundle and the branches are electrically insulated from the surrounding tissue until the ventricular apex. Thereby only the branches are activated, until the signal reaches the apex. The branches ramify as purkinje fibers, which are first also surrounded by an connective tissue sheaths insulating the fibers. Later the purkinje fibers form connections with the normal working myocardial cells to spread the signal to the myocardium [14, 21]. Both, ventricular branches and purkinje fibers, provide a fast conduction of the electrical signal, so that the activation of the ventricles occurs rapidly [104]. The overall activation of the atria takes around $110\,\mathrm{ms}$ [100] and the ventricle less then $100\,\mathrm{ms}$ [292].

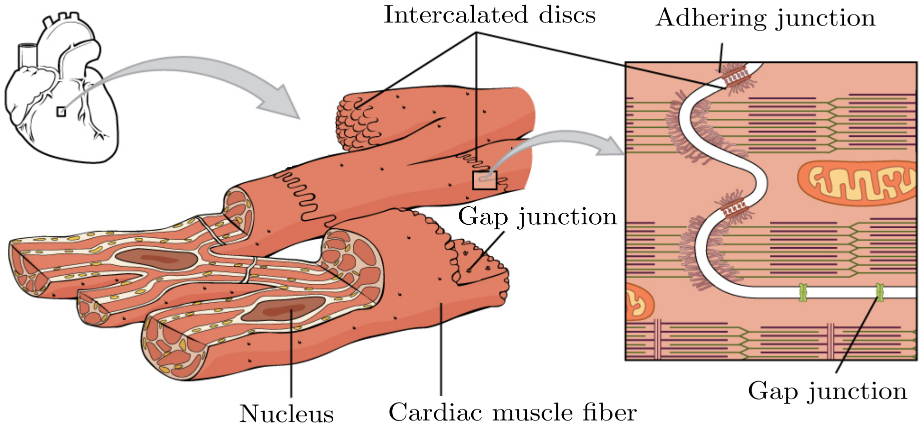

Figure 2.14: Cardiac muscle cell (adapted from [51]).

2.5 Myocardial Cell and Cellular Structures

The human heart exists of different cell types . Roughly the cell types can be classified in two categories the contractile cells and the conductile cells. The conductile cells belong to the cardiac conduction system. As explained previously, the conduction system is composed of cell clusters and special pathways, e.g. the sinoatrial node, the atrioventricular bundle, the purkinje fibers etc. Each of this components of the conduction system has specialized cell types. To the second category, the contractile cells, belong to cells of the working myocardium, which form most of the heart's tissue [102]. In the following the contractile cells are explained. Subsequently the characteristics of the conductile cells and the differences between them and the contractile cells are described. Cardiomyocytes belong to the striated muscle, to which also the skeletal muscle belongs. The mechanism of the contraction in cardiac cells and skeletal cells is similar, however, the electrical properties of the cells are different. Contraction of cardiac cells is not initiated from neuronal activity, as it is for the skeletal muscle. Instead, special cardiac cells in the sinoatrial node exist, which autonomously and spontaneously depolarize, and thus, initiate the activation. The activation in the heart continuous along the neighboring cells, which is not possible in the skeletal muscle, where the cells are insulated from each other. Additionally, the duration of the action potential is much longer in the cardiac muscle than in the skeletal muscle [102].

Cardiac muscle cells are connected through intercalated discs and form thereby fibers and fiber bundles (see Figure 2.14). The intercalated discs serve two main reasons. First, in the transverse parts of the discs the adhering junctions are located, which are used for tension transmission. Second, in the longitudinal part the gap junctions are located. The gap junctions facilitate ionic exchange between neighboring cells. The location of the gap junctions in the longitudinal part protects them from forces during contraction. Due to the intercalated discs and the thereby facilitated junctions the cardiac muscle arises as a functional syncytium, which can be seen as a three dimensional network [103, 281]. The length of a ventricular myocyte is around 72 µm and the diameter around 12 µm. However, the diameter varies for the myocytes of the left and right ventricle, the subepicardial and the subendocardial tissue and the atria [104]. Each myocyte of

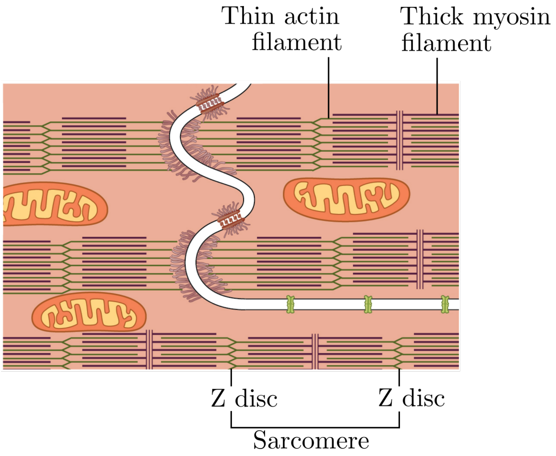

Figure 2.15: Sarcomere with actin and mysosin filaments in a cardiac muscle cell (adapted from [269]).

the heart is surrounded by fibrocollagenous connective tissue, which forms a fine network. This network support the myocytes, while transmitting force and prohibiting slippage. Additionally, a thicker network surrounds groups of myocytes bearing the sharing forces and prohibiting bad alignment of fiber bundles [157].

The myocyte is enclosed by the cell membrane, the so called sarcolemma, which separates the extracellular from the intracellular space. The extracellular space surrounds the cell and contains collagen fibers, water and electrolytes. The interior of the cell is filled up with cytoplasm, which contains water, lipids, carbon hydrates, salts and proteins. The liquid of the cytoplasm is called cytosol. Additionally, in the intracellular space the nucleus, the mitochondria, the myofibrils, the sarcoplasmatic reticulum and the cytoskeleton are located [306].

The membrane is formed by a thin lipid bilayer, which has a thickness of around $5\,\mathrm{nm}$ (see Figure 2.17a). It is almost impermeable for the most water soluble molecules. The membrane contains proteins, which span over the membrane or are attached to the surface of the membrane. The transmembrane proteins are responsible for the transportation of molecules, which allows the interaction between the cell and the environment (see e.g. Figure 2.17b) [306]. Additionally, the membrane of the myocyte has deep invaginations, the so called transverse tubules (t-tubules). The t-tubules are opened to the external environment and extend inwardly around each myofibril, to allow fast ionic exchanges deep in the myocyte. Within the cell and in close association with the t-tubules lies the sarcoplasmatic reticulum. This is a branching tubular network that surrounds the myofibril and its main function is to regulate the intracellular calcium concentration [195, 306]. Atrial cells have fewer t-tubules then ventricular cells and the specialized cells of the conduction system lack almost all t-tubules [36, 97, 300].

The mitochondria are surrounded by a doubled-layered membrane and are found near the sarcolemma and between myofibrils. They provide the energy for the myofilaments and the transmembrane pumps in the sarcolemma, due to generation of adenosine triphosphate (ATP) via oxygenation of nutrients. In the ventricular cells the mitochondria account for $25\,\%$ to $36\,\%$ of the volume and in the atria for $14\,\%$ to $20\,\%$ [306]. The myofibril has a cylindrical shape and consists of a long chain of repeating contractile units, the sarcomeres (see Figure 2.15). It takes about $45\,\%$ to $54\,\%$ of the ventricular cell volume and $41\,\%$ to $53\,\%$ of the atrial cell

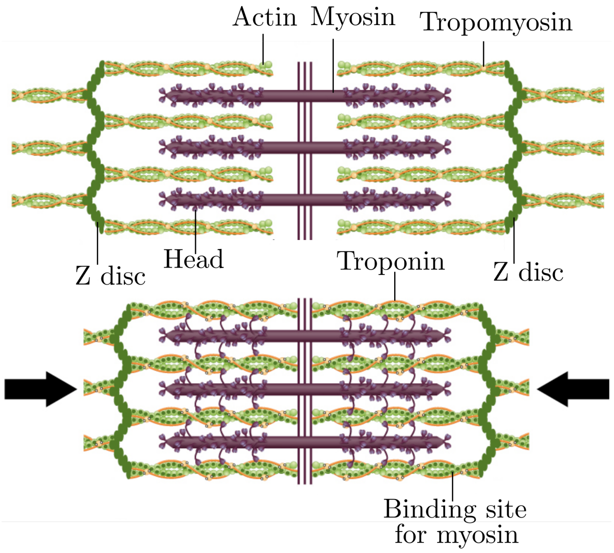

Figure 2.16: Sliding of a filament (adapted from [269]).

volume [306]. At both ends of the sarcomere the Z discs divides neighboring sarcomeres. Each sarcomere has a length of $1.6\,\mu\mathrm{m}$ to $2.2\,\mu\mathrm{m}$ [195]. The sarcomeres together with the Z discs give the muscle the striated appearance. The sarcomere contain precisely ordered arrays of thin and thick filaments, the myofilaments. Additionally, the sarcomere contains the elongated proteins titin and nebulin. The thin myofilaments consist of actin, whereas the thick filaments consist of myosin. The nebulin protein is weaved around the actin filament and thus helps to stabilize it during contraction and determines the length. The titin protein lies parallel to the myofilaments and is attached to one end to the Z disc and on the other hand to the myosin filament and thus holds the myosin filament in place [4].

The actin filament is closely associated with a set of accessory proteins. One of these proteins is tropomyosin. It is a long molecule that is attached along the groove of the actin helix. The other protein is troponin, which is a complex consisting of troponin T, troponin I and troponin C. Troponin I binds to actin and troponin T and thus inhibits actin binding to myosin. Troponin C serves as binding site for Ca^{2+} ions. During high cytosolic Ca^{2+} concentrations, Ca^{2+} bind to troponin C and leads thus to a conformation change in the troponin complex allowing actin-myosin binding. This process is reversed when cytosolic Ca^{2+} concentration decreases [195].

Thin filaments are attached to the Z disc and extends toward the middle of the sarcomere. The thick filaments overlap with the thin filaments in the middle of the sarcomere. The shortening of the sarcomere is caused by the sliding of myosin filaments past the actin filaments. During this process the length of the myosin and actin filaments does not change. The thick myosin filaments walk toward the Z disc driven by independent myosin heads which interact with the actin filaments (see Figure 2.16). Every myosin filament has around 300 heads and every head cycles about 5 times per second during a rapid contraction. Thus the actin and myosin filaments slides past each other in rate up to $15\,\mu\mathrm{m\,s^{-1}}$ and the sarcomere shortens in less than 1/50th of a second about $10\,\%$ of its length. The rapid and synchronous shortening of many sarcomeres in a myofibril enables the contraction of the heart [4].

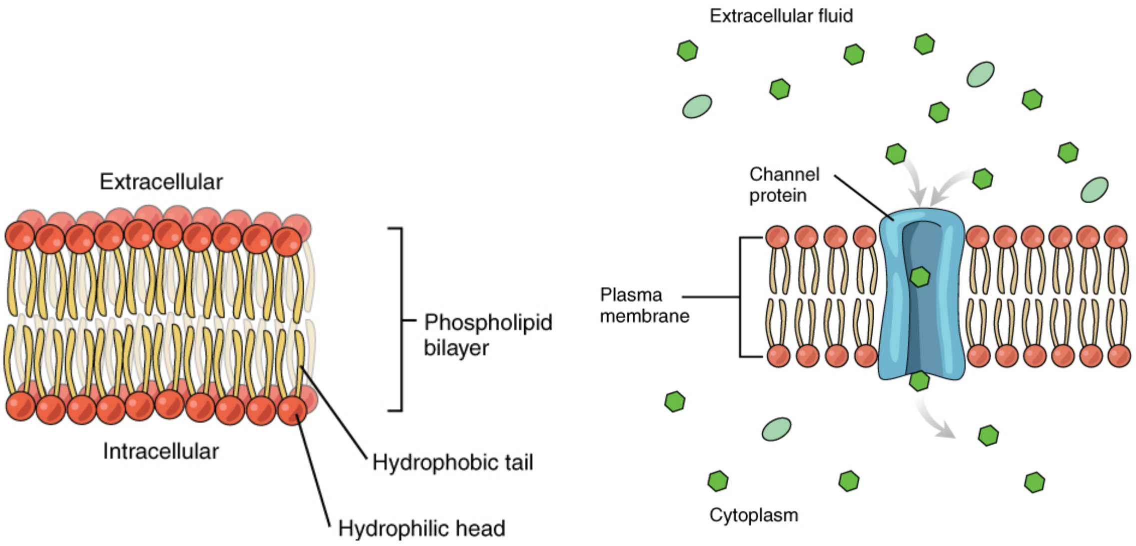

(a) Lipid bilayer

(b) Ion channel

Figure 2.17: (a) The phospholipid bilayer consists of hydrophobic tails and hydrophilic heads. The hydrophobic tails are pointing inside, which makes the membrane impermeable for polar molecules. (b) The ion channel is a transmembrane protein, which allows specific ions to pass in open state (adapted from [269]).

2.6 Molecular Functions of the Heart

2.6.1 Ionic Transportation

The cell membrane consists of a lipid bilayer with the hydrophobic tails pointing inside (see Figure 2.17a). Due to the hydrophobic inside, it is almost impossible for polar molecules to pass through. This is important for the cell to maintain the concentration of solutions if a concentration gradient exist towards the outside. However, it is necessary for the cell that certain polar molecules can pass through the membrane, for example to ingest essential nutrient, to excrete metabolism end-products, and to regulate the intracellular concentration of different ions. The transport of inorganic ions and small water soluble organic molecules is performed through different transmembrane proteins [4]. Transmembrane proteins are present in different forms in all cell membranes and they are defined by the ion type that is able to pass through. The most important categories of transmembrane proteins are ionic channels and transporter. In cardiac cells the most important transmembrane proteins are the sodium channel, calcium channel and potassium channel, the Na^+-Ca^{2+} exchanger, the Na^+-K^+ pump and the calcium pump [306].

Transporter bind the solute and undergo conformational changes to transport the solute through the membrane. In contrary, the channel interact hardly or not at all with the solute and in open state it allows the passage through the membrane as through pores (see Figure 2.17b). While transporter could be involved actively or passively in the transportation of molecules, the transportation through channels is always passive. The passive passage through channels is much faster. However, the passive transportation is limited by the concentration gradient and, additionally, in case of charged molecules it is also limited by the membrane potential. This means that the probability is high that a molecule moves to the other side if there prevails a lower concentration or a different charge. Active transporters, also called pumps, can be coupled to an energy source or make use of the ionic gradient for the transportation. Pumps are able to transport the molecules also against the electrochemical gradient [4].

2.6.1.1 Ion channel

Channel proteins form in contrast to transporter hydrophilic pores through the membrane (see Figure 2.17b). One important group of channel proteins for cardiac cells are the gap junctions, which build permeable connections between two adjacent cells. Gap junctions are relatively large permeable pores, which only connect cell interiors. Such large sized pores would pose a problem if they connect the cell interior with the extracellular space. Hence, the channel proteins that connect the interior of the cell with the extracellular space are narrow, highly selective and able to rapidly change their state between open and close. These proteins are mainly involved in the transport of ions and therefore called ion channels. It is possible for around 100 million ions to pass through open ion channels in one second. This is 10^5 times faster than in the fastest transporter protein. The channels do not have the ability to interact with an energy source to perform active transport. Hence, the passage through the channel is always in direction of the electrochemical gradient.

The main function of channels is to allow fast diffusion of inorganic ions through the membrane in the direction of the electrochemical gradient. An important property of channels is the ion selectivity; only a few inorganic ions are able to pass. This is due to the shape of the channel. The channel is narrow and the ions almost have to touch the walls of the pore, so that only ions of a specific size and charge can flow through (see Figure 2.17b). The ions also have to release all their bounded water molecules when passing through. An important property of the channels is the controlled change between open and closed state. This change is triggered by an electrical or chemical stimulus. Most channels have three states: the closed state, the open state and the inactive state. In the inactive state the channel is closed, but unable to open. These states are important for the propagation of the electrical signal in cardiac muscle cells [4].

The channels can be divided into two different types depending if they respond to an electrical or a chemical signal. The voltage-gated channel change their state in response to an electrical signal. Most of the channels responsible for the action potential are voltage-gated channels including the fast Na^+ channel, the slow Na^+ channel, the L-type Ca^{2+} channel, the T-type Ca^{2+} channel, the inward rectifier K^+ channel, the transient outward K^+ channel and the delayed rectifier K^+ channel. The sodium channels are responsible for the initiation and propagation of action potentials in cardiac cells [63]. Calcium channels are involved in different processes in the heart. They are for example responsible for automaticity in the sinoatrial and atrioventricular node but also for excitation contraction coupling [301]. Different types of potassium channels are responsible for the action potential amplitude, waveform and duration [246].

The second type of channels are the receptor-gated ones, which change their state in response to chemical signals. One important receptor-gated channel is the calcium activated channel, which gets activated by high cytosolic calcium [195]. The calcium channel in the sarcoplasmatic reticulum plays an important role in the contraction of the myocyte. Induced by a small increase of calcium concentration in the cytoplasm, the channel releases the calcium from the

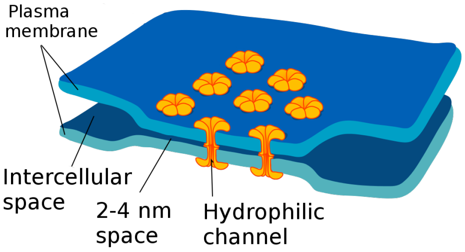

Figure 2.18: Gap junctions (adapted from [305]).

sarcoplasmatic reticulum into the cytoplasm. Due to this activation process, this channel is called calcium induced calcium release channel [307]. The contribution of the channels to the action potential is described in paragraph 2.6.2 in more detail.

2.6.1.2 Gap Junctions

Gap junctions are direct passages from the cytoplasma of one cell to the cytoplasma of a neighboring cell. They are located at the intercalated discs (see Figure 2.14). This intercellular connections allow neighboring cells to exchange molecules, and thus, to communicate. Between two adjacent cells is a small gap of around $2\,\mathrm{nm}$ to $4\,\mathrm{nm}$ width (see Figure 2.18). This gap is crossed by channel building proteins. These channels establish and electric connection between cells. Thus, if an electric impulse is injected into a cell, the neighboring cell is also immediately electrically stimulated. This is possible via the fast flux of ions through the gap junctions that transport electric charge.

2.6.1.3 Transporter and Active Transportation

Every transporter has one or more specific binding sites for the solute. It transports the solute through the lipid bilayer by changing its conformation. The modification of the conformation is reversible and independent whether the solute binding site is occupied or not. An important group of transporter are the ATP driven pumps, which transports solutes uphill by performing hydrolysis of ATP, i.e. releasing energy, which was stored in the high-energy bonds of ATP. For the cell the P-type pumps are the most important ATP driven pumps. The name derives from phosphorylization (couple with a phosphoryl group) during the pumping cycle. They are mainly responsible for maintaining the gradients of Na^+ , K^+ , H^+ and Ca^{2+} across cell membranes.

In the cytosol of the cells a very low concentration of Ca^{2+} is prevailed in contrast to the much higher concentration in the extracellular space. Thus, even a small influx of Ca^{2+} increases significantly the concentration of free Ca^{2+} in the cytosol. The fast flow down the steep concentration gradient of Ca^{2+} ions is used to transmit signals fast over the cell membrane. Thus, it is important for the cell to maintain the low concentration in the cytosol. This is done by Ca^{2+} transporters, which actively pump Ca^{2+} out of the cell. One of these transporters is the P-type Ca^{2+} ATPase. The Ca^{2+} pump is found in the membrane of sarcoplasmatic reticulum of the muscle cell. The Ca^{2+} pump accounts for about $90\,\%$ of the proteins in this organelle. The sarcoplasmatic reticulum forms a network of tubular sacs in the cytoplasm and serves as an intracellular storage of Ca^{2+} ions. If an action potential depolarizes the plasma membrane of a muscle cell, Ca^{2+} flows

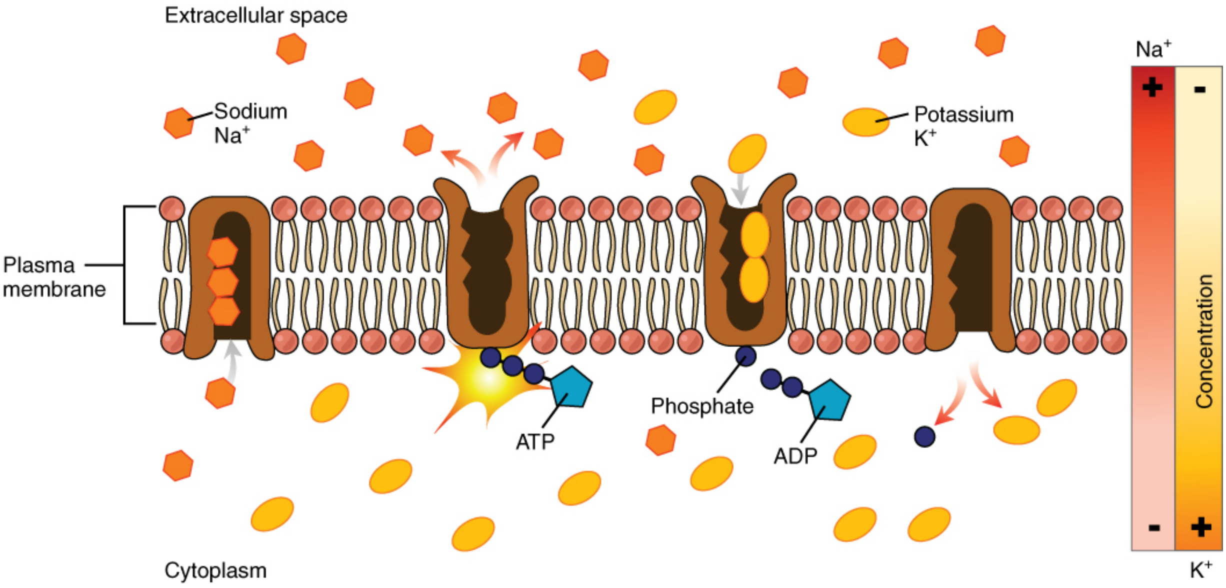

Figure 2.19: Pump Na^+-K^+ P-type ATPase(adapted from [269]).

through the Ca^{2+} releasing channels from the sarcoplasmatic reticulum in the cytosol and stimulates the contraction of the muscle cell. The Ca^{2+} ATPase pumps the Ca^{2+} from the cytosol back into the sarcoplasmatic reticulum [4].

Another pump which can be found in the sarcolemma in almost all vertebrates cells is the Na^+-K^+ P-type ATPase (see Figure 2.19). This pump is responsible for the maintenance of the high concentration of K^+ inside the cell and the low concentration outside and the low concentration of Na^+ ions inside and the high concentration outside [4, 173]. In one transportation step three sodium ions are transported outside and two potassium ions are transported inside. The activity of the pump depends on the sodium and potassium concentrations, the transmembrane voltage and the temperature [307]. The Na^+-Ca^{2+} exchanger is the primary transporter responsible for the removal of intercellular Ca^{2+} [173]. In one transportation step three sodium ions are transported inside the cell and one singe calcium ion is transported outside. This exchange can also work in opposite direction, and thus, serve as calcium entry mechanism [173, 307].

2.6.2 Action Potential

An electrical impulse which exceeds a certain threshold triggers an explosion of electrical activity. This results in a depolarization of the cell membrane and a subsequent repolarization back to the resting potential. This process is referred to as action potential. In cardiac cells different types of action potential occur. The biggest difference between nonpacemaker and pacemaker cells is their action potentials. Pacemaker cells are able to depolarize spontaneously, while nonpacemaker cells need a stimulus from adjacent cells to depolarize. Action potential of cardiac cells differ from action potential in nerve cells and skeletal muscle cells. The main difference is in the duration of the action potentials. A cardiac muscle cell of the ventricle has an action potential which lasts from $200\,\mathrm{ms}$ to $400\,\mathrm{ms}$, while the action potential duration in nerve cells is about only $1\,\mathrm{ms}$ to $2\,\mathrm{ms}$ and in skeletal muscle cells about $2\,\mathrm{ms}$ to $5\,\mathrm{ms}$ [195].

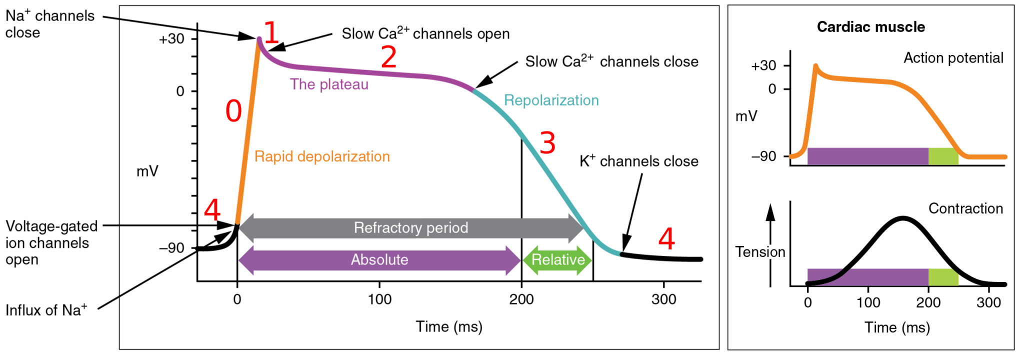

(a) (b)

Figure 2.20: Action potential curve. The five phases during the cycle are the rapid depolarization, the plateau and the repolarization phase, which are caused by in- and outflux of different ions. The tension development in cardiac muscle cell is depending on the action potential and Ca^{2+} ions in the cytosol of the cell (adapted from [269]).

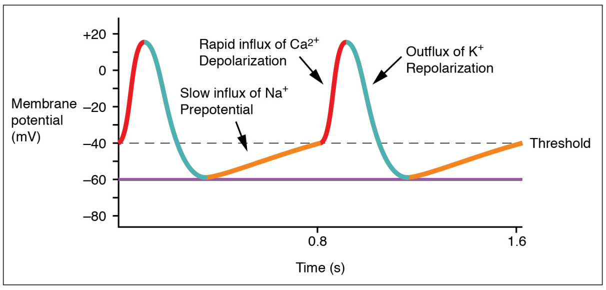

Figure 2.21: Action potential of the sinus node (adapted from [271]).

2.6.2.1 Nonpacemaker Action Potential

The plasma membrane of a muscle cell contains voltage-gated channels and transporter, which are the fundamental elements for the formation of an action potential. An action potential is triggered by a depolarization of the plasma membrane, i.e. a shift of the membrane potential to a less negative value. Repolarizations is the inverse process, thus, a shift of the membrane potential from a positive value back to the negative value. The action potential cycle in cardiac cells depends mostly on three ions: Ca^{2+}, Na^{+} and K^{+} (see Figure 2.20). Controlled by channels and transporter and these three ions the action potential cycle can be described in five phases.

In resting state (phase 4) nonpacemaker cells have a potential difference between $80\,\mathrm{mV}$ to $90\,\mathrm{mV}$ across the cell membrane. By convention, the outside of the cell is set as zero potential, and thus, the inside is negative with respect to the outside [357].

Phase 0 is the fast depolarization of the action potential. To initiate this steep increase ions enter the cell through gap junctions from a depolarized adjacent cells. Reaching a threshold of approximately $-70\,\mathrm{mV}$, fast Na^{+} channels begin to open and cause small Na^{+} flows into the cell in direction of their electrochemical gradient. This channels are called fast, because they activate and inactivate very fast. The influx of Na^{+} ions further depolarizes the membrane which leads to the opening of additional fast Na^{+} channels. Thus, once initiated the process becomes self-amplified and causes the membrane to depolarize rapidly. In a fraction of a millisecond the electrical potential of the membrane moves form the resting potential of $80\,\mathrm{mV}$ to $90\,\mathrm{mV}$ towards the the Na^+ equilibrium potential of approximately $60\,\mathrm{mV}$. Nevertheless, the Na^+ equilibrium potential is never reached due to fast closure of the channels after opening, the weaker driving force of the electrochemical gradient and the begin of repolarization fluxes in the late upstroke phase. The maximum potential which is reached is around $35\,\mathrm{mV}$ [357].

Phase 1 is the first repolarization following the fast depolarization of the action potential. This phase varies between different cell types of the heart and in nodal cells it is almost absent [220]. Voltage-gated channels open at approximately $-30\,\mathrm{mV}$. The current responsible for the depolarization phase is the transient outward current. It is composed of two currents including the larger K^+ outward current, which is mainly responsible for the depolarization, and the smaller Ca^{2+} current, which is more important during Ca^{2+} overload conditions.

Phase 2 is the so called plateau phase after the first repolarization phase. During this phase the membrane potential remains almost constant. This long plateau phase in cardiac cells is a major difference to nerve and skeletal muscle cells, where no such phase exists. Responsible for this plateau are the Ca^{2+} inward current and the K^+ outward current. Additionally, a small amount of fast Na^+ channels inactivates slowly which allows a small flux of Na^+ ions to contribute to the inward currents. The Ca^{2+} channel, which activates at $-40\,\mathrm{mV}$, results in a maximum current at approximately $0\,\mathrm{mV}$. This current is called the L-type Ca^{2+} current. The L-type Ca^{2+} current is the central aspect for many functions. The influx of Ca^{2+} ions during plateau phase triggers the opening of the calcium induced calcium released channels in the sarcoplasmatic reticulum, which in turn releases Ca^{2+} from the sarcoplasmatic reticulum into the cell. This Ca^{2+} ions initiates the mechanical contraction. L-type Ca^{2+} channel takes a few hundred milliseconds to inactivate.

Phase 3 follows the plateau phase and is the final **repolarization** phase. The L-type Ca^{2+} channel inactivates. Thus, the Ca^{2+} influx decreases. Additionally, the delayed rectifier K^+ current increases resulting in a repolarization of the membrane potential towards resting potential.

Phase 4 is the resting potential. It is near the equilibrium potential of K^+, since the cell membrane has a high permeability for K^+ ions in comparison to other ions. The resting potential is maintained by the Na^+-K^+ pump. The membrane potential stays at the resting potential until a new stimulus from a neighboring cell arrives and depolarizes the membrane, which would lead to the opening of the Na^+ channels [357].

The action potential in atrial cells is similar to the ventricular action potential. The major difference is the brief or almost absent plateau phase, due to a junctions of phase 1, 2 and 3. Cells in the purkinje fibers have an action potential similar to the ventricular cells. However, they have a more prominent phase 1 and a longer plateau phase and additionally they may feature also automaticity, i.e. spontaneous phase 4 depolarization (see Figure 2.13) [357].

2.6.2.2 Pacemaker Action Potential

The action potential in the pacemaker differs from the one of the nonpacemaker cells in the absence of a true resting potential. This is caused due to the unstable membrane potential between two action potentials and spontaneous depolarization. The spontaneous depolarization is also called phase 4 depolarization. The maximum diastolic potential in pacemaker cells is less negative (approximately $-55\,\mathrm{mV}$) in comparison to nonpacemaker cells, due to the lower permeability for K^+ ions [357]. Once the spontaneous depolarization reaches a threshold (approximately $-40\,\mathrm{mV}$) an action potential occurs. The phase 0 of the action potential is dependent from Ca^{2+} ions (through L-type Ca^{2+} channels) rather than Na^+ ions, which are negligible. T-type Ca^{2+} channels, which are absent in ventricular cells, activate at more negative potential of approximately $-60\,\mathrm{mV}$ and thus provide inward currents during phase 4 depolarization [143, 225]. However, the contribution of the T-type channels in pacemaker activity is not yet fully understood [301]. Nevertheless, T-type channels have been shown to play an important role in cardiac remodeling and arrhythmiogenesis [112, 261]. In the muscular sleeves of the pulmonary veins they potentially trigger spontaneous activation [71]. The upstroke in phase 0 is also less steep, which results in a slow conduction between nodal cells. Phase 1 is absent and phase 2 is very small. During phase 3 the membrane potential repolarizes to maximum diastolic potential. The difference between sinoatrial and atrioventricular nodal cells is that in atrioventricular nodal cells the phase 4 depolarization rate is slower. Therefore, the sinoatrial node is the primary pacemaker of the heart, but in case of failure or signal blockade the atrioventricular node is able to initiate activation in the ventricle.

Here are the main currents and channels responsible for the action potential. However, many more currents and channels contribute to the action potential. More details about various currents and channels can be found in [47, 54, 63, 198, 221, 246, 264, 301, 349, 357].

2.6.2.3 Stretch Activated Channels

Beside the important process of excitation-contraction coupling also mechano-electric coupling is possible. Most of the channel in cardiac myocyte are voltage-gated. However, a few channels are activated by mechanical stimulation. Mechanical stimulation could lead to changes in the transmembrane potential and in action potential morphology [198]. Stretch could contribute to depolarization, which triggers ectopic excitation. Persistent stretch could lead to arrhythmia, due to heterogeneities in membrane potentials, activation possibilities and refractory times [155, 198].

2.6.3 Modulation of Automaticity

The currents responsible for depolarization in pacemaker cells are influenced by neurotransmitter. Neurotransmitter are able to increase or decrease the slope of phase 4 depolarization, which leads to a shorter or longer time to reach the threshold. Neurotransmitter can activate K^+ channel that leads to hyperpolarization of the cell, i.e. the maximum diastolic potential gets more negative. This causes an increase of the time to reach the threshold and a decrease in the slope of phase 4 depolarization. The longer it takes to reach the threshold the more the heart rate is decreased. An increase of the slope in phase 4 depolarization leads to a faster heart rate.

2.6.4 Excitation-Contraction Coupling

Cardiac excitation-contraction coupling is the process which leads to a contraction of cardiac myocytes due to an electrical activation. The key ingredient for the contraction process are Ca^{2+} ions [35]. An increase of the cytosolic Ca^{2+} concentration triggers actin and myosin filaments to slide over each other. The increase in cytosolic Ca^{2+} occurs due to Ca^{2+} influx from the extracellular space and due to release of ions from intracellular pools [105].

As explained previously membrane depolarization leads to an opening of L-type Ca^{2+} channels which results in a small influx of Ca^{2+} ions into the cell from the extracellular space. This influx starts during phase 2, but has its importance during plateau phase. L-type Ca^{2+} channels are located primarily near the ryanodine receptors at the junctions of the sarcolemma with the sarcoplasmatic reticulum in the t-tubules [315]. The sarcoplasmatic reticulum is a extensive branching network surrounding the myofilaments [195]. Since the t-tubules are deep invaginations into cardiac myocytes but belong to the external sarcolemma, they allow the influx of external Ca^{2+} ions to occur deep in the myocyte. One end of the sarcoplasmatic reticulum reaches to the t-tubules. Pouches are located at this end of the sarcoplasmatic reticulum, which are called terminal cisternae. Terminal cisternae contain ryanodine receptors, which are Ca^{2+} gated Ca^{2+} channels. Additionally, to the L-type Ca^{2+} channels also the reversible Na^+-Ca^{2+} exchanger can contribute to the influx of Ca^{2+} depending on the Ca^{2+} and Na^+ concentrations [35].

Only a small influx of Ca^{2+} ions is sufficient to activate the release process in the ryanodine receptors [35]. Ca^{2+} ions enter the cytosol mainly through ryanodine receptors from the sarcoplasmatic reticulum and marginally from the extracellular space. However, without the Ca^{2+} ions entering from the extracellular space no contraction would occur [197]. The Ca^{2+} ions that are stored in the terminal cisternae of the sarcoplasmatic reticulum increase the concentration 10-fold when they enter the cytosol [210, 227]. At low Ca^{2+} concentration the troponin complex pulls tropomyosin out of its binding groove to the actin filament in such a way that it inhibits actin binding to myosin heads, and thus, preventing any force generating interactions. An increase in Ca^{2+} concentration leads to troponin C binding to Ca^{2+} ions, which in turn is followed by a conformational change in the troponin-tropomyosin complex. This conformational change leads to a movement towards the groove of the actin filament, and thus, a freeing of the binding sites of the actin molecule to the myosin heads [320]. Thus, the myosin heads are now able to walk along the actin filament leading to a shortening of the sarcomere (see Figure 2.16). The relaxation of the muscle cell follows the Ca^{2+} removal from the cytosol. This removal is performed from the P-type Ca^{2+} ATPase in the membrane of sarcoplasmatic reticulum and the sarcolemma and the Na^+-Ca^{2+} exchanger in the sarcolemma. The P-type Ca^{2+} ATPase in the membrane of sarcoplasmatic reticulum moves the intercellular Ca^{2+} back into the reservoirs of the sarcoplasmatic reticulum. With decreasing cytosolic Ca^{2+} concentration the myosin heads detach from the actin molecule and the conformational change in the troponin-tropomyosin complex reverses releasing its bound with Ca^{2+}.

2.6.4.1 Walking of Myosin Heads

The contraction of the sarcomere and thus the contraction of the muscle, is possible due to the power stroke of the myosin head and the walking of the head along the actin molecule. The contraction occurs if the cytosolic Ca^{2+} concentration is high (see Figure 2.22). The myosin

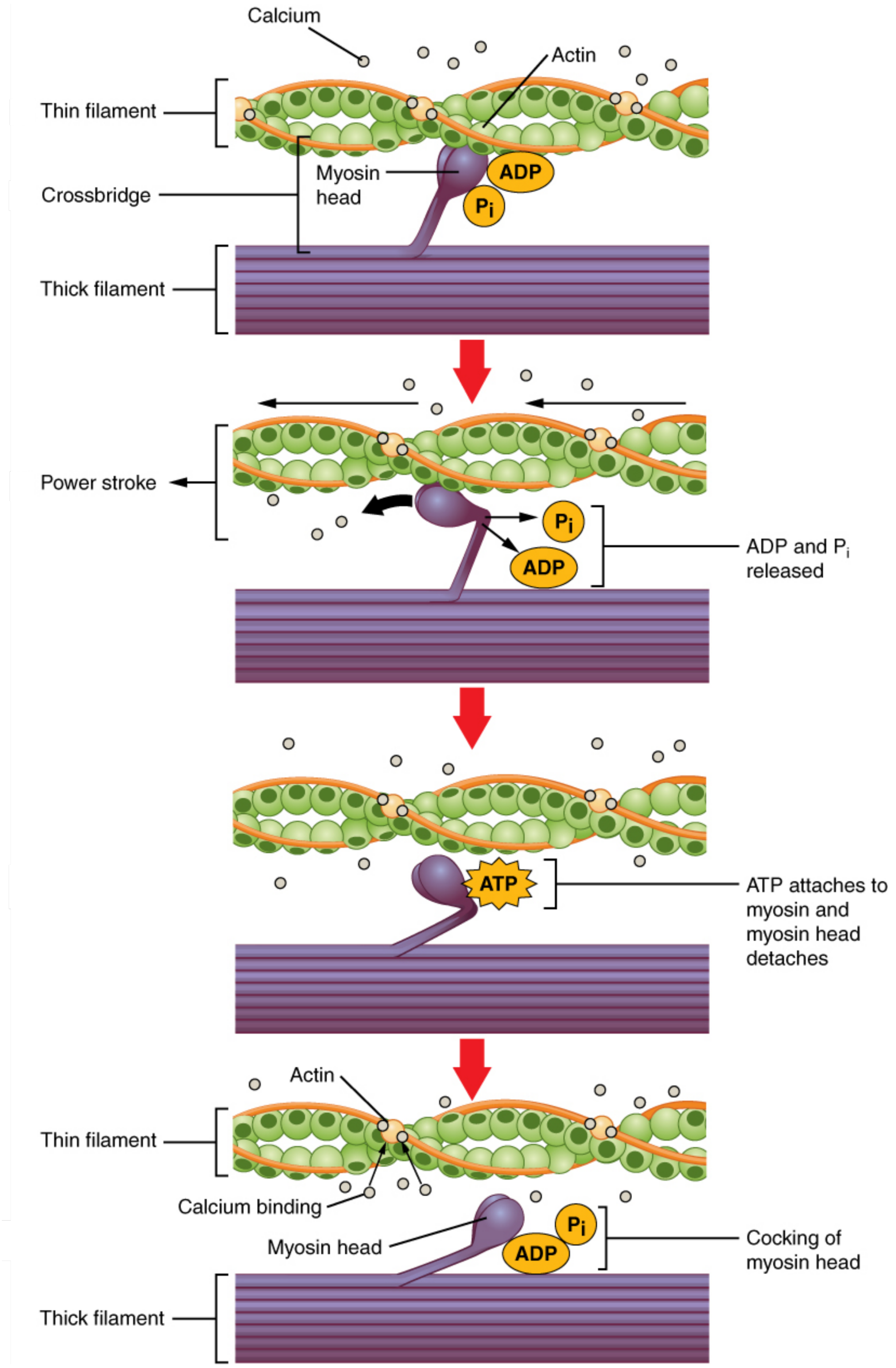

Figure 2.22: Cycle of molecular mechanism of contraction (adapted from [50]).

filaments are motor proteins which use the conformational changes in their ATP binding sites to establish a cyclic interaction with the actin filament. The cycle contains ATP binding, ATP hydrolysis and ADP release and the propelling of a filament in a single direction to a new binding site on the actin filament. The motor protein responsible for such a movement uses energy gained from ATP binding and hydrolysis to force a large movement in a part of the protein. Every walking step of the myosin on the actin filament is generated due to the swinging of the lever arm.

The cycle of binding, release and power stroke can be subdivided into 4 steps:

Attached In the attached state the myosin head is locked tightly to the actin filament without any bound nucleotide. This configuration is also called the rigor configuration, named so because it is responsible for the rigor mortis, i.e. the stiffening of the muscles after death. In a contracting muscle this state is very short, because it is rapidly terminated by the binding of ATP and the release of myosin actin binding.

Released In the released state the myosin head binds to an ATP molecule. When an ATP molecule binds on the back of the myosin head it produces immediately a slight conformation change in the regions of the actin binding sites. Thereby the affinity of the head to actin is reduced and the myosin can move along the actin filament.

Cocked During the cocked state the myosin head encloses the ATP molecule and thereby performs a conformational change in the liver arm so that the head is displaced by a distance of about 5 nm. The ATP molecule is hydrolysed, but ADP and the inorganic phosphate P stay tightly bound to the protein.

Force-generating The next state is the force generating state. The myosin head binds weakly to a new binding site on the actin filament. This causes the release of the inorganic phosphate produced by the ATP hydrolysis and simultaneously to a strong bound of the myosin head to the actin filament. This again triggers the power stroke, which is the force generating conformation change. Afterwards the myosin head regains its original conformation. The head loses the bound ADP during the power stroke.

Attached At the end of the cycle the myosin head is again in the rigor conformation, tightly bound to the actin filament. However, the important difference is that now the head is bound to a new site of the actin filament [4, 197].

3 Electrophysiology

The mathematical model of the electrophysiology is based on the electrical principles at the level of single cells as well as the electrical principles of the whole heart described in Section 2. Changes of electrical load is the fundamental property that enables the excitation of the heart muscle and, hence, the contraction of the heart muscle cells. Thus, without electrical fields life as we know today would not be possible.

In this section, first some basic principles are described, which are necessary to model electrophysiology. Afterward, the electrical principles of the cell membrane are explained. Then the definition of the membrane potential is derived for the simpler Nernst potential and the more complex Goldman-Hodgkin-Katz potential, which is needed if different types of ions are present. Finally, the electrical circuit model for the cell membrane is explained and the conduction over a three dimensional heart wall is derived.

3.1 Basic Principles

Electrochemical Potential The Gibbs energy is a thermodynamical potential. The chemical potential is the partial molar Gibbs energy of a substrate, i.e. the chemical potential μ_k of the component k in a mixture is defined as the change of the Gibbs energy of the system, if an infinitesimal amount of substance of this component is added and the temperature and the pressure remain constant:

$$\mu_k = \left(\frac{\partial G}{\partial n_k} \right)_{p,T,n_{j \neq k}} \tag{3.1}$$

with the molar Gibbs energy G, n_k the amount of substance k, the pressure p, and the temperature T.

For an ideal mixture the chemical potential μ_k for the component k is defined as

$$\mu_k = G_k(p, T) + RT \ln(x_k) \tag{3.2}$$

and the molar Gibbs energy G for an ideal homogeneous mixture as

$$G = \sum_k n_k \mu_k, \tag{3.3}$$

with R the molar gas constant, $x_k = \frac{n_k}{\sum_k n_k}$ the mole fraction of substance k, and G_k the molar Gibbs energy for the pure substance k [20, 185].

If, additionally to the chemical potential, an electrical potential is present, i.e. the substances are not electrically neutral, the resulting potential is called the electrochemical potential $\tilde{\mu}_k$ and can be calculated as

$$\tilde{\mu}_k = \mu_k + zF\Phi \tag{3.4}$$

with μ_k the chemical potential of the substance k without electrical potential, z the charge number, F the Faraday constant, and Φ the electrical potential. In case that G_k is defined as the chemical potential of the concentration $1\,\mathrm{mol\,l^{-1}}$, this can also be expressed in terms of concentrations. as

$$\tilde{\mu}_k = G_k + RT\ln(c_k) + zF\Phi\,. \tag{3.5}$$

Conservation Law The conservation law for the concentrations (or another entity) in a region can be written as

$$\frac{\mathrm{d}}{\mathrm{d}t}\int_\Omega c_k\,\mathrm{d}V = \int_\Omega f_k(c_k)\,\mathrm{d}V - \int_{\partial\Omega} \boldsymbol{J}_k \cdot \mathbf{n}\,\mathrm{d}A \tag{3.6}$$

with $c_k : \mathbb{R}^d \to \mathbb{R}$ the concentration of the substance k, $f_k(c_k)$ the source term, i.e. the production density for the substance k, $\boldsymbol{J}_k$ the flux density, $\mathbf{n}$ the outward pointing normal, and $\partial\Omega$ the boundary of the region Ω. Applying the divergence theorem $\int_\Omega \nabla\cdot\boldsymbol{J}\,\mathrm{d}V = \int_{\partial\Omega}\boldsymbol{J}\cdot\mathbf{n}\,\mathrm{d}A$, also known as Gauss's theorem, and assuming an arbitrary region Ω, thus, omitting the integrals, the equation becomes

$$\frac{\mathrm{d}}{\mathrm{d}t}c_k = f_k(c_k) - \nabla\cdot\boldsymbol{J}_k\,. \tag{3.7}$$

This conservation law contains a flux term $\boldsymbol{J}_k$ and a source term f_k. Their definitions are depending of the model [186].

Fick's Law of Diffusion The flux of an entity is proportional to the concentration gradient of this entity

$$\boldsymbol{J}_k = -\boldsymbol{D}_k\nabla c_k\,. \tag{3.8}$$

The negative sign is due to the matter flowing in direction to the concentration gradient, that means when the gradient is negative $\boldsymbol{J}_k$ should be positive. The diffusion coefficient $\boldsymbol{D}_k$ is depending on the properties of the matter. The equations can also be applied to thermal energy when c_k describes a temperature [20, 186]. Analogous to the Fick's law of diffusion Ohm's law describes the charge transport as

$$\boldsymbol{J} = -\kappa\nabla\varphi\,, \tag{3.9}$$

with $\boldsymbol{J}$ the current density, κ the conductivity, and φ the electric potential.

With Fick's law the conservation law (Equation (3.7)) can be written as

$$\frac{\mathrm{d}}{\mathrm{d}t}c_k = f_k(c_k) + \nabla\cdot\boldsymbol{D}_k\nabla c_k\,. \tag{3.10}$$

3.2 Electrical Properties of the Membrane

The cell membrane separates the interior of a cell from the exterior environment. The membrane has the property that some molecules are able to pass freely, while for other molecules the passage is restricted. The restricted passage is very important to maintain concentration differences between cytosol and extracellular space. Due to transmembrane proteins in the plasma membrane transport of molecules through the membrane is variable and changes over time. Depending on the surrounding conditions transmembrane proteins can open or close, i.e. be active or inactive. Different types of transmembrane proteins including passive channels and active transporters, enable passage through the membrane. The channels allow ions to flow only in the direction of their electrochemical gradient, while the active transporters are able to use energy to transport the ions also against their electrochemical gradient. The difference in the ion concentration between the exterior and the interior of a cell due to the selective transport through the membrane allows the formation of a potential difference across the plasma membrane. The electrical properties of the cell membrane are an indispensable attribute for the propagation of an electrical signal. The electrical signal consists of a depolarization of the cell membrane and propagation occurs through a depolarization wave spreading over tissue. Hence, without a membrane which is selective depending on the environment that would not be possible. The bilayer of the membrane forms a medium for a highly electrical resistor that separates two solutes with electrolytes. The membrane together with the electrolyte solution near the membrane acts as a capacitor, in which the inner of the membrane is a dielectric [1].

3.3 Membrane Potential

The resistor properties of the membrane allow the existence and maintenance of an electrochemical potential, which is necessary for the propagation of an electrical signal. By having a membrane potential that is able to change very quickly it is possible to rapidly conduct a signal along the cell membrane. The cell membrane separates the intracellular and the extracellular solutions and due to different ion concentrations on both sides of the membrane an electrochemical gradient arises through the membrane.

3.3.1 Nernst Equilibrium Potential

The Nernst equilibrium potential describes the potential difference that results from a concentration difference between two compartments separated by a semipermeable membrane. In analogy to the cell we assume to have two compartments separated from each other through a selectively permeable membrane, one compartment being the intracellular space (cytoplasma) and one compartment being the extracellular space. In one compartment the concentration of the K^+ and A^- ions is much higher than in the other and the membrane is selectively permeable for K^+ ions (see Figure 3.1). Initially, each compartment is assumed to be electrically neutral, which implies that each K^+ is compensated by an A^- ion. Since the membrane is permeable to K^+ and due to the concentration gradient, K^+ ions tend to diffuse through the membrane from the side with the higher concentration to the side with the lower concentration (see Figure 3.1a). Despite the tendency of the K^+ ions to pass through the membrane in direction of the concentration gradient,

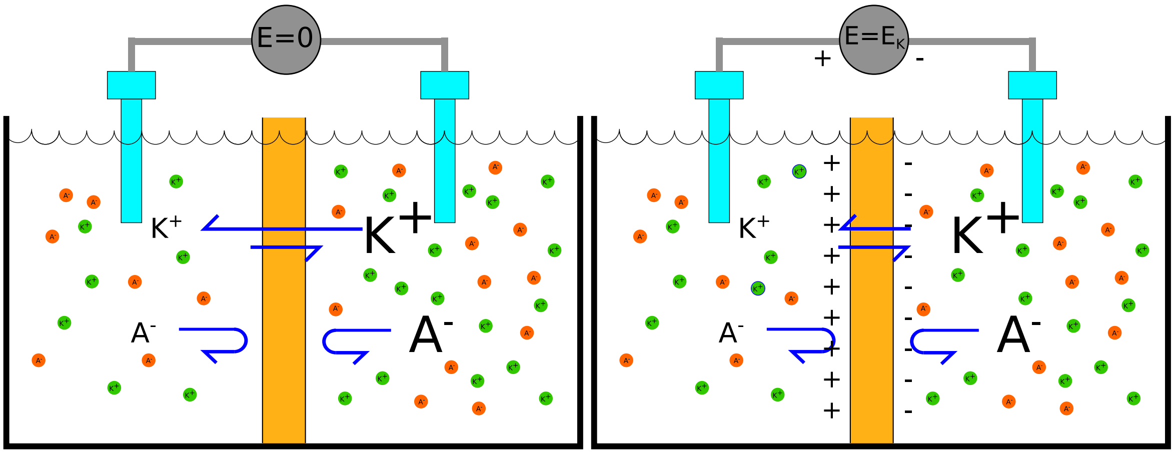

(a) Before diffusion through the membrane (b) After diffusion through the membrane

Figure 3.1: Illustration of the dynamics of a membrane potential in a 2-ion-system with two compartments.

the equalization of the concentrations of K^+ on both sides is not reached. This is due to the fact that the membrane is not permeable for A^- ions. When K^+ ions diffuse through the membrane charges are build up across the membrane, which cause the rising of an electrical field across the membrane (see Figure 3.1b). When the equilibrium is achieved, a concentration gradient still exists between the two compartments. The reason for this is the electrical potential gradient, which counteracts the concentration gradient. The flux of K^+ ions becomes zero, when the system is in equilibrium. This occurs when the potential gradient is exactly equal to the opposite concentration gradient. A zero flux does not mean that no ions pass through the membrane, but rather that the number of ions leaving the cell is the same as the number of ions entering the cell. The potential at which the equilibrium occurs is called the equilibrium potential. At equilibrium the number of K^+ ions is indifferent to the number of A^- ions in each of both compartments. This means that each compartment is not electrically neutral anymore. However, approximately one could say the concentrations remain unchanged, since only a small amount of ions is able to diffuse through the membrane due to the build up of a strong electrical field. Imbalance of charges occur only near the membrane. This small region of imbalance is called a Debye layer [186].

We can write the electrochemical potential (Equation (3.5)) for the substrate k that is able to diffuse through the membrane on the interior i and the exterior e of the cell as

$$\begin{aligned} \tilde{\mu}_k^i &= \mu_k^i + zF\Phi = G_k^i + RT\ln(c_k^i) + zF\Phi^i \\ \tilde{\mu}_k^e &= \mu_k^e + zF\Phi = G_k^e + RT\ln(c_k^e) + zF\Phi^e \end{aligned} \;. \tag{3.11}$$

At the equilibrium the difference between the interior and the exterior potential should be zero, such that

$$\begin{aligned} 0 &= \tilde{\mu}_k^i - \tilde{\mu}_k^e \\ &= G_k^i + RT\ln(c_k^i) + zF\Phi^i - G_k^e - RT\ln(c_k^e) - zF\Phi^e \,. \end{aligned} \tag{3.12}$$

The terms $G_k^i = G_k^e$ are equal since they are independent of the concentration and, thus, cancel out. Additionally, we define the membrane potential u as the difference between interior and

Ion	Plasma $[\mathrm{mmol}]$	Cytoplasma $[\mathrm{mmol}]$	Φ_{N} $[\mathrm{mV}]$
Na^+	145	10	67
K^+	4	150	-94
Ca^{2+}	1.8	10^{-4}	130
Mg^{2+}	1.5	0.8	8
Cl^-	120	20	-4.7

Table 3.1: Extra- and intracellular concentrations of ions and equilibrium potential E_{ion} in mammalian cardiac cells [61]. The concentrations of cytoplasmic Ca^{2+} ions refer to the free Ca^{2+} ions in the cytoplasma without the Ca^{2+} stores in the sarcoplasmatic reticulum.

exterior electrical potential $u = \Phi_i - \Phi_e$. Thus, the equilibrium potential can be calculated as the Nernst potential Φ_{N}

$$\Phi_{\mathrm{N}} = \frac{RT}{zF} \ln \left(\frac{c_k^i}{c_k^e} \right) , \tag{3.13}$$

with c_k^i and c_k^e the concentration of substance k in the interior and in the exterior space, respectively.

Equations (3.13) is the Nernst equation. Typical concentrations and equilibrium potentials for cardiac cells are shown in Table 3.1. In cardiac cells the membrane is highly permeable for potassium (K^+) ions and less permeable for other ion types. Hence, the equilibrium potential of the cardiac cell membrane is near the equilibrium potential of K^+ ions. However, in case that different ions types are present and the membrane is permeable for various ion types the Nernst equation cannot be applied to calculate the equilibrium potential anymore. If the membrane has zero net current it does not necessary mean that the current of each individual ion type is also zero. The influx of positive ions could be compensated by an influx of negative ions. Hence, for a membrane permeable to different ion types the equilibrium is more complicated to calculate.

3.3.2 Goldman-Hodgkin-Katz Equation

The membrane potential of the cell depends not only on K^+ ions but also on other ion types. For example sodium (Na^+), calcium (Ca^{2+}) and chloride (Cl^-) ions are also permeable through the membrane and therefore together with K^+ responsible for the membrane potential. Every type of ion has a different concentration gradient (see Table 3.1). These gradients are maintained by a multitude of passive channels and active transporters through the membrane. Because of unequal concentration proportion, e.g. $\frac{[K_e]}{[K_i]} \neq \frac{[Na_e]}{[Na_i]}$, it is not possible to reach an equilibrium. If an equilibrium for K^+ ions is reached, Na^+ ions are still not yet in equilibrium. The real membrane potential lies between the different individual Nernst equilibrium potentials.

Due to the first Fick's law we get the flux density of the diffusive part $\boldsymbol{J}_{diff}^k$ for the ion type k as

$$\boldsymbol{J}_{diff}^k = -\boldsymbol{D}_k \nabla c_k \tag{3.14}$$

and the flux density of the electrical part $\boldsymbol{J}_{el}^k$

$$\boldsymbol{J}_{el}^k = -\boldsymbol{D}_k \frac{c_k z_k F}{RT} \nabla \varphi \, . \tag{3.15}$$

Combining the diffusive part and the electric part of the flux, we obtain the Nernst-Planck equation as

$$\boldsymbol{J}^k = J^k_{diff} + J^k_{el} = -\boldsymbol{D}_k \left(\nabla c_k + \frac{c_k z_k F}{RT} \nabla \varphi \right) . \tag{3.16}$$

From the Nernst-Planck equations the Nernst equations can be obtained when setting the flux to zero and integrating over the cell membrane from the inside i to the outside e.

For the calculation over a cell membrane the Nernst-Planck equations can be written as a one-dimensional equations such as

$$\boldsymbol{J}^k = -\boldsymbol{D}_k \left(\frac{\mathrm{d}c_k}{\mathrm{d}x} + \frac{c_k z_k F}{RT} \frac{\mathrm{d}\varphi}{\mathrm{d}x} \right) . \tag{3.17}$$

Hereby the one-dimension direction x describes the direction through the membrane with $x = 0$ and $x = L$ being the beginning and the end of the membrane. For now we assume a constant electrical field through the membrane which means that although ions pass through the membrane the electrical field does not change. Thus, we can write $\frac{\mathrm{d}\varphi}{\mathrm{d}x} = -\frac{\Phi_i - \Phi_e}{L} = -\frac{\Phi}{L}$ with L the thickness of the membrane. Additionally, we define the concentrations $c_k(0) = c^i_k$ and $c_k(L) = [c^e_k]$ to be on each side of the membrane. With this assumptions and boundary conditions the Nernst-Planck equation can be solved as

$$\boldsymbol{J}^k = \frac{\boldsymbol{D}_k z_k F \Phi}{LRT} \left(\frac{c^i_k - c^e_k \exp\left(\frac{-z_k \Phi F}{RT}\right)}{1 - \exp\left(\frac{-z_k \Phi F}{RT}\right)} \right) . \tag{3.18}$$

With the constant permeability of the substance k through the membrane defined as $G_k = \frac{\boldsymbol{D}_k}{L}$ and multiplied with the amount of charge carried by mole zF we derive to the Goldman-Hodgkin-Katz equation for the current density I^k

$$I^k = \frac{G_k z^2_k F^2 \Phi}{RT} \left(\frac{c^i_k - c^e_k \exp\left(\frac{-z_k \Phi F}{RT}\right)}{1 - \exp\left(\frac{-z_k \Phi F}{RT}\right)} \right) . \tag{3.19}$$

Summing over all ion species which are present in the interior and exterior of the cell we get to the current density I for all substances

$$I = \sum_k I^k . \tag{3.20}$$

Since in general there does not exist any potential at which all individual currents are zero, we can only calculate the potential at which the net electrical current is zero, i.e. $I = 0$, hence,

$$I = \sum_k G_k z^2_k \left(\frac{c^i_k - c^e_k \exp\left(\frac{-z_k \Phi F}{RT}\right)}{1 - \exp\left(\frac{-z_k \Phi F}{RT}\right)} \right) = 0 . \tag{3.21}$$

The Goldman-Hodgkin-Katz potential Φ_{GHK} is defined as the solution to Equations (3.21). Considering only substances with valance $z_k = 1$ or $z_k = -1$, we can solve Equation (3.21) for

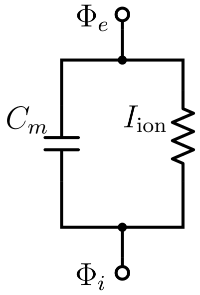

Figure 3.2: Electric Circuit model of the cell membrane

Φ_{GHK} as

$$\Phi_{\text{GHK}} = -\frac{RT}{F} \ln \left(\frac{\sum\limits_{\substack{k \\ z=1}} G_k c_k^i + \sum\limits_{\substack{k \\ z=-1}} G_k c_k^e}{\sum\limits_{\substack{k \\ z=1}} G_k c_k^e + \sum\limits_{\substack{k \\ z=-1}} G_k c_k^i} \right) . \tag{3.22}$$

For the cardiac cell with the ions K^+ , Na^+ and Cl^- we get the Goldman-Hodgkin-Katz potential

$$\Phi_{\text{GHK}} = -\frac{RT}{F} \ln \left(\frac{P_{\text{Na}^+}[\text{Na}^+]_i + P_{\text{K}^+}[\text{K}^+]_i + P_{\text{Cl}^-}[\text{Cl}^-]_e}{P_{\text{Na}^+}[\text{Na}^+]_e + P_{\text{K}^+}[\text{K}^+]_e + P_{\text{Cl}^-}[\text{Cl}^-]_i} \right) . \tag{3.23}$$

The Goldman-Hodgkin-Katz equation is in a way the general form of the Nernst equation, where the concentrations of the ions are weighted with the permeability coefficient. In case of higher K^+-ion permeability compared to Na^+ and Cl^- ions, i.e. $P_{\text{K}^+} \gg P_{\text{Na}^+}$ and $P_{\text{K}^+} \gg P_{\text{Cl}^-}$, Equation (3.23) leads to the Nernst equation (Equation (3.13)).

At the Goldman-Hodgkin-Katz potential the individual ions are not in equilibrium and, thus, fluxes of the ions through the membrane occur. Hence, the Goldman-Hodgkin-Katz potential is not a thermodynamic equilibrium potential. In the long term the fluxes over the membrane would cause a change of the concentrations in the interior and exterior of the cell and therefore lead to a change in the Goldman-Hodgkin-Katz potential. However, due to active transporter proteins in the cell membrane the concentration stays at a constant level. This potential is a stationary potential and only valid if concentrations and permeabilities do not change over time. Thus, the Goldman-Hodgkin-Katz potential is the resting membrane potential and occurs during the time when the action potential is back at the resting state and the arrival of a new stimulus, i.e. phase 4 of the action potential cycle (see Chapter 2) [1, 61, 186, 228].

3.4 Electrical Circuit Model of the Cell Membrane

The cell membrane can be modeled as a capacitor. The capacitance C can be described as

$$C = \frac{Q}{\varphi} \tag{3.24}$$

with Q the charge across the membrane and φ the voltage potential. Since the current I is $I = \frac{\mathrm{d}Q}{\mathrm{d}t}$, the capacitive current I_{cap} is

$$I_{cap} = C_m \frac{\mathrm{d}\varphi}{\mathrm{d}t}\,, \tag{3.25}$$

if C_m is constant. In the particular case of a membrane with ion channels and a potential difference between interior and exterior of the cell a simple electrical circuit model can be derived. The idea is to model the membrane as a capacitor in parallel with a resistor (see Figure 3.2). Thus, the transmembrane current I_m across the membrane is the sum of the capacitive current and the ionic current I_{ion} given by

$$I_m = C_m \frac{\mathrm{d}u}{\mathrm{d}t} + I_{\mathrm{ion}}\,, \tag{3.26}$$

with the transmembrane voltage potential $u = \Phi_i - \Phi_e$ and the membrane capacitance C_m.

3.4.1 Ionic Current Models

The ionic current I_{ion} describes the fluxes of ions into the cell and out of the cell. There exist many different models to describe I_{ion}. At the resting membrane potential, i.e. the Goldman-Hodgkin-Katz potential, the fluxes of the individual substances are not zero. They are only zero at the equilibrium potential of the substance itself. Assuming the ion channel is ohmic, it is necessary to adapt Ohm's law to also take into account the chemical potential. Thus, the pathways of the substances through the membrane can be described by a resistance in series with a battery (see Figure 3.3). This results in a linear model for the ionic flux I_k for one substance k at a potential V as

$$I_k = G_k(u - \Phi_{\mathrm{N}_k}) \tag{3.27}$$

with Φ_{N_k} the Nernst potential of the substance k and G_k as the membrane conductance for the substance k. Thus, at resting membrane potential Φ_{GHK} Equation (3.27) can be written as $I_k = G_k(\Phi_{\mathrm{GHK}} - \Phi_{N_k})$. Another model describing the fluxes of the substances is defined in Equation (3.19). Both models can be generalized as

$$I_k = G_k \psi_k(u)\,, \tag{3.28}$$

with a function ψ_k describing the voltage-current relationship. In both definitions, Equations (3.28) and (3.19), the current is zero when the potential is equal the Nernst potential, i.e. $u = \Phi_{\mathrm{N}_k}$. In squid giant axon the channels are almost linear and, thus, the linear model (Equation (3.27)) is a good choice. In vertebrate the fluxes are better described by the Goldman-Hodgkin-Katz equation (Equation (3.19)) [188].

3.4.2 Gating

The ion current through the membrane is depends on the membrane channels. To be more precise, the number of individual channels, the distribution and density, the permeability and the

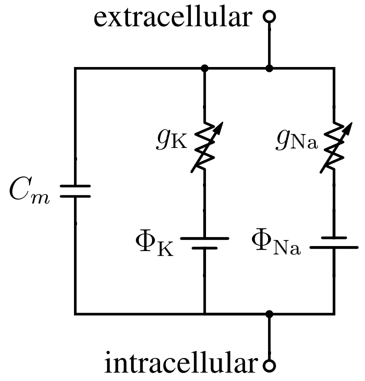

Figure 3.3: Schematic drawing of the electrical circuit through the membrane with the ionic fluxes

channel kinetics are all of great importance when describing the ionic current through a specific type of ion channel. Hence, more general the current I_k of ions k through the membrane can be described as

$$I_k = g_k(u,t)\psi_k(u) \tag{3.29}$$

with g_k the variable permeability of the membrane at potential u and time t depending on the state of the channel, e.g. open or closed. ψ_k is a function defining the relationship between voltage and current of an individual open channel (see Section 3.4.1). Generally, the permeability g_k of a substance k through the membrane can be written as

$$g_k(u,t) = \bar{g}_k \prod_p m_p^q \tag{3.30}$$

with $\bar{g}_k$ the maximum conductance, q an integer exponent and m_p the state of a given channel.

As described in Chapter 2, the membrane channels, a, can be in different states, for example in an open, closed or inactive state. To model this behavior, independent gates are assumed to control the channels. The flow of ions through the channel depends on these gates. In a two state model the gates can be in two different states, i.e. either open (O) or closed (C). The transition between open and closed states is voltage dependent. Hence, there exist voltage dependent rate constants $\alpha(\Phi)$ and $\beta(\Phi)$, which govern the transition

$$C \underset{\beta(u)}{\overset{\alpha(u)}{\rightleftharpoons}} O\,. \tag{3.31}$$

For this simple model, we can write the net rate change of open states as

$$\frac{\mathrm{d}m_p}{\mathrm{d}t} = \alpha(u)(1-m_p) - \beta(u)m_p \tag{3.32}$$

and the equilibrium m_p^∞ can be calculated as

$$m_p^\infty = \frac{\alpha(u)}{\alpha(u)+\beta(u)}\,. \tag{3.33}$$

The rate constants depends on the membrane potential and so does the equilibrium [61, 187, 188].

3.4.3 Review of Ionic Current Models

In 1952, Hodgkin and Huxley were the first to develop a model for the propagation of an electrical signal along a squid giant axon [165]. Although the original model describes the action potential of a squid nerve cell, through the years it was extended and adapted to describe action potential and propagation in various types of cells. FitzHugh (1961) and Nagumo (1962) developed, independent from each other, a simpler model, which is of great importance to the mathematical aspect, since mathematical analysis can be performed with it [121, 242]. The first one to describe cardiac cells was Noble in 1962, when he proposed a model for the purkinje fiber [253]. However, due to the lack of measurements of the ionic current at that time, the model proposed by Noble is from a physiological point of view, not correct. A revised version of the model was proposed by McAllister, Noble, and Tsien in 1975 [229]. In 1980, Yanagihara et al. developed a model for the sinoatrial node cells which is also based on the Hodgkin and Huxley model [375]. Beeler and Reuter developed the first model for ventricular cells in 1977 [28]. Adaptations to all this models are continuously published [34, 99, 107, 180, 222–224, 254, 288, 334]. Courtemanche et al. developed the first model for human atrial myocytes in 1998 [91]. In 2008, Bueno-Orovio developed a phenomenological model for the human ventricular action potential reducing the necessary parameters to four [52]. Other models need 17 [334], 22 [288], or even 67 [180] parameter to model the ventricular action potential. With the minimal model it is still possible to reproduce the correct action potential curve with only four parameter. An adaptation of this model was done by Lenk et al. [212] to describe the action potential of atrial cells.

3.5 Conduction

Cardiac tissue can be seen as a fiber network composed of cardiac cells and an extracellular matrix. An electrical stimulus initiated in one region of the heart travels along specialized conduction cells and the normal working myocardium throughout the whole heart (see Chapter 2). A model describing propagation of an electrical signal is the cable equation. Obviously, using the cable equation to describe the propagation through the heart is a simplification since the cable theory assumes an ideal infinitely long one dimensional cable. However, the cable theory can be extended to three dimensions and together with the gap junctions acting as cell to cell connections, the fiber network of the heart can be described very well with this model. This model is also referred to as bidomain model.

Assume that the cell is a cylinder with the interior being the cytoplasm, which is electrically connected to neighboring cells (see Figure 3.4). The exterior of the cable is the extracellular space and the membrane, which separates both spaces, acts as an imperfect insulator. The interior and the exterior are electrically conducting, which can be described by Ohm's law, such as

$$\left\{ \begin{array}{lcl} \boldsymbol{J}_i & = & -\boldsymbol{D}_i \nabla \Phi_i, \\ \boldsymbol{J}_e & = & -\boldsymbol{D}_e \nabla \Phi_e, \end{array} \right. \tag{3.34}$$

where i denotes the interior space and e denotes the exterior space. $\boldsymbol{D}_i$ and $\boldsymbol{D}_e$ are the intra- and extracellular conductivities, $\boldsymbol{J}_i$ and $\boldsymbol{J}_e$ are the fluxes, and Φ_i and Φ_e the potentials. Through the cell membrane some charge can move from the interior to the exterior space or from the exterior to the interior space. However, the decrease of charge on one side should result in an increase

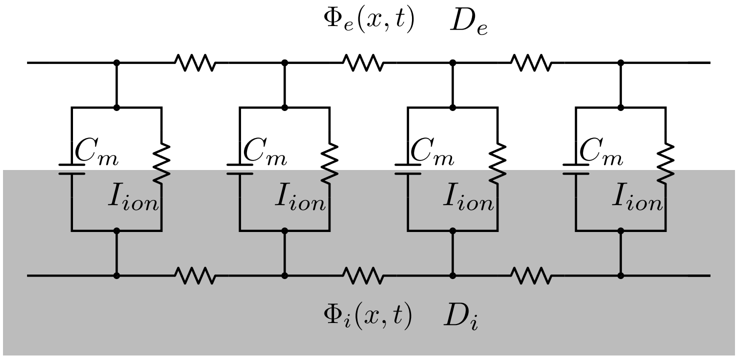

Figure 3.4: Schematic drawing of a cable

of charge on the other side by the same amount. Thus, due to Kirchhoff's law we can write the current conservation as follows

$$\begin{cases} \int_{\partial B} \boldsymbol{J}_i \mathrm{d}V + \int_B \chi I_m &= 0, \\ \int_{\partial B} \boldsymbol{J}_e \mathrm{d}V - \int_B \chi I_m &= 0, \end{cases} \tag{3.35}$$

with χ the surface-to-volume ratio, $B \subset \Omega$ an arbitrary region, and ∂B the boundary of the region B. Applying the divergence theorem and assuming an arbitrary region $B \subset \Omega$, we can write

$$\begin{cases} \nabla \cdot \boldsymbol{J}_i - \chi I_m &= 0, \\ \nabla \cdot \boldsymbol{J}_e + \chi I_m &= 0, \end{cases} \tag{3.36}$$

which together with with Equation (3.34) leads to

$$\begin{cases} \nabla \cdot \boldsymbol{D}_i \nabla \Phi_i + \chi I_m &= 0, \\ -\nabla \cdot \boldsymbol{D}_e \nabla \Phi_e + \chi I_m &= 0\,. \end{cases} \tag{3.37}$$

The bidomain equations describe the coupling of the interior and exterior cellular space taking into account different conduction properties in each space. With the transmembrane potential (actin potential) $u = \Phi_i - \Phi_e$, we derive the bidomain equations

$$\begin{cases} \chi \left(C_m \frac{\mathrm{d}u}{\mathrm{d}t} + I_{ion}(u, \mathbf{w}) \right) - \nabla \cdot (\mathbf{D}_i \nabla u) - \nabla \cdot (\mathbf{D}_i \nabla \Phi_e) &= 0, \\ -\nabla \cdot (\mathbf{D}_i \nabla u) - \nabla \cdot ((\mathbf{D}_i + \mathbf{D}_e) \nabla \Phi_e) &= 0 \end{cases} . \tag{3.38}$$

The monodomain equation is a simplification of the bidomain equations, assuming that the extracellular space has the same longitudinal to transversal conductivity ratio as the intracellular space, i.e. $\mathbf{D}_i = \lambda \mathbf{D}_e$. By inserting this into the bidomain equations we get the monodomain equation as follows

$$\chi C_m \frac{\mathrm{d}u}{\mathrm{d}t} - \nabla \cdot (\mathbf{D} \nabla u) = \chi I_{\text{ion}}(u, \mathbf{w})\ . \tag{3.39}$$

with $\mathbf{D} = \frac{\lambda}{1+\lambda} \mathbf{D}_i$ [61, 189].

4 Multiphysics Modeling of the Atrial Systole under Standard Ablation Strategies

The aim of this chapter is to develop a computational framework to investigate in-silico the performance of the heart, especially the atria, under different conditions. There exit various possibilities to use our framework. In particular, it can be used as a tool to improve the understanding and influence of different cardiac functions. Additionally, as pre-operative tool it can be used to investigate and compare different treatment options either generally or for an individual patient with patient-specific assumptions. In any case the goal is to develop a framework, which can be used to provide additional information for clinicians to decide for the best treatment.

In this chapter we demonstrate the benefit of our computational framework for the aspect of atrial fibrillation and ablation therapy. Different ablation line combinations cannot be applied in practice to the same patient. Thus, the aim of this chapter is to explain our computational framework and to apply it on various ablation pattern to compare the impact of the ablation concepts on the mechanical performance of the atria. For this purpuse, we couple electro-mechano-hemodynamic mathematical models based on biophysical principles and simulate the contractile performance of the atria. We compute systolic pressures and volumes in two patient-specific atrial geometries (one of normal size and one hypertrophied) with various ablation concepts. We found that our computational model is able to detect the differences in the left atrial contraction and ejection fraction for various electrical activation sequences resulting from different ablation line combinations. We show that multiphysics modeling has the potential to quantify the hemodynamic performance of left atria for different ablation lines, which could be used as additional pre-operative clinical information for the choice of the ablation concept in the future.

The remainder of this chapter is organized as follows. First a general overview of the disease of cardiac arrhythmia is provided in Section 4.1. In Section 4.2 we describe the geometrical and computational model that we used. We first explain the process how we get from the imaging data to the geometry of the atria with fiber orientation and ablation patterns. Secondly, we describe shortly the electrophysiological model and in more detail the mechanical model together with the basics of continuum mechanics. Finally, the hemodynamical model is explained. Section 4.3 contains the results, including the results of perfect ablation lines, imperfect ablation lines and reduced conduction velocity. Section 4.4 comprises the discussion, the clinical significance of our model and the limitations and perspectives. The chapter ends with some concluding remarks in Section 4.5.

4.1 Cardiac Arrhythmia

The propagation of the electrical signal through the heart muscle takes place in a regular fashion. Variations and modifications of this propagation sequence are called heart rhythm disorders or arrhythmia. Abnormal activation of the heart muscle can occur in various ways. They can be divided into two major categories: abnormal slow propagation (bradyarrhythmia) and abnormal fast propagation (tachyarrhythmia). Tachyarrhythmia are distinguished between supraventricular tachyarrhythmia, regarding the atria, and ventricular tachyarrhythmia, regarding the ventricles. In the course of this chapter we will focus on atrial arrhythmia.

Arrhythmia are caused from abnormal impulse initiation, abnormal impulse propagation, or both [169, 369]. Abnormal impulse initiation include three main types: altered automaticity of the pacemaker cells, abnormal automaticity of non pacemaker cells and triggered activity through afterdepolarizations. The activation of the sinus node is regulated through neurotransmitter and depends on the autonomic nervous system (see Section 2.6.3). Modification of the effects of neurotransmitter for example through pharmacologic agents can lead to increased or decreased node firing. The second type is abnormal automaticity of non pacemaker cells describing ectopic beats arising from myocardial cells, which normally do not spontaneous depolarize. The reason for this abnormal firing in non pacemaker cells is not yet fully understood, but ectopic impulses in the pulmonary veins of the left atrium are often recognized in atrial arrhythmia. The last type are triggered activity. These can arise through an action potential, which triggers an abnormal afterdepolarization. In a myocardial cell an abnormal rise of the action potential could occur during repolarization phase (early afterdepolarization) or shortly after repolarization (delayed afterdepolarization), which could lead to an additional action potential propagation [214].

Arrhythmia can also be caused by abnormal impulse propagation and reentry. It is possible that an impulse, which propagates through the heart, does not die out after one activation cycle, but returns. This can occur under special conditions, however, certain conditions favor the development of reentrant waves such as a large size of the myocardial tissue, a decreased conduction velocity, and a shortened refractory period. The development of an reentrant wave can be due to an conduction block in one part, a slowed propagation, and a reentrant circuit that is large enough to allow repolarization before the new depolarization wave arrives.

Long lasting and frequently recurring arrhythmic disorders lead to electrical and structural remodeling, which increase the possibility for further arrhythmia: Arrhythmia promotes arrhythmia [244, 245]. Many different types of cardiac arrhythmia exist. Supraventricular arrhythmia can be divided into regular and irregular arrhythmia. Atrial flutter belongs to the regular arrhythmia consisting of an large reentry circuit, which is mostly fixed. Atrial fibrillation belongs to the irregular arrhythmia consisting of a chaotic activation. Mostly atrial fibrillation is sustained by rapid firing of ectopic beats and multiple wandering reentrant circuits [214]. Supraventricular arrhythmia are not immediately life-threatening, however, sustained supraventricular arrhythmia are a leading cause of thromboembolic cerebral insults, increased risk of stroke, cardiac failure and mortality [370]. Ventricular arrhythmia can be divided into ventricular tachycardia and ventricular fibrillation. Ventricular tachycardia consists of ectopic foci firing additional action potentials. This is most common for patients with structural heart diseases. Ventricular tachycardia could lead to ventricular fibrillation, which is immediately life-threatening if not treated. Many of the sudden deaths are caused by a ventricular rhythm disorder [214].

Two options exist to treat arrhythmia. The first is antiarrhythmic drug therapy and the second is catheter ablation. Many studies show the efficiency of catheter ablation compared with drug therapy [194]. The goal of catheter ablation is to generate lesion. This ablation lesions should isolate ectopic foci so that their activation wave does not coincide and disturb the sinus rhythm activation. Additionally, ablation lesions change the arrhytmiogenic substrate, and thus, prevent reentry of the activation wave. Since most catheter use radiofrequency energy this ablation process is also called radiofrequency catheter ablation. The minimal invasive procedure of catheter ablation is performed with a catheter inserted into a blood vessel in the ingunial region and guided through the vessel to the atria [10]. The tip of the catheter is placed on myocardial wall that should be ablated and activating the catheter produces an alternating electrical current flowing through the tip. Myocardial tissue acting as a conductor possesses also a resistance which transforms radiofrequency energy into heat. If tissue is exposed for a certain time to heat, it becomes necrotic and turns into scar, and thus, it is not anymore able to propagate the activation wave. The heat evolved from the radiofrequency energy is conducted through the myocardial wall and necrotizes surrounding tissue. Important for a successful catheter ablation are lesions that are transmural, i.e. going through the whole atrial wall [60]. Many different ablation lesion are used in the clinic to treat atrial arrhythmia. However, it is not verified which ablation lesion leads to the most promising outcome.

Atrial fibrillation is the most common sustained cardiac arrhythmia [148]. Hence, we decided to demonstrate the profitableness and the good performance of our computational framework by the investigation of interventional treatment options for atrial fibrillation, which are radiofrequency catheter ablation. In clinical studies it is not possible to compare different ablation lesions on the same patient. However, with our computational model we can show the difference of diverse ablation lesions regarding activation pattern, contraction, and hemodynamics.

4.2 Materials and Methods

The biophysical model used within this study includes patient-specific geometries with anatomical fiber orientation and is composed from coupled electrophysiological, mechanical and hemodynamic models. In each of these coupled models the ablation lines are defined by different material properties in comparison to healthy tissue.

The anatomical fiber orientation is very important for a realistic and correct simulation of the electrophysiology and the contraction of the atria, since both processes take place anisotropically, with the preference in fiber direction. The integration of the fiber orientation is done for the examples in this chapter in a mostly manual way. However, since this is quite time consuming throughout the thesis the process is improved such that the fiber definition is now done in an almost automatic way. This automatication is described in Chapter 6. Additionally, the computation of the electrophysiology, which is numerically challenging, is optimized. The improved numerical method is described in Chapter 5.

4.2.1 Starting Image Data

We develop biophysical computational models from two patients: Model 1 is obtained from a cardiac computed tomography (CT) with a resolution of $0.4\,\mathrm{mm} \times 0.4\,\mathrm{mm} \times 0.8\,\mathrm{mm}$ from a 71-

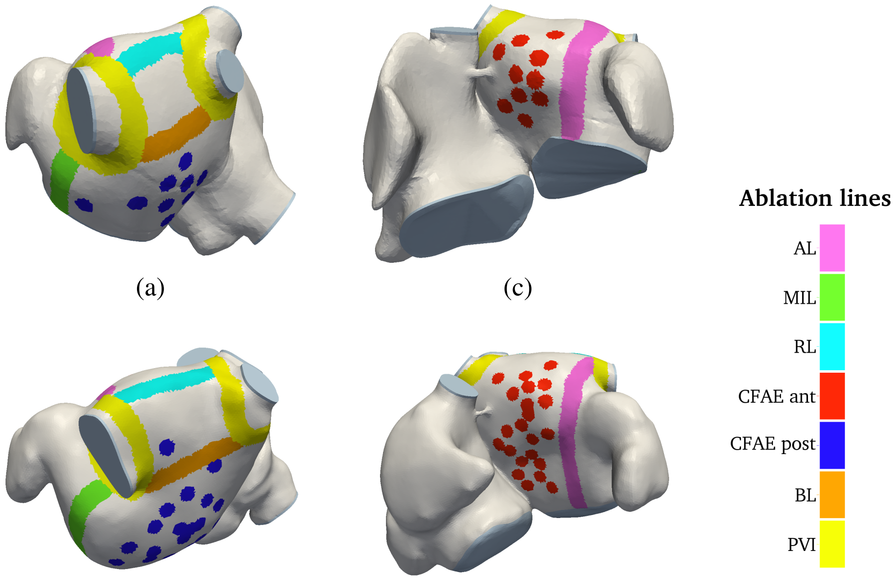

(a) (c)

(b) (d)

Figure 4.1: Segmented biatrial geometries for Model 1, (a) and (b), and Model 2, (c) and (d), with the different ablation lesions PVI, AL, MIL, CFAE, RL and BL. WACA is not shown in this figure for the sake of clarity, since it consists of a “wider PVI” lesion. Its spatial extension can be appreciated through the electrically inactive area in Figure 4.6c.

old individual without known cardiac pathological findings. Model 2 is obtained from cardiac magnetic resonance imaging (MRI) with a resolution of $1.4\,\mathrm{mm} \times 1.4\,\mathrm{mm} \times 1.5\,\mathrm{mm}$ from dilated atria of a 62-old individual with paroxysmal atrial fibrillation (AF), prior to this study. We use different image data to verify that both medical imaging techniques, CT and CMRT, can be processed with our methodology to simulate, with a patient-specific geometry, the performance of the atria.

4.2.2 Geometrical and Fiber Models

Starting from the respective images of Models 1 and 2, a surface representation of both atria is generated using the software Mimics (Materialise, Leuven, Belgium). First, the lumina of both atria are segmented manually, so that the endocardial surfaces of the atrial wall are obtained. Then, we generate the epicardium by extruding the luminal surfaces by $2\,\mathrm{mm}$. Finally, a volume mesh is created using Gmsh [129] with a maximal element size of $0.9\,\mathrm{mm}$, resulting in around 3.7×10^5 and 5.1×10^5 linear tetrahedral elements for Models 1 and 2, respectively. The size of $0.9\,\mathrm{mm}$ is chosen to ensure that the thin atrial wall has in every case at least two elements throughout the wall thickness. The segmented geometries are presented in Figure 4.1, including visualization of the ablation lines.

To both geometries, local fiber directions are assigned semi-automatically using reported knowledge of atrial fiber structure [160] and harmonic interpolation techniques [239] see Figure

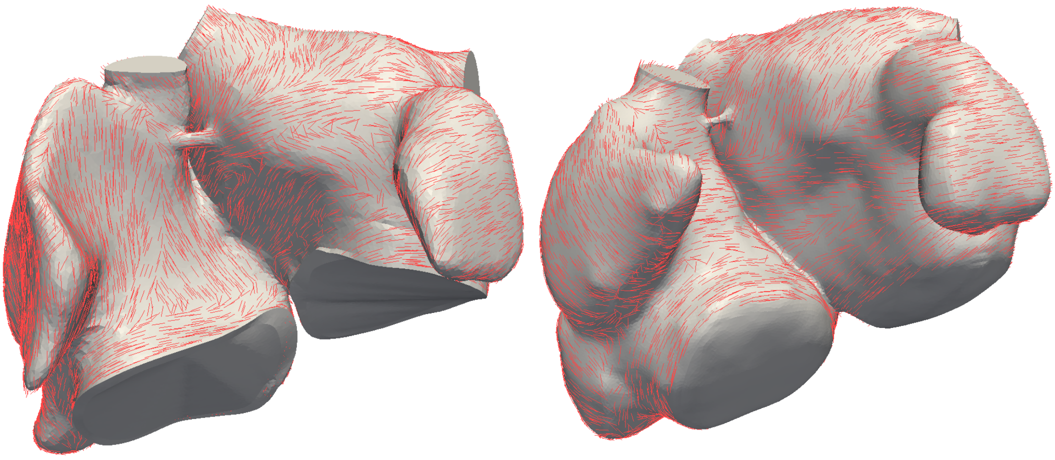

(a) (b)

Figure 4.2: Assigned fiber orientation for Model 1 (a) and Model 2 (b).

4.2. The process of defining the fiber bundles on the geometry semi-automatically or using the improved more automated way is described in more details in Chapter 6. For the following experiments we use the first, less automated, method. Briefly, we integrate the main fiber bundles in the right and left atrium (crista terminalis, pectinate muscles, circumferential vestibule fibers and Bachmann bundle), which run through the whole atrial wall thickness. In the remaining part of the tissue, we define different fiber directions on each epi- and endocardial surface of each section. The fibers are interpolated into the whole thickness using a Poisson operator.

4.2.3 Geometrical Model of Ablation Patterns

We include the following ablation lesions in both models: pulmonary vein (PVI), wide area circumferential ablation (WACA), anterior line (AL), mitral isthmus line (MIL), roofline (RL), posterior box lesion (BL), and complex fractionated atrial electrograms on both sites (CFAE), CFAE on the anterior site (CFAE-ant), CFAE on the posterior site (CFAE-post). All ablation lines are placed on a three-dimensional representation of the epicardial surface, using the software 3-matic (Materialise, Leuven, Belgium). This virtual ablation procedure is performed by a trained clinical electrophysiologist, based on the individual anatomy of the two atrial geometries. Hence, the ablations lines are comparable with the ones during a real surgical procedure. The ablation lines have an averaged width of $5\,\mathrm{mm}$ and penetrate the atrial wall entirely to the endocardial surface. Besides the study on imperfect ablation lines, we assume an ablation procedure without imperfections, such as gaps and discontinuities.

We integrate the described ablation lines as different sub-regions of the atrial domain for both models. The performed computational simulations include these specific ablation lines and all medically feasible combinations of them (denoted with a “+”).

Main diffusivity $[\mathrm{mm}^2/\mathrm{ms}]$	Off diffusivity $[\mathrm{mm}^2/\mathrm{ms}]$
0.6	0.06

Table 4.1: Parameters for the electrophysiology equations

4.2.4 Electrophysiological Model

We assume that all ablation concepts lead to a termination of atrial fibrillation, restoring normal sinus rhythm, i.e., an activation current applied solely at the sinus node.

The propagation of the electrophysiological wave is computed using the monodomain equations for the transmembrane potential and gating membrane variable [87] and the Bueno-Orovio cellular model [52]. For more details about the derivation of the electrophysiological model refer to Chapter 3. The model parameters of the cellular model are adapted to reproduce atrial excitation properties, according to Weber et al. [358]. The diffusivity is assumed transverse isotropic with a diffusivity of $0.6\,\mathrm{mm}^2/\mathrm{ms}$ in fiber direction and $0.06\,\mathrm{mm}^2/\mathrm{ms}$ perpendicular to it. These values are chosen to obtain a physiological propagation velocity and activation time for the standard atrial geometry (Model 1) without ablation lines [167]. The same diffusivity values are then used for the dilated geometry (Model 2), naturally leading to a larger activation time. We model the ablated necrotic tissue as a perfect isolator, i.e. with zero diffusivity. This implies that the necrotic tissue is no longer electrically activated and hence it does not contract.

Concerning the numerical methods, the spatial semi-discretization is performed via a linear continuous Galerkin approach, with the ionic currents computed at the element center. The time semi-discretization is fully implicit, meaning that a Newton approach has to be applied in order to solve for the nonlinearity of the reaction term. That enables working with a time step of $0.1\,\mathrm{ms}$. Since numerical computation of the electrophysiology are challenging and require the usage of a very fine discretization to compute correct propagation velocity, in Chapter 5 an efficient numerical method is described to solve electrophysiology problems.

The activation wave is plotted in Figure 4.5 for both models without any ablation and with ablation concept PVI + AL + BL.

4.2.5 Mechanical Model

To describe the mechanical model of the heart contraction a short introduction into continuum mechanics is given. The heart can be seen as a structure under forces. The deformation of the heart, in case of the cardiac muscle the deformation is called contraction, is described with the principles of the continuum mechanic theory. Thus, this chapter reviews shortly the concepts of continuum mechanics. More detailed description of the continuum mechanics can be found in [8, 26, 27, 44, 140, 171, 208, 265].

4.2.5.1 Continuum Mechanics

Continuum mechanics deals with the kinematics of deformable bodies under the effect of forces. Additionally, in continuum mechanics the body is seen as continuous in space, i.e., the microscopic or nuclear structure is not modeled in detail. Instead the body is seen as a continuum. To describe the deformation and kinematic of the bodies three main aspects need to be considered, including kinematics, balance equations and constitutive equations.

4.2.5.1.1 Kinematics The kinematic describes the deformation of a body. Assuming we have a body which occupies at time t the region $\Omega(t) \subset \mathbb{R}^3$ and a time interval $\mathcal{T} = [0, T]$, then we can define the mapping ϕ as

$$\phi : \begin{cases} \Omega_0 \times \mathcal{T} & \rightarrow \quad \mathbb{R}^3 \\ (\boldsymbol{X}, t) & \mapsto \quad \boldsymbol{x} = \phi(\boldsymbol{X}, t) \end{cases} , \tag{4.1}$$

with Ω_0 the reference configuration, $\boldsymbol{X}$ is the position of a point in reference configuration, and $\boldsymbol{x}$ the position of a point in current configuration at time t. The displacement field which is defined as the difference between reference and current configuration can be written as

$$\boldsymbol{d}(\boldsymbol{X}, t) = \boldsymbol{x} - \boldsymbol{X} . \tag{4.2}$$

The deformation gradient $\boldsymbol{F}$ is defined as

$$\boldsymbol{F}(\boldsymbol{X}, t) = \boldsymbol{I} + \nabla_{\boldsymbol{X}} d , \tag{4.3}$$

such that an infinitesimal line element for the reference configuration $\mathrm{d}\boldsymbol{X}$ is transformed in the infinitesimal line element of the current configuration $\mathrm{d}\boldsymbol{x}$ and backwards

$$\mathrm{d}\boldsymbol{x} = \boldsymbol{F}\mathrm{d}\boldsymbol{X} \text{ and } \mathrm{d}\boldsymbol{X} = \boldsymbol{F}^{-1}\mathrm{d}\boldsymbol{x} , \tag{4.4}$$

where $\nabla_{\boldsymbol{X}}$ is the gradient operator with respect to the reference configuration and $\boldsymbol{I}$ is the second order identity tensor. The deformation gradient describes the rigid body rotation and deformation. Since $\boldsymbol{F}$ is invertible and real-valued, a unique polar decomposition of $\boldsymbol{F}$ can be performed as

$$\boldsymbol{F} = \boldsymbol{R} \cdot \boldsymbol{U} \tag{4.5}$$

in an orthogonal matrix $\boldsymbol{R}$ and a positive semi-definite symmetric matrix $\boldsymbol{U}$. The matrix $\boldsymbol{R}$ describes the rotation and the matrix $\boldsymbol{U}$ describes the stretching of the space along orthogonal axes relating to the reference configuration. Rigid body translations are not contained in the deformation gradient. The right Cauchy-Green tensor $\boldsymbol{C}$ can be defined as

$$\boldsymbol{C} = \boldsymbol{F}^T\boldsymbol{F} = (\boldsymbol{R}\boldsymbol{U})^T\boldsymbol{R}\boldsymbol{U} = \boldsymbol{U}^T\boldsymbol{R}^T\boldsymbol{R}\boldsymbol{U} = \boldsymbol{U}^T\boldsymbol{U} , \tag{4.6}$$

where additionally also the rigid body rotations are removed since $\boldsymbol{C} = \boldsymbol{U}^T\boldsymbol{U}$. The last step of the equation can be performed since $\boldsymbol{R}$ is orthogonal, i.e. $\boldsymbol{R}^T\boldsymbol{R} = \boldsymbol{I}$. The right Cauchy-Green tensor transforms the quadratic infinitesimal line element in reference configuration into the quadratic infinitesimal line element in the current configuration as

$$\mathrm{d}\boldsymbol{x}^T \cdot \mathrm{d}\boldsymbol{x} = \mathrm{d}\boldsymbol{X}^T \cdot \boldsymbol{C} \cdot \mathrm{d}\boldsymbol{X} . \tag{4.7}$$

The Cauchy-Green tensor is a strain measure with the property that it is zero if no deformation occurs is defined as

$$\boldsymbol{E} = \frac{1}{2}(\boldsymbol{C} - \boldsymbol{I}) , \tag{4.8}$$

where $\boldsymbol{E}$ is called the Green-Lagrange strain. The Green-Lagrange strain is a strain measure (with basis vectors) in reference configuration. A strain measure defined in current configuration is the Euler-Almansi strain e defined as

$$\boldsymbol{e} = \frac{1}{2}(\boldsymbol{I} - \boldsymbol{F}^{-T}\boldsymbol{F}^{-1}) \,. \tag{4.9}$$

4.2.5.1.2 Balance equations

Stress measures The stress is defined as the interaction, more precise as forces, between neighboring material points in a continuum. The resultant force f is defined as the interaction at the interface area $\mathrm{d}A$ between two volumes of a body. In the assumption of a continuum the decrease of the interface area results in a convergence to the traction vector $\boldsymbol{t}$, as

$$\boldsymbol{t}(\boldsymbol{x}, \boldsymbol{n}, t) = \lim_{\Delta A \to 0} \frac{\Delta f}{\Delta A} \,, \tag{4.10}$$

where $\boldsymbol{n}$ is the normal vector of the interface area $\mathrm{d}A$. With the theorem of Cauchy the traction vector can be transformed into the Cauchy stress tensor $\boldsymbol{\sigma}$, as

$$\boldsymbol{t}(\boldsymbol{x}, \boldsymbol{n}, t) = \boldsymbol{\sigma} \cdot \boldsymbol{n} \,, \tag{4.11}$$

where $\boldsymbol{\sigma}(\boldsymbol{x}, t)$ is defined on the current configuration. As for the strains, there exist different definitions of the stress tensor. The Cauchy stress tensor is defined in the current configuration. A stress measure defined purely in the reference configuration is the so called second Piola-Kirchoff stress tensor $\boldsymbol{S}$. It can be calculated from the Cauchy stress tensor as follows

$$\boldsymbol{S} = \boldsymbol{J}\boldsymbol{F}^{-1}\boldsymbol{\sigma}\boldsymbol{F}^{-\mathrm{T}} \,, \tag{4.12}$$

with $\boldsymbol{J} = \det(\boldsymbol{F})$.

Balance of mass The balance of mass can be derived as follows. $\rho(\boldsymbol{x}, t)$ and $\rho_0(\boldsymbol{X}, t)$ are the mass densities in current and reference configuration, respectively. Integrating over the domains $\mathcal{B}$ and $\mathcal{B}_0$ leads to the mass

$$m(t) = \int_{\mathcal{B}} \rho\left(\boldsymbol{x}, t\right) \mathrm{d}v = \int_{\mathcal{B}_0} \rho_0\left(\boldsymbol{X}\right)\, \mathrm{d}V \,. \tag{4.13}$$

With $\mathrm{d}v = \boldsymbol{J}\mathrm{d}V$ holds that $\rho_0\left(\boldsymbol{x}\right)\boldsymbol{J} = \rho\left(\boldsymbol{X}\right)$. Since the mass of a region over time does not change, i.e. $m\left(\mathcal{B}, t\right) = \mathrm{const.}$, the time derivative is zero and, thus,

$$0 = \frac{\mathrm{d}m\left(\mathcal{B}, t\right)}{\mathrm{d}t} = \frac{\mathrm{d}}{\mathrm{d}t}\int_{\mathcal{B}} \rho\left(\boldsymbol{x}, t\right)\, \mathrm{d}v = \frac{\partial}{\partial t}\int_{\mathcal{B}_0} \rho_0\left(\boldsymbol{X}, t\right)\, \mathrm{d}V = \int_{\mathcal{B}_0} \frac{\partial}{\partial t}\rho_0\left(\boldsymbol{X}, t\right)\, \mathrm{d}V \tag{4.14}$$

where in the last step is possible since $\mathcal{B}_0 = \mathrm{const.}$ over time. Furthermore, it holds

$$\int_{\mathcal{B}} \rho\left(\boldsymbol{x}, t\right)\, \mathrm{d}v = \int_{\mathcal{B}_0} \rho\left(\boldsymbol{X}, t\right)\boldsymbol{J}\,\mathrm{d}V \tag{4.15}$$

and, thus,

$$0 = \frac{\mathrm{d}m\left(\mathcal{B},t\right)}{\mathrm{d}t} = \int_{\mathcal{B}_0} \frac{\partial \rho\left(\boldsymbol{X},t\right)}{\partial t}\boldsymbol{J} + \rho\left(\boldsymbol{X},t\right)\frac{\partial}{\partial t}\boldsymbol{J}\,\mathrm{d}V \tag{4.16}$$

With $\frac{\partial}{\partial t}\boldsymbol{J} = \boldsymbol{J}\mathrm{div}(\boldsymbol{v})$ with $\boldsymbol{v}$ as the current velocity field and $\frac{\partial\rho(\boldsymbol{X},t)}{\partial t} = \frac{\mathrm{d}\rho(\boldsymbol{X},t)}{\mathrm{d}t}$ it follows

$$\begin{aligned}\frac{\mathrm{d}m\left(\mathcal{B},t\right)}{\mathrm{d}t} &= \int_{\mathcal{B}_0}\left(\frac{\partial \rho\left(\boldsymbol{X},t\right)}{\partial t} + \rho\left(\boldsymbol{X},t\right)\mathrm{div}(\boldsymbol{v})\right)\boldsymbol{J}\,\mathrm{d}V \\ &= \int_{\mathcal{B}} \frac{\mathrm{D}\rho\left(\boldsymbol{x},t\right)}{\mathrm{D}t} + \rho\left(\boldsymbol{x},t\right)\mathrm{div}(\boldsymbol{v})\,\mathrm{d}v\end{aligned} \tag{4.17}$$

This is valid for all arbitrary but fixed regions $\mathcal{B}$ and can therefore be written as

$$0 = \dot{\rho}\left(\boldsymbol{x}\right) + \rho\mathrm{div}(\boldsymbol{v})\,. \tag{4.18}$$

Balance of linear momentum The balance of momentum of a body in current material configuration can be formulated as the rate of change of the momentum equal to the sum of all forces acting on the body. This can be written as

$$\frac{\mathrm{d}}{\mathrm{d}t}\int_{\mathcal{B}} \rho\boldsymbol{v}\,\mathrm{d}v = \int_{\mathcal{B}} \rho\boldsymbol{b}\,\mathrm{d}v + \int_{\partial\mathcal{B}} \boldsymbol{t}\,\mathrm{d}a\,, \tag{4.19}$$

where $\rho_t(\boldsymbol{x},t)$ is the mass density, $\boldsymbol{b}(\boldsymbol{x},t)$ is the body force, and $\boldsymbol{t}(\boldsymbol{x},t)$ is the surface traction. Using the divergence theorem and the mass balance the balance of linear momentum can be written for the current configuration as

$$\mathrm{div}\left(\boldsymbol{\sigma}\right) + \rho\boldsymbol{b} = \rho\ddot{\boldsymbol{d}}\,. \tag{4.20}$$

By changing the integration domain to the reference configuration it can be formulated as

$$\mathrm{div}\left(\boldsymbol{F}\cdot\boldsymbol{S}\right) + \rho_0\boldsymbol{b}_0 = \rho_0\ddot{\boldsymbol{d}}\,, \tag{4.21}$$

with the mass density $\boldsymbol{b}_0$ in reference configuration.

4.2.5.2 Constitutive equations

Constitutive equations describe the relation between strains and stresses. Thus, they characterize the material property. To describe the myocard material in continuum mechanical theory we need to make some assumptions and simplifications. The first simplification is to describe the material as a continuum without taking into account the microscopical structuring. With this simplification, concerning the investigations we assume that all relevant material properties are considered and we are not forgetting any significant aspects arising from microscopical structure.

The material behavior can be represented by rheological models, where the behavior is described by a combination of constitutive elements arranged in serial and parallel fashion analogous to an electrical circuit. However, non-linear materials and large deformations cause more complicated combining laws. We used a simplified model for the myocardial tissue described in

[67]. Thus, we assume that deformations remain small enough that the simple natural rules of parallel and series connection apply.

In this work the second Piola-Kirchhoff stress tensor in myocardial tissue $\boldsymbol{S}$ is composed by two main components, an passive component $\boldsymbol{S}_p$ and an active component $\boldsymbol{S}_\tau$

$$\boldsymbol{S} = \boldsymbol{S}_p + \boldsymbol{S}_\tau \,. \tag{4.22}$$

The passive component S_p describes the passive material of the myocard, i.e. the collagen and the elastin matrix. The passive component is represented by and elastic element, a volume penalty term, and a viscous element

$$\boldsymbol{S}_p = \frac{\partial \Psi_{\text{elast}}}{\partial \boldsymbol{E}} + \frac{\partial \Psi_{\text{vol}}}{\partial \boldsymbol{E}} + \frac{\partial \Psi_{\text{visco}}}{\partial \dot{\boldsymbol{E}}} \tag{4.23}$$

where Ψ_{elast} is a hyperelastic potential, Ψ_{vol} is the volume penalty term, and Ψ_{visco} a viscous pseudo-potential. For the elastic part the Mooney-Rivlin material is used which can be mathematically described as

$$\Psi_{\text{elast}}(\overline{\boldsymbol{I}}_1, \overline{\boldsymbol{I}}_2) = c_1 \left(\overline{\boldsymbol{I}}_1 - 3\right) + c_2 \left(\overline{\boldsymbol{I}}_2 - 3\right) \,, \tag{4.24}$$

with c_1 and c_2 the material stiffness parameters. $\overline{\boldsymbol{I}}_1 = \boldsymbol{J}^{-\frac{2}{3}} \boldsymbol{I}_1$ and $\overline{\boldsymbol{I}}_2 = \boldsymbol{J}^{-\frac{4}{3}} \boldsymbol{I}_2$ are the modified invariants based on the invariants of the Cauchy-Green tensor defined as

$$\boldsymbol{I}_1 = \operatorname{tr}(\boldsymbol{C}) \quad \text{and} \quad \boldsymbol{I}_2 = \frac{1}{2} \left(\operatorname{tr}^2(\boldsymbol{C}) - \operatorname{tr}\left(\boldsymbol{C}^2\right)\right) \,. \tag{4.25}$$

The volume penalty term Ψ_{vol}, which enforces quasi-incompressibility, is defined as

$$\Psi_{\text{vol}}(\boldsymbol{J}) = \varepsilon \left(\boldsymbol{J}^\gamma + \frac{1}{\boldsymbol{J}^\gamma} - 2 \right) \,, \tag{4.26}$$

with penalty parameters ε and γ. The third term of the passive part of the Piola-Kirchhoff stress tensor is the viscous part Ψ_{visco} which is defined as as

$$\Psi_{\text{visco}}(\dot{\boldsymbol{E}}) = \frac{\eta}{2} \operatorname{tr}(\dot{\boldsymbol{E}}^2) \,, \tag{4.27}$$

with the viscous damping η.

The active part $\boldsymbol{S}_\tau$ of the stress tensor is defined as

$$\boldsymbol{S}_\tau(t) = \tau(t) \boldsymbol{f}_0 \otimes \boldsymbol{f}_0 \,, \tag{4.28}$$

where $\tau(t)$ is the stress and $\boldsymbol{f}_0$ is the vector pointing in fiber direction, since contraction take place only in direction of the fibers (see Chapter 2). The stress is time dependent and depending on the transmembrane potential u computed with the electrophysiology equations. If the transmembrane potential reaches a certain threshold, which corresponds to a threshold for releasing Ca^{2+} ions from the sarcoplasmatic reticulum into the cell, contraction is initiated. The stress increases asymptotically towards the stress value σ_0. Decreasing the transmembrane potential underneath the threshold, the active stress decreases asymptotically to 0. This relation can be written as

$$\begin{array}{rcl} \dot{\tau}(t) & = & -|z|\tau(t) + \sigma_0|z|_+ \\ z(t) & = & |z(t)|_+ - |z(t)|_- \text{ with } \begin{cases} |z(t)|_+ = \alpha_{\max}\mathbb{1}_{u>C} \\ |z(t)|_- = \alpha_{\min}\mathbb{1}_{u<C} \end{cases} \end{array} \tag{4.29}$$

with the control variable z pending on the transmembrane potential u and the threshold C. $\mathbb{1}$ is the indicator function.

In this chapter we additionally assign different materials for the ablation lines, the valves and the ring around the valves. For the ablation lines and the ring around the valves the material is almost the same as the myocard material beside the active component, which is missing in the ablation lines and the valve rings. The second Piola-Kirchhoff stress tensor in ablation lines $\boldsymbol{S}_{\text{abl}}$ and the valve rings $\boldsymbol{S}_{\text{ring}}$ is defined as

$$\boldsymbol{S}_{\text{abl}} = \boldsymbol{S}_{\text{ring}} = \frac{\partial \Psi_{\text{elast}}}{\partial \boldsymbol{E}} + \frac{\partial \Psi_{\text{vol}}}{\partial \boldsymbol{E}} + \frac{\partial \Psi_{\text{visco}}}{\partial \dot{\boldsymbol{E}}}. \tag{4.30}$$

The second Piola-Kirchhoff stress tensor in the valves $\boldsymbol{S}_{\text{valve}}$ is

$$\boldsymbol{S}_{\text{valve}} = \frac{\partial \Psi_{\text{elast}}}{\partial \boldsymbol{E}} + \frac{\partial \Psi_{\text{visco}}}{\partial \dot{\boldsymbol{E}}}. \tag{4.31}$$

4.2.5.3 Governing Equations

To describe the deformation of the heart caused by the contraction of the myocytes, we choose the balance of momentum in reference configuration to describe the model (Equation 4.21). Since the body forces $\boldsymbol{b}$ are not considered, due to their marginal influence on cardiac contraction, the equation simply reads as

$$\operatorname{div}(\boldsymbol{F} \cdot \boldsymbol{S}) = \rho_0 \ddot{\boldsymbol{d}} \text{ in } \Omega_0, \tag{4.32}$$

with Ω_0 the myocardial tissue domain.

The heart is situated inside the pericardium in the thorax (see Chapter 2). The pericardium, neighboring organs and the rib cage prevent the heart from moving freely and exert forces on the epicardial surface of the heart. Atria and ventricles are both attached to the heart skeleton. Thus, the skeleton acts as connector between atria and ventricles allowing interaction between them. Therefore, simulating only the atria or the ventricle by themselves the forces exerted by the other part have to be taken into account. Finally, the cut surfaces of the veins of the right and left atrium and the cut surfaces of the aorta and the pulmonary artery need also to be considered. They have an effect on the displacement of the heart, since they are connected with the rest of the circulatory system. All external traction acting on the epicardium Γ_0^{epi}, forces of the ventricle acting at the atrioventricular plane between atria and ventricle Γ_0^{avp} and the forces of the vessels acting on the veins and arteries Γ_0^{ves}, are modeled as a spring and a dashpot in parallel. The spring and dashpot is assumed to act always normal to the reference epicardium (see [285] for more details). In the tangential direction no traction is assumed, since the pericardial fluid reduces friction. In reference configuration the spring and dashpot boundary condition can be written as

$$\boldsymbol{t}_{\text{epi}} = \boldsymbol{N}(k_i \boldsymbol{d} \cdot \boldsymbol{N} + c_i \dot{\boldsymbol{d}} \cdot \boldsymbol{N}) \text{ on } \Gamma_0^{\text{spring},i} \in \{\Gamma_0^{\text{epi}}, \Gamma_0^{\text{avp}}, \Gamma_0^{\text{ves}}\}, \tag{4.33}$$

where $\boldsymbol{N}$ is the reference surface normal, k_i the spring stiffness, and c_i the damping viscosity for each surface i. In this chapter we used an extended formulation, where the spring stiffness is divided into two different parameters for tension k_i^{ten} and compression k_i^{com} such that the equation can be written as

$$\boldsymbol{t}_{\mathrm{epi}} = \boldsymbol{N}(k_i^{\mathrm{ten}}\boldsymbol{d} \cdot \boldsymbol{N}\mathbb{1}_{\boldsymbol{d}\cdot\boldsymbol{N}>0} + \boldsymbol{N}k_i^{\mathrm{com}}\boldsymbol{d} \cdot \boldsymbol{N}\mathbb{1}_{\boldsymbol{d}\cdot\boldsymbol{N}<0} + c_i\dot{\boldsymbol{d}} \cdot \boldsymbol{N}) \text{ on } \Gamma_0^{\mathrm{spring},i} \in \{\Gamma_0^{\mathrm{epi}}, \Gamma_0^{\mathrm{avp}}, \Gamma_0^{\mathrm{ves}}\}. \tag{4.34}$$

Inside the heart the blood pressure $p_{A,j}$ acts on the cardiac walls. The varying blood pressure is computed with the Windkessel model (see Section 4.2.7) for the right ($j = r$) and left ($j = l$) atrium. The blood acts normal onto the endocardial wall in the deformed state, which leads to

$$\boldsymbol{t}_{p_{A,j}} = p_{A,j}J\boldsymbol{F}^{-T}\boldsymbol{N} \text{ on } \Gamma_0^{\mathrm{endo},j} \text{ for } j \in \{r, l\}, \tag{4.35}$$

in reference configuration.

Combining all equations (Equations (4.32),(4.33) and (4.35)) the strong form of the elastodynamic boundary value problem in reference configuration can be formulated as

$$\begin{array}{lcll}
\mathrm{div}\,(\boldsymbol{P}) & = & \rho_0\ddot{\boldsymbol{d}} & \text{in } \Omega_0, \\
\boldsymbol{P}\boldsymbol{N} & = & p_{A,j}J\boldsymbol{F}^{-T}\boldsymbol{N} & \text{on } \Gamma_0^{\mathrm{endo},j} \text{ for } j \in \{r, l\}, \\
\boldsymbol{P}\boldsymbol{N} & = & \boldsymbol{N}(k_i\boldsymbol{d}\boldsymbol{N} + c_i\dot{\boldsymbol{d}}\boldsymbol{N}) & \text{on } \Gamma_0^{\mathrm{spring},i} \text{ for } i \in \{\mathrm{epi}, \mathrm{avp}, \mathrm{ves}\},
\end{array} \tag{4.36}$$

with the first Piola-Kirchhoff stress tensor $\boldsymbol{P} = \boldsymbol{F}\boldsymbol{S}$.

4.2.5.4 Prestress

Medical imaging techniques can only capture the organs inside the body under the mechanical impact of the surrounding tissue and blood. For the heart this means for example, that during imaging blood inside the cardiac chambers is acting as pressure onto the cardiac walls. Thus, the segmented geometry of the heart in reference configuration is not stress-free. To consider the stress in the mechanical simulation a we use a modified updated Lagrangian formulation presented in [128]. Therefore, we use a multiplicative split of the deformation gradient to compute a displacement free configuration which is in equilibrium with external loads. With this technique we take into account the blood pressure acting onto the endocardial wall. However, residual stresses of the cardiac muscle are not considered, since the identification of these stress values in patient-specific hearts is extremely challenging and imprecise.

4.2.5.5 Mechanical Model Parameters

The mechanical behavior of myocardial tissue of both atria is characterized by both its passive stiffness and its ability to contract, triggered by the electrical signal. The tissue mechanical model is based on the nonlinear elastodynamic equations, with the passive part represented as a nearly incompressible Mooney–Rivlin material, plus an active stress component [67]. We use a simplified version of an excitation contraction model [39] retaining three parameters: the maximal active tension, the myosin attachment and detachment rate. The activation function for the Bestel model at each structural element is equal to 1 once the element center is electrically activated.

Table 4.2: Parameters for the mechanical equations

$\rho_0[\mathrm{kg/m^3}]$	$c_1[\mathrm{Pa}]$	$c_2[\mathrm{Pa}]$	$\eta[\mathrm{Pa\,s}]$	$\varepsilon[\mathrm{Pa}]$	γ	$\sigma_0[\mathrm{Pa}]$	$\alpha_{\max}[\frac{1}{\mathrm{s}}]$	$\alpha_{\min}[\frac{1}{\mathrm{s}}]$	C
10^3	2×10^4	2×10^1	0	10^7	1	10^5	20	-30	1

(a) Myocard

$\rho_0[\mathrm{kg/m^3}]$	$c_1[\mathrm{Pa}]$	$c_2[\mathrm{Pa}]$	$\eta[\mathrm{Pa\,s}]$	$\varepsilon[\mathrm{Pa}]$	γ
10^3	2×10^4	2×10^1	0	10^7	1

(b) Ablation lines and valve rings

$\rho_0[\mathrm{kg/m^3}]$	$c_1[\mathrm{Pa}]$	$c_2[\mathrm{Pa}]$	$\eta[\mathrm{Pa\,s}]$
10^{-1}	2.02×10^6	2×10^1	0

(c) Valves

$k_{\mathrm{epi}}^{\mathrm{ten}}[\frac{\mathrm{kPa}}{\mathrm{mm}}]$	$k_{\mathrm{epi}}^{\mathrm{com}}[\frac{\mathrm{kPa}}{\mathrm{mm}}]$	$c_{\mathrm{epi}}[\frac{\mathrm{kPa\,s}}{\mathrm{mm}}]$
5×10^{-2}	5×10^1	0

$k_{\mathrm{avp}}^{\mathrm{ten}}[\frac{\mathrm{kPa}}{\mathrm{mm}}]$	$k_{\mathrm{avp}}^{\mathrm{com}}[\frac{\mathrm{kPa}}{\mathrm{mm}}]$	$c_{\mathrm{avp}}[\frac{\mathrm{kPa\,s}}{\mathrm{mm}}]$
5×10^{-1}	5×10^{-1}	0

$k_{\mathrm{ves}}^{\mathrm{ten}}[\frac{\mathrm{kPa}}{\mathrm{mm}}]$	$k_{\mathrm{avp}}^{\mathrm{com}}[\frac{\mathrm{kPa}}{\mathrm{mm}}]$	$c_{\mathrm{ves}}[\frac{\mathrm{kPa\,s}}{\mathrm{mm}}]$
5	5	0

(d) Boundary conditions

A similar coupling strategy was performed by Corrado et al. [88] through a scaled electrical potential obtaining realistic electromechanical physiological response.

The maximal active tension (or contractility) is fixed as $10\times10^5\,\mathrm{Pa}$ for both Models 1 and 2. This values was chosen since it leads to physiological ejection fractions (EF) of $21\,\%$ in the non-dilated atria. Additionally, in the non-dilated atria we obtain an ejected volume which corresponds to an atrial contribution to the end-diastolic ventricular volume of $38\,\%$ of Model 1 as reported in a clinical study [6]. The myosin attachment and detachment rate is set to 20 and $-30\,\mathrm{s}^{-1}$, respectively, in order to assure pressures in physiological range. At each spatial point the model independently converts the electrical activation into an active tension, which is applied in the local fiber direction. We remark that, since the ablated tissue is not activated, it does not contract, as we assume that contraction is solely induced by the electrical signal as routinely observed in clinical practice, i.e. no stretch-activated channels are modeled. Moreover, we consider the interaction with the pericardium and external tissue by including an elastic model in the surface normal direction on the epicardium [234]. As the title of this chapter suggests, since we are interested in the systolic performance of the atria only, the ventricle is considered as a passive stiffness on the heart base. All parameters of the mechanical model are summarized in Table 4.2.

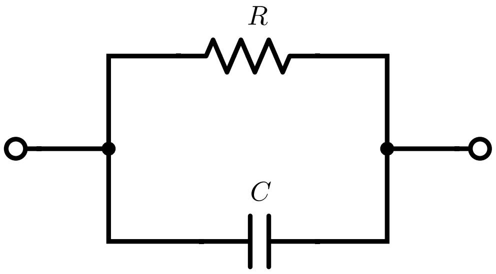

Figure 4.3: Original 2-element windkessel model

4.2.6 Numerical discretization of the Mechanical Model

The numerical solution of the solid model is performed using linear continuous finite elements for the space-semidiscretization, while the time semi-discretization is backward Euler with implicit treatment of the elastic forces.

4.2.7 Hemodynamical Model

The blood flow in human is defined by the circulatory system, which is composed of a closed loop containing two main circulations, the pulmonary circulation and the systemic circulation (see Chapter 2). Both circulations are maintained by the periodic contraction and relaxation of heart chambers. However, they are very different in terms of volume and pressure. The left heart is responsible for the systemic circulation and needs to pump the blood through the whole body, while the right heart pumps the blood only to the lung. Thus, the pressures are higher in the systemic circulation and the left heart than in the pulmonary circulation and right heart. During one heartbeat the pressure in the ventricle changes due to myocardial contraction and heart valves preventing backflow of blood. The heartbeats induce a pulsatile blood flow in the aorta and arteries, which changes the further it goes. This change arises due to the elasticity of the blood vessels.

To model realistic contraction of the heart it is necessary to take into account the blood flow and pressure and the circulatory system. However, a fully 3D model of the circulatory system with fluid-structure interaction would increase model complexity and computational time to a unreasonable extend. Hence, lumped models are used to simulate the blood and its impact on the contraction. In 1733 Stephan Haas was the first who presented a windkessel model to describe blood flow and blood pressure and later in 1899 Otto Frank extended the model [267]. A windkessel is a physically-based mathematical representation of the relation between mean pressures and flow rates in a certain geometry [319]. The windkessel is an analogy to the windkessel used in fire engines, where the air chamber transforms the periodic high pressure inflow to a steady outflow. In the circulatory system the blood vessels can be seen as windkessel, due to their elasticity. The original windkessel model uses two elements to describe the blood pressure, one is the vessel compliance and the other is the vessel resistance (see Figure 4.3).

The blood flow and blood pressure in the heart chamber and the vessels can be described with the full non-linear Navier-Stokes equations with a non-Newtonian constitutive relation of the blood. However, to decrease system complexity the model can be reduced to one-dimensional models by modeling blood as an incompressible Newtonian fluid, assuming axisymmetry of the blood vessels and integrating over the cross-sectional area [267, 268].

There exist an analogy of the models to the electrical circuit and since representation is simpler with an electrical circuit this is used in most cases. In the analogy blood volume represents electrical charge, pressure difference represents electrical potential and blood flow represents current. Thus, we can write the equivalent of Ohm's law for the blood flow as

$$q(t) = \frac{p(t)}{R}\,, \tag{4.37}$$

with current density $q(t)$, pressure $p(t)$, and vessel resistance R. The vessel elasticity can be interpreted as a capacitor and, thus, the flow through the elastic blood vessel can be written as

$$q(t) = C\frac{\mathrm{d}p(t)}{\mathrm{d}t}\,, \tag{4.38}$$

with compliance C of the vessel in analogy to the electrical capacitance.

An extension of the two-element windkessel model with a capacitor and a resistance in parallel is the three-element windkessel model which has an additional resistance upstream (see Figure 4.4). While the two-element windkessel model takes into account the ventricular compliance and peripheral resistance the additional resistance in the three-element windkessel model This additional resistance For the derivation of the equation for the three-element windkessel model we use Kirchhoff's current law

$$q(t) = \frac{p_V(t) - p_0(t)}{R_2} + C\frac{\mathrm{d}(p_V(t) - p_0(t))}{\mathrm{d}t} \tag{4.39}$$

together with Ohm's law

$$q(t) = \frac{p_A(t) - p_V(t)}{R_1}\,. \tag{4.40}$$

Substituting the second equation into the first leads to

$$(1 + \frac{R_1}{R_2})q(t) + R_1C\frac{\mathrm{d}q(t)}{\mathrm{d}t} = \frac{p(t)}{R_2} + C\frac{\mathrm{d}p(t)}{\mathrm{d}t} \tag{4.41}$$

which is the three-element windkessel equation.

We use the three-element windkessel model to simulate blood in the atria and blood flow into the ventricle. To couple the windkessel model with the contraction of the atrium we use

$$q(t) = -\frac{\mathrm{d}V}{\mathrm{d}t} \tag{4.42}$$

with V the volume of the atrium. The hemodynamical model parameters used are summarized in Table 4.3.

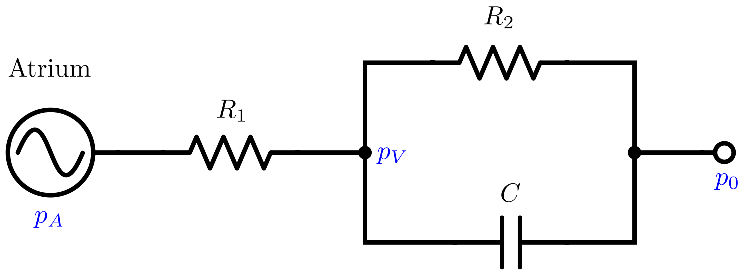

Figure 4.4: 3-element windkessel model

$C[\mathrm{m^4s^2/kg}]$	$R_1[\mathrm{kg/m^4s}]$	$R_2[\mathrm{kg/m^4s}]$
18.7548×10^6	3.3423×10^{-9}	10

Table 4.3: Parameters for the hemodynamical model

4.2.7.1 Hemodynamical Model Parameter and Numerical Methods

The interaction of the atrial wall with the blood is considered through monolithically coupling a windkessel model with the elastic myocardial wall. In our case, we assign a single pressure degree-of-freedom per cardiac chamber. The left ventricle is modeled as constant capacitance of $1.88 \times 10^8\,\mathrm{m^3/Pa}$ acting as a passive elastic component. We use the same ventricular hemodynamics for both models, Model 1 and Model 2, since we assume that the ventricles are not influenced by atrial fibrillation and the resulting dilation of the atria. The mitral valve is modeled as flow resistance between the atrial and ventricular chambers, which took high values when the ventricular pressure is higher than the atrial pressure (hence restricting the leakage into the atria) and low values when the atrial pressure exceeds the ventricular one, allowing blood only to flow in atrial-ventricular direction. This results in variations of the atrial chamber pressure between 8 and $15\,\mathrm{mmHg}$ for Model 1 and 8 and $18\,\mathrm{mmHg}$ for Model 2 without ablated tissue, for atrial diastole and systole, respectively.

In our model we assume that no backflow in the pulmonary veins exists, thus all blood leaving the atrium is flowing into the ventricle.

Both solid and hemodynamic models are coupled implicitly in time, leading to a single system of equations, which is solved iteratively using block-LU preconditioner with a parallel iterative GMRES method, allowing an efficient algebraic treatment of the solid-Windkessel coupling.

4.3 Results

4.3.1 Perfect Ablation Lines

To illustrate the versatility of the multiphysics modeling framework, we compare 15 different ablation concepts representing current clinical ablation standards on the two bi-atrial models presented above. We analyze the simulation results in terms of activation sequence and duration, volume over time and the correlation of the amount of inactive and ablated tissue with EF.

Figure 4.5 shows the activation map for Model 1 without any ablation lines (top left). The activation map corresponds well with an experimentally gained activation map [94] and the ac-

Table 4.4: Ejection fraction (EF) of left atria with different ablation concepts for Model 1 and Model 2.

Ablation lines	Max. atrial output [ml]	EF [%]	ΔEF pp	Ablated tissue [%]	Inactive tissue [%]	Time max contraction [s]
Model 1						
No Ablation	18.7	20.68	0	0	0	0.2588
PVI	15.7	17.31	3.37	10.0	14.7	0.2582
PVI+AL	14.6	16.20	4.48	14.3	19.0	0.2632
PVI+MIL	15.1	16.69	3.99	12.1	16.9	0.257
PVI+CFAE	14.6	16.13	4.54	13.9	18.6	0.2586
PVI+BL	13.6	15.02	5.66	13.5	21.7	0.2568
PVI+RL	15.1	16.72	3.96	11.8	16.6	0.258
PVI+CFAE posterior	15.1	16.71	3.97	11.6	16.3	0.2576
PVI+CFAE anterior	15.1	16.74	3.94	12.2	17.0	0.2588
PVI+AL+RL	14.1	15.63	5.05	16.2	20.9	0.2636
PVI+MIL+RL	14.5	16.08	4.60	14.0	18.8	0.257
PVI+AL+BL	12.7	14.02	6.66	17.9	26.0	0.263
PVI+MIL+BL	13.5	14.95	5.73	15.7	23.9	0.2572
PVI+AL+CFAE+RL	13.1	14.44	6.24	20.1	24.8	0.2638
PVI+MIL+CFAE+RL	13.5	14.95	5.73	17.9	22.7	0.2572
WACA	13.8	15.24	5.44	13.0	21.6	0.2586
Model 2						
No Ablation	25.4	15.77	0	0	0	0.2716
PVI	22.9	14.24	1.53	7.9	12.7	0.2718
PVI+AL	21.1	13.14	2.63	11.0	15.8	0.279
PVI+MIL	21.9	13.59	2.18	9.4	14.2	0.2706
PVI+CFAE	20.8	12.95	2.82	13.3	18.1	0.2744
PVI+BL	21.4	13.30	2.47	10.8	19.6	0.2714
PVI+RL	22.7	14.08	1.69	9.4	14.1	0.2712
PVI+CFAE posterior	21.7	13.46	2.31	10.4	15.2	0.2722
PVI+CFAE anterior	22.1	13.74	2.03	10.9	15.6	0.2736
PVI+AL+RL	20.9	12.97	2.80	12.5	17.2	0.2786
PVI+MIL+RL	21.6	13.42	2.34	10.8	15.6	0.2704
PVI+AL+BL	19.6	12.19	3.58	13.9	22.7	0.279
PVI+MIL+BL	20.3	12.63	3.14	12.2	21.1	0.2706
PVI+AL+CFAE+RL	18.8	11.71	4.06	17.9	22.6	0.2832
PVI+MIL+CFAE+RL	19.6	12.17	3.60	16.2	21.0	0.2732
WACA	21.6	13.45	2.31	8.9	17.1	0.2724

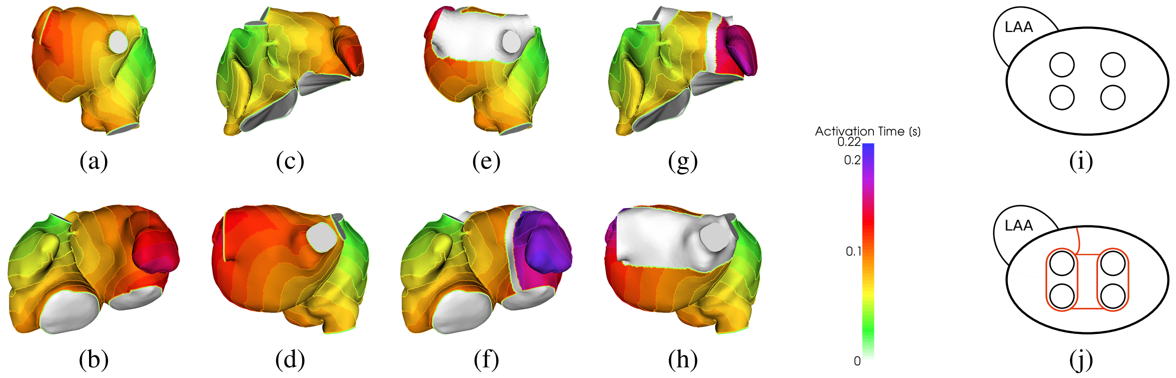

Figure 4.5: Isochrones of the propagation wave for Model 1 (top) and Model 2 (bottom) without, (a)-(d), and with, (e)-(h), ablation concepts including PVI + AL + BL. We include a scheme of the LA and the LA appendage (LAA) with the ablation concept (red) for sake of clarity.

tivation times lay in the same range as atria in clinical surgery [211]. For Model 2 the activation pattern is similar, besides the fact that the overall activation takes longer. In Model 1 the activation of the complete atria takes around $120\,\mathrm{ms}$ and in Model 2 around $150\,\mathrm{ms}$.

Figure 4.6 shows isochrones of the propagation wave of Model 1 with the simulated sinus rhythm and different ablation lesions, while Figure 4.7 presents the atrial time–volume curves. Circumferential PVI does not significantly alter the excitation sequence in the left atrium, since only the orifices of the PVs are not activated anymore (see Figures 4.6a and 4.6b). The WACA ablation procedure disables a larger amount of contractile tissue compared to standard PVI, which has a significant impact on maximal atrial output (see Table 1), although the activation pattern is not altered (see Figure 4.6c). A considerably different activation pattern is observable when comparing PVI + AL and PVI + MIL. The combination PVI + MIL does not alter the excitation sequence compared to only PVI, whereas PVI + AL has a significant impact. AL blocks the activation on the anterior side of the left atrium. The left appendage is thus only activated from the posterior side, resulting in a significant increase in activation time (around $50\,\mathrm{ms}$ in both models) (see Figures 4.6d and 4.6e). The ablation PVI + BL does not significantly alter the excitation sequence but inactivates a large portion of left atrial tissue on the roof (see Figure 4.6f and Table 4.4). The ablation lesion PVI + CFAE leads to small inhomogeneities in the activation on the anterior and posterior side and a slight increase in activation time (see Figure 4.6g). For Model 2, the results of the activation sequence are similar apart from the natural prolongation of the activation time due to the increased size of the atria.

Figure 4.7 shows the computed time-volume curves of the left atrium until left atrial peak systole for both Models 1 and 2 with the basic ablation line combinations. The plots show that for all ablation lines the time from the onset of contraction to peak systole are identical except for the combination PVI + AL. Additionally to the already stated delay at peak systole for PVI + AL (see also Table 4.4, the descent of the volume curve is less steep, i.e. in comparison to other ablation lines the ejected blood volume is at all time points lower. These observations can be seen in the volume curves for both Model 1 and Model 2.

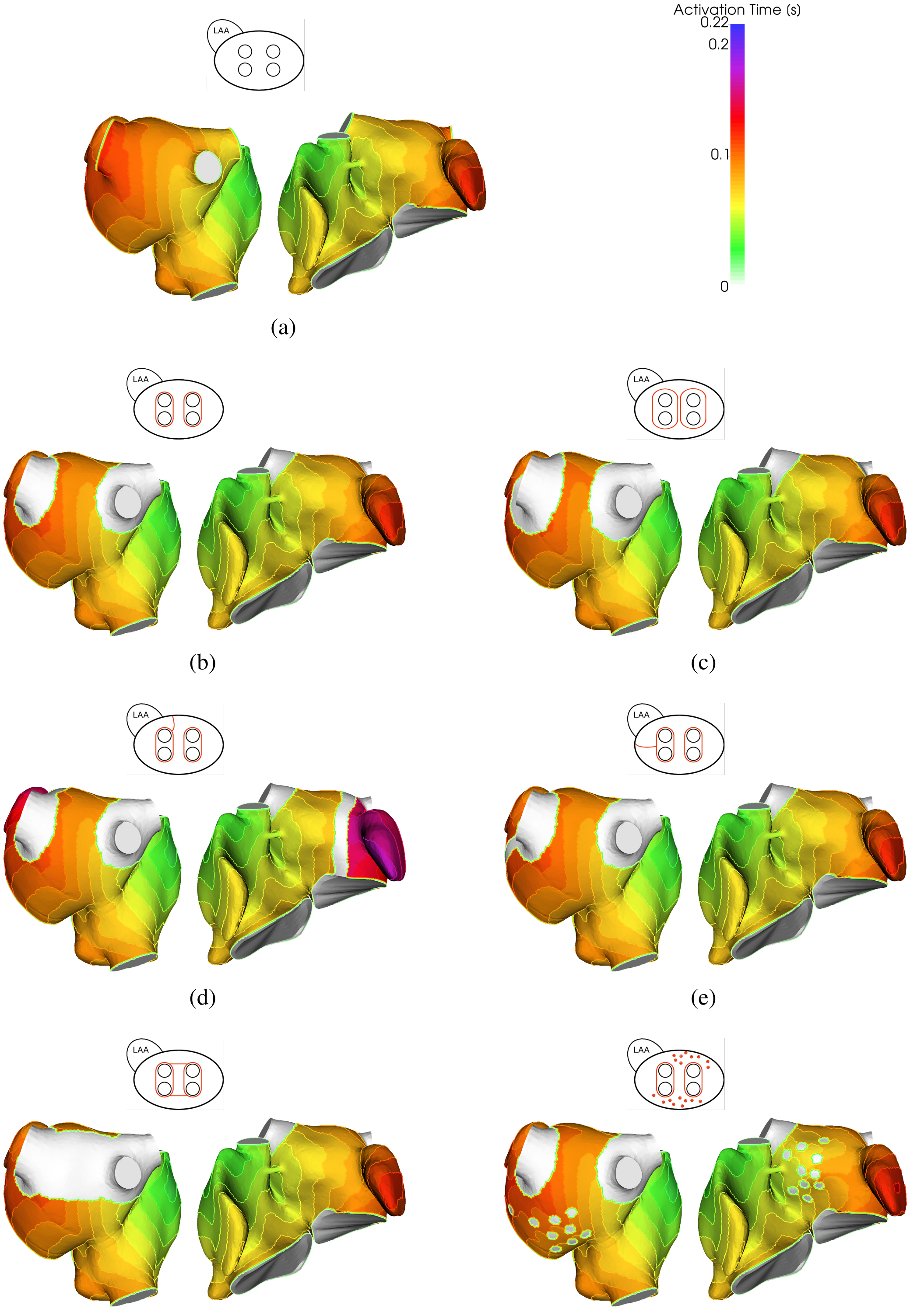

(a)

(b)

(c)

(d)

(e)

(f)

(g)

Figure 4.6: Isochrones of the propagation wave in sinus rhythm for Model 1 without ablation and with generic ablation lesions. A schematic representation of the ablation lesions is given at the top of each model, which shows the left atrium with the left atrial appendage (LAA) and the four pulmonary veins (circles) from an epicardial latero-dorsal view. The red lines represent the ablation lesions. (a) Activation without ablation lesions; (b) PVI; (c) WACA procedure; (d) PVI + AL; (e) PVI + MIL; (f) PVI +BL; (g) PVI + CFAE ablation.

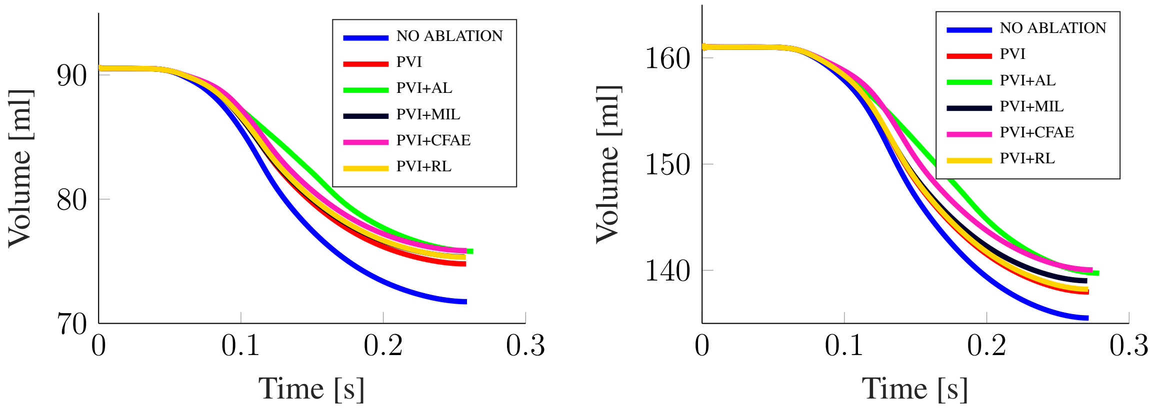

(a)

Figure 4.7: Computed volume curve for (a) Model 1 and (b) Model 2. The curves end at their peaks systole, i.e. maximal contraction of the atria. Shown in the plots are the volume curves for no ablation (blue), PVI (red), PVI + AL (green), PVI + MIL (black), PVI + CFAE (purple) and PVI + RL (yellow).

Table 4.4 summarizes the results for all ablation approaches in terms of the change (Δ) in EF due to ablation lesions is compared to the baseline model without ablation and a healthy sinus rhythm.

Figure 4.8 depicts the results for all ablation concepts ordered by ΔEF. It shows that the more extensive the ablation approach, thus electrically isolating more tissue, the greater is the reduction of left atrial output. In both models the ablation pattern including AL inactivated a larger portion of tissue and decreased left atrium (LA) EF more than the combination with MIL.

In Figure 4.9 the amounts of ablated tissue and inactive tissue are plotted against ΔEF. Model 1 shows a strong correlation (correlation coefficient $R^2 = 0.98$) between inactive tissue and ΔEF and a weaker correlation ($R^2 = 0.75$) between ablated tissue and ΔEF. The correlations for Model 2 show similar behavior for inactive tissue and ΔEF ($R^2 = 0.85$), and ablated tissue and ΔEF ($R^2 = 0.88$).

4.3.2 Imperfect Ablation Lines

To study the effect of imperfect ablation lines, we perform additional simulations with gaps at different locations in the AL and MIL.

In the AL we include gaps in the upper part, in the middle part and in the lower part of the line and in the MIL we include a gap in the middle of the line (see Figure 4.10). Figure 4.11 shows the activation pattern of the PVI and the PVI + AL ablation concept in comparison to a PVI + AL ablation with gaps on different locations. Figure 4.12 shows the activation pattern of the ablation concepts PVI, PVI + MIL without a gap and PVI + MIL with a gap. The gaps have an average thickness of $3\,\mathrm{mm}$ and go through the entire thickness of the wall. They are modeled as healthy tissue. A complete AL slows the activation of the LAA significantly, while a gap in the line reduces the activation time to a certain level, depending on the location of the gap. The gap in the middle part of the AL reduces the activation time of the LAA the most; the

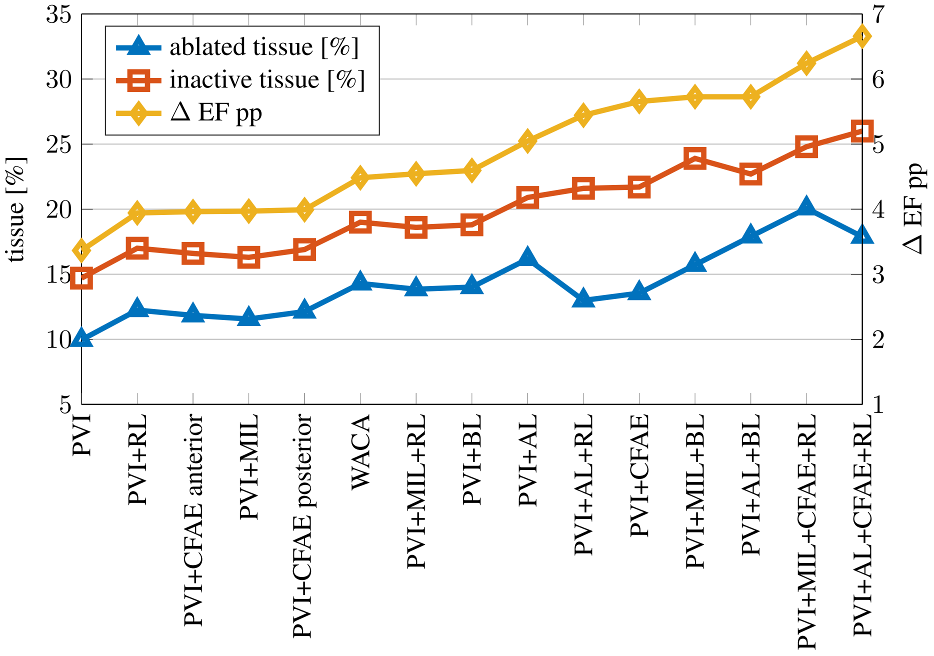

(a)

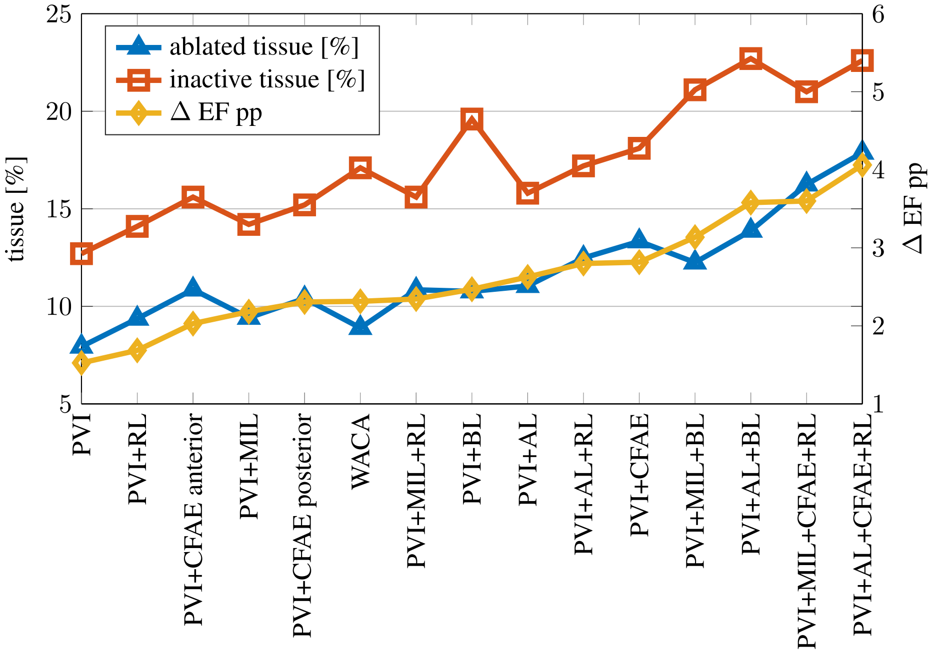

(b)

Figure 4.8: Plot for all combinations of ablation lines for (a) Model 1 and (b) Model 2 including the change of EF percentage points (pp), the ablated volume (%) and the inactive volume (%). From left to right Δ EF increases.

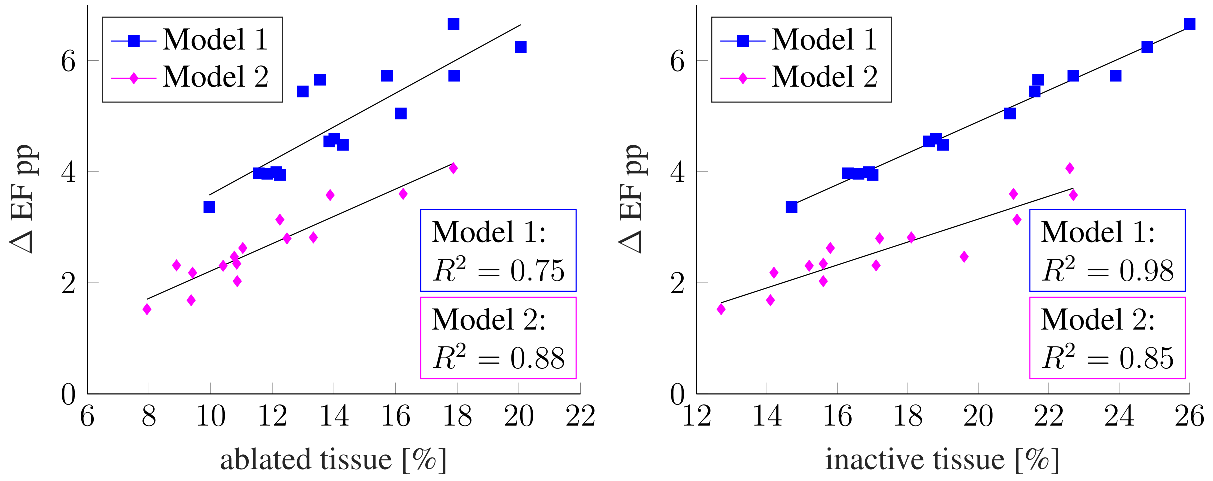

(a)

(b)

Figure 4.9: (a) Plot of ablated tissue (%) against ΔEF percentage points (pp) for Model 1 (blue rectangle) and Model 2 (purple diamond) for all combinations of ablation lines. (b) Plot of inactive tissue (%) against ΔEF pp for Model 1 (blue rectangle) and Model 2 (purple diamond) for all combinations of ablation lines.

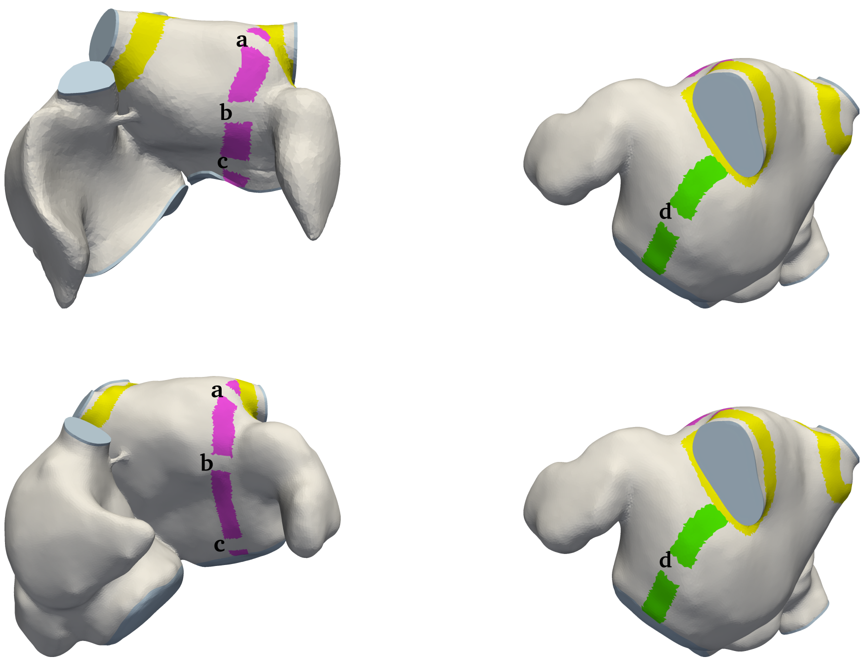

Figure 4.10: Gaps in the ablation lines. For Model 1 (top) and Model 2 (bottom) three gaps in the anterior line (a, b, c) and one gap in the mitral isthmus line (d) are tested. The gaps are situated in the upper part of the AL (a); the middle part of the AL (b) and the lower part of the AL (c); and in the mitral isthmus line (d).

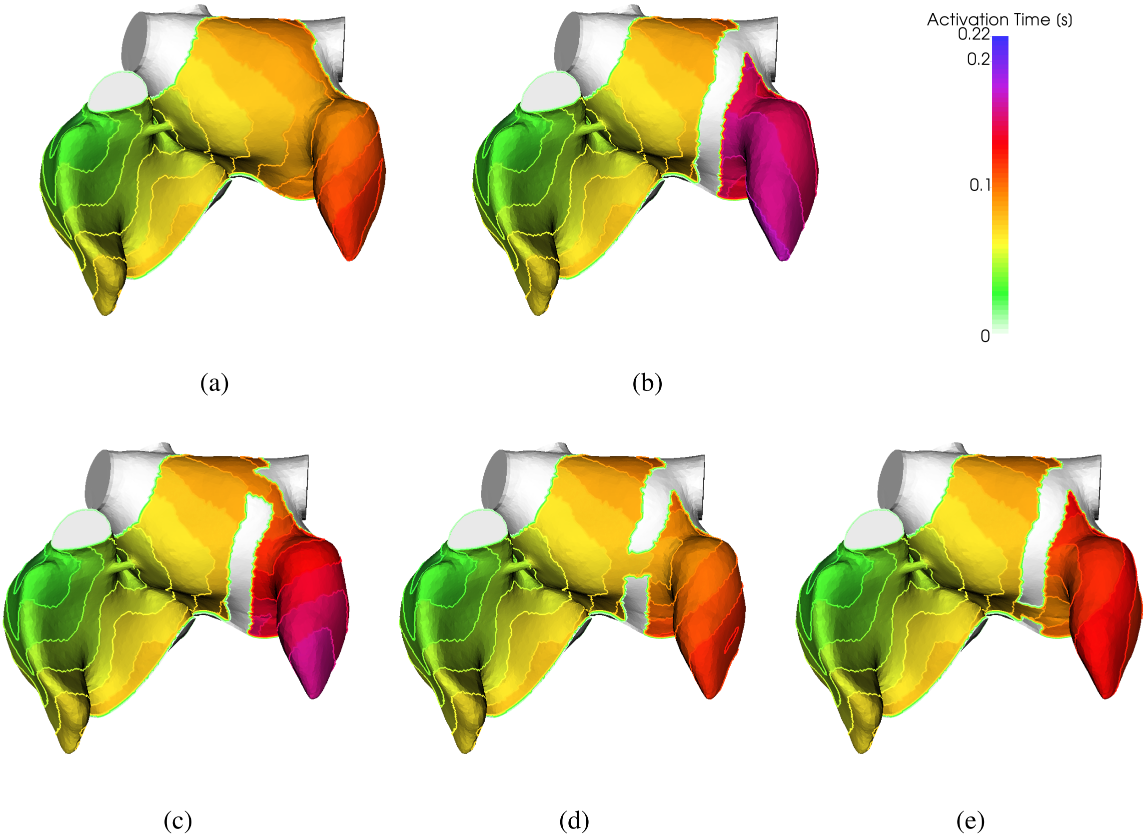

(a) (b)

(c) (d) (e)

Figure 4.11: Activation time for the atria with PVI ablation (a) and PVI + AL ablation (b) in comparison with the activation times for the PVI + AL ablation concept with gaps in the AL. (c) gap in the upper part of the AL, (d) gap in the middle part of the AL and (e) gap lower part of the AL.

gap in the upper part of the AL reduces the least. This behavior is also visible in the atrial output curves (see Figures 4.13a and 4.14a). The volume curve for the PVI + AL ablation with a gap in the middle part is steeper than the curve of the ablation with a continuous AL. A gap in the MIL does not significantly alter the activation pattern, since the MIL itself does not change the activation pattern. However, an impact on the ejection fraction is visible. Since more contractile tissue exists, the atrial output is bigger when including a gap in the MIL (see Figures 4.13b and 4.14b and Table 4.5). The results obtained with Model 1 are analogous as with Model 2.

4.3.3 Reduced Conduction Velocity

In diseased atria it may appear that the conduction velocity is reduced due to, for example, the presence of fibrosis. To investigate the influence of a reduced conduction velocity on the contractility of the left atria we perform additional simulations with different diffusion coefficients. We apply a homogeneous reduction of the diffusion coefficient in all atrial tissue, see e.g., Reference [204] for taking into account uniform gap junction remodeling. As there exist many types of atrial remodeling [313] we study three different reductions of the diffusion coefficient, i.e.

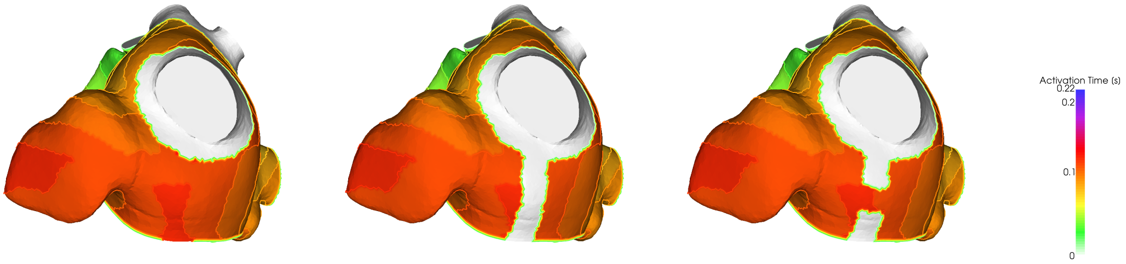

(a) (b) (c)

Figure 4.12: Activation time for PVI ablation concept (right), PVI + MIL (middle) and PVI + MIL with a gap in the mitral isthmus line.

Table 4.5: Ejection fraction (EF) of left atria with a gap in the ablation lines for different ablation concepts for Model 1 and Model 2.

Ablation lines	Max. atrial output [ml]	EF [%]	ΔEF pp	Time max contraction [s]
Model 1				
No Ablation	18.7	20.68	0	0.2588
PVI+MIL	15.2605	16.871 45	3.806 677	0.2576
PVI+AL gap top	14.8486	16.416 07	4.262 058	0.262
PVI+AL gap middle	14.9819	16.563 44	4.114 687	0.2586
PVI+AL gap bottom	14.8366	16.402 81	4.275 325	0.2598
Model 2				
No Ablation	25.4	15.77	0	0.2716
PVI+MIL	22.109	13.743 57	2.023 398	0.2708
PVI+AL gap top	21.269	13.2214	2.545 565	0.278
PVI+AL gap middle	21.594	13.423 43	2.343 536	0.274
PVI+AL gap bottom	21.52	13.377 43	2.389 537	0.2766

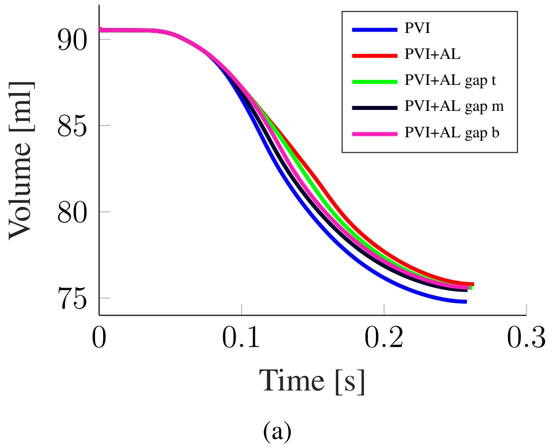

(a) (b)

Figure 4.13: Volume curves for Model 1. (a) AL with gaps on top t, middle m and bottom b of the line. (b) MIL with a gap.

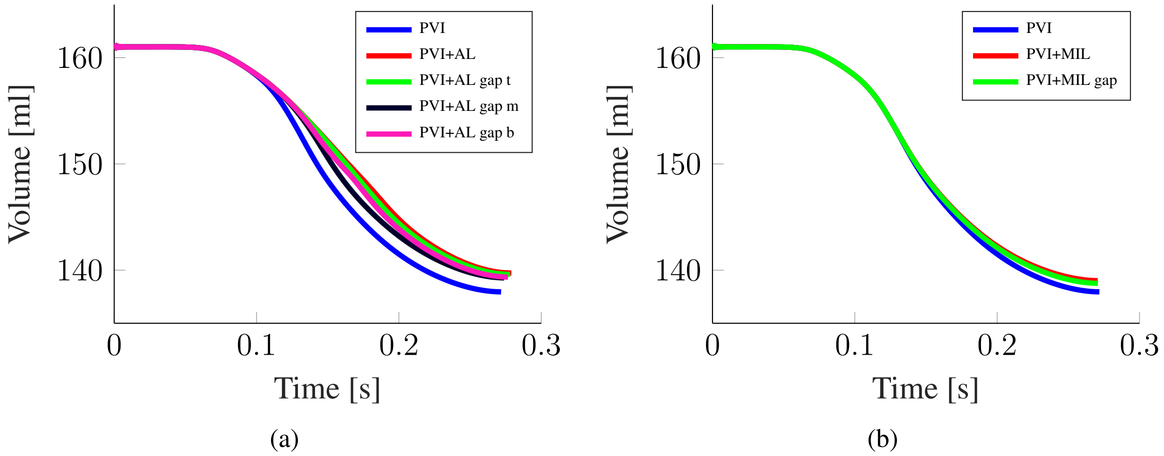

(a) (b)

Figure 4.14: Volume curves for Model 2. (a) AL with gaps on top t, middle m and bottom b of the line. (b) MIL with a gap.

75, 50, and 25 %. Figure 4.15 shows the activation map for Model 1 for the ablation concepts PVI, PVI + AL, and PVI + MIL for the different diffusion coefficients. Decreasing the diffusion coefficient leads to a prolongation of the activation time, which is more clearly visible in the ablation strategy PVI + AL (Figure 4.15 (middle row)). In Figure 4.16 the volume over time is plotted for the ablation concept PVI + AL for different diffusion coefficients until the moment of maximal contraction. One can see that the time of maximal contraction is delayed, additionally also the minimal volume is bigger. Thus with decreasing conduction velocity the ejection fraction decreases too, see Figure 4.16a. Note that the result with a reduced diffusion coefficient is qualitatively the same as for the result with the larger diffusion coefficient besides the fact that the differences between the ablation concepts are bigger. The detailed results for all diffusivities and ablation lines for both models are summarized in Table 4.6.

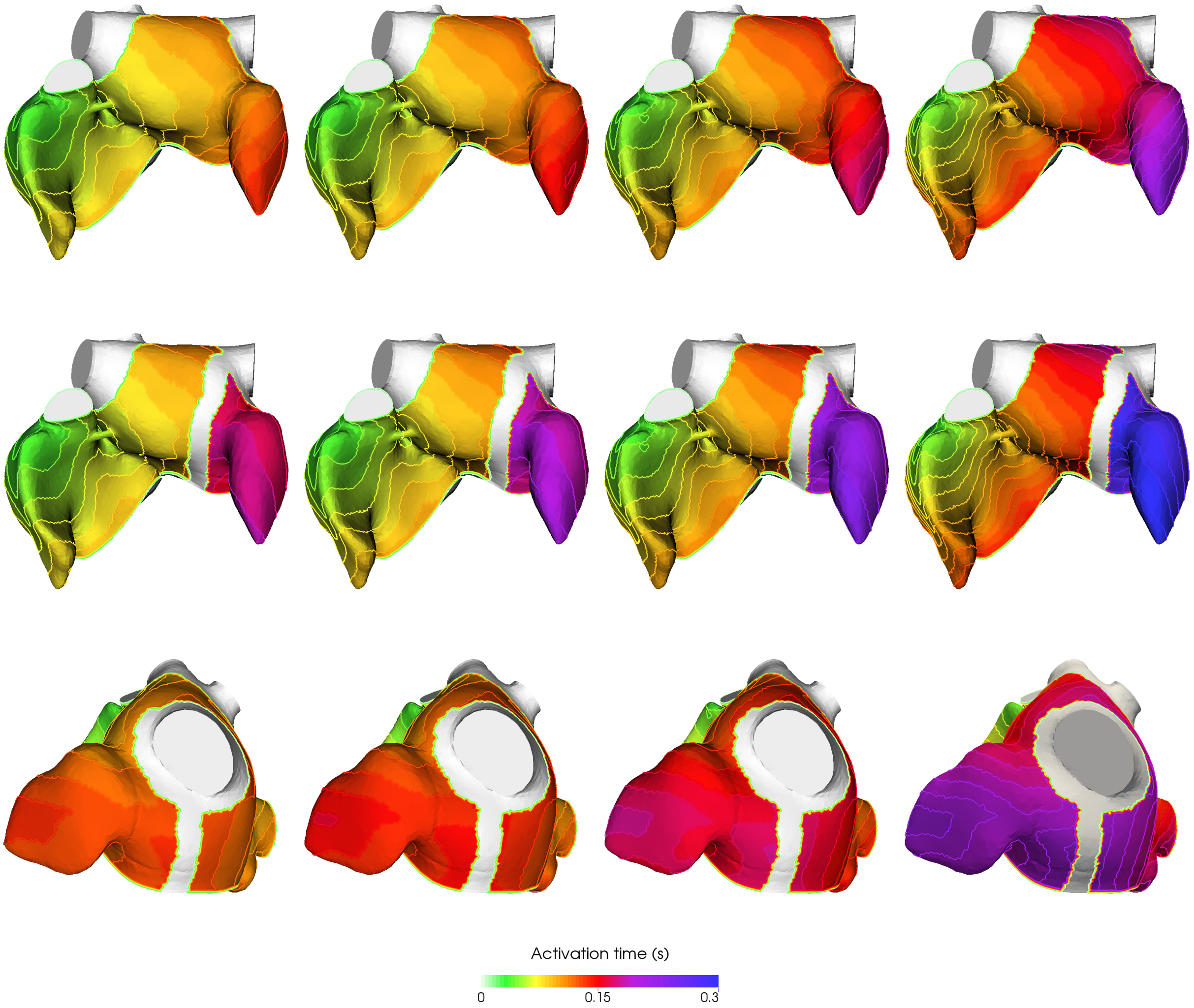

Figure 4.15: Activation time for Model 1 for the left atria with the diffusivities $0.6\,\mathrm{mm}^2/\mathrm{ms}$, $0.45\,\mathrm{mm}^2/\mathrm{ms}$, $0.3\,\mathrm{mm}^2/\mathrm{ms}$ and $0.15\,\mathrm{mm}^2/\mathrm{ms}$ (form left to right) and the ablation concepts PVI, PVI + AL and PVI + MIL (from top to bottom).

4.4 Discussion

We developed a coupled electro-mechano-hemodynamic model of atria which could be used pre-operatively to gain additional information about atrial function and possible clinical outcomes for several options of radiofrequency ablation. While previous computational models of atrial ablation investigated electrical propagation, this study focuses on left atrial ejection performance depending on the activation pattern. With our model we calculated the electrical, mechanical and hemodynamic response of two patient-specific atrial geometries with different ablation lines. This multiphysical coupling allows to investigate influences of the electrical activation on the succeeding myocardial contraction and pressure development. A prolonged activation time for AL ablation is noticeable due to the delayed activation of the left atrial appendage (see Figure 4.6). This time delay is reflected in a delayed peak systole (see Figure 4.7). In the aspect of

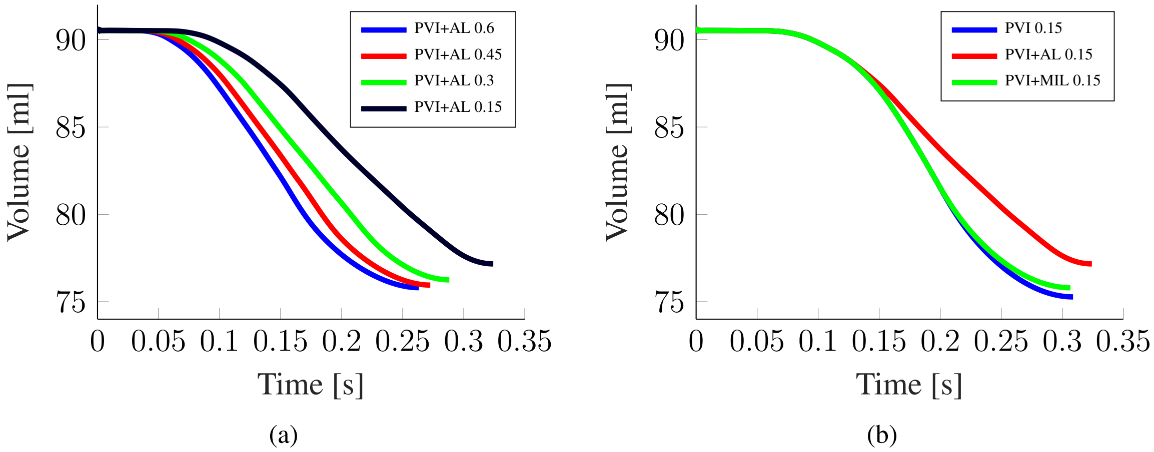

(a)

(b)

Figure 4.16: Volume curves for Model 2 for the AL with gaps (a) and MIL with a gap (b).

successful therapy outcome this time delay of peak systole is important since delayed left atrial contraction is a known cause of poor left-sided atrio-ventricular coupling. If the time delay is too large it could happen that the start of LA appendage outflow occurs after the beginning of ventricular contraction. This on the other hand may lead to adversely affected left atrial transport function and to electrical and mechanical remodeling [312, 323, 324].

Our model is able to verify that ablation concepts which isolate larger portions of the left atrial tissue lead to a stronger decrease in the active contraction of the atrium. In the non-dilated model the LA EF decrease has as strong correlation with the percentage of inactive tissue, while in the dilated model the correlation is slightly less distinctive.

The results indicate a linear correlation between the change in EF and the amount of inactive tissue (see Figure 4.9). In the non-dilated atrium the strong linear correlation of the decrease of EF with the amount of inactive tissue indicates that rather the spatial extension than the location of the ablation line is the key aspect impacting the mechanical performance of the atria after ablation. A recent clinical study [83] based on magnetic resonance imaging, demonstrated the correlation between the extent of scar tissue after radiofrequency ablation and decrease in LA EF, consistent with our findings. The difference between Model 1 and Model 2 in the reduction of EF can be explained by the fixed width of the ablation line used in the simulations. This results in a lager percentage of ablated tissue in small atria, see Model 1.

Investigating the differences in the atrial mechanical output with simulations of imperfect lines confirms that atrial EF is mainly proportional to the amount of remaining contractile tissue after ablation.

The results in diseased atria are qualitatively the same as in atria with normal conduction velocity. However, in the case of a reduced conduction velocity the contractility of the chamber is also reduced and moreover the differences between the ablation concepts are more relevant. This motivates further studies about the proper choice of the ablation strategy taking also into account mechanical and hemodynamical criteria.

Table 4.6: Ejection fraction (EF) of left atria with different diffusion coefficients for the basic ablation concepts PVI, PVI + AL and PVI + MIL for Model 1 and Model 2.

Diffusivity $[\mathrm{mm\,s^{-1}}]$	Ablation lines	Max. atrial output [ml]	EF [%]	ΔEF pp	Time max. contraction [s]	Time activation [s]
Model 1						
0.6	No ablation	18.70	20.68	0	0.26	0.12
	PVI	15.66	17.31	3.36	0.26	0.12
	PVI + AL	14.65	16.20	4.48	0.26	0.17
	PVI + MIL	15.09	16.69	3.99	0.26	0.12
0.45	PVI	15.60	17.25	3.43	0.27	0.14
	PVI + AL	14.50	16.03	4.65	0.27	0.19
	PVI + MIL	15.04	16.63	4.05	0.27	0.14
0.3	PVI	15.49	17.12	3.55	0.28	0.16
	PVI + AL	14.20	15.70	4.98	0.29	0.23
	PVI + MIL	14.94	16.51	4.17	0.28	0.16
0.15	PVI	15.18	16.78	3.90	0.31	0.21
	PVI + AL	13.29	14.69	5.99	0.32	0.31
	PVI + MIL	14.65	16.20	4.48	0.31	0.21
Model 2						
0.6	No ablation	25.36	15.77	0	0.27	0.15
	PVI	22.91	14.24	1.52	0.27	0.15
	PVI + AL	21.14	13.14	2.63	0.28	0.2
	PVI + MIL	21.86	13.59	2.18	0.27	0.15
0.45	PVI	22.78	14.16	1.61	0.28	0.17
	PVI + AL	20.81	12.93	2.83	0.29	0.23
	PVI + MIL	21.73	13.51	2.26	0.28	0.17
0.3	PVI	22.53	14.01	1.76	0.30	0.2
	PVI + AL	20.15	12.52	3.24	0.31	0.27
	PVI + MIL	21.50	13.37	2.40	0.30	0.2
0.15	PVI	21.84	13.58	2.19	0.34	0.26
	PVI + AL	18.20	11.31	4.45	0.36	0.36
	PVI + MIL	20.86	12.97	2.80	0.33	0.26

pp percentage points

4.4.1 Clinical Significance

For the aspect of atrial arrhythmia this chapter demonstrated that the computational framework can be used for investigating the difference between various ablation concepts. From the clinical point of view there is currently no general evidence that favors particular ablation lines [49, 77, 175]. The impact on the hemodynamic performance predicted by multiphysics modeling could be used as additional pre-operative criteria for choosing the ablation concept. However, the computational framework can also be used, besides atrial arrhythmia, for other cardiac in-silico studies. The model is able to compute electrophysiology coupled with cardiac mechanics and hemodynamics. Thus, the model is perfectly suited to investigate cardiac disease and treatment that are based on electrophysiological propagation. Besides common cardiac arrhythmia, left bundle branch block (LBBB) is a cardiac disease originating from an abnormality in the electrical conduction. The computational framework described in this chapter can also be used to investigate and validate cardiac resynchronization therapy (CRT), for example on the placement of the device. CRT is the treatment option for LBBB and other dissynchronized ventricular contraction.

Using electrical remodeled cell model parameters with the computational framework we can investigate the occurrence of arrhythmia in the presence of fibrosis, the termination with certain ablation lines, and the effects on the mechanical and hemodynamical performance. Is the contraction performance of the atria reduced, for example during atrial arrhythmia or after an extensive ablation procedure, thrombus formation is possible. Mostly thrombosis occurs in the left atrial appendage (LAA). With our computational framework we can investigate the mechanical performance of the LAA and evaluate the ejection of the LAA under different electrophysiological conditions.

4.4.2 Limitations and Perspectives

This study considered the three main aspects of the atrial physiology, namely the electrical propagation, the tissue contractility and the hemodynamic feedback. The blood pressure was represented using a lumped parameter model and hence spatial variations of the flow behavior inside each chamber are neglected. Further investigations could analyze the effect of different ablation lines on the flow behavior of the blood in the left atria, the left atrial appendage and the mitral valve to study possible clot formation for minimizing stroke risk in AF [370].

Since the focus of this study was to evaluate the hemodynamic performance of the left atria under different ablation concepts where only the geometry was taken patient-specific, all other model parameter are chosen from the literature, what allowed to obtain activation patterns and atrial pressures in a physiological range. However, to use our model for predictive purposes it is necessary to adapt the parameter to patient-specific atrial properties and future work may also include the estimation of constitutive tissue properties using clinical measurements and data [37, 64, 206, 207, 234, 240] assimilation approaches. In any case, the sensitivity of the model's output to the physical parameters (constitutive constants, fiber directions, wall thickness variability, etc.) should be estimated using uncertainty quantification techniques as it was done for example for abdominal aortic aneurysm [40]. An effective probabilistic framework used in cardiac electrophysiology was developed and applied for estimation patient-specific parameter in [201]. An important work has of course to be later carried out in investigating if these uncertainties may influence the clinical decision associated to the model's output.

In this study we did not take into account the role of fibrotic tissue and fibrosis in dilated atria and around ablation lesions. Fibrosis could lead to a slowed propagation of the electrical signal and to different propagation patterns if the distribution of the fibrosis is not homogeneous. Fibrosis would also influence contractile properties of the atria and thus deviating hemodynamic performance is expected.

Additionally, remodeling of the atrial myocytes after long-lasting fibrillation would lead to changes in the electrical and contractile properties of the atria. The impact of atrial myocyte remodeling on the electrophysiology and the mechanical performance of the atria was investigated by Adeniran et al. [2] but without taking into account the effect of ablation lines. In this study, we assumed that after the ablation procedure all remodeling of the myocytes is reversed after some time. Since the focus of this study was at long-term performance, we did not investigate the hemodynamic performance immediately after the surgical intervention where remodeled atrial myocytes are still present. Investigating the influence of partially remodeled atria could be an aspect of further studies.

A further interesting and clinically relevant application of our sophisticated multiphysics framework is to study the effect of incomplete ablation lines on mechanical performance, which is known to lead to complicated electrical propagation patterns and reentrant waves.

Two improvements of the computation model to make it more suitable for clinical practice are described in the following chapters. First, since the electrophysiology computation are numerically challenging and require the usage of very fine discretization we implemented a new numerical discretization method, which allows the usage of adaptive high-order polynomial orders and thereby a reduction of degrees of freedom (see Chapter 5). Additionally, to reduce manual work for the creation of the patient-specific geometry we build a framework to equip the geometry with fibers in an automated way (see Chapter 6).

4.5 Closure

This chapter described the computational model developed. To demonstrate the importance and the benefit of our model for clinical practice, we investigated the impact of standard ablation strategies on the mechanical performance of the atria. We showed that our model can be used pre-operatively to supply the surgeon with additional information. All possible radiofrequency ablation strategies can be applied, tested and evaluated with our computational model. The outcome of the simulation provides insights in atrial function, namely the electrical propagation, mechanical performance and hemodynamical feedback, when using a certain ablation concept. Additionally, we demonstrated that our model can also be used to investigate and compare ablation concepts in terms of the existence of a correlation between tissue and ejection fraction. Thus, we could show a strong linear correlation between inactive tissue and ejection fraction and a less strong correlation between ablated tissue and ejection fraction.

Acknowledgment

This chapter contains the results already published in [172] and reprinted here by permission from Springer Customer Service Centre GmbH: Springer Nature, Cardiovascular Engineering and Technology, Multiphysics Modeling of the Atrial Systole under Standard Ablation Strategies, Julia M. Hörmann, Cristóbal Bertoglio, Andreas Nagler et al., © Biomedical Engineering Society 2017 (2017)

5 An Adaptive Hybridizable Discontinuous Galerkin Approach for Cardiac Electrophysiology

Cardiac electrophysiology simulations are numerically challenging due to the propagation of a steep electrochemical wave front and thus require discretizations with small mesh sizes to obtain accurate results. In this chapter, we present an approach based on the Hybridizable Discontinuous Galerkin method (HDG), which is an efficient approach to high-order accuracy. HDG allows to reduce the overall degrees of freedom in the final linear system to those only on the element interfaces. Additionally, we propose a rule for a suitable integration accuracy for the ionic current term depending on the polynomial order and the cell model to handle high-order polynomials. Our results show that for the same number of degrees of freedom coarse high-order elements provide more accurate results than fine low-order elements. The discontinuous function space of the HDG method has additionally the advantage of the simple usage of p-adaptive methods, thus, we present an efficient p-adaptive strategy for accurately tracking the wave front. Introducing p-adaptivity further reduces computational costs while maintaining accuracy by restricting the use of high-order elements to resolve the wave front. For a patient-specific simulation of a cardiac cycle p-adaptivity reduces the average number of degrees of freedom by 95% compared to the non-adaptive model. In addition to reducing computational costs, using coarse meshes with our p-adaptive high-order HDG method also simplifies practical aspects of mesh generation and postprocessing.

The remainder of the chapter is organized as follows. In Section 5.1 we summarize the electrophysiology model problem and recall the CG and HDG discretization approaches. We then discuss the strategies used for the calculation of the ionic current term with focus on high polynomial degrees of the function spaces. In Section 5.2 we detail the setups of the numerical experiments and the cell model we use, and exemplify the ionic current integration rule for a specific cell model. We also determine a practical choice for the stabilization parameter in HDG. The numerical results comprise an academic geometry for benchmarking purposes and a simulation on a patient-specific heart, where both CG and (p-adaptive) HDG methods are assessed.

5.1 Theory

5.1.1 Electrophysiology Equations

The classical monodomain model for the domain $\Omega \subset \mathbb{R}^d$ is given in the following way (see Section 3.5): Find the transmembrane potential $u : \Omega \times (0, T] \to \mathbb{R}$ and the gating variables

$\mathbf{w} : \Omega \times (0,T] \to \mathbb{R}^m$ such that

$$\begin{cases} \chi(C_m \partial_t u - I_{\text{ion}}(u,\mathbf{w}) - I_{\text{stim}}(t)) &= \nabla \cdot (\mathbf{D}\nabla u) & \text{in } \Omega \times (0,T], \\ \partial_t \mathbf{w} - \mathbf{g}(u,\mathbf{w}) &= 0 & \text{in } \Omega \times (0,T], \\ \mathbf{n} \cdot (\mathbf{D}\nabla u) &= 0 & \text{on } \partial\Omega \times (0,T], \\ u(\boldsymbol{x},0) &= u_0(\boldsymbol{x}) & \text{in } \Omega, \\ \mathbf{w}(\boldsymbol{x},0) &= \mathbf{w}_0(\boldsymbol{x}) & \text{in } \Omega. \end{cases} \tag{5.1}$$

The physical (given) constants are: the ratio of membrane area per tissue volume χ, the local membrane capacitance C_m, the electrical conductivity tensor $\mathbf{D}$, the initial conditions u_0 and w_0, the outward pointing unit normal vector $\mathbf{n}$ to $\partial\Omega$. The given non-linear functions $I_{\text{ion}} : \mathbb{R}^{m+1} \to \mathbb{R}$ and $\mathbf{g} : \mathbb{R}^{m+1} \to \mathbb{R}^m$ describe the total ionic current flow through the membrane of the myocyte and the kinetics of the gating variables as defined by the cell model, respectively. $I_{\text{stim}} : \Omega \times (0,T] \to \mathbb{R}$ denotes the applied external stimulus current. Note that the stimulus current I_{stim} is ignored throughout the derivation of the discretization methods to improve readability, since it has no influence on it.

5.1.2 Continuous Galerkin Approximation

In this section we describe the spatial discretization of Equation (5.1) by a Continuous Galerkin approximation. As a first step towards the Continuous Galerkin formulation, we multiply the equation with a test function $\varphi \in V$, with $V \subseteq H^1(\Omega)$ a subset of the Sobolev space $H^1(\Omega) = W^{1,2}(\Omega) := \{v \in L^2(\Omega) : D^\alpha v \in L^2(\Omega), |\alpha| \leq 1\}$, and integrate over the bounded domain $\Omega \subset \mathbb{R}^d$

$$C_m \int_\Omega \partial_t u \, \varphi \, \mathrm{d}\mathbf{x} - \int_\Omega I_{\text{ion}} \, \varphi \, \mathrm{d}\mathbf{x} = \frac{1}{\chi} \int_\Omega \nabla \cdot (\mathbf{D}\nabla u) \, \varphi \, \mathrm{d}\mathbf{x} \, , \tag{5.2}$$

where in the definition of the Sobolev space $\alpha = (\alpha_1, ..., \alpha_n) \in \mathbb{N}^n$ is a multi-index and $D^\alpha v$ is defined as $D^\alpha v = \frac{\partial^{|\alpha|} v}{\partial x_1^{\alpha_1}, ..., \partial x_n^{\alpha_n}}$.

Let us assume a domain Ω and a triangulation $\mathcal{T}_h$ of this domain with elements of characteristic size h. We will denote each of these elements as K. Discretization with regard to the triangulation equipped with piecewise continuous polynomials of degree p leads to the finite dimensional space $V_h^p \subset V$, defined as

$$V_h^p = \{v \in H^1(\Omega) : v|_K \in \mathcal{P}^p(K) \text{ for element } K \in \mathcal{T}_h\} \, , \tag{5.3}$$

where $\mathcal{P}^p(K)$ is the set of polynomials of maximal degree p on a domain K. Integrating the right hand side of Equation (5.2) by parts leads to the spatial approximation: find an approximation $u_h(t) \in V_h^p$ such that

$$C_m \int_{\mathcal{T}_h} \partial_t u_h \, \varphi_h \, \mathrm{d}\mathbf{x} + \frac{1}{\chi} \int_{\mathcal{T}_h} \mathbf{D}\nabla u_h \cdot \nabla \varphi_h \, \mathrm{d}\mathbf{x} \;\; = \;\; \int_{\mathcal{T}_h} I_{ion}(u_h, \mathbf{w}) \, \varphi_h \, \mathrm{d}\mathbf{x} \;\; , \tag{5.4}$$

for all $\varphi_h \in V_h^p$. This approximation is conforming. Note that, the gating variables $\mathbf{w}$ are not yet discretized in this formulation. There exist different methods to approximate the ionic current term I_{ion} and to discretize the gating variables $\mathbf{w}$. They are explained in detail in Section 5.1.5.

5.1.3 Hybridizable Discontinuous Galerkin Approximation

The Discontinuous Galerkin approximation is non-conforming as opposed to the Continuous Galerkin approximation. The finite dimensional solution space is not contained in the infinite dimensional space V. The starting point for the DG method is the mixed formulation for the diffusion term of Equation (5.1), i.e.,

$$\left\{ \begin{array}{rcl} C_m \partial_t u - \frac{1}{\chi} \nabla \cdot \mathbf{q} & = & I_{\mathrm{ion}}(u, \mathbf{w}) \\ \mathbf{q} - \mathbf{D} \nabla u & = & 0 \end{array} \right. . \tag{5.5}$$

The derivation of the HDG approximation is based on the work of Nguyen et al. [247] for the linear convection-diffusion equation. For the spatial discretization, we define the finite element spaces of piecewise discontinuous polynomials on the element's volume

$$W_h^p = \{ v \in L^2(\Omega) : v|_K \in \mathcal{P}^p(K) \, \forall K \in \mathcal{T}_h \} \tag{5.6}$$

and on the element's edges

$$M_h^p = \{ \mu \in L^2(\mathcal{E}_h) : \mu|_e \in \mathcal{P}^p(e) \text{ for face } \gamma \in \mathcal{E}_h \} \ , \tag{5.7}$$

with $\mathcal{E}_h$ the set of all interior and boundary faces e. An interior face between the two elements K_1 and K_2 is defined as $e = \partial K_1 \cap \partial K_2$ and a boundary face is defined as $e = \partial K \cap \partial \Omega$. With these definitions we multiply the first and the second line of Equation (5.5) with test functions $\varphi_h \in W_h^p$ and $\boldsymbol{\psi}_h \in [W_h^p]^d$, respectively. Integration over the element K and an additional integration by parts leads to the weak formulation: find $(u_h, \mathbf{q}_h) \in W_h^p \times [W_h^p]^d$ such that for all elements $K \in \mathcal{T}_h$ it holds

$$\left\{ \begin{array}{rcl} C_m \int_K \partial_t u_h \, \varphi \, \mathrm{d}\mathbf{x} + \frac{1}{\chi} \int_K \mathbf{q}_h \cdot \nabla \varphi \, \mathrm{d}\mathbf{x} - \frac{1}{\chi} \int_{\partial K} \mathbf{n} \cdot \hat{\mathbf{q}}_h \, \varphi \, \mathrm{d}\mathbf{x} & = & I_K \, , \\ \int_K \mathbf{D}^{-1} \mathbf{q}_h \boldsymbol{\psi} \, \mathrm{d}\mathbf{x} + \int_K u_h \nabla \cdot \boldsymbol{\psi} \, \mathrm{d}\mathbf{x} - \int_{\partial K} \lambda_h \mathbf{n} \cdot \boldsymbol{\psi} \, \mathrm{d}\mathbf{x} & = & 0 \, , \end{array} \right. \tag{5.8}$$

with $I_K(u_h, \mathbf{w}, \varphi) = \int_K I_{\mathrm{ion}}(u_h, \mathbf{w}) \, \varphi \, \mathrm{d}\mathbf{x}$. Here, λ_h and $\hat{\mathbf{q}}_h$ are the so called numerical traces over ∂K and $\mathbf{n}$ is the outward unit normal vector of ∂K. The trace variable $\lambda_h \in M_h^p$ is single valued on each face.

Note For the Local Discontinuous Galerkin (LDG) method the traces $\hat{\mathbf{q}}_h$ and λ_h are defined explicitly using for example a central or upwind flux as

$$\begin{array}{lrclrcl} \text{Central flux:} & \lambda_h & = & \{\{u_h\}\}, & \hat{\mathbf{q}}_h & = & \{\{\mathbf{q}_h\}\} \\ \text{Upwind flux:} & \lambda_h & = & \{\{u_h\}\} + \frac{\boldsymbol{\beta}}{2} [\![u_h]\!], & \hat{\mathbf{q}}_h & = & \{\{\mathbf{q}_h\}\} - \frac{\boldsymbol{\beta}}{2} [\![\mathbf{q}_h \cdot \mathbf{n}]\!] \end{array} \tag{5.9}$$

where the vector $\boldsymbol{\beta}$ is mostly chosen as $\boldsymbol{\beta} = \boldsymbol{n}$ or $\boldsymbol{\beta} = -\boldsymbol{n}$. The mean values and jumps are defined as

$$\begin{array}{l} \{\{u\}\} = \frac{u_1 + u_2}{2}, [\![u]\!] = \mathbf{n}_1 u_1 + \mathbf{n}_2 u_2, \\ \{\{\mathbf{q}\}\} = \frac{\mathbf{q}_1 + \mathbf{q}_2}{2}, [\![\mathbf{q} \cdot \mathbf{n}]\!] = \mathbf{n}_1 \cdot \mathbf{q}_1 + \mathbf{n}_2 \cdot \mathbf{q}_2, \end{array} \tag{5.10}$$

at the face $\gamma = \partial K_1 \cap \partial K_2$ between the two elements K_1 and K_2.

For the HDG method we introduce a consistent penalization of the difference of u_h and λ_h at each face and thus consider numerical traces $\hat{\mathbf{q}}_h$ of the form

$$\hat{\mathbf{q}}_h = \mathbf{q}_h - \tau(u_h - \lambda_h)\mathbf{n}\,, \text{ on } \partial K \tag{5.11}$$

with the stabilization parameter τ. To close the system, we need an additional equation for the trace variable, which consists in enforcing the jump across of the numerical trace of the flux $\hat{\mathbf{q}}$ along each edge e to be zero, i.e.,

$$[\![\hat{\mathbf{q}} \cdot \mathbf{n}]\!] = \mathbf{0}, \text{ on all } \gamma \in \mathcal{E}_h\,. \tag{5.12}$$

The extended system of equations corresponding to the HDG method can be written as: Find $(u_h(t), \mathbf{q}_h(t), \lambda_h(t)) \in W_h^p \times [W_h^p]^d \times M_h^p$ such that,

$$\left\{ \begin{array}{rcl} \displaystyle\sum_K \left(\int_K C_m \partial_t u_h \varphi \, \mathrm{d}\mathbf{x} + \frac{1}{\chi} \int_K \mathbf{q}_h \nabla \varphi \, \mathrm{d}\mathbf{x} - \frac{1}{\chi} \int_{\partial K} \mathbf{q}_h \cdot \mathbf{n} \varphi - \tau(u_h - \lambda_h)\varphi \, \mathrm{d}\mathbf{x} \right) & = & \\ \displaystyle\sum_K I_K(u_h, \mathbf{w}_h, \varphi) & & \\ \displaystyle\sum_K \left(\int_K \mathbf{D}^{-1} \mathbf{q}_h \boldsymbol{\psi} \, \mathrm{d}\mathbf{x} + \int_K u_h \nabla \cdot \boldsymbol{\psi} \, \mathrm{d}\mathbf{x} - \int_{\partial K} \lambda_h \mathbf{n} \cdot \boldsymbol{\psi} \, \mathrm{d}\mathbf{x} \right) & = & 0 \\ \displaystyle\sum_K \left(\int_{\partial K} \mathbf{q}_h \cdot \mathbf{n} \mu \, \mathrm{d}\mathbf{x} - \int_{\partial K} \tau(u_h - \lambda_h)\mu \, \mathrm{d}\mathbf{x} \right) & = & 0 \end{array} \right. \tag{5.13}$$

for all $(\varphi, \boldsymbol{\psi}, \mu) \in W_h^p \times [W_h^p]^d \times M_h^p$. The positive stabilization parameter τ has to be set by the user and we will analyze its impact on the results in the numerical experiments. We can write the system of equations after some simple manipulations as follows

$$\left\{ \begin{array}{rcl} m(\partial_t u_h, \varphi) - b(\varphi, \mathbf{q}) + a(u_h, \varphi) - c(\lambda_h, \varphi) & = & f(u_h, \mathbf{w}, \varphi_h) \\ d(\mathbf{q}_h, \boldsymbol{\psi}) + b(u_h, \boldsymbol{\psi}) - e(\lambda_h, \boldsymbol{\psi}) & = & 0 \\ e(\mu, \mathbf{q}_h) - c(\mu, u_h) + h(\lambda_h, \mu) & = & 0 \end{array} \right. \tag{5.14}$$

with the bilinear forms and the non-linear functional f given by

$$\begin{array}{rclrcl} m(u, \varphi) & = & \sum_K \int_K C_m \chi u \varphi \, \mathrm{d}\mathbf{x}, & d(\mathbf{q}, \boldsymbol{\psi}) & = & \sum_K \int_K \mathbf{D}^{-1} \mathbf{q} \boldsymbol{\psi} \, \mathrm{d}\mathbf{x}, \\ a(u, \varphi) & = & \sum_K \int_{\partial K} \tau u \varphi \, \mathrm{d}\mathbf{x}, & e(\lambda, \boldsymbol{\psi}) & = & \sum_K \int_{\partial K} \lambda \boldsymbol{\psi} \cdot \mathbf{n} \, \mathrm{d}\mathbf{x}, \\ b(u, \boldsymbol{\psi}) & = & \sum_K \int_K u \nabla \cdot \boldsymbol{\psi} \, \mathrm{d}\mathbf{x}, & f(u, \mathbf{w}, \varphi) & = & \chi \sum_K I_K(u, \mathbf{w}, \varphi)\,, \\ c(\lambda, \varphi) & = & \sum_K \int_{\partial K} \varphi \tau \lambda \, \mathrm{d}\mathbf{x}, & h(\lambda, \mu) & = & \sum_K \int_{\partial K} \tau \lambda \mu \, \mathrm{d}\mathbf{x}, \end{array} \tag{5.15}$$

for all $(u, \mathbf{q}, \lambda)$ and $(\varphi, \boldsymbol{\psi}, \mu)$ in $W_h^p \times [W_h^p]^d \times M_h^p$. Denoting the degrees of freedom U, Q, Λ associated to the unknown discrete functions $u_h, \mathbf{q}_h, \lambda_h$, respectively, we can write the resulting system in matrix form as:

$$\begin{bmatrix} M & 0 & 0 \\ 0 & 0 & 0 \\ 0 & 0 & 0 \end{bmatrix} \begin{bmatrix} \partial_t U \\ \partial_t Q \\ \partial_t \Lambda \end{bmatrix} + \begin{bmatrix} A & B & -C \\ -B^T & D & -E \\ -C^T & E^T & H \end{bmatrix} \begin{bmatrix} U \\ Q \\ \Lambda \end{bmatrix} = \begin{bmatrix} F(U) \\ 0 \\ 0 \end{bmatrix} \tag{5.16}$$

After time discretization, we use static condensation (Schur complements) on the element level to reduce the global system size as it is usual in HDG [84]. For that purpose, we eliminate the interior variables U and Q in an element-by-element fashion, so that the remaining degrees of freedom are those of the trace variable Λ on the faces of $\mathcal{E}_h$. The final matrix system looks then as follows

$$K\Lambda = L \tag{5.17}$$

with

$$K = H - \begin{bmatrix} -C^T & E^T \end{bmatrix} \begin{bmatrix} A & B \\ -B^T & D \end{bmatrix}^{-1} \begin{bmatrix} -C \\ -E \end{bmatrix} \tag{5.18}$$

and

$$L = - \begin{bmatrix} -C^T & E^T \end{bmatrix} \begin{bmatrix} A & B \\ -B^T & D \end{bmatrix}^{-1} \begin{bmatrix} F(U) - M\partial_t U \\ 0 \end{bmatrix} . \tag{5.19}$$

5.1.4 Time Discretization

For both CG and HDG we use a semi-implicit method for the time discretization [115, 363], which is very popular in computational electrophysiology. This method splits the system into two steps. In a first step a backward Euler for the diffusive term, i.e. the first equation in Eq. (5.1), is solved for t_{n+1}, whereby the spacial derivative is evaluated at a time t_{n+1} and the ionic current term I_{ion} is evaluated at a time t_n. In a second step the values $\tilde{U}^{n+1}$ are used to solve the system of ordinary differential equations (second equations in Eq. (5.1)) for the gating variables $\mathbf{w}$ with a backward difference scheme.

- Step 1: Linear backward Euler for $\tilde{U}^{n+1}$ with known $\tilde{U}^n$ and $\mathbf{w}^n$

$$\mathbf{M}\frac{\tilde{U}^{n+1} - \tilde{U}^n}{\Delta t} + \frac{1}{\chi C_m}\mathbf{A}\tilde{U}^{n+1} - \frac{1}{C_m} I_{\text{ion}}(U^n, \mathbf{w}^n) = 0 \,. \tag{5.20}$$

- Step 2: Linear backward Euler for $\mathbf{w}^{n+1}$ with known $\tilde{U}^{n+1}$ and $\mathbf{w}^n$

$$\frac{\mathbf{w}^{n+1} - \mathbf{w}^n}{\Delta t} - \mathbf{g}(\tilde{U}^{n+1}, \mathbf{w}^{n+1}) = 0 \,. \tag{5.21}$$

The value $\tilde{U}$ is depends on the discretization method, either it is simply U or it is defined in a more complex way (see the following paragraph).

For the CG and the HDG methods the matrices $\mathbf{M}$ and $\mathbf{A}$ are defined differently. For the CG method they are defined as

$$\mathbf{M}_{ji} = \textstyle\int_{\mathcal{T}_h} \varphi_h^i \varphi_h^j \,\mathrm{d}\mathbf{x} \quad \text{and} \quad \mathbf{A}_{ji} = \textstyle\int_{\mathcal{T}_h} \mathbf{D}\nabla\varphi_h^i \cdot \nabla\varphi_h^j \,\mathrm{d}\mathbf{x} \tag{5.22}$$

for $\varphi_h^i, \varphi_h^j \in \{\varphi_h^k : k = 1 \dots m_{\text{CG}}\}$ basis of V_h^p and $m_{\text{CG}} = \dim(V_h^p)$. Additionally, the term $\tilde{U} = U$ in the CG case is defined as $U = (U_1, \dots, U_n)^T$ with $u_h = \sum U_k \varphi_k \in V_h^p$. For the HDG method the matrix $\mathbf{M}$ is defined as

$$\mathbf{M} = \left[\begin{smallmatrix} M & 0 & 0 \\ 0 & 0 & 0 \\ 0 & 0 & 0 \end{smallmatrix}\right] , \, M_{ji} = \textstyle\sum_K \int_K C_m \chi \varphi^i \varphi^j \,\mathrm{d}\mathbf{x}, \tag{5.23}$$

for $\varphi^i, \varphi^j \in \{\varphi^k : k = 1 \dots m_{\mathrm{HDG}_1}\}$ basis of W_h^p and $m_{\mathrm{HDG}_1} = \dim(W_h^p)$. The matrix $\mathbf{A}$ is defined as

$$\mathbf{A} = \begin{bmatrix} A & B & -C \\ -B^T & D & -E \\ -C^T & E^T & H \end{bmatrix} . \tag{5.24}$$

The matrix entries of $\mathbf{A}$ are given in relation to Equation (5.15) by

$$\begin{array}{rclrcl} A_{ji} & = & \sum_K \int_{\partial K} \tau \varphi^i \varphi^j \,\mathrm{d}\mathbf{x}, & D_{ji} & = & \sum_K \int_K \mathbf{D}^{-1} \boldsymbol{\psi}^i \boldsymbol{\psi}^j \,\mathrm{d}\mathbf{x}, \\ B_{ji} & = & \sum_K \int_K \varphi^i \nabla \cdot \boldsymbol{\psi}^j \,\mathrm{d}\mathbf{x}, & E_{ji} & = & \sum_K \int_{\partial K} \mu^i \boldsymbol{\psi}^j \cdot \mathbf{n}, \\ C_{ji} & = & \sum_K \int_{\partial K} \varphi^i \tau \mu^j \,\mathrm{d}\mathbf{x}, & H_{ji} & = & \sum_K \int_{\partial K} \tau \mu^i \mu^j \,\mathrm{d}\mathbf{x}, \end{array} \tag{5.25}$$

for $\boldsymbol{\psi}^i, \boldsymbol{\psi}^j \in \{\boldsymbol{\psi}^k : k = 1 \dots m_{\mathrm{HDG}_2}\}$ basis of $[W_h^p]^d$ and $m_{\mathrm{HDG}_2} = \dim([W_h^p]^d)$ and $\mu^i, \mu^j \in \{\mu^k : k = 1 \dots m_{\mathrm{HDG}_3}\}$ basis of M_h^p and $m_{\mathrm{HDG}_3} = \dim(M_h^p)$. The term $\tilde{U}$ is defined as $\tilde{U} = (U, Q, \Lambda)^T$ in the HDG case with

$$\begin{array}{rclrcl} u_h & = & \sum U_k \varphi_k \in W_h^p \,, & U & = & (U_1, \dots, U_{m_{\mathrm{HDG}_1}})^T \\ \mathbf{q}_h & = & \sum Q_k^{i=1,\dots,3} \psi_{i=1,\dots,3}^k \in W_h^p \,, & Q & = & (Q_1, \dots, Q_{m_{\mathrm{HDG}_2}})^T \\ \lambda_h & = & \sum \Lambda_k \mu_k \in M_h^p \,, & \Lambda & = & (\Lambda_1, \dots, \Lambda_{m_{\mathrm{HDG}_3}})^T \end{array} \tag{5.26}$$

with $Q_k = (Q_k^1, Q_k^2, Q_k^3)^T$ and $\boldsymbol{\psi} = (\psi_1, \psi_2, \psi_3)^T$, for $d = 3$.

5.1.5 Ionic Current Approximation

Due to its non-linearity, there exist several methods to approximate the element integral of the ionic current term I_{ion} in Galerkin formulations for cardiac electrophysiology

$$I_K = \int_K I_{\mathrm{ion}}(u, \mathbf{w}) \varphi \,\mathrm{d}\mathbf{x} \tag{5.27}$$

with both u and φ given through spatial polynomial functions of degree p, see e.g. [131, 203, 280] and references therein. In the CG approximation we have $u, \varphi \in V_h^p$ and in the HDG case $u, \varphi \in W_h^p$. In both discretization methods it holds $u|_K \in \mathcal{P}^p(K)$ and, thus, the ionic current term I_K over one element K can be approximated using the same methods for both, CG and HDG.

For the approximation of the ionic current term there exist two different approaches. The first one projects the non-linear ionic current term I_{ion} into a suitable space $V_h^{\tilde{p}}$, so that the term can be written as

$$I_{\mathrm{ion}}(u, \mathbf{w}) \approx \sum I_i \theta^i \,, \tag{5.28}$$

with $\theta^i \in \{\theta^k : k = 1 \dots m_{\tilde{p}_1}\}$ basis of $V_h^{\tilde{p}}$, $m_{\tilde{p}_1} = \dim(V_h^{\tilde{p}})$, and $I_i \in \mathbb{R}$. Since it holds that $I_i \in \mathbb{R}$ the values I_i can be factored out of the integral and additionally the integral and the sum can be interchanged. To do so, this approach leads to a computationally efficient matrix multiplication of the form

$$I_K = N(I_1, \dots, I_m)^T \,, \tag{5.29}$$

and is thus referred to as matrix-based assembly. The matrix N is defined as

$$N_{ji} = \int_K \theta^i \varphi^j \, \mathrm{d}\mathbf{x}\,, \tag{5.30}$$

with $\varphi^j \in \{\varphi^k : k = 1 \dots m_{\tilde{p}_2}\}$ the basis of V_h^p and $m_{\tilde{p}_2} = \dim(V_h^p)$. When using this approach the order of the polynomials $\tilde{p}$ is mostly chosen the same as $\tilde{p} = p$ the order of the approximation of the potential u or the gating variables $\mathbf{w}$, which will be defined later in this section. To increase computational speed an additional option is to lump the matrix N, so that only diagonal entries remain.

The second approach approximates the integral of the ionic current term I_{ion} using integration rules as

$$I_K \approx \sum_{\ell=1}^{b_K} \alpha_\ell I_{\text{ion}}(u(q_\ell), \mathbf{w}(q_\ell))\varphi(q_\ell)\,, \tag{5.31}$$

with α_ℓ the quadrature weights and b_K the number of integration points on the element K.

Approximation of the Gating variables For the gating variables $\mathbf{w}$ different approximations are possible. For an polynomial order $\hat{p}$ the gating variables can be approximated using $\mathbf{w} \approx \sum w_i \vartheta_i$ with $\vartheta_i \in \{\vartheta^k : k = 1 \dots m_{\hat{p}}\}$ basis of $V_h^{\hat{p}}$, $m_{\hat{p}} = \dim(V_h^{\hat{p}})$. However, the gating variables are non-diffusing approximations which avoid spacial interpolation. For both approaches, the matrix-based assembly and the approach using integration rules, holds, if the non-diffusing gating variables $\mathbf{w}$ are defined on appropriate points and no spacial interpolation is needed. For the first one, using a nodal basis $\{\theta^i : i = 1, \dots, m_{\tilde{p}_1}\}$ for $V_h^{\tilde{p}}$, for which holds $\theta^i(x_j) = \delta_{ij}\ \forall i, j$ for set of associated nodes $\{x_i : i = 1, \dots, m_{\tilde{p}_1}\}$ [46], $\mathbf{w}$ needs to be defined on the nodes x_i. Thus, the gating variables $\mathbf{w}$ are approximated with the the same polynomial order as the ionic current term. For the second approach $\mathbf{w}$ needs to be defined on the integration points q_l. However, it is also possible to approximate the gating variables with its own polynomial order $\hat{p}$ different than the polynomial order of the ionic current term $\tilde{p}$ and the order of the action potential p. This makes an interpolation or a suitable projection necessary, but it can reduce computational cost since the gating variables have to be solved only on the nodes and not on every integration points. Note that according to [16] the polynomial order of the gating variables and the ionic current term needs to be high enough, i.e. $\hat{p}, \tilde{p} \geq p$, to assure the full convergence rate for high-order polynomials.

In this work, the number of quadrature points b_K is chosen depending on the polynomial degree p of the finite element spaces on element K. Concretely, assuming that I_{ion} has the potential u involving polynomial expressions in u of degree up to k_{ion}, we propose to choose the quadrature order to integrate exactly polynomials of degree $p(k_{ion} + 1)$, since the integral in the weak form comprises not only $I_{ion}(u)$ but also the test function. For the integration rule we do not take into account the additional non-polynomial terms in the model, e.g. the Heaviside function. Note that for high-order curved geometry descriptions there could still be a small integration error, but it is expected to be of higher order than the discretization error. For the numerical examples we use hexahedral and tetrahedral elements with appropriate intergration rules. An example will be shown in Section 5.2.2. Note that keeping track of $\mathbf{w}_\ell$ and I_{ion} in quadrature points can be interpreted as a polynomial approximation of at least degree $\lceil((k_{ion}+1)p+1)/2\rceil - 1$ in the discontinuous setting by Lagrange polynomials through the integration points.

We want to remark that other ionic current approximations could also be used, e.g. where the gating variables are stored at the degrees of freedom of the finite element approximation of the potential. However, additionally investigating the effect of the type of ionic current approximation is out of the scope of this work.

5.1.6 p-Adaptivity for HDG

The HDG method allows for a straightforward adaption of the degree of the polynomial basis functions since different polynomial degrees between neighboring elements can be independently chosen. A key ingredient is to apply a proper error indicator for selecting the local polynomial order. In this work we choose a simplified version of the error indicator presented in [17] based on the jump of the gradient of the potential across the face γ. Therefore, on each element K the error indicator for the time step n is defined via the numerical gradient on the faces $\hat{\mathbf{q}}$ as

$$e_K^n = \sum_{\gamma\in\partial K} \|\hat{\mathbf{q}}_\gamma^n \cdot \mathbf{n}\|^2_{L_2(\gamma)} \frac{1}{A_\gamma} \tag{5.32}$$

with A_γ the surface area of the face. Then the new degree on the element is calculated via

$$p_K^n = p_K^{n-1} + \lceil \frac{1}{\omega} \ln\left(\frac{e_K}{e_{tol}}^{n-1}\right)\rceil \tag{5.33}$$

for a constant $\omega = 1.66$ according to [17], which is estimated from convergence rates of high-order CG elements, and a given error tolerance e_{tol}. This value leads to satisfactory results, that were also quite insensitive to slight variations.

The adaption of the polynomial degree is calculated for each element independently, while the polynomial degree of the face is defined by the higher of the two polynomial degrees of the elements sharing this face.

5.2 Numerical Experiments

5.2.1 Academic Problem Setup

In our test we use a modified version of the problem setup from [248]. The geometry corresponds to a myocardial tissue cuboid of size $12\,\mathrm{mm} \times 4\,\mathrm{mm} \times 2\,\mathrm{mm}$, see Figure 5.1a. To start the propagation of the electrochemical wave we use the initial condition

$$u(\mathbf{x},0) = 0.5(1-\tanh(1000(x-2))), \tag{5.34}$$

shown in Figure 5.1b.

Given that our study focuses on the investigation of different spatial approximations of the problem, we restrict the cardiac electrophysiology problem to the model of Bueno-Orovio et al. [52], which is able to reproduce important physiological properties, e.g. action potential curves

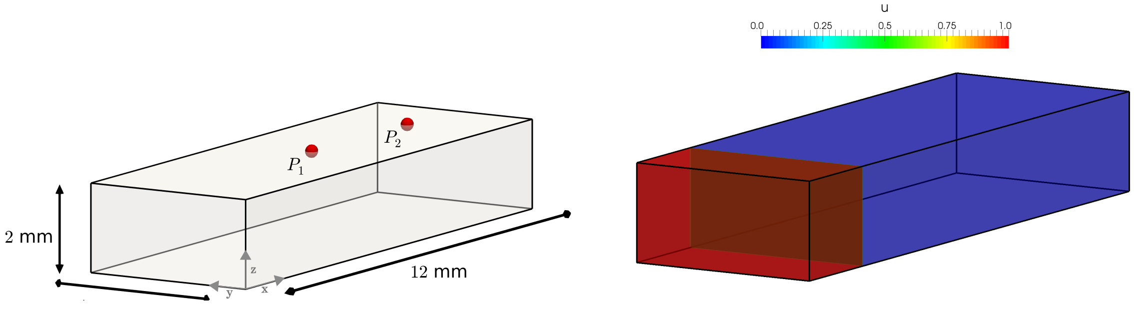

(a) (b)

Figure 5.1: Myocardial tissue slab. (a) Rectangular domain ($12\,\mathrm{mm} \times 4\,\mathrm{mm} \times 2\,\mathrm{mm}$). The time difference in activation is measured between the two red points P_1 and P_2 ($x_1 = 6\,\mathrm{mm}$, $y_1 = 2\,\mathrm{mm}$, $z_1 = 2\,\mathrm{mm}$ and $x_2 = 10\,\mathrm{mm}$, $y_2 = 2\,\mathrm{mm}$, $z_2 = 2\,\mathrm{mm}$). (b) Initial condition.

and upstroke velocities, with only three gating variables and three ionic currents. The model is given as

$$\begin{array}{rcl} \partial_t \tilde{u} & = & \nabla \cdot (\sigma \nabla v) - I_{ion}(\tilde{u}, \mathbf{w}), \\ \partial_t w_1 & = & (1 - H(\tilde{u} - \theta_{w_1}))(w_{1,\infty} - w_1)/\tau_{w_1}^- - H(\tilde{u} - \theta_{w_1})w_1/\tau_{w_1}^+, \\ \partial_t w_2 & = & (1 - H(\tilde{u} - \theta_{w_2}))(w_{2,\infty} - w_2)/\tau_{w_2}^- - H(\tilde{u} - \theta_{w_2})w_2/\tau_{w_2}^+, \\ \partial_t w_3 & = & ((1 + \tanh(k_{w_3}(\tilde{u} - u_{w_3})))/2 - w_3)/\tau_{w_3}, \end{array} \tag{5.35}$$

with $H(\cdot)$ the Heaviside function. The transmembrane potential u is related with the dimensionless variable $\tilde{u}$ as $u = 85.7\tilde{u} - 84$. The computation of the ionic current I_{ion} is as follows

$$\begin{array}{rcl} I_{ion}(\tilde{u}, \mathbf{w}) & = & I_{fi} + I_{so} + I_{si}, \\ I_{fi} & = & -w_1 H(\tilde{u} - \theta_{w_1})(\tilde{u} - \theta_{w_1})(u_u - \tilde{u})/\tau_{fi}, \\ I_{so} & = & (\tilde{u} - u_0)(1 - H(\tilde{u} - \theta_{w_2}))/\tau_0 + H(\tilde{u} - \theta_{w_2})\tau_{so}, \\ I_{si} & = & -H(\tilde{u} - \theta_{w_2})w_2 w_3/\tau_{si}. \end{array} \tag{5.36}$$

and with the definitions of the functions

$$\begin{array}{rcl} \tau_v^- & = & (1 - H(\tilde{u} - \theta_v^-))\tau_{v_1}^- + H(\tilde{u} - \theta_v^-)\tau_{v_2}^-, \\ \tau_w^- & = & \tau_{w_1}^- + (\tau_{w_2}^- - \tau_{w_1}^-)(1 - \tanh(k_w^-(\tilde{u} - u_w^-)))/2, \\ \tau_{so} & = & \tau_{so1} + (\tau_{so2} - \tau_{so1})(1 - \tanh(k_{so}(\tilde{u} - u_{so})))/2, \\ \tau_s & = & (1 - H(\tilde{u} - \theta_w))\tau_{s_1} + H(\tilde{u} - \theta_w)\tau_{s2}, \\ \tau_s & = & (1 - H(\tilde{u} - \theta_o))\tau_{o_1} + H(\tilde{u} - \theta_o)\tau_{o2}, \\ w_\infty & = & (1 - H(\tilde{u} - \theta_o))(1 - \tilde{u}/\tau_{w_\infty} + H(\tilde{u} - \theta_o)w_\infty^*, \\ v_\infty & = & \begin{cases} 1 & u < \theta_v^- \\ 0 & \tilde{u} \geqslant \theta_v^- \end{cases}. \end{array}$$

The parameter values, which can be adapted to model different cell types, can be found in the original work [52]. In the present study we choose the epicardial parameter values (see Table

u_o	u_u	θ_v	θ_w	θ_v^-	θ_o	τ_{v1}^-
0	1.55	0.3	0.13	0.006	0.006	60
τ_{v2}^-	τ_v^+	τ_{w1}^-	τ_{w1}^-	K_w^-	u_w-	τ_w^+
1150	1.4506	60	15	65	0.03	200
τ_{fi}	τ_{o1}	τ_{o2}	τ_{so1}	τ_{so2}	k_{so}	u_{so}
0.11	400	6	30.0181	0.9957	2.0458	0.65
τ_{s1}	τ_{s2}	k_s	u_s	τ_{si}	τ_{w_∞}	w_∞^*
2.7342	16	2.0994	0.9087	1.8875	0.07	0.94

Table 5.1: Epicardial model parameter values.

5.1). If not indicated otherwise, the diffusion coefficient is chosen as $\sigma = 0.1\,\mathrm{mm}^2/\mathrm{ms}$. The time step is chosen as $\Delta t = 0.1\,\mathrm{ms}$, and different mesh sizes are used as indicated for each experiment.

To compare the results we calculate the conduction velocity cv in all simulations by measuring the activation times (acttime$(\cdot)$) of point $P_1(6,2,2)$ and point $P_2(10,2,2)$ (see Figure 5.1a) and with the distance between the two points obtain the conduction velocity via $cv = \|P_2 - P_1\|/(\text{acttime}(P_2) - \text{acttime}(P_1))$. We define the activation time as the time when the voltage is larger than $1.7\,\mathrm{mV}$, which is equivalent to the value of 1 for the dimensionless variable u in the chosen cellular model. The converged conduction velocity amounts to around $0.73\,\mathrm{mm\,ms}^{-1}$.

5.2.2 Choice of the Ionic Current Integration Formula

Here we briefly describe the application of the rule defined in Section 5.1.5 to the ionic model [52]. We identify the maximal polynomial degree of u in the model as $k_{ion} = 2$ through I_{fi}. Therefore, we choose the number of quadrature points b_K such that polynomials of degree d

$$d = (k_{ion} + 1)p = 3p \tag{5.37}$$

are exactly integrated.

We need a definition of an integration rule for the ionic current term that varies with the polynomial order. This necessity is visualized in Figure 5.2 for $\sigma = 0.1\,\mathrm{mm\,ms}^{-2}$ and $\tau = 1\,\mathrm{mm\,ms}^{-1}$ and $h = 1\,\mathrm{mm}$. We observe, in general, two types of issues arising when a fixed number of integration points is chosen. The first issue is a propagation block, which means that no propagation takes place. This could happen if the ionic flow from the neighboring element is not sufficient to reach the threshold for the self depolarization in an element. It occurs in our examples when the polynomial degree is increased above a certain value, see e.g. the case $b_K = 1, 8, 27$ in Figure 5.2a. For one integration point ($b_K = 1$) only at polynomial degrees zero and one the propagation takes place. For $b_K = 8$ propagation takes place until degree three and for $b_K = 27$ no propagation occurs for degree six, eight, nine, twelve and thirteen. The second issue is observed with $b_K = 27$ where the interaction between different computational errors, for example the insufficient integration of the ionic current term and coarse meshes, could lead to a propagation for some polynomial degrees (6,10 and 11) but with incorrect results. This is the second issue. In the above mentioned cases for $b_K = 27$ and every time for $b_K = 64$ for high polynomial degrees a propagation takes place but the computed conduction velocity is incorrect,

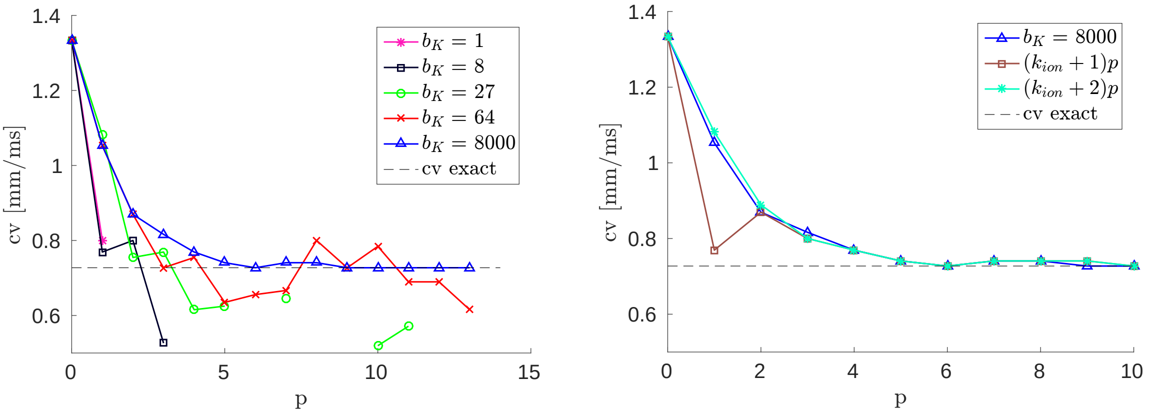

(a) (b)

Figure 5.2: Conduction velocity plotted over the polynomial degree p for varying number of integration points b_K. (a) Comparison between different constant numbers of integration points. (b) Comparison between adapted number of integration points and a large constant number.

since the error in the computation of the ionic current dominates. This can be observed in the oscillating behavior of the computed conduction velocity for increasing polynomial degree (see Figure 5.2a).

Note that considerably increasing the number of integration points (e.g. $b_K = 8000$) leads to a smooth convergence curve with respect to an increase of the polynomial order. However, using too many integration points results in an increased computational cost without a significant gain in the accuracy of the results. Finally, the adaptation of b_K in dependence of the polynomial order as defined in Equation (5.37) is able to give convergence at a much lower cost (see Figure 5.2b). However, for polynomial degree one for the adapted integration points, the conduction velocity is lower than expected. This is due to the additional non-polynomial terms in the model in the calculation of the ionic current term. For low order $p = 1$, we experimentally determined that using integration exact to degree 3 is not accurate enough. Thus, we tested a stricter rule for the integration points so that polynomials of degree d

$$d = (k_{ion} + 2)p = 4p \tag{5.38}$$

are exactly integrated. This stricter rule (Equations (5.38)) solves the problem with low polynomial degrees but it has almost no influence for the computation with higher polynomial degrees (see Figure 5.2b). Hence, to reduce the computational cost for high polynomial degrees we decided to use the rule from Equation (5.37) for high order polynomials, but for $p = 1$ we use the rule defined in Equation (5.38) so that in any case at least polynomials of degree 4 are exactly integrated, i.e.

$$d = \begin{cases} 3p & , p > 1 \\ 4p & , p \leq 1 \end{cases} . \tag{5.39}$$

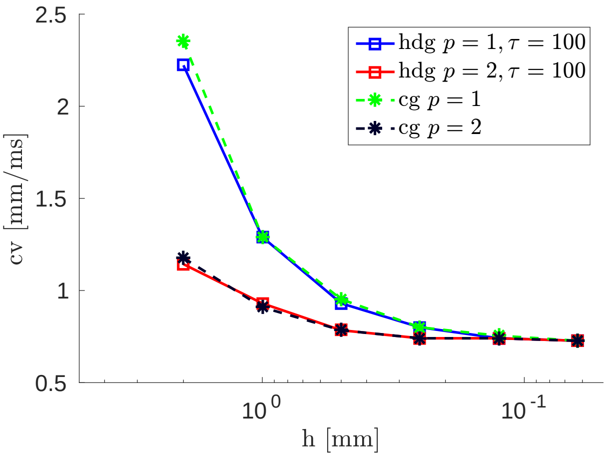

Figure 5.3: Conduction velocity (cv) plotted over the element size h for $\sigma = 0.1\,\mathrm{mm}^2/\mathrm{ms}$. The HDG solution for large τ is the same as the CG solution.

5.2.3 Choice of the Stabilization Parameter

In this section we study the influence of the HDG stabilization parameter τ on the solution quality. First, from Equation (5.11) we can observe that a large stabilization parameter $\tau \to \infty$ forces the solution u_h to be continuous, therefore reproducing the CG solution. This is verified in Figure 5.3, where the solutions are almost identical and thus the curves are the same.

Figure 5.4 presents results for different electrical conductivities σ in a wide range of values of physiological interest [196, 290]. Firstly, we can see that with increasing polynomial order p the influence of the stabilization parameter decreases. In Figure 5.4a only $h = 0.5\,\mathrm{mm}$ is plotted since propagation for $h = 2\,\mathrm{mm}$ takes place only for larger polynomial degrees. In all plots in Figure 5.4 it is visible that for larger τ, the conduction velocity is overestimated and for smaller τ it is underestimated. A small τ could also lead to the case that no propagation takes place. This propagation block can be seen in the plots, when no value for the conduction velocity is plotted. Decreasing the element size also leads to a decrease of the influence of the stabilization parameter. Nevertheless, over- and underestimation is still visible for high and low stabilization parameters, respectively.

In Figure 5.5 the results for a more detailed range of $\tau = 0.1$ to $1\,\mathrm{mm/ms}$ (5.5a) and $\tau = 1$ to $10\,\mathrm{mm/ms}$ (5.5b) are plotted. We conclude that a reasonable value for the stabilization parameter τ for a wide range of physiological diffusivities and element sizes is $\tau = 1\,\mathrm{mm/ms}$ using the minimal cell model [52]. For other cell models the behavior of the stabilization parameter can be easily tested in a similar fashion. Note that one should not use too low polynomial degrees to ensure only a small dependence on τ.

5.2.4 Time Discretization

For the sake of completeness, we briefly present the results of a time step refinement for a polynomial order of $p = 2$. In Figure 5.6 one can see the conduction velocity for different combinations of spatial and temporal refinement. For temporal refinement we consider time steps of $\Delta t = 10^{-1}$, 10^{-2}, 10^{-3} and $10^{-4}\,\mathrm{ms}$ and for spatial refinement element size of $h = 2$, 1,

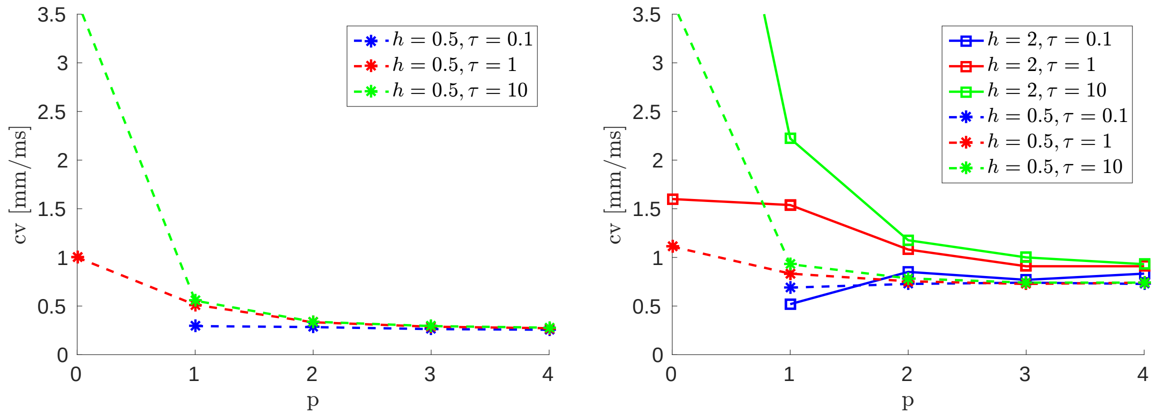

(a) $\sigma = 0.01\,\mathrm{mm}^2/\mathrm{ms}$

(b) $\sigma = 0.1\,\mathrm{mm}^2/\mathrm{ms}$

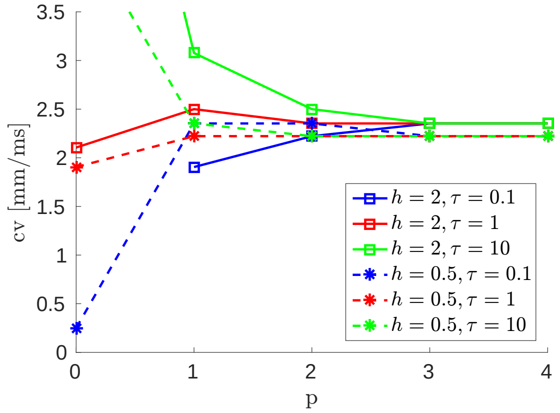

(c) $\sigma = 1\,\mathrm{mm}^2/\mathrm{ms}$

Figure 5.4: Conduction velocities for different HDG stabilization parameters τ and diffusion coefficients σ.

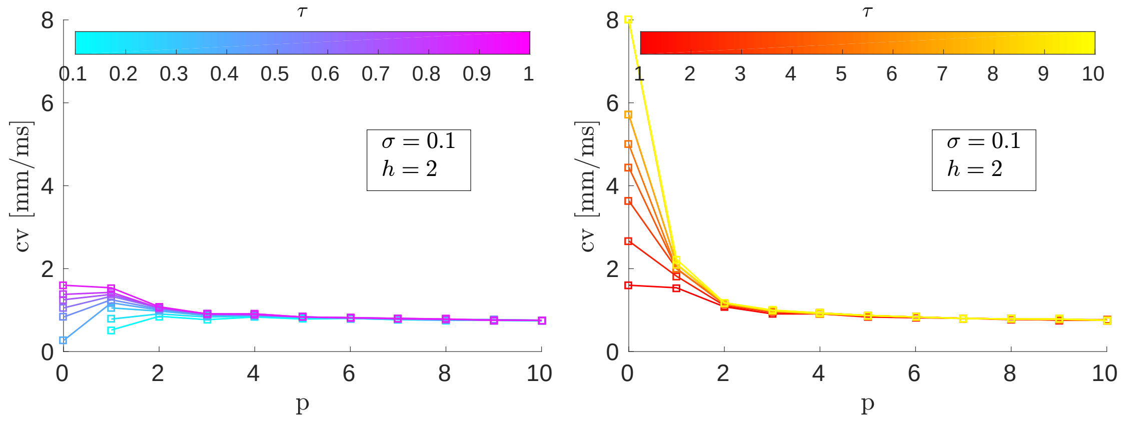

(a) τ =0.1 to $1\,\mathrm{mm/ms}$

(b) τ =1 to $10\,\mathrm{mm/ms}$

Figure 5.5: Detailed analysis of the influence of the stabilization parameter τ for $\sigma = 0.1$.

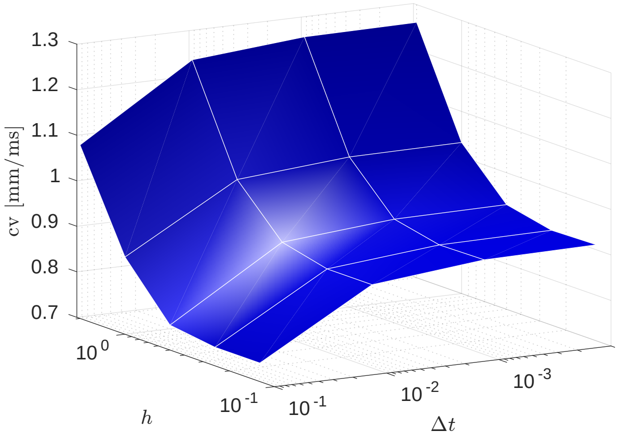

Figure 5.6: Conduction velocity plotted over the element size h and the time step Δt for a polynomial order of $p = 2$. The range from the element size is $h = 2$, 1, 0.5, 0.25 and $0.125\,\mathrm{mm}$ and the time steps are $\Delta t = 10^{-1}$, 10^{-2}, 10^{-3} and $10^{-4}\,\mathrm{ms}$.

0.5, 0.25 and $0.125\,\mathrm{mm}$. With a time step of $\Delta t = 0.1\,\mathrm{ms}$ the solution is not yet fully converged in terms of temporal errors. However, decreasing the time step does not change the convergence behavior of the general solution. Thus, analyzing different spatial discretization methods can be done on a coarser time step, without missing important characteristics of the solution. Figure 5.6 shows that with the semi-implicit time discretization, the conduction velocity is overestimated for a coarse element size, while for a large time step it is underestimated.

5.2.5 Convergence and Efficiency Analysis with h and p Refinement

Next we analyze the change in conduction velocity when decreasing element size and increasing polynomial order for the HDG method for both tetrahedral and hexahedral meshes. Additionally, we compare the HDG discretization method with CG discretizations in more detail. For the HDG method we use a stabilization parameter $\tau = 1\,\mathrm{mm\,ms}^{-1}$ (see Section 5.2.3). For both methods, HDG and CG, the rule for the integration points for the ionic current is adapted to the polynomial degree as defined in Sections 5.1.5 and 5.2.2.

To compare the results we record the number of degrees of freedom (ndof) and the number of non-zeros in the system matrix (nnz), since they can be seen as the key factors for the calculation time [130]. For the CG method, we consider these quantities directly from the discrete system for the potential u_h. In HDG we do it for the condensed system involving only the trace variables Λ_h. We want to point out that for low order, HDG has more degrees of freedom than CG while for high order, HDG has less degrees of freedom than CG, i.e., the ndof for HDG increases more slowly with increasing order [130].

First, we compare the HDG and CG methods for hexahedral meshes. Both methods appear to deliver similar results in terms of precision versus ndof and nnz (see Figure 5.7). It is also evident that both ways, i.e., to increase the degree or to reduce the mesh size, are valid to better approximate the conduction velocity.

Additionally, our results suggest that to achieve a converged conduction velocity for HDG and CG and independent of the mesh type, approximately the same number of degrees of freedom and non-zero entries in the system matrix are needed, except for a polynomial order $p = 0$ in HDG. For the ndof this can be seen in Figure 5.7a where the polynomial order is kept fixed and the element size is decreasing, and more clearly in Figure 5.7c, where the element size is kept fixed and polynomial order is increasing, and similarly for the nnz in Figure 5.7b and Figure 5.7d.

For the same number of degrees of freedom, if the result is approximated with high-order elements instead of small sized lower order elements, the obtained conduction velocity is closer to the exact solution (see Figure 5.8a). In terms of number of nnz, increasing the polynomial order or decreasing the element size leads to the same result (see Figure 5.8b). Thus, the HDG method becomes increasingly competitive as the polynomial degree is increased. For $h = 0.5$ the conduction velocity increases slightly at one point, although due to convergence behavior the conduction velocity should decrease. The slight increase may happen as we measure only a scalar value to identify the convergence of the solution. A coarse time step, a coarse mesh and the averaging of the values around the measuring point could lead to small rounding errors, which cause a slight change in the computed conduction velocity. However, the convergence behavior of the overall problem does not change.

In Figure 5.9, we compare tetrahedral with hexahedral meshes. Note that for a fixed h, tetrahedral meshes have a larger number of elements than hexahedral meshes. Although for a fixed h in CG both mesh discretizations, hexahedral and tetrahedral, deliver the same ndof in the structured mesh, in HDG (and particularly high order) the tetrahedral mesh involves a considerably larger number of degrees of freedom. However, we can clearly appreciate that we roughly require the same number of degrees of freedom and nnz with tetrahedral and hexahedral meshes for achieving similar precision, i.e., the precision is only depending on the ndof and is independent form the element type. Note that for high-order tetrahedral elements we use optimized nodal sets, the so called warp and blend points, to avoid ill-conditioned interpolation and negative impact on linear solvers [153].

5.2.6 Results for p-Adaptivity

The previous results show that increasing the polynomial order in HDG is a very efficient way to improve accuracy. In order take advantage of the latter fact and move towards more efficient codes for computing wave propagation, as it has been postulated in previous works, it is obvious to think about increasing the resolution at the wave front only. And the option of doing this in a very convenient way, is one of our main motivations for using HDG. Therefore, we now show the results of HDG using a p-adaptive approach.

We start the simulation with element order of $p = 0$ everywhere, define a maximal polynomial order $p_{\max}$, and apply the adaptivity strategy specified in Section 5.1.6. Figure 5.10 shows the result of a p-adaptive simulation for element size $h = 0.5\,\mathrm{mm}$ and $p_{\max} = 10$. As expected, the method selects a high polynomial degree at the position of the steep electrochemical wave front, and after some time, when the wave has passed, the polynomial degree decreases again.

We now present in more detail the results for different values of h, $p_{\max}$ and e_{tol} in Table 5.2, by comparing the error between computed conduction velocity and the exact one. The table shows the error of the constant polynomial degree, $p = p_{\max}$ everywhere, and the adaptive polynomial

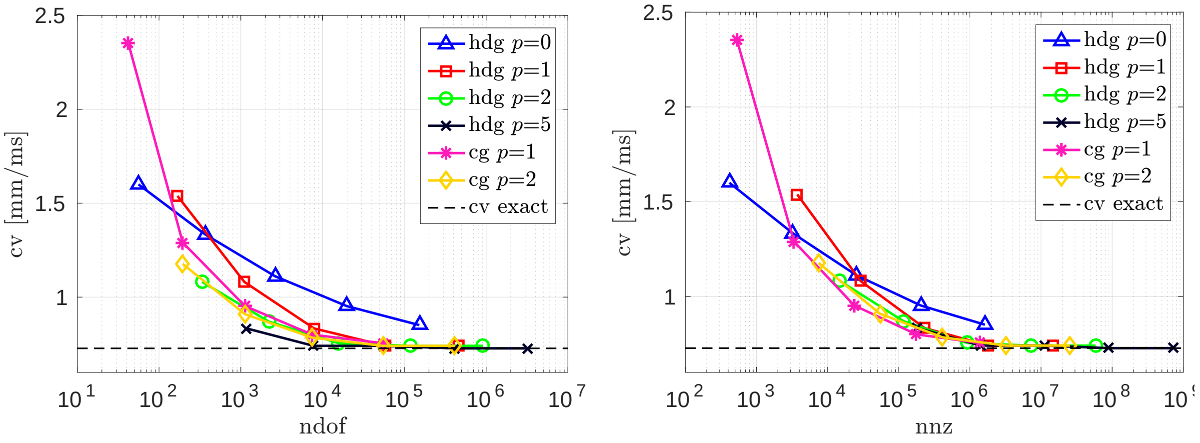

(a) number of degrees of freedom (ndof) via h-refinement (b) number of non-zeros in system matrix (nnz) via h-refinement

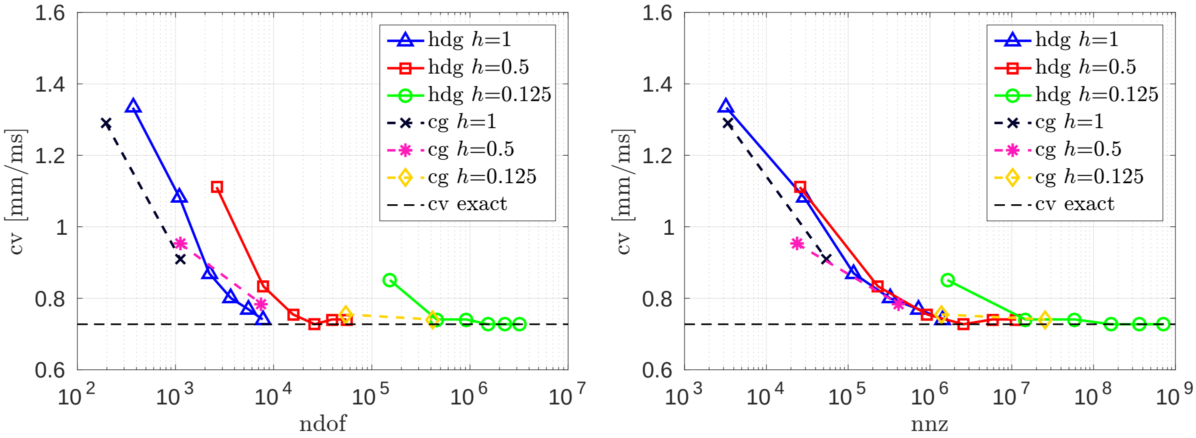

(c) number of degrees of freedom (ndof) via p-refinement (d) number of non-zeros in system matrix (nnz) via p-refinement

Figure 5.7: Conduction velocity plotted over ndof and nnz. (a) and (b) show the conduction velocity for the element sizes $h = 2, 1, 0.5, 0.25$ and $0.125\,\mathrm{mm}$. (c) and (d) show the conduction velocity for polynomial order $p = 0, 1, 2, 3, 4$ and 5 for HDG and $p = 1$ and 2 for CG.

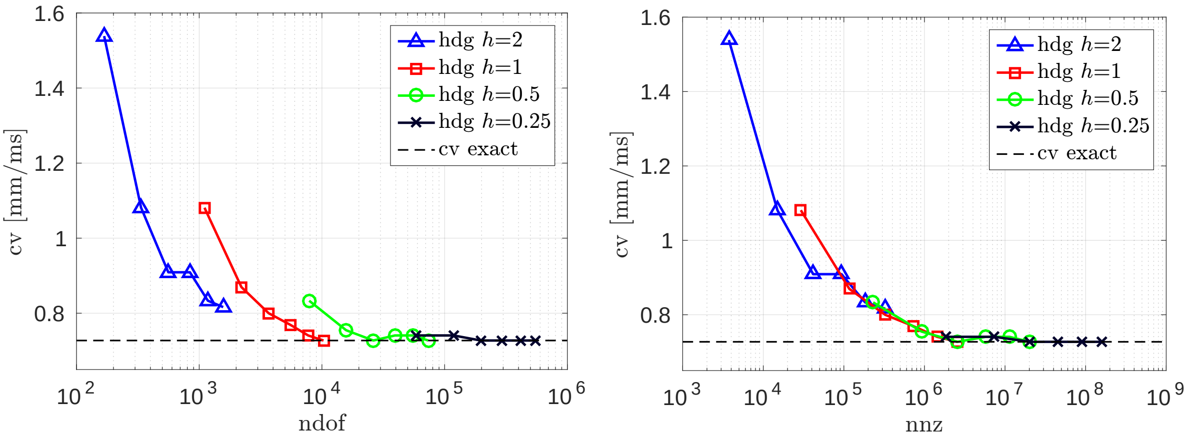

(a) number of degrees of freedom (ndof)

(b) number of non-zeros in system matrix (nnz)

Figure 5.8: This is a closeup of the results for HDG from Figures 5.7c and 5.7d. The conduction velocity for polynomial order $p = 1$, 2, 3, 4, 5 and 6 is plotted.

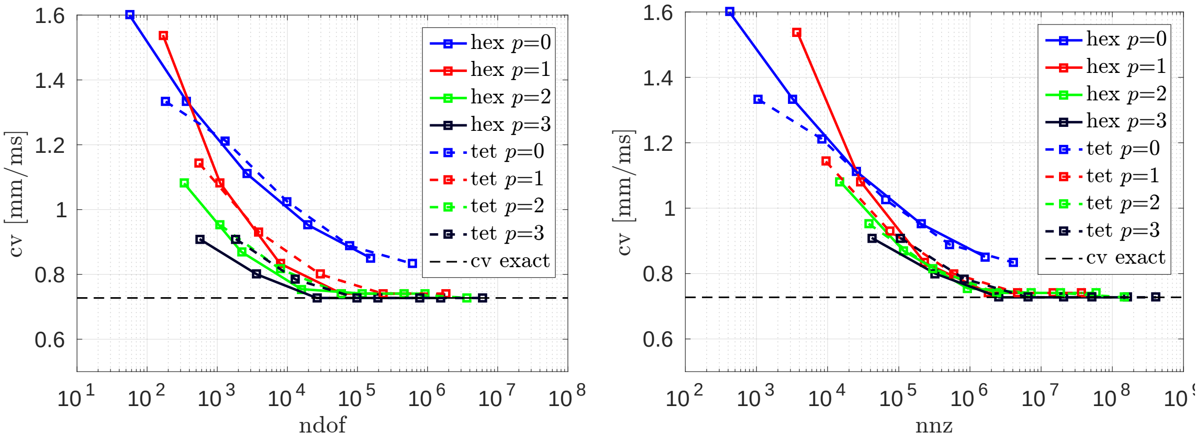

(a) number of degrees of freedom (ndof)

(b) number of non-zeros in system matrix (nnz)

Figure 5.9: Comparison between hexahedral (hex) and tetrahedral (tet) elements. The conduction velocity is plotted for element sizes of $h = 2$, 1, 0.5, 0.25 and $0.125\,\mathrm{mm}$. The difference between different element types is relatively small.

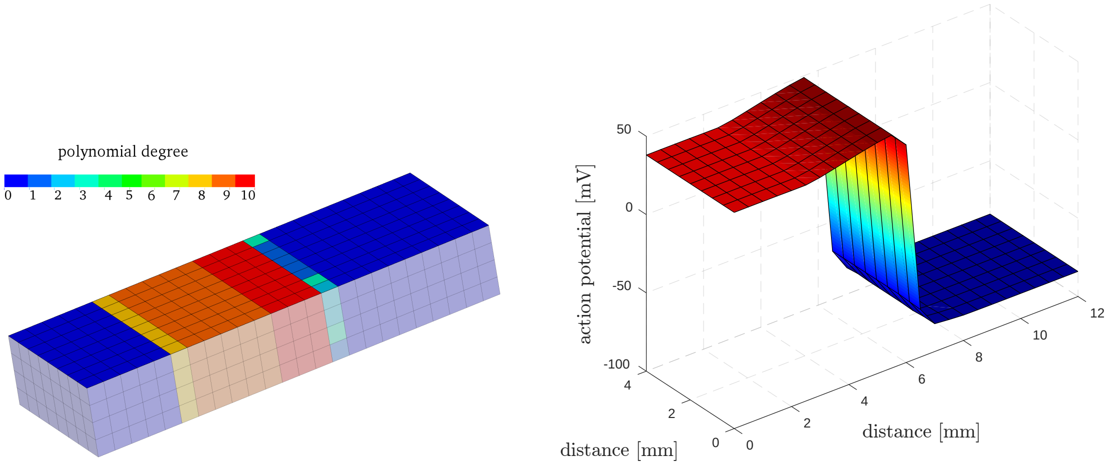

(a) polynomial degree distribution (b) action potential

Figure 5.10: Polynomial degree and action potential at time $6\,\mathrm{ms}$. The element size is $0.5\,\mathrm{mm}$ and the tolerance was chosen as $e_{tol} = 10^{-4}$ (a) Distribution of the adaptively chosen polynomial degree. (b) Action potential of the upper surface. At the steep electrochemical wave front the polynomial degree is high.

degree until degree $p_{\max}$. Note that the adaptive simulation always utilize the highest polynomial degree. To identify the influence of the error tolerance we calculated the error indicator without normalizing for three different element sizes $h = 2$, 1 and $0.5\,\mathrm{mm}$, i.e., we use $A_\gamma = 1$ in Equation (5.32). The tested error tolerances are $e_{tol} = 10^{-2}$, 10^{-4} and 10^{-8} (see Table 5.2). From Table 5.2 we can see that the error decreases with increasing polynomial degree for the p-constant method for such a large tolerance. This is not the case for the p-adaptive method with an error tolerance of $e_{tol} = 10^{-2}$, i.e. p-adaptivity with a large error tolerance is not able to reproduce the p-constant solution. Only for small element sizes and small polynomial degrees the method is able to approximate the result of the p-constant method. Decreasing the error tolerance leads to a better approximation of the p-constant result as it can be seen in Table 5.2 for $e_{tol} = 10^{-4}$ and $e_{tol} = 10^{-8}$. However, a smaller error tolerance increases the number of high-order elements (Figure 5.11). For a coarse tolerance (e.g. $e_{tol} = 10^{-2}$) the number of elements with high order over time is small and it also decreases rapidly again. Decreasing the tolerance increases the number of high-order elements and over time the decrease of the number of high-order elements is slower (Figure 5.11). A further decrease of the tolerance $e_{tol} = 10^{-8}$ results in a large number of high-order elements without returning to low order once the wave front has passed. The elements remain at high order until the action potential is returned to resting potential (Figure 5.11). This results almost in a constant polynomial degree over time. Thus, the smaller the error tolerance the more the constant method is approached.

Comparing different error tolerances for different element sizes shows large differences if the error indicator is not normalized (Figure 5.12). For an error tolerance of $e_{tol} = 10^{-4}$ the element order does not decrease in the simulation with element size $h = 2\,\mathrm{mm}$. Using a normalized error indicator calculation as stated in Equation (5.32) and an error tolerance of $e_{tol} = 10^{-4}$ we can see that in all cases the polynomial degrees return to low order (Figure 5.12) and also the difference between constant and adaptive method is small (Table 5.2). Figure 5.13 shows the

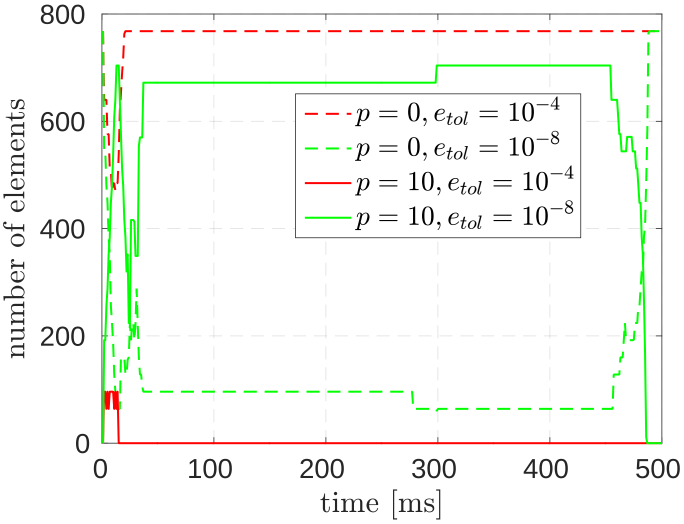

Figure 5.11: Number of elements with polynomial order of $p = 0$ and $p = 10$ during a p-adaptive simulation plotted over time. The element size is $h = 0.5\,\text{mm}$.

		p-const	**p-adaptive**			
	e_{tol}		10^{-2}	10^{-4}	10^{-8}	10^{-4} normalized
	$p_{\max}$	**error**$=\lvert\text{cv-cv}^{\text{exact}}\rvert\ /\text{cv}^{\text{exact}}$				
$h = 2\,\text{mm}$	2	48.5%	52.62%	48.5%	44.37%	44.37%
	4	25.12%	62.25%	22.37%	25.12%	34.75%
	5	14.12%	89.75%	16.87%	14.12%	27.87%
	7	10%	103.5%	22.37%	10%	10%
	10	3.12%	44.37%	37.5%	3.12%	3.12%
$h = 1\,\text{mm}$	2	19.62%	19.62%	19.62%	16.87%	19.62%
	4	5.87%	1.75%	5.87%	5.87%	5.87%
	5	1.75%	2.38%	1.75%	3.12%	1.75%
	7	1.75%	7.88%	0.37%	1.75%	0.37%
	10	0.37%	7.88%	0.37%	0.37%	0.37%
$h = 0.5\,\text{mm}$	2	3.12%	2.38%	3.12%	3.12%	3.12%
	4	1.75%	1.75%	0.37%	0.37%	0.37%
	5	1.75%	14.12%	0.37%	0.37%	0.37%
	7	0.37%	41.62%	0.37%	0.37%	0.37%
	10	0.37%	62.25%	2.38%	0.37%	0.37%

Table 5.2: Comparison of the relative error to the exact conduction velocity of standard HDG method with the p-adaptive method for different polynomial degrees and different error tolerances e_{tol}. $p_{\max}$ is the maximal polynomial order allowed, h is the element size and cv is the conduction velocity.

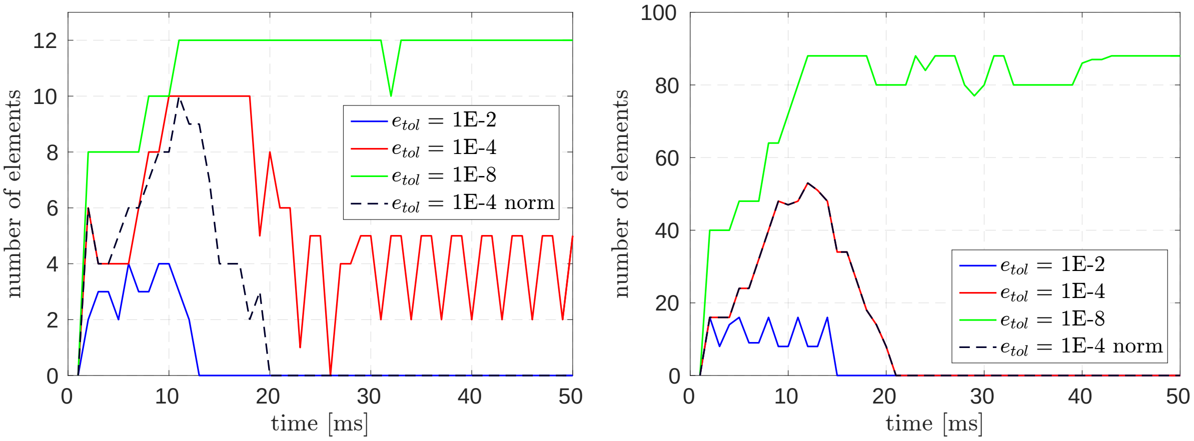

(a) $h = 2\,\mathrm{mm}$ (b) $h = 1\,\mathrm{mm}$

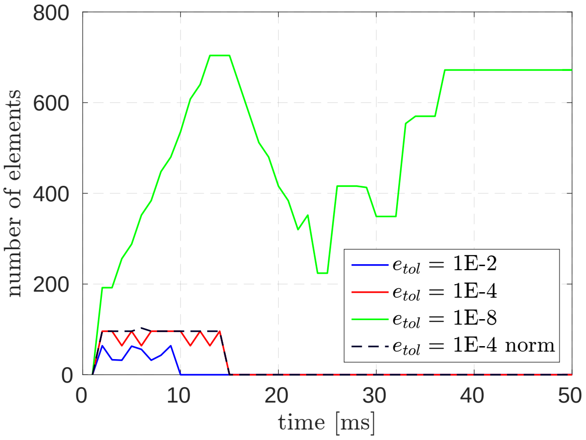

(c) $h = 0.5\,\mathrm{mm}$

Figure 5.12: Number of elements with polynomial order of $p = 10$ during a p-adaptive simulation plotted over time for different element sizes h =2, 1 and $0.5\,\mathrm{mm}$ until a time of $50\,\mathrm{ms}$.

distribution of the polynomial degrees at different times for a calculation with a normalized error indicator for a mesh with $h = 0.5\,\mathrm{mm}$ element size. Slight differences in the polynomial order along the width of the geometry are due to rounding errors. This asymmetry in the polynomial order distribution arises only after many time steps due to accumulated effects of an integer decision (which degree) from a continuous field that is almost the same (subject to roundoff). The polynomial degree increases when the electrochemical wave arrives and after around $10\,\mathrm{ms}$ the polynomial degree decreases again. Thus, our results verify that the error indicator calculation according to Equation (5.32) is a good option for localizing high degrees to the elements close to the wave front.

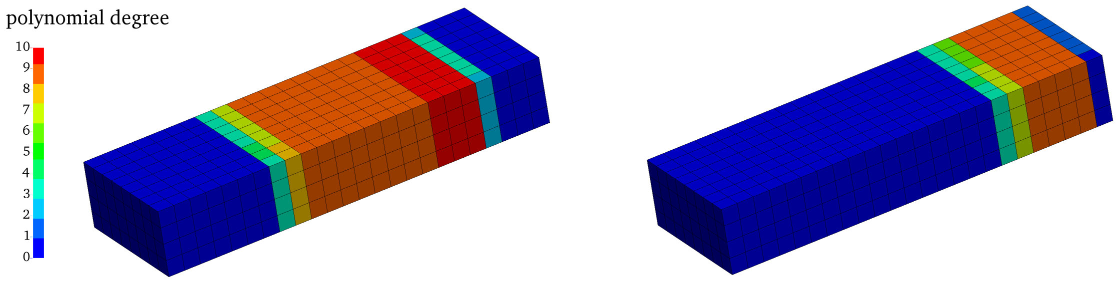

(a) time $10\,\mathrm{ms}$ (b) time $17\,\mathrm{ms}$

Figure 5.13: Polynomial degree distribution for two different time steps for a mesh with element size of $0.5\,\mathrm{mm}$ and a normalized error indicator.

5.2.7 Computations on a Real Biventricular Geometry

To show the applicability of our method to real cardiac electrophysiology simulations, we use our p-adaptive HDG implementation to solve the electrophysiological propagation problem for a real human ventricle geometry. For this purpose we segmented the left and right ventricle from magnetic resonance images acquired in a healthy 33 year old female volunteer, with a dual-phase whole-heart 3D b-SSFP sequence [346] on a 1.5T Philips Achieva MRI scanner, acquisition matrix 212x209x200, acquired voxel size $2\,\mathrm{mm} \times 2\,\mathrm{mm} \times 2\,\mathrm{mm}$, repetition time $4.5\,\mathrm{ms}$, echo time $2.2\,\mathrm{ms}$, echo train length 26 and flip angle 90°. The diastasis was used to generate the computational mesh.

To investigate different levels of mesh refinement we use tetrahedral elements with a maximal element size of $2\,\mathrm{mm}$, $1\,\mathrm{mm}$ and $0.5\,\mathrm{mm}$, which results in three meshes with $59\,801$, $393\,302$ and $2\,904\,351$ number of elements, respectively. On real heart geometries mesh refinement leads inevitably to a slight change of the geometry. Hence, we examined if the differences in the geometry are strongly influencing the results, or coarser meshes with high-order elements are able to reproduce the activation propagation accurately.

We initiate the propagation of the electrical wave with a stimulus current on the apex. The maximal polynomial degree is set to five and at the beginning all polynomial degrees are set to zero. For computational reasons we use the integration rule defined in Equation (5.37) in this example for all polynomial degrees . The coarsest mesh shows a slightly faster activation than the finer ones, while only very small differences are in the activation are visible between the two finer ones (see Figure 5.14). The activation time of a sample point in the middle of the posterior wall at the junction between left and right ventricle has been captured for the different levels of refinement. The activation time of the sample point for the coarsest mesh is measured as about $40.7\,\mathrm{ms}$, for the finer one about $45.4\,\mathrm{ms}$ and for the finest mesh about $46.3\,\mathrm{ms}$.

When using non-adaptive HDG elements for the example with a maximal element size of $1\,\mathrm{mm}$ one would have during all time steps $17\,739\,225$ ndof. In comparison, with the p-adaptive HDG method we have between $844\,725$ minimal and $2\,275\,660$ maximal ndof. The ndof averaged over the whole simulation are depending of course on the particular case, i.e. the geometry, the simulation time and the activation sequence influence the ndof over time. In our example for an element size of $1\,\mathrm{mm}$ we show the average ndof until different specifications of the end of the

specified simulation end	time	averaged ndof over time
end of activation	$0.15\,\mathrm{s}$	$1\,709\,905$
end of systole	$0.3\,\mathrm{s}$	$1\,278\,179$
diastasis	$0.5\,\mathrm{s}$	$1\,107\,227$
end of heart cycle	$1.0\,\mathrm{s}$	$988\,151$

Table 5.3: Ndof averaged from start until given time, for the example with $1\,\mathrm{mm}$ maximal element size.

simulation, e.g. the end of the activation or the end of the heart cycle. The averaged ndof can be seen in Table 5.3. The average ndof decrease the longer the simulation lasts since only one activation cycle is calculated and only around the wave front high polynomial degrees are used. The decrease of the ndof is very useful, in particular when the calculated activation is coupled to a mechanical simulation and the whole heart cycle is simulated. In this case the activation takes place only in a short period of time, while the overall simulation takes much longer.

The electrophysiological simulation can also be coupled to mechanical simulations to calculate electromechanics in the heart. The mechanical simulation is solved using continuous finite elements, while for the electrophysiological simulation we use p-adaptive HDG discretization, but both meshes are the same. We couple the mechanical simulation through the action potential, which is stored for each element a the integration points. For more details about the coupling and the mechanical simulation we refer to our work described in [172]. In Figure 5.15 the activation time and the displacement at peak systole is shown for the ventricular geometry with a maximal element size of $1\,\mathrm{mm}$.

5.3 Closure

In this chapter we proposed and analyzed the use of an adaptive high-order Hybridizable Discontinuous Galerkin (HDG) method for efficiently calculating the electric propagation in human hearts. As compared to classical DG method an HDG discretization reduces the degrees of freedom through static condensation on the element level, so that only the degrees of freedom defined on the faces between the elements show up in the global system of equations. An advantage of the HDG method (as well as for other DG methods) is the simple usage of spatially varying high-order elements, due to the discontinuity between the elements that is captured through numerical fluxes. An approach with high-order elements in turn additionally needs a good approximation of the integral of the ionic current term. In this work we have defined a rule for a suitable integration accuracy depending on the polynomial order and the cell model selected by the requirement to exactly integrate the leading current term. Furthermore we have defined and explained a practical choice of the stabilization parameter for the HDG discretization for the electrophysiological problem. Comparing CG and HDG methods, we have seen a similar performance for low-order elements, but an increase in efficiency for high-order elements.

The electrophysiology calculation is determined by a steep electrochemical wave front, which travels through cardiac tissue. We proposed a simplification of an error indicator previously reported to localize it and to define an error indicator, which can be used to suggest the appropriate order of the element and in this way realize a p-adaptive HDG approach for cardiac electrophys-

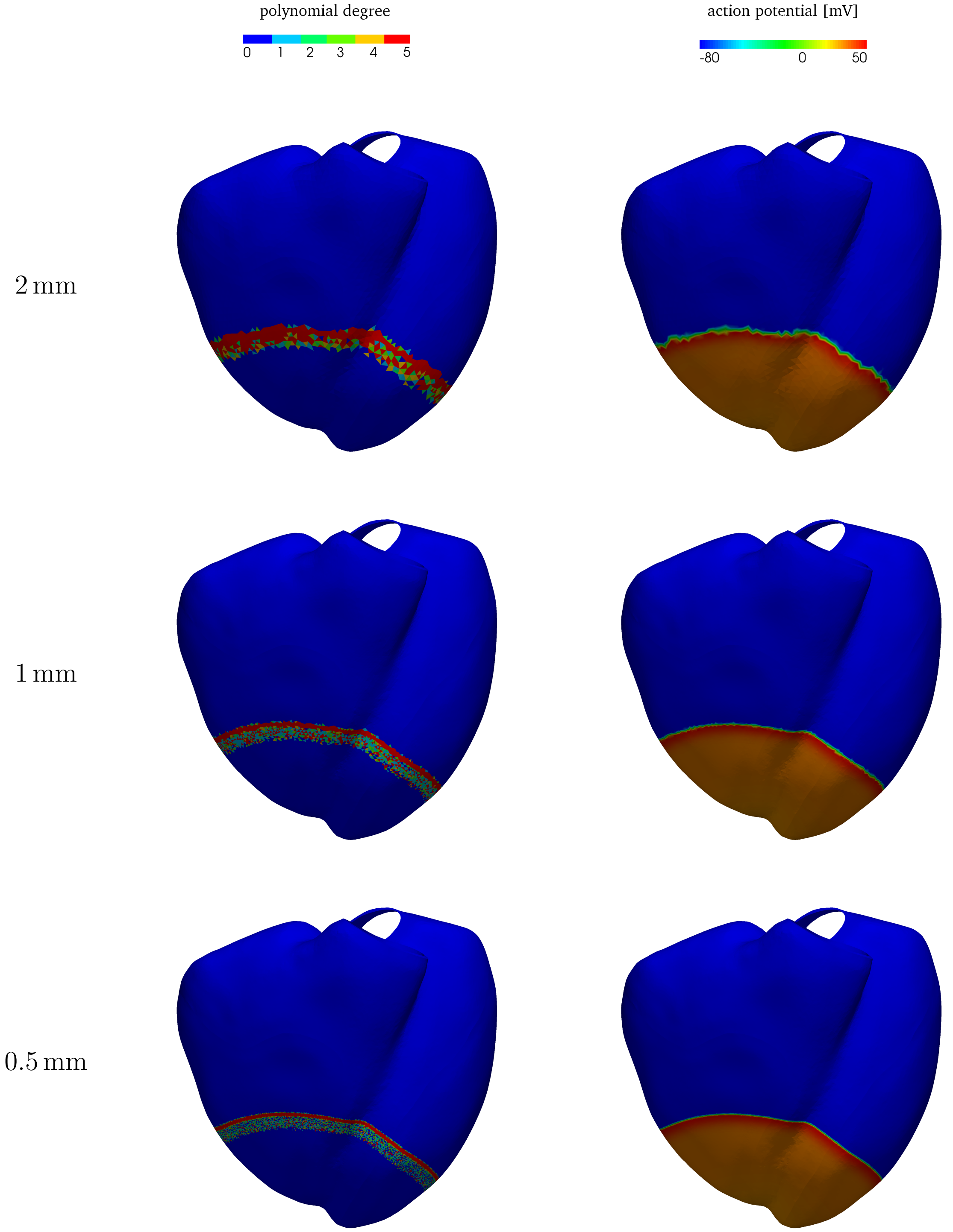

Figure 5.14: Polynomial degree and action potential at time $0.05\,\mathrm{s}$.

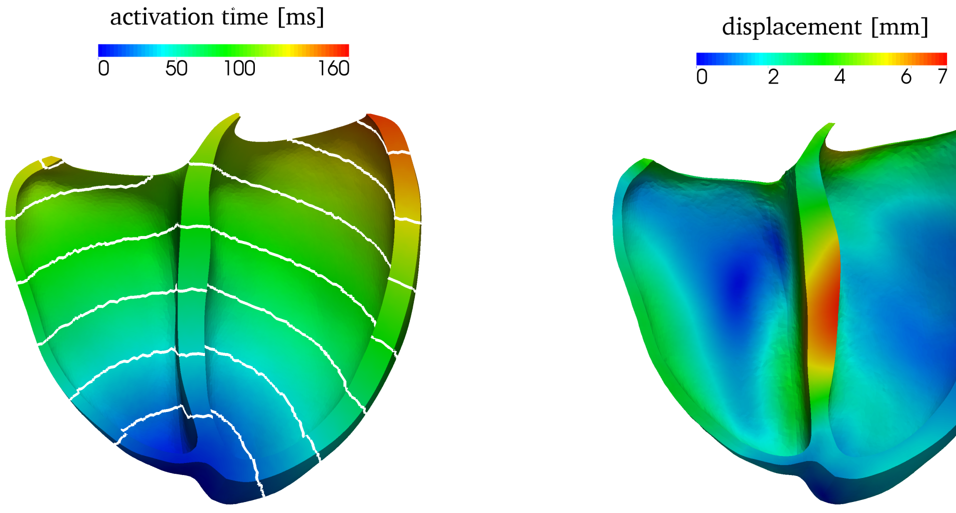

(a) Activation time

(b) Displacement

Figure 5.15: Activation time with isochrones at each $20\,\mathrm{ms}$ and the displacement at peak systole at about $0.3\,\mathrm{s}$ for a real heart geometry with an element size of approximately $1\,\mathrm{mm}$.

iology. In summary, HDG shows great potential to efficiently solve large scale electrophysiological problems for complex geometries using coarse meshes and p-adaptive high-order elements, which can be additionally coupled with cardiac mechanical simulations.

Acknowledgment

This chapter contains the results already published in [166] and reprinted here by permission from John Wiley and Sons: John Wiley and Sons, International Journal of Numerical Methods in Biomedical Engineering, An adaptive hybridizable discontinuous Galerkin approach for cardiac electrophysiology, Julia M. Hoermann, Cristóbal Bertoglio, Martin Kronbichler, et al., Copyright © 2018 John Wiley & Sons, Ltd. (2018)

6 Registration and Fiber Generation

Knowledge of appropriate local fiber architecture is necessary to simulate patient-specific electromechanics in the human heart. However, it is not yet possible to reliably measure in-vivo fiber directions especially in human atria. Thus, we present in this chapter a method which defines the fiber architecture in arbitrarily shaped atria using image registration and reorientation methods based on atlas atria with fibers predefined from detailed histological observations. Thereby, it is possible to generate detailed fiber families in every new patient-specific geometry in an automated, time-efficient process. We demonstrate the good performance of the image registration and fiber definition on ten differently shaped human atria. Additionally, we show that characteristics of the electrophysiological activation pattern which appear in the atlas atria also appear in the patients' atria. We arrive to analogous conclusions for coupled electro-mechano-hemodynamical computations.

The remainder of this chapter is organized as follows. First, in Section 6.1 the theory of registration and fiber interpolation is explained in detail. In Section 6.2 we first characterize the method to define the fibers of the atlas atria. Then we describe the process of image registration, fiber reorientation and fiber lifting to generate the fibers in the patient's atria. We shortly describe the electro-mechano-hemodynamical model, with which we simulate the functions of the atria with defined and mapped fibers. In Section 6.3 we describe the results of the registration and mapping procedure in comparison to the defined fibers. Additionally, we compare, analyze and discuss the results of the electromechanical simulation with mapped fiber in all atria.

6.1 Theory

Image registration is important for digital image processing. It consists of aligning two images of the same object. Image registration is used in many fields and for many different applications. An important field is the medical sector, where image registration is for example used to fuse images taken from different imaging modalities or to compare images taken at different time steps. In the simulation sector it can be used to compare experimental data with simulation results and to estimate material parameter using inverse analysis [30, 42]. However, registration can also be used to improve the geometrical model necessary for simulations. Transforming the geometry of the heart of a patient to match the heart of the other patients is needed to transfer spatial information available only in one geometry to the new heart automatically. More precisely, fiber orientation in the atria is not available in-vivo, due to thin structures in the atria and insufficient image resolution. Additionally, defining fibers manually would increase the effort of the model creation which would be an issue when doing a big study. Thus, image registration techniques can overcome this issue while automatically or semi-automatically generating the fiber orientations.

The whole process of registration and fiber generation can be divided into three main different steps. The first step is to compute a rigid or affine transformation using landmarks and the iterative closest point algorithm, the second step is the registration process, and the last step is the interpolation and fiber deformation.

6.1.1 Rigid Transformation

Two geometries are aligned by using rigid transformation. Thereby the source geometry is rotated and translated to match the target geometry. Usually the optimization is defined in a least square sense. Rigid motion as a first step of image registration is used if landmarks or corresponding points are defined on source and target image that should be optimally aligned. The following derivation is based on [18, 321]. Let $S = \{\boldsymbol{s}_1, \boldsymbol{s}_2, ..., \boldsymbol{s}_{n_l}\}$ and $T = \{\boldsymbol{t}_1, \boldsymbol{t}_2, ..., \boldsymbol{t}_{n_l}\}$ be corresponding landmarks in the source and target geometry, respectively, where $\boldsymbol{s}_i, \boldsymbol{t}_i \in \mathbb{R}^d$. For a 3D geometry the dimension is $d = 3$. A rigid transformation is defined through a rotation $\boldsymbol{R}$ and a translation $\boldsymbol{b}$, so that the optimization is defined through

$$(\boldsymbol{R}, \boldsymbol{b}) = \underset{\boldsymbol{R} \in SO(d),\, \boldsymbol{b} \in \mathbb{R}^d}{\arg\min} \sum_{i=1}^{n_l} w_i \parallel (\boldsymbol{R}\boldsymbol{s}_i + \boldsymbol{b}) - \boldsymbol{t}_i \parallel^2 \ , \tag{6.1}$$

where w_i are weights and $SO(d)$ is the group of all rotations in $\mathbb{R}^d$. The translation $\boldsymbol{b}$ can be neglected if the centroid of geometry is translated to the origin, such that the points are defined as

$$\boldsymbol{x}_i := \boldsymbol{s}_i - \bar{\boldsymbol{s}} \quad \boldsymbol{y}_i := \boldsymbol{t}_i - \bar{\boldsymbol{t}} \tag{6.2}$$

with

$$\bar{s} = \frac{1}{\sum_{i=1}^{n_l} w_i} \sum_{i=1}^{n_l} w_i \boldsymbol{s}_i \quad \bar{\boldsymbol{t}} = \frac{1}{\sum_{i=1}^{n_l} w_i} \sum_{i=1}^{n_l} w_i \boldsymbol{t}_i \tag{6.3}$$

Proof. To solve the optimization problem to find the optimal translation $\boldsymbol{b}$, if the rotation $\boldsymbol{R}$ is fixed, we need to find the roots of the derivative of $D(\boldsymbol{b}) = \sum_{i=1}^{n_l} w_i \parallel (\boldsymbol{R}\boldsymbol{s}_i + \boldsymbol{b}) - \boldsymbol{t}_i \parallel^2$ with respect to $\boldsymbol{b}$. Thus,

$$\begin{aligned} 0 &= \frac{\mathrm{d}D(\boldsymbol{b})}{\mathrm{d}\boldsymbol{b}} = \sum_{i=1}^{n_l} 2w_i(\boldsymbol{R}\boldsymbol{s}_i + \boldsymbol{b} - \boldsymbol{t}_i) = \\ &= 2\boldsymbol{b}\sum_{i=1}^{n_l} w_i + 2\boldsymbol{R}\sum_{i=1}^{n_l} w_i \boldsymbol{s}_i - 2\sum_{i=1}^{n_l} w_i \boldsymbol{t}_i \, . \end{aligned} \tag{6.4}$$

Substituting Equations (6.3) into Equation (6.4) we get

$$\boldsymbol{b} = \bar{\boldsymbol{t}} - \boldsymbol{R}\bar{\boldsymbol{s}} \, . \tag{6.5}$$

Using this relation in the objective function and the definition for the translated points (Equation 6.2) the optimization problem changes to

$$\boldsymbol{R} = \underset{\boldsymbol{R} \in SO(d)}{\arg\min} \sum_{i=1}^{n_l} w_i \parallel \boldsymbol{R}\boldsymbol{x}_i - \boldsymbol{y}_i \parallel^2 \ . \tag{6.6}$$

□

The optimal rotation can be computed as

$$\boldsymbol{R} = \boldsymbol{V} \begin{pmatrix} 1 & & & & \\ & 1 & & & \\ & & \ddots & & \\ & & & 1 & \\ & & & & \det(\boldsymbol{V}\boldsymbol{U}^T) \end{pmatrix} \boldsymbol{U}^T \tag{6.7}$$

with the covariance matrix $\boldsymbol{S}$

$$\boldsymbol{S} = \boldsymbol{X}\boldsymbol{W}\boldsymbol{Y}^T = \begin{pmatrix} | & | & & | \\ \boldsymbol{x}_1 & \boldsymbol{x}_2 & \dots & \boldsymbol{x}_n \\ | & | & & | \end{pmatrix} \begin{pmatrix} w_1 & & & \\ & w_2 & & \\ & & \ddots & \\ & & & w_n \end{pmatrix} \begin{pmatrix} | & | & & | \\ \boldsymbol{y}_1 & \boldsymbol{y}_2 & \dots & \boldsymbol{y}_n \\ | & | & & | \end{pmatrix}^T \tag{6.8}$$

and the singular value decomposition $\boldsymbol{S} = \boldsymbol{U}\boldsymbol{\Sigma}\boldsymbol{V}^T$, where $\boldsymbol{U}$ and $\boldsymbol{V}$ are orthogonal matrices describing rotations and $\boldsymbol{\Sigma}$ is a diagonal matrix describing scaling.

Proof. The minimization problem can be simplified as

$$\begin{aligned} \underset{\boldsymbol{R}\in SO(d)}{\arg\min} \textstyle\sum_{i=1}^{n_l} \parallel \boldsymbol{R}\boldsymbol{x}_i - \boldsymbol{y}_i \parallel^2 &= \underset{\boldsymbol{R}\in SO(d)}{\arg\min} \textstyle\sum_{i=1}^{n_l} w_i \left(\boldsymbol{x}_i^T\boldsymbol{x}_i - 2\boldsymbol{y}_i^T\boldsymbol{R}\boldsymbol{x}_i + \boldsymbol{y}_i^T\boldsymbol{y}_i\right) = \\ &= \underset{\boldsymbol{R}\in SO(d)}{\arg\min} \left(-2\textstyle\sum_{i=1}^{n_l} \boldsymbol{w}_i\boldsymbol{y}_i^T\boldsymbol{R}\boldsymbol{x}_i\right) \\ &= \underset{\boldsymbol{R}\in SO(d)}{\arg\max} \left(\textstyle\sum_{i=1}^{n_l} \boldsymbol{w}_i\boldsymbol{y}_i^T\boldsymbol{R}\boldsymbol{x}_i\right) . \end{aligned} \tag{6.9}$$

where the second step holds since the removed terms are not depending on $\boldsymbol{R}$. Note that it holds, as well

$$\sum_{i=1}^{n_l} w_i\boldsymbol{y}_i^T\boldsymbol{R}\boldsymbol{x}_i = \operatorname{tr}\left(\boldsymbol{W}\boldsymbol{Y}^T\boldsymbol{R}\boldsymbol{X}\right) . \tag{6.10}$$

Additionally, using the properties of the trace and Equation (6.8) and applying the singular value decomposition on $\boldsymbol{S} = \boldsymbol{U}\boldsymbol{\Sigma}\boldsymbol{V}^T$ this can be written as

$$\operatorname{tr}\left(\boldsymbol{W}\boldsymbol{Y}^T\boldsymbol{R}\boldsymbol{X}\right) = \operatorname{tr}\left(\boldsymbol{R}\boldsymbol{X}\boldsymbol{W}\boldsymbol{Y}^T\right) = \operatorname{tr}\left(\boldsymbol{R}\boldsymbol{S}\right) = \operatorname{tr}\left(\boldsymbol{R}\boldsymbol{U}\boldsymbol{\Sigma}\boldsymbol{V}^T\right) = \operatorname{tr}\left(\boldsymbol{\Sigma}\boldsymbol{V}^T\boldsymbol{R}\boldsymbol{U}\right) . \tag{6.11}$$

Since $\boldsymbol{V}$, $\boldsymbol{R}$ and $\boldsymbol{U}$ are orthogonal matrices also $\boldsymbol{M} = \boldsymbol{V}^T\boldsymbol{R}\boldsymbol{U}$ is orthogonal. The product of rows or columns $\boldsymbol{m}_j$ of the orthogonal matrix $\boldsymbol{M}$ are thus $1 = \boldsymbol{m}_j^T\boldsymbol{m}_j = \sum_i mij^2$. Hence, it follows for all matrix entries $|m_{ij}| \leq 1\, \forall i, j$. To maximize $\operatorname{tr}(\boldsymbol{\Sigma}\boldsymbol{M})$ knowing about the orthogonality of $\boldsymbol{M}$ it means to set $\boldsymbol{M}$ as the identity matrix, because $\boldsymbol{\Sigma}$ is a diagonal matrix with non-negative values and

$$\operatorname{tr}(\boldsymbol{\Sigma}\boldsymbol{M}) = \sum_{i=1}^{d} \sigma_i m_{ii} \leq \sum_{i=1}^{d} \sigma_i . \tag{6.12}$$

Hence, it holds $\boldsymbol{I} = \boldsymbol{M} = \boldsymbol{V}^T\boldsymbol{R}\boldsymbol{U} \Rightarrow \boldsymbol{R} = \boldsymbol{V}\boldsymbol{U}^T$. To prevent $\boldsymbol{R}$ to be a reflection ($\det(R) = -1$) instead of a rotation ($\det(R) = 1$) the matrix $\boldsymbol{M}$ has to be defined as

$$\boldsymbol{M} = \operatorname{diag}\left(1, 1, \ldots, 1, \det(\boldsymbol{V}\boldsymbol{U}^T)\right) .$$

□

With the optimal rotation $\boldsymbol{R}$, the optimal translation $\boldsymbol{t}$ can be computed with Equation (6.5). Using the optimal rotation and translation the source geometry is transformed, i.e. all nodes $\tilde{\boldsymbol{n}}_i$ of the source image are transformed onto the nodes $\boldsymbol{n}_i^{\mathrm{rg}}$

$$\boldsymbol{n}_i^{\mathrm{rt}} = \boldsymbol{R}\tilde{\boldsymbol{n}} + \boldsymbol{t}\,. \tag{6.13}$$

6.1.2 Iterative Closest Point

To improve the alignment of the two geometries iterative transformations are performed. Therefor all nodes of the geometry are used for optimization. Since no node to node correspondence between source and target image exists an adapted iterative closest point (ICP) algorithm is applied. An ICP algorithm can be divided into two steps: First, for each point of the initial source geometry I_0 the closet point of the target geometry is defined [38, 70]. In case of Finite Element discretization the points can be associated with the nodes of the discretization. Since beforehand an rigid transformation already took place the nodes of the source geometry I_0 are the nodes $\boldsymbol{n}_i^{\mathrm{rg}}$. The second step consists of finding parameters which minimize the objective function $f(\boldsymbol{p})$

$$f(\boldsymbol{p}) = \sum_{i=1}^{n_n} \parallel (A(\boldsymbol{p})\boldsymbol{x} + s(\boldsymbol{p})) - \boldsymbol{y} \parallel^2 \tag{6.14}$$

where n_n is the number of source points,

$$\boldsymbol{p} = (t_1, t_2, t_3, r_x, r_y, r_z, h_{xy}, h_{xz}, h_{yx}, h_{yz}, h_{zx}, h_{zy}, s_x, s_y, s_z)$$

contains the parameter defining the translation $t_{(\cdot)}$, rotation $r_{\cdot}$, shear $h_{(\cdot)}$ and resize $s_{(\cdot)}$. The function $s(\boldsymbol{p})$ can be defined as a translation vector $\boldsymbol{s}$ and the transformation $A(\boldsymbol{p})$ as a transformation matrix $\boldsymbol{A}$ as

$$s(\boldsymbol{p}) = \boldsymbol{s} = \begin{bmatrix} t_1 \\ t_2 \\ t_3 \end{bmatrix} \quad \text{and} \quad A(\boldsymbol{p}) = \boldsymbol{A} = \boldsymbol{H}\boldsymbol{R}_x\boldsymbol{R}_y\boldsymbol{R}_z\boldsymbol{S} \tag{6.15}$$

with the rotation matrices

$$\boldsymbol{R}_x = \begin{bmatrix} 1 & 0 & 0 \\ 0 & \cos(r_x) & -\sin(r_x) \\ 0 & \sin(r_x) & \cos(r_x) \end{bmatrix}, \boldsymbol{R}_y = \begin{bmatrix} \cos(r_y) & 0 & \sin(r_y) \\ 0 & 1 & 0 \\ -\sin(r_y) & 0 & \cos(r_y) \end{bmatrix}, \boldsymbol{R}_z = \begin{bmatrix} \cos(r_z) & -\sin(r_z) & 0 \\ \sin(r_z) & \cos(r_z) & 0 \\ 0 & 0 & 1 \end{bmatrix} \tag{6.16}$$

and the shear and resize matrices

$$\boldsymbol{H} = \begin{bmatrix} 1 & h_{xy} & h_{xz} \\ h_{yx} & 1 & h_{yz} \\ h_{zx} & h_{zy} & 1 \end{bmatrix} \text{ and } \boldsymbol{S} = \begin{bmatrix} s_x & 0 & 0 \\ 0 & s_y & 0 \\ 0 & 0 & s_z \end{bmatrix} \tag{6.17}$$

Depending on the requirements the transformation matrix can define a rigid transformation as a rotation or resize and shear as an affine transformation. The optimization problem is solved using the limited memory Broyden-Fletcher-Goldfarb-Shanno (L-BFGS) algorithm [57, 219]. This algorithm is used to solve large scale unconstrained optimization problems, but requires only limited memory. Using the optimal translation $\boldsymbol{s}$ and transformation $\boldsymbol{A}$ of the kth iteration step, each node $\boldsymbol{X}_k$ of the source geometry I_k gets transformed via $\boldsymbol{X}_{k+1} = \boldsymbol{A}\boldsymbol{X}_k + \boldsymbol{s}$ onto the new node location $\boldsymbol{X}_{k+1}$ and a new source geometry I_{k+1} of the next step is defined. In a new iteration the same steps, i.e. finding the closest points and minimizing the objective function, are performed with I_{k+1} as new input. This is done in an iterative way until the error between the transformed source geometry and the target geometry is sufficiently small.

6.1.3 Registration

The registration process is divided into two parts. The first one is the difference measure between the two images and the second is the regularization. The regularization is necessary since the registration is an ill-posed problem [233].

Image registration is the task to find an optimal transformation $\boldsymbol{\varphi}(\boldsymbol{X})$ of the source image, which minimizes the difference to the target image. We denote the source image $I_s : \Omega \to \mathbb{R}$ and the target image as $I_t : \Omega \to \mathbb{R}$ where $\Omega \subset \mathbb{R}^d$ with $d \in \{2, 3\}$ for a 2D or 3D image, respectively. To define the optimal transformation a definition of a distance measure is necessary, which compares the transformed images to the target image. The registration problem can then be defined as: given a distance measure $\mathcal{D}$ and two images I_s and I_t find a transformation $\boldsymbol{\varphi}(\boldsymbol{X}) : \mathbb{R}^d \to \mathbb{R}^d$ such that $\mathcal{D}(I_s, I_t, \boldsymbol{\varphi}) = \min$. However, this problem is ill-posed and needs an additional regularization to overcome the ill-posedness.

We consider here only non-parametric image registration. A non-parametric transformation cannot be represented with certain parameter. The transformation is defined as

$$\boldsymbol{\varphi}(\boldsymbol{X}) = \boldsymbol{X} + \boldsymbol{u}(\boldsymbol{X}), \tag{6.18}$$

where $\boldsymbol{u} : \mathbb{R}^d \to \mathbb{R}^d$ is a spatially varying displacement field. Additionally, the regularization $\mathcal{S}$, which is necessary to compute a stable solution, is considered to be a bilinear form based on the $L_2(\Omega)$-norm, such that

$$\mathcal{S}(\boldsymbol{u}) :=\| \mathcal{B}\boldsymbol{u} \|^2_{L_2(\Omega)} , \tag{6.19}$$

where $\mathcal{B}$ is a differential operator. With this additional definition the registration problem can be redefined as: given a distance measure $\mathcal{D}$, two images I_s and I_t and a regularization parameter $\alpha > 0$ find a displacement $\boldsymbol{u}(\boldsymbol{X})$ such that

$$\mathcal{J}(\boldsymbol{u}) := \mathcal{D}(I_s, I_t, \boldsymbol{u}) + \alpha\mathcal{S}(\boldsymbol{u}) = \min . \tag{6.20}$$

In particular, in our registration process we use the sum of squared differences (SSD) as distance measure given by

$$\mathcal{D}(\boldsymbol{u}) := \frac{1}{2}\int_\Omega \left(I_s\left(\boldsymbol{X} + \boldsymbol{u}\left(\boldsymbol{X}\right)\right) - I_t\right)^2 \mathrm{d}\mathbf{X}, \tag{6.21}$$

and an elastic potential as regularizer given as

$$\mathcal{S}(\boldsymbol{u}) := \int_\Omega \frac{\lambda + \mu}{2} \| \nabla \cdot \boldsymbol{u}(\boldsymbol{X}) \|^2 + \frac{\mu}{2}\sum_{i=1}^{d} \| \nabla u_i(\boldsymbol{X}) \|^2 \ \mathrm{d}\mathbf{X}, \tag{6.22}$$

where λ and μ are the Lamé constants [48]. In contrary to Section 4.2.5 the elastic potential is based on the linear elasticity theory since for the regularizer the assumption of small deformations and a linear material is sufficient.

To solve the registration problem we use a Gauss-Newton method [142, 259] together with a multiresolution approach [213]. For the Gauss-Newton method the gradient of $\mathcal{J}$ needs to be computed. Image registration deals with 2D or 3D images, which are defined on discrete cells and can be pixels or voxels. Thus, two ways exist for solving the optimization problem: solve the optimization and then discretize or discretize the objective function and then solve the optimization. The first approach leads to a nonlinear system of partial differential equations with appropriate boundary conditions, which is then solved using discretization methods [118]. We use the second approach, which follows the ideas of Haber et al. [141, 142]. Hence, the objective function or more precise the differential operators of the function are discretized and then an optimization problem is solved. The discrete version of the displacement $\boldsymbol{u}^h$ is defined using a collocated grid, i.e. everything is stored at the cell centers. The discretized form of the regularizer $\mathcal{S}$ is defined as follows

$$\boldsymbol{S}^h(\boldsymbol{u}^h) := \frac{\lambda+\mu}{2} \parallel \nabla^h \cdot \boldsymbol{u}^h \parallel^2 + \frac{\mu}{2} \sum_{i=1}^{d} \parallel \nabla^h u_i^h \parallel^2 \ , \tag{6.23}$$

with the discretized differential operators of the gradient ∇^h and divergence $\nabla^h \cdot$ defined as

$$\nabla^h u_i^h = (\partial_1^h u_i^h, \ldots, \partial_d^h u_i^h)^T \text{ and } \nabla^h \cdot \boldsymbol{u}^h = \sum_{i=1}^{d} \partial_i^h u_i^h \,, \tag{6.24}$$

where ∂_d^h is a finite difference defined between neighboring cells. The derivative of the regularizer is then the Navier-Lamé operator as

$$\boldsymbol{S}_u^h(\boldsymbol{u}^h) = (\lambda+\mu)(\nabla^h \cdot)\nabla^h \cdot \boldsymbol{u}^h - \mu \Delta^h \boldsymbol{u}^h =: \boldsymbol{B}\boldsymbol{u}^h \,, \tag{6.25}$$

with the standard discrete Laplace operator Δ^h. The discretization of the SSD is as follows

$$\boldsymbol{D}(\boldsymbol{u}^h) := \frac{1}{2} \parallel I_s(\boldsymbol{u}^h) - I_t \parallel^2 \tag{6.26}$$

with the derivative

$$\boldsymbol{D}_u(\boldsymbol{u}^h) := I_{s\boldsymbol{u}}(\boldsymbol{u}^h)^T (I_s(\boldsymbol{u}^h) - I_t) \,. \tag{6.27}$$

Hence, the discrete objective function is defined as

$$\boldsymbol{J}^h(\boldsymbol{u}^h) := \boldsymbol{D}(\boldsymbol{u}^h) + \alpha \boldsymbol{S}(\boldsymbol{u}^h) \tag{6.28}$$

The optimization problem is solved with a Gauss-Newton method [142, 259]. Therefore, in each iteration step the gradient of the objective function (6.28) has to be computed as

$$\boldsymbol{J}_{\boldsymbol{u}}^h(\boldsymbol{u}^h) = I_{s\boldsymbol{u}}\left(\boldsymbol{u}\right)^T \left(I_s\left(\boldsymbol{X}+\boldsymbol{u}\right) - I_t\left(\boldsymbol{X}\right)\right) + \alpha \boldsymbol{B}\boldsymbol{u} \,. \tag{6.29}$$

Afterwards, the system of linear equations has to be solved for $\Delta \boldsymbol{u}$

$$\boldsymbol{H}\Delta \boldsymbol{u} = -\boldsymbol{J}_{\boldsymbol{u}}^h \tag{6.30}$$

with the Hessian $\boldsymbol{H} = I_{s\boldsymbol{u}}\left(\boldsymbol{u}\right)^T I_{s\boldsymbol{u}}\left(\boldsymbol{u}\right) + \alpha \boldsymbol{B}$. Until the solution is below a tolerance the same steps are performed with an updated value for $\boldsymbol{u}_{k+1}^h = \boldsymbol{u}_k^h + \Delta \boldsymbol{u}$.

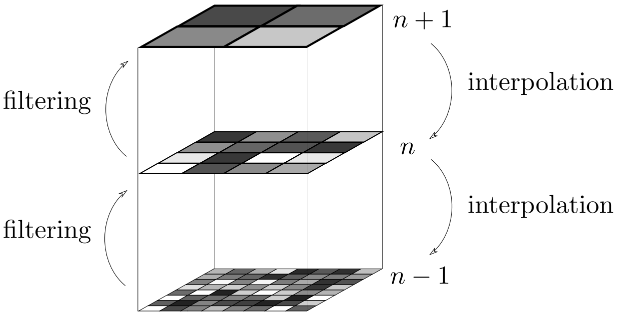

Figure 6.1: Multigrid approach for the solution of the minimization problem.

6.1.3.1 Multiresolution approach

To improve the optimization method an additional usage of a multiresolution approach is advisable [213, 216]. From the binary images several levels of coarse grids are consecutively created using convolution with a Gaussian smoothing function. The smoothed image is hereby resampled to an image at a coarser scale with doubled voxelsize (see Figure 6.1. The minimization starts at the coarsest level. The result of the minimization at level n is then linearly interpolated to the grid at level $n-1$ and this result is used as a starting point at the new level. This minimization-interpolation steps are performed at each level until at the finest level, the original binary image, the final transformation $\boldsymbol{u}^*$ is determined.

6.1.4 Interpolation and Fiber Reorientation

The last step in the fiber estimation process is to transfer the fiber orientations from one geometry to the new geometry. To do this, first the mesh is transformed with the initially computed rigid $\boldsymbol{R}$ and affine $\boldsymbol{A}$ transformation with the corresponding translation $\boldsymbol{t}$ and $\boldsymbol{s}$ as

$$\boldsymbol{n} = \boldsymbol{A}(\boldsymbol{R}\tilde{\boldsymbol{n}} + \boldsymbol{t}) + \boldsymbol{s}\,, \tag{6.31}$$

where $\tilde{\boldsymbol{n}}$ are the original mesh nodes.

Then, the transformation $\tilde{\boldsymbol{u}}$ of each mesh node $\boldsymbol{n}$ is computed from the optimal transformation $\boldsymbol{u}^*$. This is done using inverse distance weighting for a certain number num of nearest voxel centers $\boldsymbol{X}_i$ for $i = 1, \ldots, num$ such as

$$\tilde{\boldsymbol{u}}(n) = \frac{1}{w} \sum_{i=1}^{num} w_i \boldsymbol{u}^*(\boldsymbol{X}_i)\,, \tag{6.32}$$

with the weight w_i of the ith neighbor defined as $w_i = \frac{1}{|\boldsymbol{n} - \boldsymbol{X}_i|^2}$ and the sum of all weights $w = \sum_{i=1}^{num} w_i$.

Additionally, the deformation gradient $\boldsymbol{F}$ is calculated at each node using the rigid $\boldsymbol{R}$ and the affine $\boldsymbol{A}$ transformation matrix and the Jacobian of the displacement field $\boldsymbol{u}^*$ as

$$\boldsymbol{F} = \boldsymbol{A}\boldsymbol{R}(\boldsymbol{I} + \nabla \boldsymbol{u}^*)\,. \tag{6.33}$$

There exist two strategies to reorient the fiber direction, the first is the finite strain (FS) method and the second is the preservation of principal directions (PPD) method [5]. The first strategy reorients the fiber direction using the rotational component $\mathcal{R}$ of the deformation gradient $\boldsymbol{F} = \mathcal{R}\mathcal{U}$, which is computed as

$$\mathcal{R} = \boldsymbol{F}(\boldsymbol{F}^T\boldsymbol{F})^{-\frac{1}{2}} \,. \tag{6.34}$$

The fiber $\boldsymbol{f}$ is then reoriented as

$$\boldsymbol{f}' = \mathcal{R}\boldsymbol{f} \,, \tag{6.35}$$

with the new fiber orientation $\boldsymbol{f}'$.

In the FS strategy only the rotation is considered for the reorientation of the fiber direction, while the shearing, stretching and non-affine deformations are not taken into account. For these reasons we use the PPD principle, where the fiber direction is reoriented using the total deformation gradient as

$$\boldsymbol{f}' = \frac{\boldsymbol{F}\boldsymbol{f}}{\mid \boldsymbol{F}\boldsymbol{f} \mid} \,. \tag{6.36}$$

When mapping not only one fiber direction but orientational information in form of a second order tensor $\boldsymbol{D}$, consisting of three directions $\boldsymbol{f}$, $\boldsymbol{n}$, and $\boldsymbol{s}$ and corresponding values λ_i defined as $\boldsymbol{D} = \lambda_1 \boldsymbol{f} \otimes \boldsymbol{f} + \lambda_2 \boldsymbol{n} \otimes \boldsymbol{n} + \lambda_3 \boldsymbol{s} \otimes \boldsymbol{s}$, the PPD strategy is more complex. The rotation matrix is defined so that the principal direction is rotated using Equation (6.36), while the second direction $\boldsymbol{n}$ is rotated so that it is perpendicular to the rotated principal direction $\boldsymbol{f}'$ and lays in the plane spanned by $\boldsymbol{f}'$ and $\boldsymbol{n}' = \frac{\boldsymbol{F}\boldsymbol{n}}{|\boldsymbol{F}\boldsymbol{n}|}$ (see [5]).

To map the fiber orientation of the deformed geometry to the new geometry again an inverse distance weighting of the mesh nodes of the geometries is used (see Equation 6.32)

$$\tilde{\boldsymbol{f}} = \frac{1}{w} \sum_{i=1}^{num} w_i \boldsymbol{f}' \,. \tag{6.37}$$

A last optional step to improve the result of the fiber orientation is to use harmonic lifting. This means, that only on the surface of the geometry the fiber orientations are registered. The surface fiber orientation of each node is then projected onto the tangential plane of this node as

$$\tilde{\boldsymbol{f}}_{\tan} = (\boldsymbol{n} \times \tilde{\boldsymbol{f}}) \times \boldsymbol{n} \,, \tag{6.38}$$

with $\boldsymbol{n}$ the normal of the node.

6.1.5 Harmonic Lifting

Harmonic lifting is performed for each of the three components of the fiber vector $\tilde{\boldsymbol{f}}_{\tan}$ [239]. Thus, solve the partial differential equations to compute the fiber field

$$\boldsymbol{g}(\boldsymbol{x}) = (g_1(\boldsymbol{x}), \ldots, g_d(\boldsymbol{x}))$$

for each component $i = 1, \ldots, d$

$$\begin{array}{rcll} \Delta \boldsymbol{g}_i(\boldsymbol{x}) & = & 0 & \text{for} \;\; \boldsymbol{x} \in \Omega \\ \boldsymbol{g}_i(\boldsymbol{x}) & = & \tilde{\boldsymbol{f}}^i_{\tan}(\boldsymbol{x}) & \text{for} \;\; \boldsymbol{x} \in \partial\Omega \,, \end{array} \tag{6.39}$$

with Ω and $\partial\Omega$ the domain and the surface of the target geometry, respectively. Afterwards, normalize the fiber directions using $\tilde{\boldsymbol{g}} = \frac{\boldsymbol{g}}{\|\boldsymbol{g}\|}$.

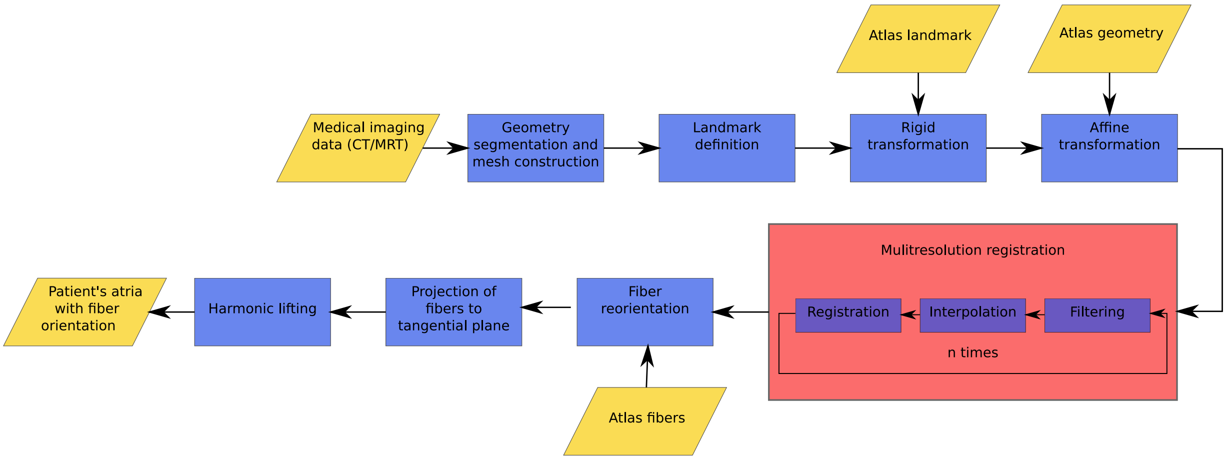

Figure 6.2: Processing pipeline for the registration and fiber estimation for the patients' atria

6.2 Methods

In this section the methods are described to generate the atlas atria and based on the theory of Section 6.1 the process of registration and fiber interpolation is explained. Additionally the electro-mechano-hemodynamical model that is used for computation is explained shortly.

Several steps are necessary for the estimation of the fiber architecture in patient's atria. Firstly, an atlas atria with a physiologically detailed fiber architecture has to be created. This is done once at the beginning and the atlas is then used for fiber estimation for all atrial geometries. For each patient the following procedure is performed, see Figure 6.2. From medical imaging data, a geometry is created, which is registered to the atlas. Then, the deformed atlas with reoriented fibers is used to generate the fibers of the patient. Finally, the fibers are realigned so that they are tangential to the surface and at last a harmonic lifting is performed.

At the end of this chapter we will also briefly describe how computations using an electro-mechano-hemodynamical model are performed with the results of the fiber generation as geometrical input.

6.2.1 Geometry Creation

To construct the geometry of a patient's atria we use segmentation, design modification and meshing tools. First, a surface representation is generated using the software Mimics (Materialise, Leuven, Belgium). For this, the lumen of both atria is segmented manually so that the endocardial surfaces are obtained. To generate the epicardial surface we extrude the endocardial surface by $2\,\mathrm{mm}$, which corresponds to an average thickness of the atrial wall [29]. Additionally, we add an interatrial muscular bridge between the right and the left atrium, the Bachmann bundle, to allow a physiological propagation of the electrical signal. Finally, we create a 3D volume mesh with tetrahedral elements with a maximal element size of $0.9\,\mathrm{mm}$ using Gmsh [129]. This leads to about two to three elements trough the atrial wall. Note that this does not pose accuracy issues in the computations, since we use higher order spatial discretizations.

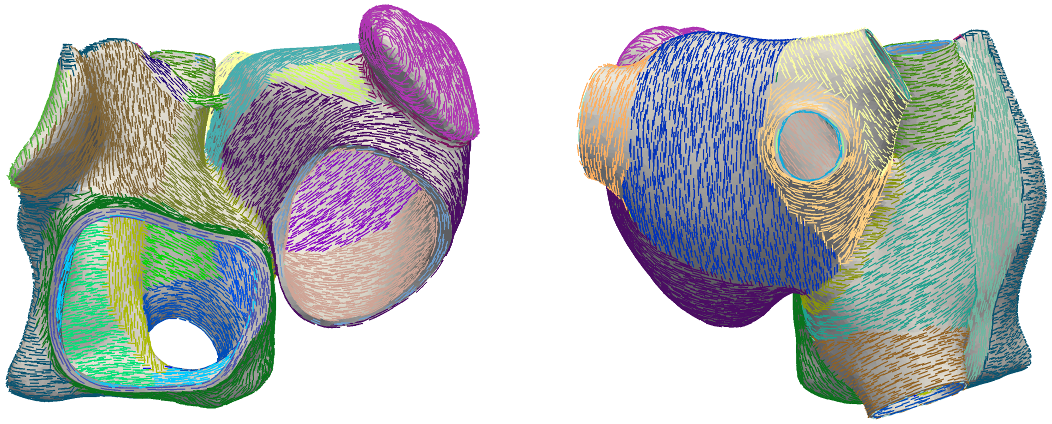

(a) Posterior view (b) Anterior view

Figure 6.3: Fiber direction of atlas atria. The colors represent the regions with different fiber directions.

6.2.2 Fiber Definition for Atlas Atria

For the atlas atria we define the fiber orientation using reported detailed knowledge of atrial fiber structure [160]. The geometry of the atlas are the atria of a 71-old individual without known cardiac pathological findings. The model was obtained from a cardiac CT image with a resolution of $0.4\,\mathrm{mm} \times 0.4\,\mathrm{mm} \times 0.8\,\mathrm{mm}$. The atlas geometry is then created identically as any other patients' atria and as has just been described in Section 6.2.1.

To define the fibers in the atlas atria we divide the epicardial and endocardial wall of the left and right atrium into regions with a constant fiber direction (see colored regions in Figure 6.3). In doing so, we manually set the main fiber bundles crista terminalis, pectinate muscles, circumferential vestibule fibers and the Bachmann bundle. Additionally, also other prominent bundles and fiber alignment in the right and left atrium are defined. In the right atrium endocardial and epicardial fiber directions coincide, i.e. the fiber bundle direction is constant throughout the whole thickness of the wall. In contrary, different fiber bundles throughout the thickness of the wall run in the left atrium at the posterior wall. To model this we assign different fiber directions on the epicardial and endocardial surface. After defining a fiber direction on each node on the surface, we interpolate the fibers into the volume using harmonic lifting techniques [239]. The atlas atria with fiber directions and the different regions can be seen in Figure 6.3.

6.2.3 Atlas Geometry Registration

The deformation of the atlas atria to the shape of the patients' atria is done in two major steps. First, an affine transformation is calculated and second the actual elastic registration process is computed. The registration process is performed in MATLAB (Release 2017a, The MathWorks, Inc., Natick, Massachusetts, United States)

6.2.3.1 Affine Transformation

For the affine transformation, 13 landmarks on the atlas and the patients' geometry are defined around the orifices of pulmonary veins and around the valvular orifices to the ventricles and the Bachmann bridge (Figure 6.4a). First, we compute a rigid motion that aligns optimally in a least square sense the two sets of landmark points using Singular Value Decomposition (see Section 6.1.1). Note that the landmarks are only used for the rigid transformation, which is needed to generally align the two geometries. Furthermore, three landmarks are sufficient for a unique rigid transformation. Second, we perform an Iterative Closest Point affine registration for the sets of all mesh points of the geometries (see Section 6.1.2). Figure 6.5a shows the atria of Patient 1 and the atlas atria after calculating and applying the rigid and the affine transformation to the atlas atria.

6.2.3.2 Registration

For the registration we use an algorithm which we already successfully used for material modeling and parameter identification of biological materials [30]. To use the registration methods for a meshed geometry it is necessary to create a 3D voxel representation of the geometry. Therefore, for each grid point we identify if it is located close to a mesh node and create a binary 3D image out of them. The walls in the binary image are slightly thicker than the original walls in the mesh. Nevertheless, this does not yield a problem, since the interpolation back to the mesh nodes after the registration is performed with a weighted nearest neighbor principle. This means that for every mesh node the final transformation is computed as a weighted mean over neighboring voxel centers (see Section 6.1.4), which allows also without pointwise correlation a good interpolation.

To match the atlas geometry to the patients geometry we create a 3D binary voxel representation of the atria with a voxel size of $0.6\,\mathrm{mm}$ (see Figure 6.4b). This is done for both the atlas atria and the patient's atria.

In Section 6.1.3 the theory of the registration is described. Applied to the atlas and the patient's atria it can be formulated as follows: We denote the image of the patient's atria by $I_p : \Omega \to \{0,1\}$ and the image of the atlas atria by $I_a : \Omega \to \{0,1\}$, where $\Omega \subset \mathbb{R}^3$ is the 3D image cube. We want to find a transformation φ such that the deformed atlas I_a is similar to the patient's atria I_p. We use the standard distance measure sum of squared differences (SSD), which is given by

$$\mathcal{D}(\boldsymbol{\varphi}) := \frac{1}{2}\int_{\Omega} (I_a(\boldsymbol{\varphi}(\boldsymbol{X})) - I_p(\boldsymbol{X}))^2 \,\mathrm{d}\mathbf{X}, \tag{6.40}$$

with $\boldsymbol{\varphi}(\boldsymbol{X}) = \boldsymbol{X} + \boldsymbol{u}(\boldsymbol{X})$ and $\boldsymbol{u}(\boldsymbol{X}) : \mathbb{R}^3 \to \mathbb{R}^3$ a spatially varying displacement field. To overcome the inherent ill-posedness of the image registration problem [118], an elastic potential as regularization $\mathcal{S}$ is added [142]. Therefore, we formulate the registration problem as: find a displacement field $\boldsymbol{u}^*$ such that

$$\boldsymbol{u}^* = \arg\min\left[\mathcal{D}(\boldsymbol{u}) + \alpha\mathcal{S}(\boldsymbol{u})\right] \tag{6.41}$$

with the regularization parameter $\alpha > 0$. We use a regularization parameter of $\alpha = 0.1$ in this work as suggested in [30]. To solve the optimization problem we use a Gauss-Newton method [142]. Additionally we use a multiresolution approach (see Section 6.1.3.1). In our case we use $n = 4$ levels of resolution.

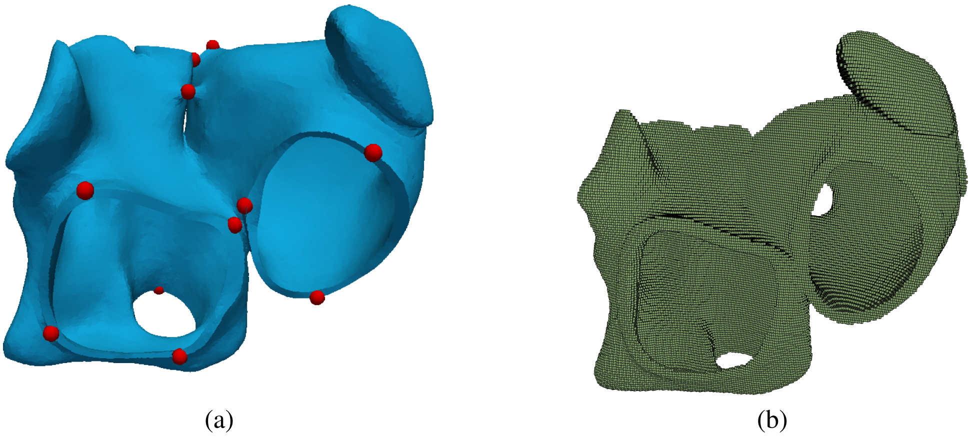
(a)
(b)

Figure 6.4: (a) The landmarks defined on the atlas atria. (b) The binary image of the atlas.

6.2.3.3 Interpolation and Atlas Fiber Reorientation

The last step in the fiber estimation process is to transfer the fibers of the atlas atria to the patient's atria (see Section 6.1.4). To do this we first calculate the transformation of each mesh node from the optimal transformation $\boldsymbol{u}^*$ of the voxels. For each mesh node the nearest voxels are determined. Using the transformation defined in these voxels, the transformation of the mesh node is computed using the inverse distance weighting average of the voxel centers. Additionally, the deformation gradient is calculated at each node using the affine transformation matrix and the Jacobian of the displacement field $\boldsymbol{u}$. To reorient the fiber directions, two strategies are possible, the finite strain strategy and the strategy of principal directions [5]. The finite strain strategy uses the rotational component of the deformation gradient to reorient the fibers. Whereas, the strategy of preservation of principal directions takes also into account the deformation component of the affine transformation. Thus, the whole deformation gradient is used for the reorientation. We use the strategy of principal direction. To map the fiber orientation of the deformed atlas atria to the patient's atria we use again an inverse distance weighting of the mesh nodes of the geometries. We map only the fiber orientation to the surface of the patient's atria. Then we project the fiber orientation to the tangential plane of the surface nodes and perform afterwards a harmonic lift step to compute the fiber orientation in the interior of the atrial wall (see Section 6.1.5). To improve readability, for now on we will use the keyword *mapped* for the fibers, which are generated on the patients' atria through registration and interpolation techniques.

6.2.4 Electro-mechanico-hemodynamical Computations

The details of the electrophysiological, mechanical and hemodynamical models are described in previous work [172]. For the electrophysiological part, we calculate the monodomain equations with the minimal cell model from [52]. The parameter set of the cell model is adapted to reproduce atrial activation and a physiological action potential curve for the atrial cell according to [212]. The diffusivity is assumed transverse isotropic with a diffusion coefficient of $\sigma_1 = 0.1\,\mathrm{mm}^2/\mathrm{ms}$ in fiber direction and a diffusion coefficient of $\sigma_2 = 0.01\,\mathrm{mm}^2/\mathrm{ms}$ perpendicular to it. To receive physiological propagation we use high-order Hybridizable Discontinuous

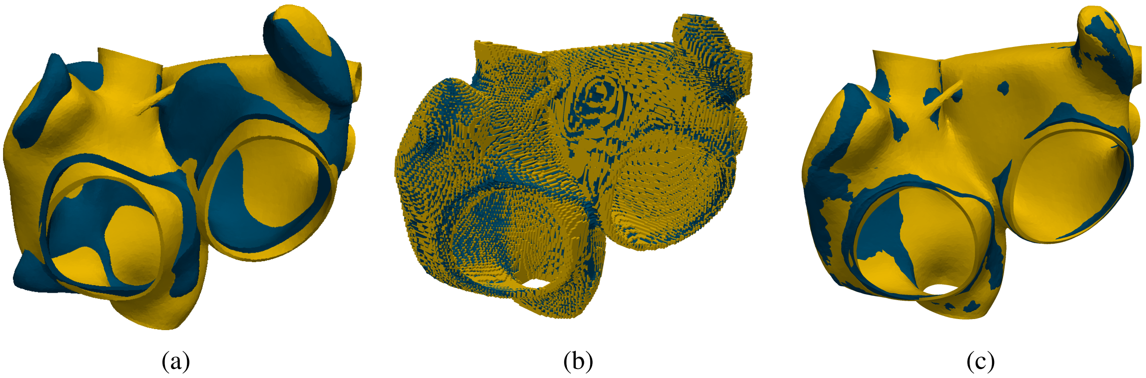
(a) (b) (c)

Figure 6.5: Atlas atria (blue) and patient's atria (yellow) at different steps of the registration process: (a) meshed geometry after affine transformation, (b) binary images after registration and (c) the meshed geometry after the registration and interpolation to the tetrahedral nodes.

Galerkin (HDG) methods [166] with a maximal order of five. For time discretization we use a semi-implicit discretization [115, 363], i.e. linear terms implicit and the non-linear parts explicit in time with at time step of $0.1\,\mathrm{ms}$.

The mechanical model is coupled to the electrical model via the elecrical signal which triggers the contraction. The model is based on nonlinear elastodynamic equations with a passive and an active part. The passive material is modelled as nearly incompressible Mooney-Rivlin material, while the active part is described by an active stress component [39, 66]. The maximal active tension is defined as $100\,\mathrm{kPa}$. The computation of the mechanical model is performed using tetrahedral quadratic continuous finite elements for space discretization and a generalized-α method for time discretization [79]. For the hemodynamical model we use a three-element Windkessel model [319], which is coupled monolithically with the elastic myocardial wall.

6.3 Results

To demonstrate the performance of our method we investigate on one hand the difference between mapped and defined fibers and on the other hand we demonstrate the functionality of our method on ten different patients' atria. We enumerate the atria of the patients by Patient 1 to Patient 10.

In the following part A, we show a comparison between mapped fibers and defined fibers. For that, we manually define for Patient 1 the fiber orientation, performing the same steps as for the atlas atria described in Section 6.2.2. Then, we first map the atlas fibers to Patient 1 and second, we map the fibers of Patient 1 to the atlas atria. Afterwards, we compare the fiber orientations, the electrophysiological activation and the mechanical contraction between the two pairs of mapped fibers and manually defined fibers.

In the second part, the fiber orientation for ten differently shaped atria are generated and the electrophysiological activation pattern and the contractions are computed.

6.3.1 Comparison of Defined and Mapped Fibers

6.3.1.1 Fibers

The results of the fiber estimation in Patient 1 and the atlas are shown in Figures 6.6 and 6.7, respectively. The mapped fibers are overall arranged in quite a similar way as the defined fibers (Figures 6.6a and 6.6b). Between the superior vena cava and the inferior vena cava the fibers in the crista terminalis are aligned longitudinally, while the pectinate muscles lay perpendicular to them. Around the vestibulum and the orifices of the veins, the fibers run in circumferential direction. Although the atlas atria has three pulmonary veins compared to four pulmonary veins of Patient 1, the mapped fibers in this area run in circumferential direction around the orifices in both cases (i.e. in case of the atlas registered to Patient 1 as well as in case of the Patient 1 registered to the atlas atria).

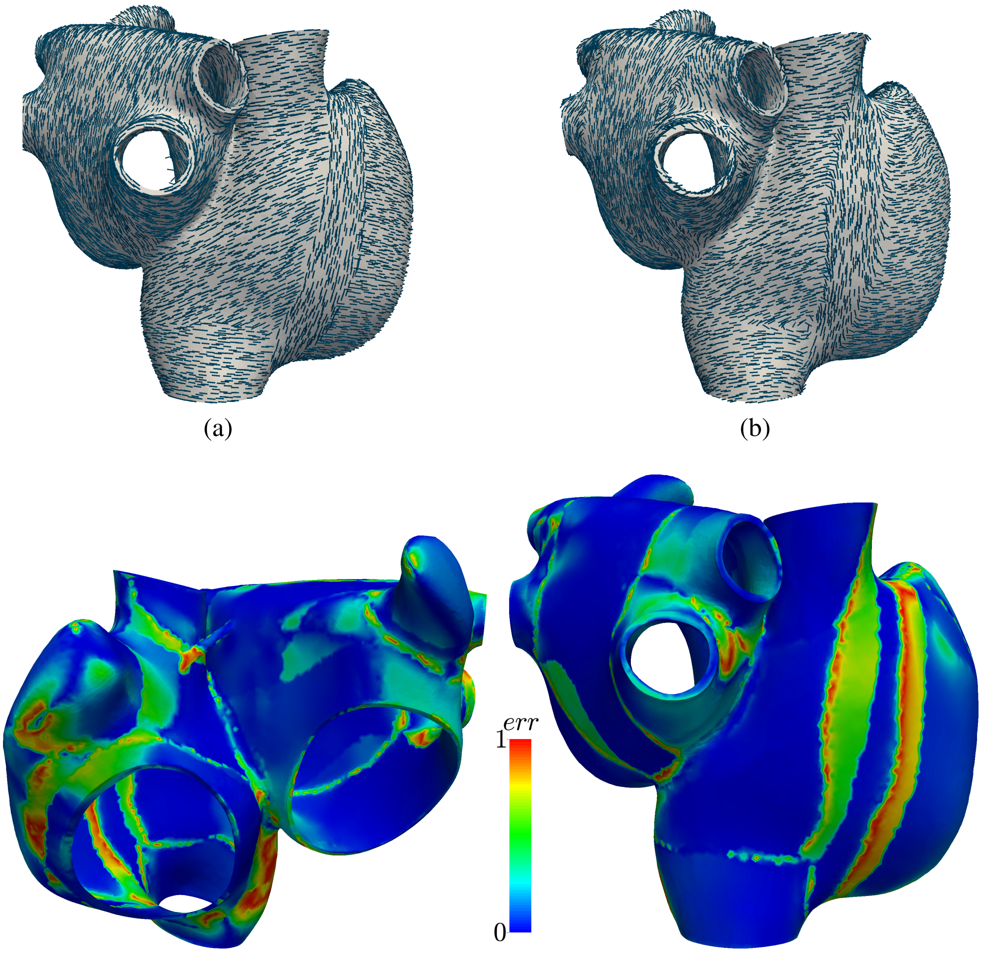

(a)

(b)

(c)

Figure 6.6: Patient 1 fibers. (a) Defined fiber orientations in Patient 1. (b) Mapped fiber orientation in Patient 1. (c) Difference in fiber direction between defined and mapped fiber orientation. The difference is calculated as $err = 1 - |f_{\text{mapped}}^{T} f_{\text{defined}}|$.

Figure 6.6c shows that the error between mapped and manually defined fibers is small in general (blue color), where larger differences are concentrated at the boundaries between different fiber bundles. For example, the fiber bundle of the crista terminalis is shifted, i.e. it runs a few millimeters further to the left in the mapped case (see Figures 6.6a and 6.6b), causing big differences in the error calculation (see Figures 6.6c, 6.7). The error is calculated as $err = 1 - |f_{\text{mapped}}^{T} f_{\text{defined}}|$. Some differences are also visible at the boarders of the circumferential fibers around the veins.

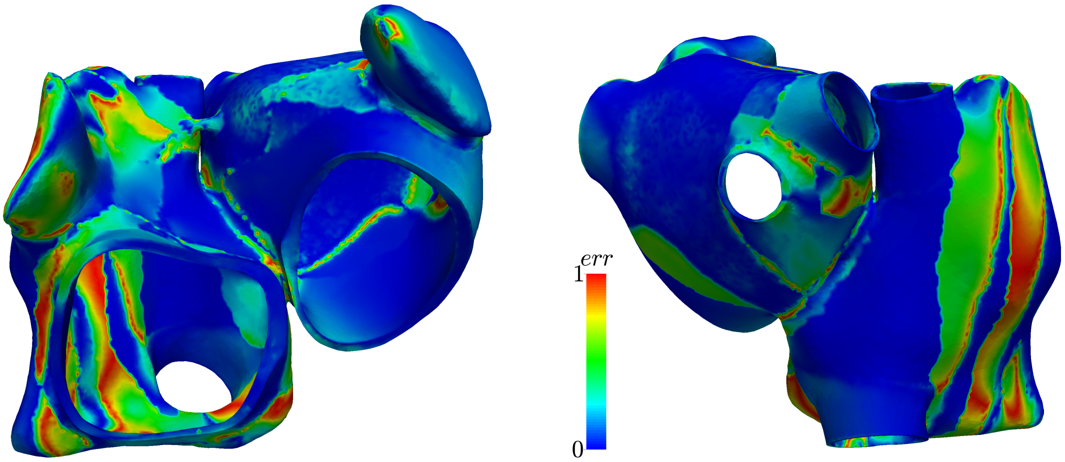

Figure 6.7: Atlas fibers. Difference in fiber direction between defined and mapped fiber orientation.

6.3.1.2 Electrophysiology

In Figure 6.8 the results of the electrophysiological simulations are shown for the atlas atria and Patient 1 atria. Here, the activation times obtained from mapped fibers and manually defined fibers are compared. The overall activation pattern is very similar for both fiber architectures: the signal travels fast along the crista terminalis, at the same spots the activation travels from the right atrium to the left atrium, and the tip of the left appendage is activated at last. Moreover, in both cases it is clearly visible that the activation of the left atrium occurs through the Bachmann bundle. Differences in the activation can be seen at the borders of the fiber bundles (compare with Figures 6.3 and 6.6), as expected due to the aforementioned differences in the fiber orientation. Characteristics in the activation pattern which appear in the atria with defined fibers also appear in the atria with fibers mapped from it. This can be seen for Patient 1, where the activation sequence is analogous to the atlas atria with defined fibers (compare Figures 6.8a and 6.8e).

The transfer of the activation characteristics from the defined to the registered atria are also visible in the activation time. The atlas atria with defined fibers and the Patient 1 atria with mapped fibers take both longer to activate than the Patient 1 atria with defined fibers and the atlas with mapped fibers (see Table 6.1). The maximal difference in activation time is for the atlas atria around $18\,\%$ and for Patient 1 $16\,\%$. In the atlas atria the region with the biggest difference is the tip of the right appendage, while for Patient 1 it is around the left appendage (see Figure 6.8). These differences are acceptable due to the fact that they appear in the appendages of the atria, which are less important for the ejection fraction (see next paragraph and Table 6.1).

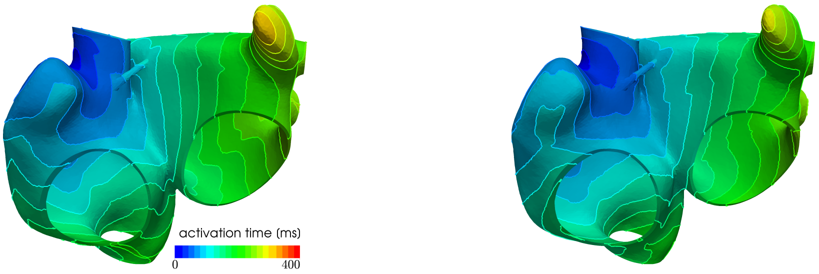

(a) Patient 1 mapped fibers (b) Patient 1 defined fibers

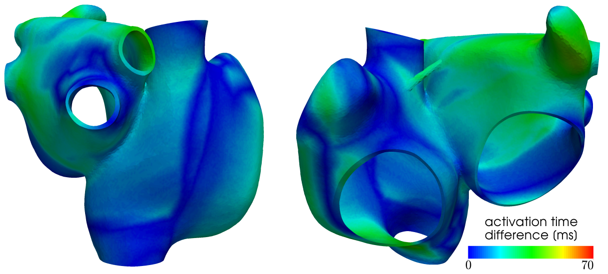

(c) Patient 1 activation time difference

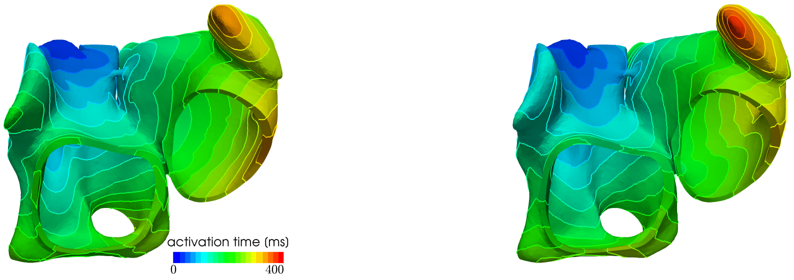

(d) Atlas mapped fibers (e) Atlas defined fibers

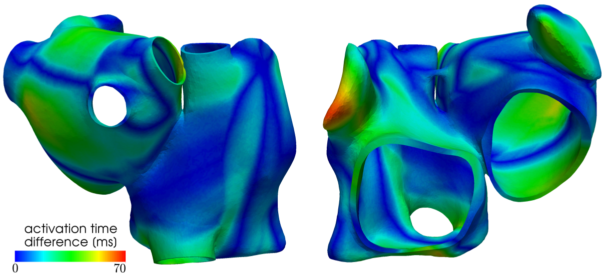

(f) Atlas activation time difference

Figure 6.8: Results of electrophysiology simulations. Activation times of Patient 1 atria and atlas atria with mapped fibers and defined fibers and activation time differences. The difference is calculated as diff $= |(\text{activation time})_{\text{mapped}} - (\text{activation time})_{\text{defined}}|$. (a) Activation time with mapped fibers for Patient 1. (b) Activation time with defined fibers for Patient 1. (c) Difference between the activation times with mapped fibers to defined fibers of Patient 1. (d) Activation time with mapped fibers for the atlas. (e) Activation time with defined fibers for the atlas. (f) Difference between the activation times with mapped fibers to defined fibers of the atlas atria.

6.3.1.3 Mechanical Contraction

The mechanical contraction is coupled with the electrophysiology via the transmembrane potential. The results of the contraction between mapped and defined fibers for the atlas atria and Patient 1 are shown in Figures 6.10-6.11. At the top of each figure the displacements are shown at the time of maximal contraction of the right and left atrium, respectively. The contour plots in the bottom of each figure show the contour of the atria at differently positioned slices through the atria. Figure 6.9 shows the position of the slices. Slice 1, visualized in Figure 6.9a, cuts the atria in the plane of the standard 4-chamber-view and Slice 2 (see Figure 6.9b) cuts the atria in a plane parallel to the heart skeleton. We analyzed also the volume curves of the left and right atrium over time until maximal contraction of each chamber (see Figure 6.12). Additionally, in Figure 6.12 also the pressures in the right and left atrium are plotted. Only small differences in the volume curves for the atlas atria with mapped and defined fibers are visible. The contraction of the atlas with defined fibers is slightly faster than the contraction of the atlas with mapped fibers due to the difference in electrical propagation speed.

To investigate the influence of the different activation we plotted the volume of actively contracting tissue, i.e. the tissue where the action potential is above a threshold, over time. In the plot the active tissue is compared for the atlas atria with defined fibers to the atlas atria with mapped fibers. Figure 6.13a shows the right atrium and Figure 6.13b left atrium. It is visible in the plot that for the right atrium slightly more tissue is active in the atrium with defined fibers than with mapped fibers at the same time. This is consistent with the faster decrease in the volume curve (see Figure 6.12a). The slight shift of the fibers of the crista terminalis on the posterior side of the right atrium (see Paragraph 6.3.1.1) in the mapped case, leads to fibers in the thickened wall of the crest not running along the crest. This is the reason for the folding near the terminal crest during contraction of the right atrium (see Figure 6.11). Especially in Figure 6.11d the folding of the terminal crest is visible. However, both mapped and defined fibers fold in the regions of fiber orientation change. Differences in the displacement of the left atrial wall of the atlas atria during contraction exist near characteristic shapes, which only exist in individual atria, for example, the pronounced buckle in the inferior wall of the right appendage and the distinctive shape of the tip of the right appendage. Since these characteristics are different and only present in individual atria, the registration process, especially the fiber interpolation, cannot map the correct fiber directions in this regions. However, they are also not known from anatomical studies. In Patient 1 we have a very smooth shaped atria. The difference in displacements during contraction is smaller between mapped and defined fibers (see Figures 6.10 and 6.11). Also the volume and pressure curves, the ejection fraction and the time of maximal contraction are similar. Only the displacement of the pulmonary veins, the caval veins and the left appendage, differ slightly. For the atlas atria and the atria of Patient 1 characteristic values of the activation and contraction are listed in Table 6.1.

6.3.2 Performance Study

In Figure 6.15 all patient's atria with mapped fibers are shown. Although, the geometry of the atria has a different shape in every patient, the registration is able to deform the atlas shape to the correct patient's shape. Additionally, the fiber architecture of the atria is well defined, i.e. every atria has the same fibers bundles which run in the same directions, for example the

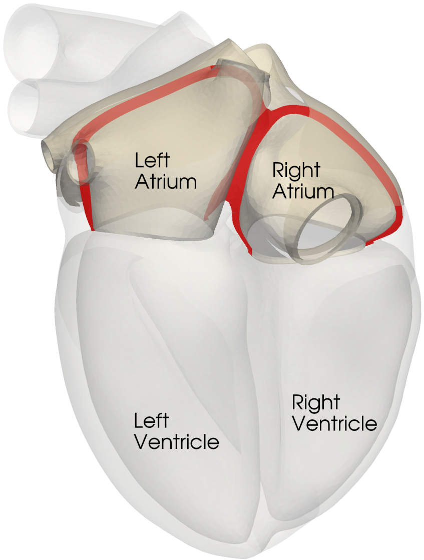

(a) Slice 1

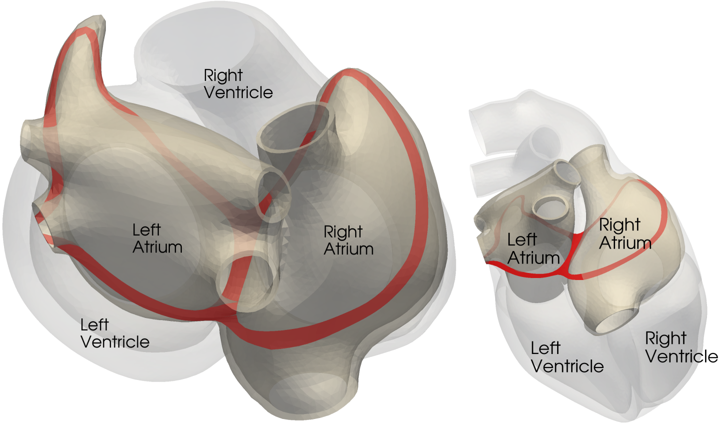

(b) Slice 2

Figure 6.9: Illustrating the slices through the atria which are used to show the contraction. (a) Slice through the atria in the plane of the 4-chamber-view. (b) Slice through the atria in a plane parallel to the heart skeleton.

crista terminalis, the pectinate muscles, the circumferential vestibule fibers etc. Unusual shapes as in Patient 9 are handled well (see Figure 6.15h). Although the geometry has a bump on the left atrium the fiber direction around it is smooth and also the pump is equipped with fibers. Patient 5, which has an additional right pulmonary vein orifice has physiological fiber orientation in the region of the pulmonary orifices (see Figure 6.15d). It is important to remark that no unphysiological fiber orientations were detected.

The results of the electrophysiological simulations are shown in Figure 6.16, where the activation patterns of all patients' atria are shown. It is visible, that the characteristics of the electrophysiological activation pattern which appear in the atlas atria also appear in the patients' atria. One example is the increased propagation speed due to circumferential vestibule fibers in

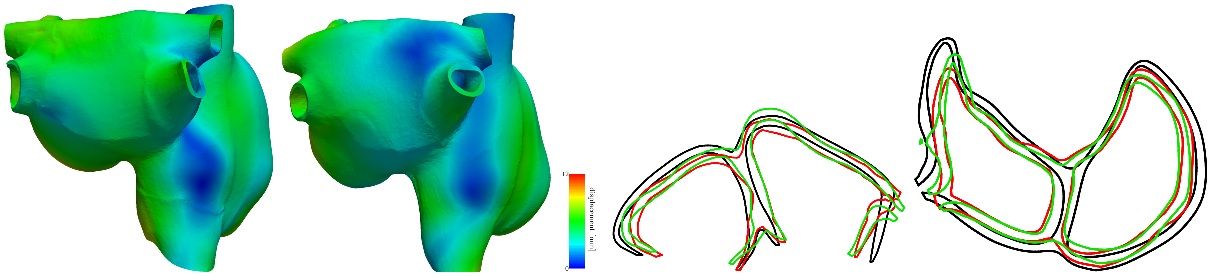

(a) Mapped fibers (b) Defined fibers (c) View 1 (d) View 2

Figure 6.10: Deformation difference between mapped and defined fibers in the atria for Patient 1 at the time of maximal contraction of the left atrium (time = $0.31\,\mathrm{s}$). (a) and (b) Displacement of the atria for mapped and defined fibers. (c) and (d) Slices through the right and left atrium in the plane shown in Figure 6.9a and Figure 6.9b, respectively. The black contour shows the atrium in the relaxed state, the green contour the contracted atria with defined fibers and the red contour line the contracted atria with mapped fibers.

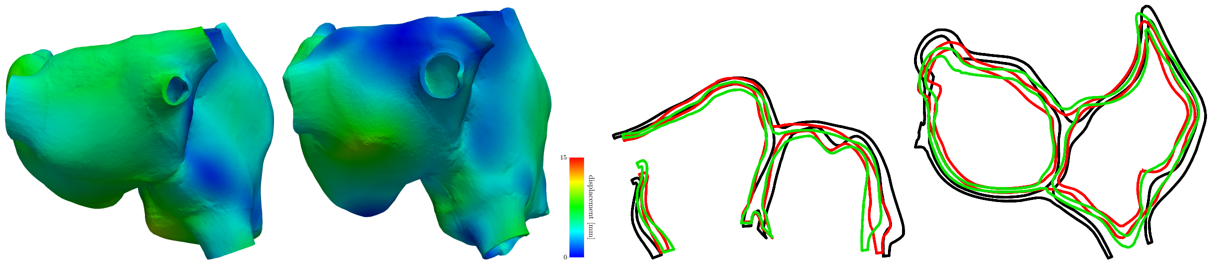

(a) Mapped fibers (b) Defined fibers (c) View 1 (d) View 2

Figure 6.11: Deformation difference between mapped and defined fibers in the atria for the atlas atria at the time of maximal contraction of the left atrium (time = $0.35\,\mathrm{s}$). (a) and (b) Displacement of the atria for mapped and defined fibers. (c) and (d) Slices through the right and left atrium in the plane shown in Figure 6.9a and Figure 6.9b, respectively. The black contour shows the atrium in the relaxed state, the green contour the contracted atria with defined fibers and the red contour line the contracted atria with mapped fibers.

the posterior wall of the left atrium. When the signal reaches the fibers around the vestibule on the posterior left atrial wall, the activation in circumferential direction around the vestibule increases, which is recognizable due to a more or less distinct triangular shape of the activation pattern in this region in each patient's atria (see Figure 6.16). The signal travels from the right atrium to the left atrium through the Bachmann bundle if the septum is small and the distance between Bachmann bundle and other interatrial connections is big (see Figures 6.16a, 6.16d, and 6.16i). In other atria, the activation through the Bachmann bundle is less important, since other interatrial connections are nearby (see e.g. Figure 6.16e, 6.16g, and 6.16h). Both scenarios are physiological [226]. The region which is activated last is the left atrial appendage. However, the overall activation time depends of course on the size and shape of the atria.

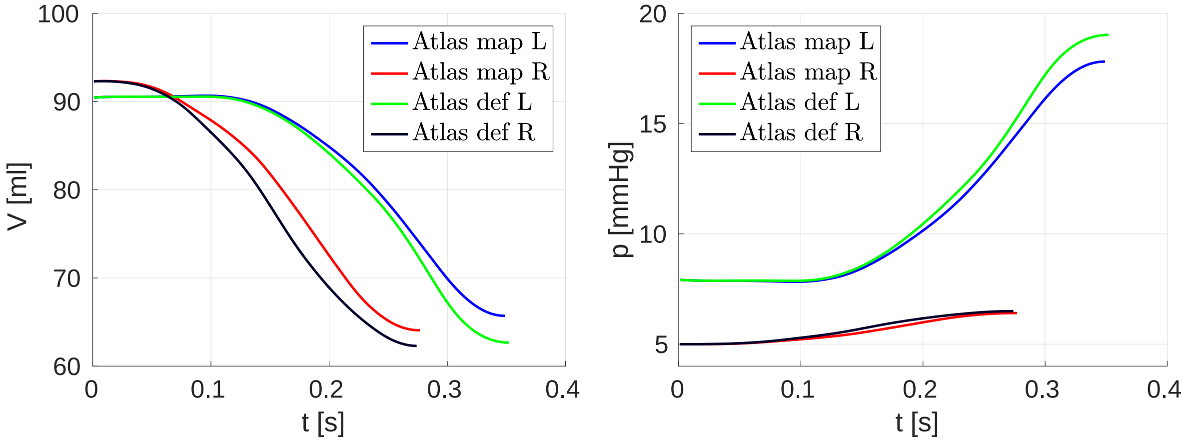

(a) Volume Atlas

(b) Pressure Atlas

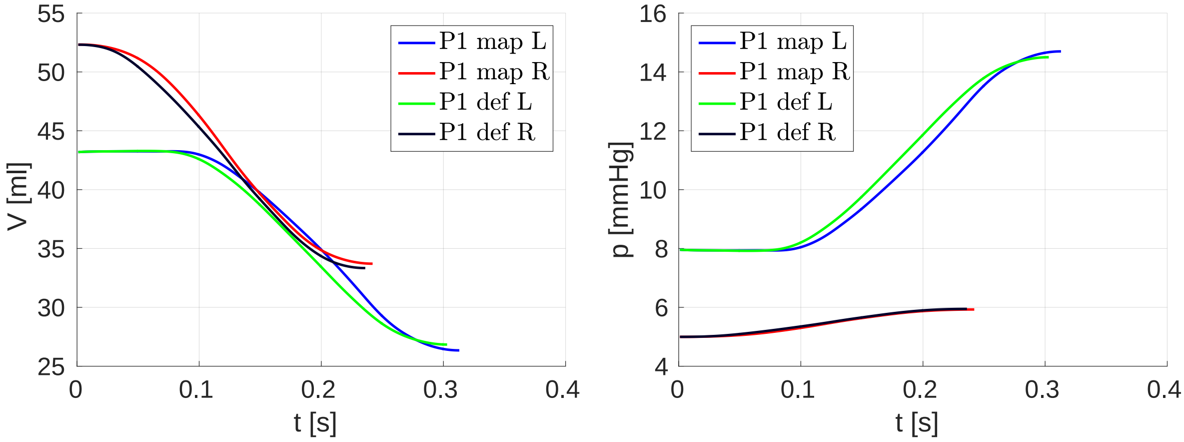

(c) Volume Patient 1

(d) Pressure Patient 1

Figure 6.12: Volume (V) and pressure (p) curves plotted over time of the right (R) and left (L) atrium of Patient 1 and the atlas geometry for mapped fibers (map) and defined fibers (def).

Figure 6.17 shows the contour lines of the atria of Patient 2-10 at end-systole. All atria perform a physiologically reasonable contraction. The volume and pressure curves until maximal contraction are plotted in Figure 6.14. Despite the differences in volume of the atria, all atria show physiological volume and pressure curves over time. The atrial geometries have been obtained from patients receiving treatment for atrial arrhythmia, thus, some of the geometries are dilated due to sustained atrial arrhythmia and atrial volume is high in some of the patients' atria (see Figure 6.14 and Table 6.2). Hence, these cases are a good test for our approach. However, our method is able to register the atria and to transfer the fiber orientations although the volume of atlas and patient's atria varies significantly. Additionally, also with such dilated geometry, mechanical contraction can be computed without problems. The ejected volume increases slightly with increasing atrial volume, but the ejection fraction decreases in dilated atria due to a high initial volume (see Table 6.2).

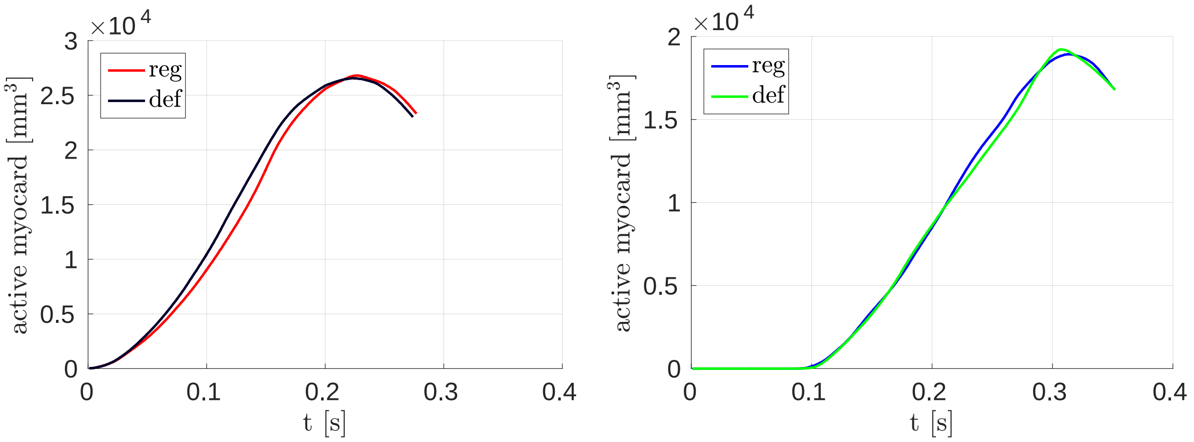

(a) Right Atrium (b) Left Atrium

Figure 6.13: Volume of active contracting tissue over time for the atlas atria with defined and mapped fibers

Table 6.1: Summary of electrophysiology and contraction outputs for defined and mapped fiber orientations in atlas and Patient 1 geometries.

	Activation Time [s]	Start Activation [s]	Max/Min Volume [ml]	EF [%]	Max Pressure [mmHg]	Time Min. Volume [s]
Left						
Atlas map.	0.338	0.098	90.2 / 65.7	27.6	17.8	0.349
Atlas def.	0.376	0.090	90.2 / 62.7	30.9	19.0	0.352
Patient 1 map.	0.317	0.076	43.1 / 26.3	39.5	14.7	0.313
Patient 1 def.	0.288	0.062	43.1 / 26.8	38.3	14.5	0.303
Right						
Atlas map.	0.262	0	92.2 / 64.1	31.0	6.4	0.277
Atlas def.	0.277	0	92.2 / 62.3	33.2	6.5	0.274
Patient 1 map.	0.212	0	52.3 / 33.7	36.0	5.9	0.242
Patient 1 def.	0.212	0	52.3 / 33.3	36.7	5.9	0.236

6.4 Discussion

The proposed approach is able to register differently shaped atria to each other and to create physiological reasonable fiber architecture for patient-specific geometries. We show this using ten different human atria with various shapes. Geometric differences in the shape of the atria, as for example the number of pulmonary veins, are handled well. The fibers can be reoriented

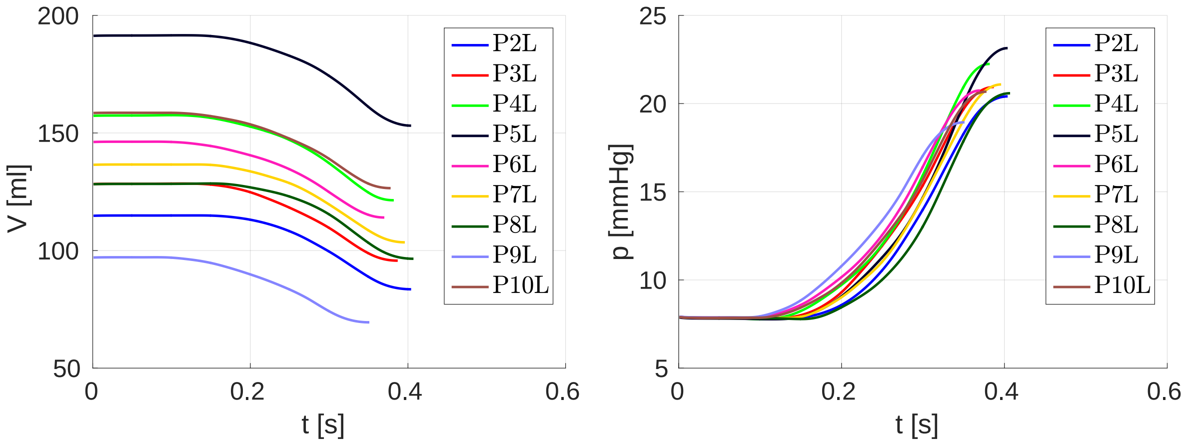

(a) Volume Left Atrium

(b) Pressure Left Atrium

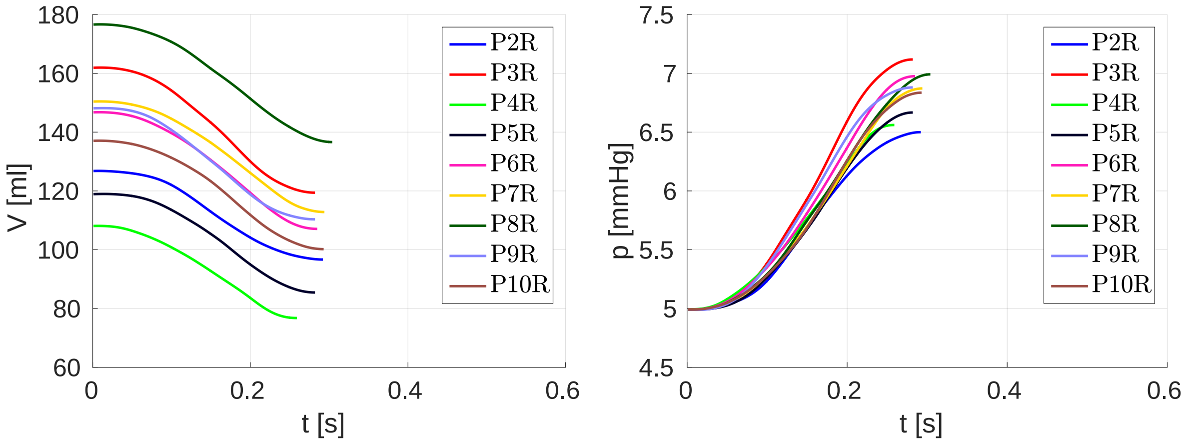

(c) Volume Right Atrium

(d) Pressure Right Atrium

Figure 6.14: Volume (V) and pressure (p) curves plotted over time of the right (R) and left (L) atrium for Patient 2-10.

according to the deformation calculated in the registration process and applied to the patient's atria.

The activation sequence in the patient's atria is similar to the sequence in the atlas atria, thus, it is very important to have an exact fiber definition in the atlas atria.

Using the proposed pipeline to define the fiber orientation on the atria, an exact atlas atria is needed. As the shape of the atria in patients varies very much, an atlas atria should be used which itself is similar to the patient's atria. Although, the method was able to handle a varying number of pulmonary veins, for a better accuracy of the fiber definition at the pulmonary orifices it is suggested to use an atlas with the common number of pulmonary orifices. As for atrial arrhythmia simulations the pulmonary veins play an important role, it could be more convenient to use different atlases with the appropriate number of pulmonary orifices.

Small differences in fiber orientation lead to small differences in the electrical activation pattern. However, the mechanical contraction showed to be more sensitive to the fiber orientation. Individual shapes of the atria, for example additional bulges, cause the registration to deform the

Table 6.2: Maximal and minimal volume and ejection fraction for Patient 2-10

	Left		Right	
	Max/Min Volume [ml]	EF [%]	Max/Min Volume [ml]	EF [%]
Patient 2	114.6 / 83.5	27.4	126.6 / 96.7	24.2
Patient 3	128.0 / 95.7	25.6	161.7 / 119.4	26.5
Patient 4	157.0 / 121.4	23.0	108.0 / 76.8	29.4
Patient 5	191.0 / 153.1	20.1	118.8 / 85.4	28.5
Patient 6	145.9 / 114.0	22.1	146.6 / 107.1	27.4
Patient 7	136.2 / 103.5	24.2	150.2 / 112.8	25.6
Patient 8	128.0 / 96.5	24.9	176.4 / 136.6	23.2
Patient 9	96.8 / 69.5	28.8	147.9 / 110.3	25.9
Patient 10	158.2 / 126.5	20.4	136.9 / 100.2	27.4

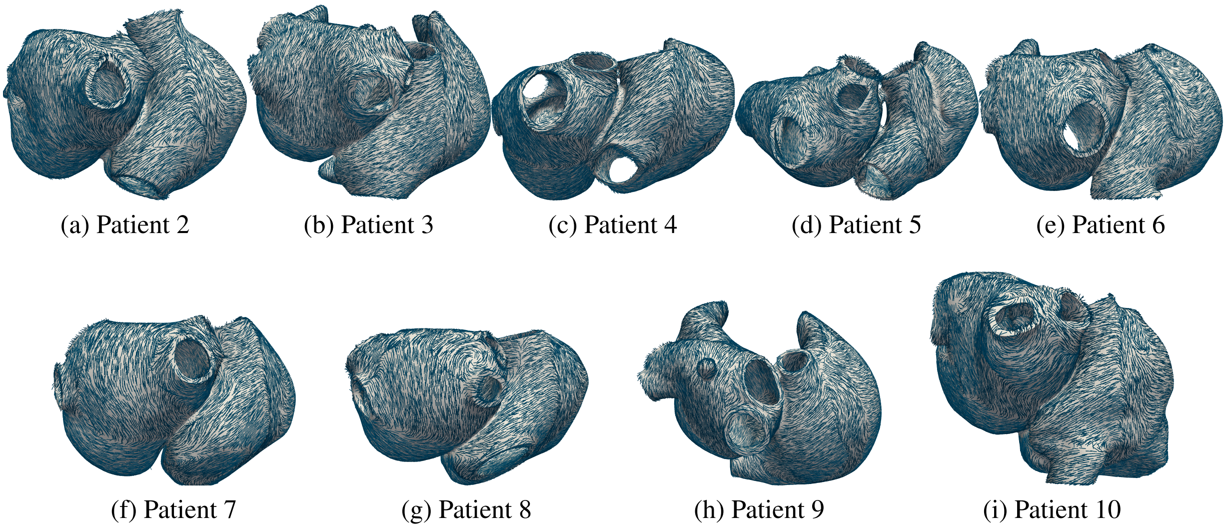
(a) Patient 2 (b) Patient 3 (c) Patient 4 (d) Patient 5 (e) Patient 6

(f) Patient 7 (g) Patient 8 (h) Patient 9 (i) Patient 10

Figure 6.15: Mapped fiber orientation for Patient 2-10.

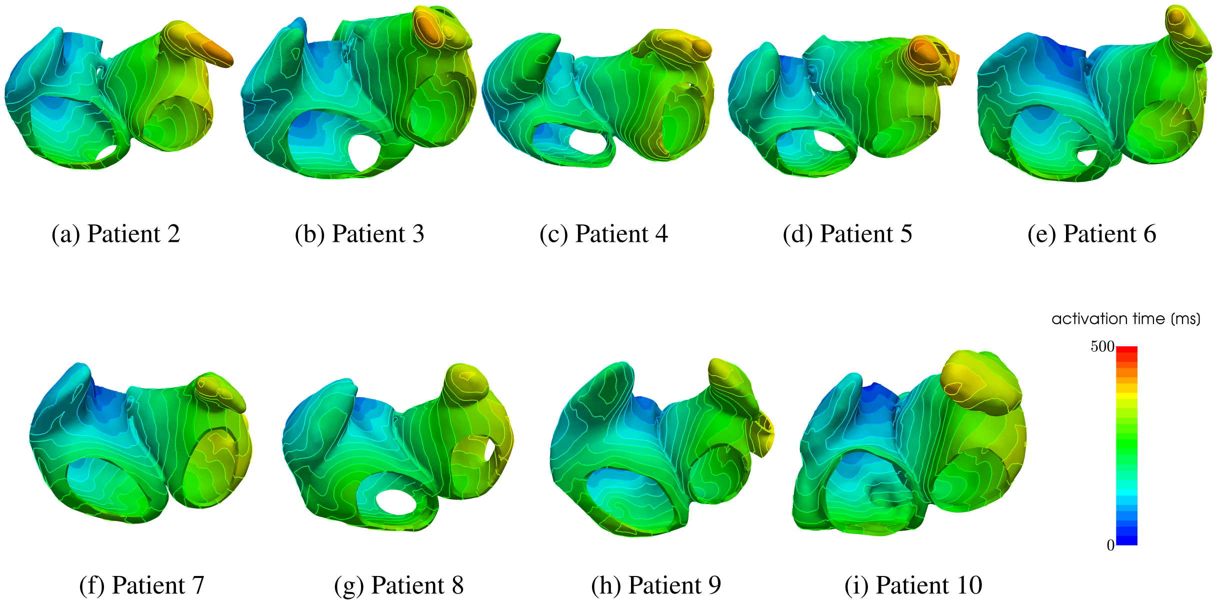

(a) Patient 2 (b) Patient 3 (c) Patient 4 (d) Patient 5 (e) Patient 6

(f) Patient 7 (g) Patient 8 (h) Patient 9 (i) Patient 10

Figure 6.16: Activation times for the patients' atria Patient 2 to Patient 10 with mapped fiber orientation.

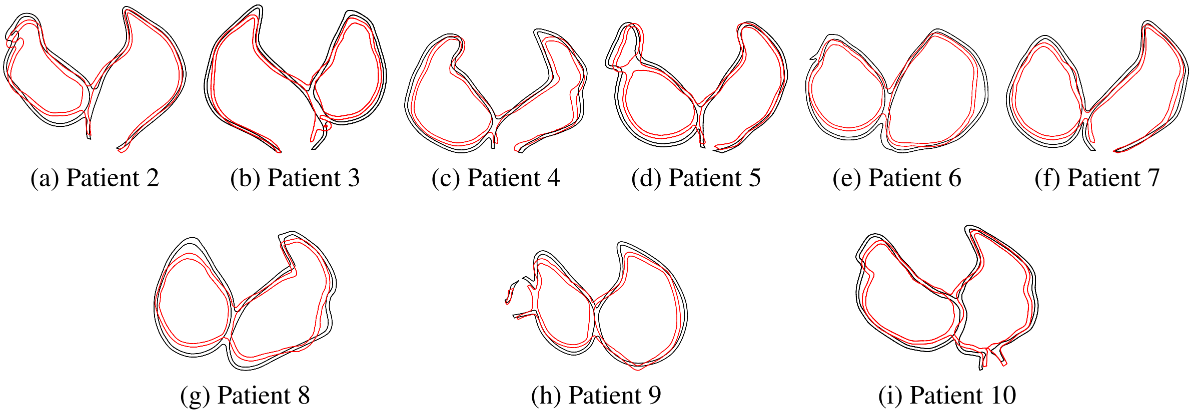

(a) Patient 2 (b) Patient 3 (c) Patient 4 (d) Patient 5 (e) Patient 6 (f) Patient 7

(g) Patient 8 (h) Patient 9 (i) Patient 10

Figure 6.17: Displacements at maximal contraction of the left ventricle for Patient 2-10 in the 2-chamber-view. The black contour shows the relaxed atria and red contour shows the contracted atria.

atlas atria more to match the individual patient atria, which in turn could lead to strongly varying fiber orientation in the bulges. However, since it is not possible to visualize the fiber orientation in-vivo in the atria, it is not measurable what is the correct fiber definition in these bulges and which appear only in single individuals. Our registration algorithm is able to define fiber orientation everywhere in the atria, i.e. also in bulges. However, to improve the performance of the registration and fiber reorientation, different atlas atria could be used for different shaped atria, for example from ex-vivo DTMRI [278]. With a similarity measurement between the atlas atria and the patients' atria, for instance the size of the deformation map of the registration, one could find the most similar atlas to be used along with the proposed approach, which would then lead to the most physiological results regarding the fiber orientation and, thus, the activation and contraction.

6.5 Closure

A local fiber definition is important for patient-specific electrophysiological and mechanical modeling of the atria. We presented a method to automatically define the fiber orientation on arbitrarily shaped atria. To do so we use a single pair of atlas atria with a detailed predefined fiber orientation. Using image registration techniques and reorientation methods we are able to map the fibers to different atria, even if the shape of the atria differ significantly. The method needs as input only the segmented geometry together with a few landmarks and does not require additional user interaction. Our method is thus very convenient, especially if a study with many individual atria is carried out. We compared the result of the fiber mapping with manually defined fibers. The same fiber bundles were visible in defined and mapped atria and the performed electrophysiology and contraction simulation showed similar results for defined and mapped fibers. Using our registration method for fiber mapping to patients' atria, the activation pattern of the patients showed the same characteristics as the atlas. Thus, with a detailed atlas we have the same activation properties also in patient's atria. We demonstrated the good performance of our method with ten different human atria. Different shapes of the atria are handled very well during the registration process. The electrophysiological, contraction and hemodynamical simulation with atria with mapped fibers showed physiologically reasonable results in terms of activation pattern, spatial contraction, volume and pressure curves, and ejection fraction.

Acknowledgment

This chapter contains the results already published in [168] and reprinted here by permission from John Wiley and Sons: John Wiley and Sons, International Journal of Numerical Methods in Biomedical Engineering, Automatic mapping of atrial fiber orientations for patient-specific modeling of cardiac electromechanics using image registration. Julia M. Hoermann, Martin R. Pfaller, Linda Avena, et al., Copyright © 2019 John Wiley & Sons, Ltd. (2019)

7 Summary and Outlook

7.1 Summary

Cardiac simulations are becoming an important tool for understanding, diagnosis and clinical treatment of heart diseases. Thus, the goal was to develop and improve a framework to simulate the (patho-) physiological function of the heart.

Therefore, a framework was developed that can be used for cardiac simulations to evaluate electrical, mechanical and hemodynamical performance of the cardiac system for healthy and pathological cases. This model can be used to investigate different treatment options. To show the functionality of the model, the focus was laid on the atria and cardiac performance for different treatment options for atrial fibrillation, since atrial fibrillation is the most common cardiac arrhythmia and morbidity statistics reveal an increasing incidence.

First, a coupled electro-mechano-hemodynamical model to study cardiac performance was developed. In a study on different treatment options for atrial fibrillation, it was shown that with the model it is possible to evaluate and compare different ablation strategies under the aspect of electrical propagation, contracting performance and hemodynamic response. For a patient undergoing atrial ablation the model can be used beforehand to validate the different treatment options. Using the simulation techniques, all ablation strategies can be tested before surgical intervention utilizing the individual patient-specific shape of the atrial geometry. With the coupled model it is possible to first investigate the electrical propagation pattern, that varies depending on the ablation lines, together with the overall activation time. Second, it is possible to simulate the contraction, which is triggered by the electrical signal, to compute the mechanical performance, the ejection fraction but also the intraatrial volume over time. With the simulations it was shown that the volume curve over time is strongly depending on the activation pattern, and thus, the ablation process. Improper ablation lines lead to a slowdown of the cardiac output and a decrease of ejection fraction. Third, the hemodynamical model which is coupled to the structural deformation of the heart muscle provides additional details about the pressure development. Thus, with the model it is possible to supply the medical doctors with additional information, and hence, help to decide for the best treatment option. Additionally, standard ablation concepts on different patients in the study were investigated, where a strong correlation between inactive tissue and ejection fraction was verified. Also a tendency of one ablation line to be the worst in terms of electrical propagation duration and ejection fraction was shown.

To make cardiac computations more valuable for clinical application it is necessary to improve them in terms of efficiency, i.e. to reduce computational time and cost without loss of accuracy. Electrophysiology simulation, which are numerically challenging due to the propagation of a steep electrochemical wave front, require very fine spatial discretizations. Therefore, in this thesis the usage of an adaptive high-order Hybridizable Discontinuous Galerkin method for an efficient computation of cardiac electrical propagation was presented. The advantage of a discontinuous function space is the straight-forward implementation of high-order discretizations, which can be defined either globally for the whole domain or locally in a region of interest. Additionally, the Hybridizable Discontinuous Galerkin method allows a reduction of the degrees of freedom by static condensation on element level to those defined on the faces, compared to the standard Discontinuous Galerkin method. To investigate the performance of the Hybridizable Discontinuous Galerkin method it was compared against the Continuous Galerkin method. Thus, a similar performance for low-order elements, but an increase in efficiency for high-order elements for the Hybridizable Discontinuous Galerkin method was shown. However, when using high-order elements one faces additional problems came up regarding the ionic current term. Therefore, a method to solve the ionic current integral with a suitable accuracy depending on the polynomial order was proposed. The electrophysiology simulation is determined by the steep wave front, and thus, in this thesis it was shown that high-order elements are only necessary around the wave front. The same results can be achieved with a global high-order computation as with a local time varying increase of the polynomial degree around the wave front. Therefore, in this thesis a method to accurately track the wave front and adapt the polynomial degree accordingly was presented. Adaptive high-order elements allow a reduction of the number of degrees of freedom, which is very important for cardiac simulations including a whole heartbeat. This was shown with a coupled electro-mechanical simulation considering a real human biventricular geometry.

To improve cardiac simulation for clinical purpose, the patient-specific aspect needs to be taken into account. An individual patient-specific geometry of the heart muscle can be extracted from medical imaging devices. However, until now reliably in-vivo visualization of the patient's fiber orientations are not possible in human atria. Consequently, a physiological fiber definition is essential for correct electrophysiology and contraction simulations. Therefore, in this thesis a method to define fiber orientation on arbitrarily shaped atria was presented. With this method it is possible to generate detailed fiber families in every new patient-specific geometry in an automated, time-efficient process. The method is based on image registration and reorientation methods and needs for input an atlas atria with fibers predefined from detailed histological observations together with a few landmarks, as well. It was shown in this thesis that the framework is able to map the fibers to different atria, even if the shape of the atria differ significantly. Computed electrophysiological, contraction and hemodynamical simulations based on this framework showed physiological results. In a comparison between defined and mapped fibers, it was shown that the same fiber bundles were visible and that the results of electrophysiology and contraction simulation were quite well comparable. Thus, the automated, time and effort-saving framework to define fiber orientation is very convenient.

To conclude, in this thesis a framework to compute electro-mechano-hemodynamical simulations was developed, with the main focus on atria. Additionally, a method to improve electrophysiology simulation due to the usage of p-adaptive high-order elements based on the Hybridizable Discontinuous Galerkin method was proposed. Finally, a method to define fiber orientation on arbitrarily shaped atria in an automated time-efficient process was developed. Using all the presented components, it is possible to perform a study with many individual atria by computing the atrial performance in an accurate and automated way.

7.2 Outlook

In this thesis a model to compute electro-mechano-hemodynamical simulations in the atria with mapped fiber definition and accurate computation of the electrophysiology was presented. With such a model performance of various atria can be computed and investigated, for example with respect to different clinical treatment options. However, in this thesis pathophysiology were only taken into account in a limited way. When computing the mechanical performance of atria under standard ablation concepts, healthy conduction velocity and reduced ones were tested. Long-lasting fibrillation may lead to changes in the electrical properties, which could influence the outcome of the ablation surgery. Different studies have investigated the influence of ablation lines on the termination and non-termination of atrial fibrillation and to find the best possible treatment [92, 295, 302–304, 336, 356]. However, none of them investigated the effect of atrial fibrillation on the mechanical contraction performance. A study investigating also the contraction was performed from Adeniran et al. [2], which did not take into account the hemodynamic feedback. A future step is to determine the impact of atrial fibrillation on electro-mechanical performance for different ablation lines, including perfect and incomplete ablation lines. In this thesis, also incomplete ablation lines were investigated, however, without electrical remodeling of the myocytes. Incomplete ablation lines can be a source of atrial fibrillation recurrence, which was tested in [58, 92, 295, 302, 303] with electrophysiological models.

The process of atrial fibrillation occurrence and formation is not fully understood until now and many questions remain to answer [244]. Arrhythmia leads to electrical and mechanical remodeling of myocytes and tissue, which itself promotes arrhythmia [7, 56, 376]. Single cell remodeling, which includes alternations in ion channel properties, needs to be included into tissue models, where on the other hand structural remodeling takes place, which consists of integration of fibrosis into atrial tissue. Computational models of electrical and mechanical remodeling can help to understand the process and to improve clinical treatment.

Although, atrial fibrillation is the most common cardiac arrhythmia, other cardiac diseases exist, which are worth simulating. Arrhythmia can occur also in the ventricle, which leads to death if untreated [182]. Additionally, structural remodeling in the ventricle, which could lead to heart failure, is an interesting aspect to model. Structural remodeling in the ventricle can occur after myocardial infarction, pressure or volume overload and myocarditis [85]. Computer simulations of cardiac remodeling could predict structural remodeling and help patients to receive optimal treatment. Cardiac resynchronization therapy is an established therapy to treat heart failure. However, the non-responder rate is high , and thus, an identification of patients that are promising for a successful treatment, is necessary [22, 93, 289]. This is precisely the point where computer simulations can help to improve the performance of the therapy. Simulation can be used to predict the outcome of the treatment, optimize the placement of the pacing lead and identify non-responders.

For investigating the mechanical contraction and the ejection fraction of the heart muscle a lumped model for the blood flow is sufficient. However, to examine blood flow and to study the effect of cardiovascular diseases regarding blood movement a full model of the fluid is necessary. An interesting aspect when investigating blood flow and pathological processes are thrombus formations. Thrombosis is a vascular disease where blood clots that could occlude the blood vessel, are formed inside the vessels. Thrombosis could lead to myocardial infarction and stroke and thus is a serious disease [125]. Atrial fibrillation is a leading cause of thromboembolic cerebral insults, since in patients with atrial fibrillation it is common that left atrial thrombus formation occurs [148, 328]. A study suggesting that the shape of the left atrial appendage might influence the formation of a thrombus during atrial fibrillation can be found in [374]. First computational fluid dynamics simulations investigating the blood flow in the atrial appendage used previously estimated motion of the atrial wall from medical images [273]. Fluid-structure interaction, where the contraction of the atrial wall is triggered by the electrical stimulation, which is computed with an electrophysiology model, is the next step. With this model different arrhythmia settings can be tested and compared with respect to blood flow and thrombus formation and also the influence of ablation lines on the blood dynamics can be analyzed.

The computational model, which was developed in this thesis incorporates the state of the art understanding about cardiac function and behavior. However, experimental work and new studies need to be carried out to increase the knowledge. This knowledge needs to be included into the computational model. For example, experiments on the material behavior of cardiac muscular tissue at different locations, e.g. left ventricle, right ventricle, atria, etc., and with fibrotic and remodeled tissue, can improve the material model used in the simulation. Additionally, increased knowledge about the pericardium and the pericardial sac would facilitate the understanding of the bearing of the heart, which would be necessary to improve the boundary condition in the computational model. Hence, computational modeling and experimental work have to go hand in hand, influencing each other to provide a thorough understanding of the heart and its pathologies.

To improve the computational model not only general experiments are necessary, but also an adaption of the model to take into account patient-specific requirements. The patient-specific aspect is of highest priority, when considering the usage of the computational model to compare treatment options. Throughout this thesis already individual patient-specific geometries of the patient's hearts were used. However accurate segmentation of the atrial geometry was done thoroughout this thesis with major human involvement. Using more automated methods which reduce user-workload but still can get accurate results for complex atrial geometries with decent human interaction can be used to improve efficiency for the model generation as described in [152]. With more detailed imaging devices in future also the information about patient-specific fiber alignment could be incorporated into the model. Additionally, location of scar and fibrotic tissue in remodeled and diseased hearts could be identified with contrast-enhanced cardiac magnetic resonance imaging [9]. Furthermore, using aspects of image-based modeling can create a better foundation for the computational model. Thus, images of different medical image modalities at different stages, e.g. before, during and after the ablation, provide additional information, which could be used first to validate the model and later to improve the personalization of the model [231, 232]. Including this information into the model would increase the accuracy of the model, in particular when modeling arrhythmia and contraction. Of course, in addition an accurate material model of the fibrotic tissue is necessary or a homogenized model for the fibrosis included uniformly between myocardial cells. During clinical examinations and surgical treatment many patient data is created, for example blood pressures, electrical activity using electrocardiography, etc. Using inverse analysis and the measured values the model parameter can be adapted accordingly to create a patient-specific model.

Experiments and clinical measurements can not only improve the model and adapt it to the patient, but also be used for validation. Validation is a mandatory requirement for a model that is to be used for clinical diagnosis. Since a comprehensive validation of the computational model is not possible, single steps towards this goal have to be made. These steps include verification of the numerical model, parameter identification, sensitivity analysis and validation against experiments [354].

Bibliography

[1] G. Adam, P. Läuger, and G. Stark. *Physikalische Chemie Und Biophysik*. Springer-Lehrbuch. Springer Berlin Heidelberg, Berlin, Heidelberg, 2009.

[2] I. Adeniran, D. H. MacIver, C. J. Garratt, J. Ye, J. C. Hancox, and H. Zhang. Effects of Persistent Atrial Fibrillation-Induced Electrical Remodeling on Atrial Electro-Mechanics – Insights from a 3D Model of the Human Atria. *PLOS ONE*, 10(11), Nov. 2015.

[3] N. M. Al-Saady, O. A. Obel, and A. J. Camm. Left atrial appendage: Structure, function, and role in thromboembolism. *Heart*, 82(5):547–554, Nov. 1999.

[4] B. Alberts, A. Johnson, J. Lewis, D. Morgan, M. Raff, K. Roberts, and P. Walter. *Molekularbiologie der Zelle*. Wiley-VCH Verlag GmbH & Co. KGaA, Weinheim, 6 edition, Apr. 2017.

[5] D. C. Alexander, C. Pierpaoli, P. J. Basser, and J. C. Gee. Spatial transformations of diffusion tensor magnetic resonance images. *IEEE Transactions on Medical Imaging*, 20(11):1131–1139, Nov. 2001.

[6] T. Alhogbani, O. Strohm, and M. G. Friedrich. Evaluation of left atrial contraction contribution to left ventricular filling using cardiovascular magnetic resonance. *Journal of Magnetic Resonance Imaging*, 37(4):860–864, Apr. 2013.

[7] M. Allessie, J. Ausma, and U. Schotten. Electrical, contractile and structural remodeling during atrial fibrillation. *Cardiovascular Research*, 54(2):230–246, May 2002.

[8] H. Altenbach. *Kontinuumsmechanik*. Springer Berlin Heidelberg, Berlin, Heidelberg, 2012.

[9] B. Ambale-Venkatesh and J. a. A. C. Lima. Cardiac MRI: A central prognostic tool in myocardial fibrosis. *Nature Reviews Cardiology*, 12(1):18–29, Oct. 2014.

[10] A. Ames and W. G. Stevenson. Catheter Ablation of Atrial Fibrillation. *Circulation*, 113(13):e666–e668, Apr. 2006.

[11] R. H. Anderson, M. R. Boyett, H. Dobrzynski, and A. F. M. Moorman. The Anatomy of the Conduction System: Implications for the Clinical Cardiologist. *Journal of Cardiovascular Translational Research*, 6(2):187–196, Apr. 2013.

[12] R. H. Anderson and A. C. Cook. The structure and components of the atrial chambers. *EP Europace*, 9(suppl_6):vi3–vi9, Nov. 2007.

[13] R. H. Anderson, J. Yanni, M. R. Boyett, N. J. Chandler, and H. Dobrzynski. The anatomy of the cardiac conduction system. *Clinical Anatomy*, 22(1):99–113, Jan. 2009.

[14] A. Ansari, S. Yen Ho, and R. H. Anderson. Distribution of the Purkinje fibres in the sheep heart. *The Anatomical Record*, 254(1):92–97, Jan. 1999.

[15] T. Arentz, R. Weber, G. Bürkle, C. Herrera, T. Blum, J. Stockinger, J. Minners, F. J. Neumann, and D. Kalusche. Small or Large Isolation Areas Around the Pulmonary Veins for the Treatment of Atrial Fibrillation? Results From a Prospective Randomized Study. *Circulation*, 115(24):3057–3063, June 2007.

[16] C. J. Arthurs, M. J. Bishop, and D. Kay. Efficient simulation of cardiac electrical propagation using high order finite elements. *Journal of Computational Physics*, 231(10):3946–3962, May 2012.

[17] C. J. Arthurs, M. J. Bishop, and D. Kay. Efficient simulation of cardiac electrical propagation using high-order finite elements II: Adaptive p-version. *Journal of Computational Physics*, 253:443–470, Nov. 2013.

[18] K. S. Arun, T. S. Huang, and S. D. Blostein. Least-Squares Fitting of Two 3-D Point Sets. *IEEE Transactions on Pattern Analysis and Machine Intelligence*, PAMI-9(5):698–700, Sept. 1987.

[19] O. V. Aslanidi, M. A. Colman, J. Stott, H. Dobrzynski, M. R. Boyett, A. V. Holden, and H. Zhang. 3D virtual human atria: A computational platform for studying clinical atrial fibrillation. *Progress in biophysics and molecular biology*, 107(1):156–168, Oct. 2011.

[20] P. Atkins and J. de Paula. *Atkins' Physical Chemistry*. W. H. Freeman, New York, 8th edition edition, Mar. 2006.

[21] A. Atkinson, S. Inada, J. Li, J. O. Tellez, J. Yanni, R. Sleiman, E. A. Allah, R. H. Anderson, H. Zhang, M. R. Boyett, and H. Dobrzynski. Anatomical and molecular mapping of the left and right ventricular His–Purkinje conduction networks. *Journal of Molecular and Cellular Cardiology*, 51(5):689–701, Nov. 2011.

[22] A. Auricchio and F. W. Prinzen. Non-Responders to Cardiac Resynchronization Therapy. *Circulation Journal*, 75(3):521–527, 2011.

[23] A. Baher, Z. Qu, A. Hayatdavoudi, S. T. Lamp, M.-J. Yang, F. Xie, S. Turner, A. Garfinkel, and J. N. Weiss. Short-term cardiac memory and mother rotor fibrillation. *American Journal of Physiology - Heart and Circulatory Physiology*, 292(1):H180–H189, Jan. 2007.

[24] M. L. Bakker, A. F. Moorman, and V. M. Christoffels. The atrioventricular node: Origin, development, and genetic program. *Trends in cardiovascular medicine*, 20(5):164–171, 2010.

[25] J. D. Bayer, R. C. Blake, G. Plank, and N. A. Trayanova. A Novel Rule-Based Algorithm for Assigning Myocardial Fiber Orientation to Computational Heart Models. *Annals of Biomedical Engineering*, 40(10):2243–2254, Oct. 2012.

[26] E. Becker and W. Bürger. *Kontinuumsmechanik.* Number Bd. 20 in Leitfäden der angewandten Mathematik und Mechanik. Teubner, Stuttgart, 1975.

[27] W. Becker and D. Gross. *Mechanik elastischer Körper und Strukturen.* Springer, Berlin Heidelberg, 2002. OCLC: 248918525.

[28] G. W. Beeler and H. Reuter. Reconstruction of the action potential of ventricular myocardial fibres. *The Journal of Physiology*, 268(1):177–210, June 1977.

[29] R. Beinart, S. Abbara, A. Blum, M. Ferencik, K. Heist, J. Ruskin, and M. Mansour. Left Atrial Wall Thickness Variability Measured by CT Scans in Patients Undergoing Pulmonary Vein Isolation. *Journal of Cardiovascular Electrophysiology*, 22(11):1232–1236, Nov. 2011.

[30] A. Bel-Brunon, S. Kehl, C. Martin, S. Uhlig, and W. A. Wall. Numerical identification method for the non-linear viscoelastic compressible behavior of soft tissue using uniaxial tensile tests and image registration – Application to rat lung parenchyma. *Journal of the Mechanical Behavior of Biomedical Materials*, 29:360–374, Jan. 2014.

[31] Y. Belhamadia. A Time-Dependent Adaptive Remeshing for Electrical Waves of the Heart. *IEEE Transactions on Biomedical Engineering*, 55(2):443–452, Feb. 2008.

[32] M. Bendahmane and K. H. Karlsen. Convergence of a finite volume scheme for the bidomain model of cardiac tissue. *Applied Numerical Mathematics*, 59(9):2266–2284, Sept. 2009.

[33] O. Bernus, B. Van Eyck, H. Verschelde, and A. V. Panfilov. Transition from ventricular fibrillation to ventricular tachycardia: A simulation study on the role of Ca(2+)-channel blockers in human ventricular tissue. *Physics in Medicine and Biology*, 47(23):4167–4179, Dec. 2002.

[34] O. Bernus, R. Wilders, C. W. Zemlin, H. Verschelde, and A. V. Panfilov. A computationally efficient electrophysiological model of human ventricular cells. *American Journal of Physiology - Heart and Circulatory Physiology*, 282(6):H2296–H2308, June 2002.

[35] D. M. Bers. Cardiac excitation–contraction coupling. *Nature*, 415(6868):198–205, Jan. 2002.

[36] D. M. Bers. Excitation-Contraction Coupling. In D. P. Zipes and J. Jalife, editors, *Cardiac Electrophysiology: From Cell to Bedside (Sixth Edition)*, pages 161–169. W.B. Saunders, Philadelphia, 2014.

[37] C. Bertoglio, D. Barber, N. Gaddum, I. Valverde, M. Rutten, P. Beerbaum, P. Moireau, R. Hose, and J.-F. Gerbeau. Identification of artery wall stiffness: In vitro validation and in vivo results of a data assimilation procedure applied to a 3D fluid–structure interaction model. *Journal of Biomechanics*, 47(5):1027–1034, Mar. 2014.

[38] P. J. Besl and N. D. McKay. A method for registration of 3-D shapes. *IEEE Transactions on Pattern Analysis and Machine Intelligence*, 14(2):239–256, Feb. 1992.

[39] J. Bestel, F. Clément, and M. Sorine. A Biomechanical Model of Muscle Contraction. In W. J. Niessen and M. A. Viergever, editors, *Medical Image Computing and Computer-Assisted Intervention – MICCAI 2001*, number 2208 in Lecture Notes in Computer Science, pages 1159–1161. Springer Berlin Heidelberg, Oct. 2001.

[40] J. Biehler, M. W. Gee, and W. A. Wall. Towards efficient uncertainty quantification in complex and large-scale biomechanical problems based on a Bayesian multi-fidelity scheme. *Biomechanics and Modeling in Mechanobiology*, 14(3):489–513, June 2015.

[41] V. N. Biktashev and A. V. Holden. Re-entrant activity and its control in a model of mammalian ventricular tissue. *Proc. R. Soc. Lond. B*, 263(1375):1373–1382, Oct. 1996.

[42] A. M. Birzle, C. Martin, L. Yoshihara, S. Uhlig, and W. A. Wall. Experimental characterization and model identification of the nonlinear compressible material behavior of lung parenchyma. *Journal of the Mechanical Behavior of Biomedical Materials*, Aug. 2017.

[43] Blausen.com staff (2014). Medical gallery of Blausen Medical 2014. *WikiJournal of Medicine*, 1(2), 2014.

[44] J. Bonet and R. D. Wood. *Nonlinear Continuum Mechanics for Finite Element Analysis*. Cambridge University Press, Sept. 1997.

[45] M. R. Boyett and H. Dobrzynski. The Sinoatrial Node Is Still Setting the Pace 100 Years After its Discovery. *Circulation Research*, 100(11):1543–1545, June 2007.

[46] S. C. Brenner and L. R. Scott. *The Mathematical Theory of Finite Element Methods*, volume 15 of *Texts in Applied Mathematics*. Springer New York, New York, NY, 2008.

[47] M. Brini and E. Carafoli. Mammalian Calcium Pumps in Health and Disease. In D. P. Zipes and J. Jalife, editors, *Cardiac Electrophysiology: From Cell to Bedside (Sixth Edition)*, pages 43–53. W.B. Saunders, Philadelphia, 2014.

[48] C. Broit. *Optimal Registration of Deformed Images*. PhD thesis, University of Pennsylvania, Philadelphia, PA, USA, 1981.

[49] A. G. Brooks, M. K. Stiles, J. Laborderie, D. H. Lau, P. Kuklik, N. J. Shipp, L.-F. Hsu, and P. Sanders. Outcomes of long-standing persistent atrial fibrillation ablation: A systematic review. *Heart Rhythm*, 7(6):835–846, June 2010.

[50] D. Browne. Muscular System Module 3: Contraction and Relaxation. OpenStax CNX. Dec 19, 2013 http://cnx.org/contents/0a025ef3-e01f-4b6a-b524-6caf807c6bb0@1.

[51] D. Browne. Muscular System Module 6: Cardiac Muscle Tissue. OpenStax CNX. Jan 1, 2014 http://cnx.org/contents/8ff1e0a4-661b-4f24-88a2-372a2aee031a@1.

[52] A. Bueno-Orovio, E. M. Cherry, and F. H. Fenton. Minimal model for human ventricular action potentials in tissue. *Journal of Theoretical Biology*, 253(3):544–560, Aug. 2008.

[53] M. Buist, G. Sands, P. Hunter, and A. Pullan. A Deformable Finite Element Derived Finite Difference Method for Cardiac Activation Problems. *Annals of Biomedical Engineering*, 31(5):577–588, May 2003.

[54] F. F. Bukauskas. Molecular Organization, Gating, and Function of Gap Junction Channels. In D. P. Zipes and J. Jalife, editors, *Cardiac Electrophysiology: From Cell to Bedside (Sixth Edition)*, pages 85–94. W.B. Saunders, Philadelphia, 2014.

[55] R. Burattini and G. Gnudi. Computer identification of models for the arterial tree input impedance: Comparison between two new simple models and first experimental results. *Medical and Biological Engineering and Computing*, 20(2):134–144, Mar. 1982.

[56] B. Burstein and S. Nattel. Atrial Fibrosis: Mechanisms and Clinical Relevance in Atrial Fibrillation. *Journal of the American College of Cardiology*, 51(8):802–809, Feb. 2008.

[57] R. H. Byrd, J. Nocedal, and R. B. Schnabel. Representations of quasi-Newton matrices and their use in limited memory methods. *Mathematical Programming*, 63(1-3):129–156, Jan. 1994.

[58] C. Cabo, A. M. Pertsov, W. T. Baxter, J. M. Davidenko, R. A. Gray, and J. Jalife. Wavefront curvature as a cause of slow conduction and block in isolated cardiac muscle. *Circulation Research*, 75(6):1014–1028, Dec. 1994.

[59] C. Cabo, A. M. Pertsov, W. T. Baxter, J. M. Davidenko, and J. Jalife. Measurements of curvature in an ionic model of cardiac tissu. *Chaos, Solitons & Fractals*, 5(3-4):481–489, 1995.

[60] H. Calkins, K. H. Kuck, R. Cappato, J. Brugada, A. J. Camm, S.-A. Chen, H. J. G. Crijns, R. J. Damiano, D. W. Davies, J. DiMarco, J. Edgerton, K. Ellenbogen, M. D. Ezekowitz, D. E. Haines, M. Haissaguerre, G. Hindricks, Y. Iesaka, W. Jackman, J. Jalife, P. Jais, J. Kalman, D. Keane, Y.-H. Kim, P. Kirchhof, G. Klein, H. Kottkamp, K. Kumagai, B. D. Lindsay, M. Mansour, F. E. Marchlinski, P. M. McCarthy, J. L. Mont, F. Morady, K. Nademanee, H. Nakagawa, A. Natale, S. Nattel, D. L. Packer, C. Pappone, E. Prystowsky, A. Raviele, V. Reddy, J. N. Ruskin, R. J. Shemin, H.-M. Tsao, D. Wilber∧, H. Calkins, K. H. Kuck, R. Cappato, S.-A. Chen, E. N. Prystowsky, K. H. Kuck, A. Natale, D. E. Haines, F. E. Marchlinski, H. Calkins, D. W. Davies, B. D. Lindsay, R. Damiano, D. L. Packer, J. Brugada, A. J. Camm, H. J. G. Crijns, J. DiMarco, J. Edgerton, K. Ellenbogen, M. D. Ezekowitz, M. Haissaguerre, G. Hindricks, Y. Iesaka, W. M. Jackman, P. Jais, J. Jalife, J. Kalman, D. Keane, Y.-H. Kim, P. Kirchhof, G. Klein, H. Kottkamp, K. Kumagai, M. Mansour, F. Marchlinski, P. McCarthy, J. L. Mont, F. Morady, K. Nademanee, H. Nakagawa, S. Nattel, C. Pappone, A. Raviele, V. Reddy, J. N. Ruskin, R. J. Shemin, H.-M. Tsao, D. Wilber, N. Ad, J. Cummings, A. M. Gillinov, H. Heidbuchel, C. January, G. Lip, S. Markowitz, M. Nair, I. E. Ovsyshcher, H.-N. Pak, T. Tsuchiya, D. Shah, T. W. Siong, and P. E. Vardas. 2012 HRS/EHRA/ECAS Expert Consensus Statement on Catheter and Surgical Ablation of Atrial Fibrillation: Recommendations for Patient Selection, Procedural Techniques, Patient Management and Follow-up, Definitions, Endpoints, and Research Trial Design. *Europace*, 14(4):528–606, Apr. 2012.

[61] E. Carmeliet and J. Vereecke. Ionic basis of resting and action potential. In *Cardiac Cellular Electrophysiology*, Basic Science for the Cardiologist, pages 7–66. Springer US, Boston, MA, 2002.

[62] E. E. Carmeliet. Chloride ions and the membrane potential of Purkinje fibres. *The Journal of Physiology*, 156(2):375–388, Apr. 1961.

[63] W. A. Catterall. Voltage-Gated Sodium Channels and Electrical Excitability of the Heart. In D. P. Zipes and J. Jalife, editors, *Cardiac Electrophysiology: From Cell to Bedside (Sixth Edition)*, pages 1–11. W.B. Saunders, Philadelphia, 2014.

[64] R. Chabiniok, P. Moireau, P.-F. Lesault, A. Rahmouni, J.-F. Deux, and D. Chapelle. Estimation of tissue contractility from cardiac cine-MRI using a biomechanical heart model. *Biomechanics and Modeling in Mechanobiology*, 11(5):609–630, May 2012.

[65] R. Chabiniok, V. Y. Wang, M. Hadjicharalambous, L. Asner, J. Lee, M. Sermesant, E. Kuhl, A. A. Young, P. Moireau, M. P. Nash, D. Chapelle, and D. A. Nordsletten. Multiphysics and multiscale modelling, data–model fusion and integration of organ physiology in the clinic: Ventricular cardiac mechanics. *Interface Focus*, 6(2), Apr. 2016.

[66] D. Chapelle, P. Le Tallec, P. Moireau, and M. Sorine. Energy-preserving muscle tissue model: Formulation and compatible discretizations. *International Journal for Multiscale Computational Engineering*, 10(2), 2012.

[67] D. Chapelle, P. L. Tallec, P. Moireau, and M. Sorine. An energy-preserving muscle tissue model: Formulation and compatible discretizations. *International Journal for Multiscale Computational Engineering*, 10(2):189–211, 2012.

[68] M. Chauvin, D. C. Shah, M. Haïssaguerre, L. Marcellin, and C. Brechenmacher. The Anatomic Basis of Connections Between the Coronary Sinus Musculature and the Left Atrium in Humans. *Circulation*, 101(6):647–652, Feb. 2000.

[69] F. F. Ch'en, R. D. Vaughan-Jones, K. Clarke, and D. Noble. Modelling myocardial ischaemia and reperfusion. *Progress in Biophysics and Molecular Biology*, 69(2-3):515–538, 1998.

[70] Y. Chen and G. Medioni. Object Modelling by Registration of Multiple Range Images. *Image Vision Comput.*, 10(3):145–155, Apr. 1992.

[71] Y.-C. Chen, S.-A. Chen, Y.-J. Chen, C.-T. Tai, P. Chan, and C.-I. Lin. T-Type Calcium Current in Electrical Activity of Cardiomyocytes Isolated from Rabbit Pulmonary Vein. *Journal of Cardiovascular Electrophysiology*, 15(5):567–571, May 2004.

[72] E. M. Cherry and S. J. Evans. Properties of two human atrial cell models in tissue: Restitution, memory, propagation, and reentry. *Journal of Theoretical Biology*, 254(3):674–690, Oct. 2008.

[73] E. M. Cherry and F. H. Fenton. Suppression of alternans and conduction blocks despite steep APD restitution: Electrotonic, memory, and conduction velocity restitution effects. *American Journal of Physiology - Heart and Circulatory Physiology*, 286(6):H2332–H2341, June 2004.

[74] E. M. Cherry, H. S. Greenside, and C. S. Henriquez. A space-time adaptive method for simulating complex cardiac dynamics. *Physical Review Letters*, 84(6):1343, 2000.

[75] E. M. Cherry, H. S. Greenside, and C. S. Henriquez. Efficient simulation of three-dimensional anisotropic cardiac tissue using an adaptive mesh refinement method. *Chaos: An Interdisciplinary Journal of Nonlinear Science*, 13(3):853–865, Sept. 2003.

[76] E. M. Cherry, H. M. Hastings, and S. J. Evans. Dynamics of Human Atrial Cell Models: Restitution, Memory, and Intracellular Calcium Dynamics in Single Cells. *Progress in biophysics and molecular biology*, 98(1):24–37, Sept. 2008.

[77] Y. Cho, W. Lee, E.-A. Park, I.-Y. Oh, E.-K. Choi, J.-W. Seo, and S. Oh. The anatomical characteristics of three different endocardial lines in the left atrium: Evaluation by computed tomography prior to mitral isthmus block attempt. *EP Europace*, 14(8):1104–1111, Aug. 2012.

[78] S. S. Chugh, R. Havmoeller, K. Narayanan, D. Singh, M. Rienstra, E. J. Benjamin, R. F. Gillum, Y.-H. Kim, J. H. McAnulty, Z.-J. Zheng, M. H. Forouzanfar, M. Naghavi, G. A. Mensah, M. Ezzati, and C. J. L. Murray. Worldwide Epidemiology of Atrial Fibrillation: A Global Burden of Disease 2010 Study. *Circulation*, 129(8):837–847, Feb. 2014.

[79] J. Chung and G. M. Hulbert. A Time Integration Algorithm for Structural Dynamics With Improved Numerical Dissipation: The Generalized-α Method. *Journal of Applied Mechanics*, 60(2):371–375, June 1993.

[80] R. Clayton, O. Bernus, E. Cherry, H. Dierckx, F. Fenton, L. Mirabella, A. Panfilov, F. Sachse, G. Seemann, and H. Zhang. Models of cardiac tissue electrophysiology: Progress, challenges and open questions. *Progress in Biophysics and Molecular Biology*, 104(1-3):22–48, Jan. 2011.

[81] R. H. Clayton. Vortex filament dynamics in computational models of ventricular fibrillation in the heart. *Chaos: An Interdisciplinary Journal of Nonlinear Science*, 18(4):043127, Dec. 2008.

[82] L. Clerc. Directional differences of impulse spread in trabecular muscle from mammalian heart. *The Journal of Physiology*, 255(2):335–346, Feb. 1976.

[83] H. Cochet, D. Scherr, S. Zellerhoff, F. Sacher, N. Derval, A. Denis, S. Knecht, Y. Komatsu, M. Montaudon, F. Laurent, B. M. Pieske, M. Hocini, M. Haïssaguerre, and P. Jaïs. Atrial Structure and Function 5 Years After Successful Ablation for Persistent Atrial Fibrillation: An MRI Study. *Journal of Cardiovascular Electrophysiology*, 25(7):671–679, July 2014.

[84] B. Cockburn, J. Gopalakrishnan, and R. Lazarov. Unified Hybridization of Discontinuous Galerkin, Mixed, and Continuous Galerkin Methods for Second Order Elliptic Problems. *SIAM Journal on Numerical Analysis*, 47(2):1319–1365, Jan. 2009.

[85] J. N. Cohn, R. Ferrari, and N. Sharpe. Cardiac remodeling—concepts and clinical implications: A consensus paper from an international forum on cardiac remodeling. *Journal of the American College of Cardiology*, 35(3):569–582, Mar. 2000.

[86] P. Colli Franzone and L. F. Pavarino. A parallel solver for reaction–diffusion systems in computational electrocardiology. *Mathematical Models and Methods in Applied Sciences*, 14(06):883–911, June 2004.

[87] P. Colli Franzone, L. F. Pavarino, and S. Scacchi. *Mathematical Cardiac Electrophysiology*, volume 13 of *MS&A*. Springer International Publishing, Cham, 2014.

[88] C. Corrado, J.-F. Gerbeau, and P. Moireau. Identification of weakly coupled multiphysics problems. Application to the inverse problem of electrocardiography. *Journal of Computational Physics*, 283:271–298, Feb. 2015.

[89] K. D. Costa, P. J. Hunter, J. S. Wayne, L. K. Waldman, J. M. Guccione, and A. D. McCulloch. A Three-Dimensional Finite Element Method for Large Elastic Deformations of Ventricular Myocardium: II—Prolate Spheroidal Coordinates. *Journal of Biomechanical Engineering*, 118(4):464–472, Nov. 1996.

[90] Y. Coudière and C. Pierre. Stability and convergence of a finite volume method for two systems of reaction-diffusion equations in electro-cardiology. *Nonlinear Analysis: Real World Applications*, 7(4):916–935, Sept. 2006.

[91] M. Courtemanche, R. J. Ramirez, and S. Nattel. Ionic mechanisms underlying human atrial action potential properties: Insights from a mathematical model. *American Journal of Physiology - Heart and Circulatory Physiology*, 275(1):H301–H321, July 1998.

[92] L. Dang, N. Virag, Z. Ihara, V. Jacquemet, J.-M. Vesin, J. Schlaepfer, P. Ruchat, and L. Kappenberger. Evaluation of Ablation Patterns Using a Biophysical Model of Atrial Fibrillation. *Annals of Biomedical Engineering*, 33(4):465–474, Apr. 2005.

[93] J.-C. Daubert, L. Saxon, P. B. Adamson, A. Auricchio, R. D. Berger, J. F. Beshai, O. Breithard, M. Brignole, J. Cleland, D. B. DeLurgio, K. Dickstein, D. V. Exner, M. Gold, R. A. Grimm, D. L. Hayes, C. Israel, C. Leclercq, C. Linde, J. Lindenfeld, B. Merkely, L. Mont, F. Murgatroyd, F. Prinzen, S. F. Saba, J. S. Shinbane, J. Singh, A. S. Tang, P. E. Vardas, B. L. Wilkoff, J. L. Zamorano, I. Anand, C. Blomström-Lundqvist, J. P. Boehmer, H. Calkins, S. Cazeau, V. Delgado, N. A. M. Estes, D. Haines, F. Kusumoto, P. Leyva, F. Ruschitzka, L. W. Stevenson, and C. T. Torp-Pedersen. 2012 EHRA/HRS expert consensus statement on cardiac resynchronization therapy in heart failure: Implant and follow-up recommendations and managementA registered branch of the European Society of Cardiology (ESC), and the Heart Rhythm Society; and in collaboration with the Heart Failure Society of America (HFSA), the American Society of Echocardiography

(ASE), the American Heart Association (AHA), the European Association of Echocardiography (EAE) of the ESC and the Heart Failure Association of the ESC (HFA).Endorsed by the governing bodies of AHA, ASE, EAE, HFSA, HFA, EHRA, and HRS. *EP Europace*, 14(9):1236–1286, Sept. 2012.

[94] R. De Ponti, S. Y. Ho, J. A. Salerno-Uriarte, M. Tritto, and G. Spadacini. Electroanatomic Analysis of Sinus Impulse Propagation in Normal Human Atria. *Journal of Cardiovascular Electrophysiology*, 13(1):1–10, Jan. 2002.

[95] K. A. Deck and W. Trautwein. Ionic currents in cardiac excitation. *Pflüger's Archiv für die gesamte Physiologie des Menschen und der Tiere*, 280(1):63–80, Mar. 1964.

[96] P. Deuflhard, B. Erdmann, R. Roitzsch, and G. T. Lines. Adaptive finite element simulation of ventricular fibrillation dynamics. *Computing and Visualization in Science*, 12(5):201–205, June 2009.

[97] K. M. Dibb, J. D. Clarke, M. A. Horn, M. A. Richards, H. K. Graham, D. A. Eisner, and A. W. Trafford. Characterization of an Extensive Transverse Tubular Network in Sheep Atrial Myocytes and its Depletion in Heart Failure. *Circulation: Heart Failure*, 2(5):482–489, Sept. 2009.

[98] J.-M. Dieudonné. The left ventricle as confocal prolate spheroids. *The bulletin of mathematical biophysics*, 31(3):433–439, Sept. 1969.

[99] D. DiFrancesco and D. Noble. A model of cardiac electrical activity incorporating ionic pumps and concentration changes. *Philosophical Transactions of the Royal Society of London B: Biological Sciences*, 307(1133):353–398, 1985.

[100] P. Dilaveris, V. Batchvarov, J. Gialafos, and M. Malik. Comparison of Different Methods for Manual P Wave Duration Measurement in 12-Lead Electrocardiograms. *Pacing and Clinical Electrophysiology*, 22(10):1532–1538, Oct. 1999.

[101] O. Dössel, M. W. Krueger, F. M. Weber, M. Wilhelms, and G. Seemann. Computational modeling of the human atrial anatomy and electrophysiology. *Medical & Biological Engineering & Computing*, 50(8):773–799, Aug. 2012.

[102] J. M. Downey and G. Heusch. Sequence of Cardiac Activation and Ventricular Mechanics. In N. Sperelakis, Y. Kurachi, A. Terzic, and M. V. Cohen, editors, *Heart Physiology and Pathophysiology (Fourth Edition)*, pages 3–18. Academic Press, San Diego, 2001.

[103] D. Drenckhahn. *Anatomie, Makroskopische Anatomie, Histologie, Embryologie, Zellbiologie: Band 1: Zellen- und Gewebelehre, Entwicklungslehre, Skelett- und Muskelsystem, Atemsystem, Verdauungssystem, Harn- und Genitalsystem.* Urban & Fischer Verlag/Elsevier GmbH, München, 16 edition, Oct. 2002.

[104] D. Drenckhahn. *Anatomie, Makroskopische Anatomie, Embryologie und Histologie des Menschen.: Band 2: Herz-Kreislauf-System, Lymphatisches System, Endokrine Drüsen, Nervensystem, Sinnesorgane, Haut.* Urban & Fischer Verlag/Elsevier GmbH, München, 16 edition, 2004.

[105] G. Droogmans, B. Nilius, H. De Smedt, J. B. Parys, and L. Missiaen. Electromechanical and Pharmacomechanical Coupling in Vascular Smooth Muscle Cells. In N. Sperelakis, Y. Kurachi, A. Terzic, and M. V. Cohen, editors, *Heart Physiology and Pathophysiology (Fourth Edition)*, pages 501–517. Academic Press, San Diego, 2001.

[106] Y. E. Earm and D. Noble. A model of the single atrial cell: Relation between calcium current and calcium release. *Proceedings of the Royal Society of London. Series B, Biological Sciences*, 240(1297):83–96, May 1990.

[107] L. Ebihara and E. A. Johnson. Fast sodium current in cardiac muscle. A quantitative description. *Biophysical Journal*, 32(2):779–790, Nov. 1980.

[108] B. Echebarria and A. Karma. Mechanisms for initiation of cardiac discordant alternans. *The European Physical Journal Special Topics*, 146(1):217–231, July 2007.

[109] D. B. Ennis, T. C. Nguyen, J. C. Riboh, L. Wigström, K. B. Harrington, G. T. Daughters, N. B. Ingels, and D. C. Miller. Myofiber angle distributions in the ovine left ventricle do not conform to computationally optimized predictions. *Journal of Biomechanics*, 41(15):3219–3224, Nov. 2008.

[110] T. Eriksson, A. Prassl, G. Plank, and G. Holzapfel. Influence of myocardial fiber/sheet orientations on left ventricular mechanical contraction. *Mathematics and Mechanics of Solids*, 18(6):592–606, Aug. 2013.

[111] G. Ernst, C. Stöllberger, F. Abzieher, W. Veit-Dirscherl, E. Bonner, B. Bibus, B. Schneider, and J. Slany. Morphology of the left atrial appendage. *The Anatomical Record*, 242(4):553–561, Aug. 1995.

[112] S. I. Ertel, E. A. Ertel, and J.-P. Clozel. T-Type Ca2+ Channels and Pharmacological Blockade: Potential Pathophysiological Relevance. *Cardiovascular Drugs and Therapy*, 11(6):723–739, Dec. 1997.

[113] M. Ethier and Y. Bourgault. Semi-Implicit Time-Discretization Schemes for the Bidomain Model. *SIAM Journal on Numerical Analysis*, 46(5):2443–2468, Jan. 2008.

[114] F. Fenton and A. Karma. Vortex dynamics in three-dimensional continuous myocardium with fiber rotation: Filament instability and fibrillation. *Chaos: An Interdisciplinary Journal of Nonlinear Science*, 8(1):20–47, 1998.

[115] M. A. Fernández and N. Zemzemi. Decoupled time-marching schemes in computational cardiac electrophysiology and ECG numerical simulation. *Mathematical Biosciences*, 226(1):58–75, July 2010.

[116] M. A. Fernandez-Teran and J. M. Hurle. Myocardial fiber architecture of the human heart ventricles. *The Anatomical Record*, 204(2):137–147, Oct. 1982.

[117] M. Fink, D. Noble, L. Virag, A. Varro, and W. R. Giles. Contributions of HERG K+ current to repolarization of the human ventricular action potential. *Progress in Biophysics and Molecular Biology*, 96(1):357–376, Jan. 2008.

[118] B. Fischer and J. Modersitzki. Ill-posed medicine—an introduction to image registration. *Inverse Problems*, 24(3):034008, June 2008.

[119] G. Fischer, B. Tilg, R. Modre, G. J. M. Huiskamp, J. Fetzer, W. Rucker, and P. Wach. A Bidomain Model Based BEM-FEM Coupling Formulation for Anisotropic Cardiac Tissue. *Annals of Biomedical Engineering*, 28(10):1229–1243, Oct. 2000.

[120] R. Fitzhugh. Thresholds and Plateaus in the Hodgkin-Huxley Nerve Equations. *The Journal of General Physiology*, 43(5):867–896, May 1960.

[121] R. FitzHugh. Impulses and Physiological States in Theoretical Models of Nerve Membrane. *Biophysical Journal*, 1(6):445–466, July 1961.

[122] R. Foale, P. Nihoyannopoulos, W. McKenna, A. Kleinebenne, A. Nadazdin, E. Rowland, G. Smith, and A. Klienebenne. Echocardiographic measurement of the normal adult right ventricle. *British Heart Journal*, 56(1):33–44, July 1986.

[123] O. Frank. *Die Grundform des arteriellen pulses: Mathematische Analyse. Erste Abhandlung*. 1899.

[124] P. C. Franzone, P. Deuflhard, B. Erdmann, J. Lang, and L. F. Pavarino. Adaptivity in Space and Time for Reaction-Diffusion Systems in Electrocardiology. *SIAM Journal on Scientific Computing*, 28(3):942–962, Jan. 2006.

[125] B. Furie and B. C. Furie. Mechanisms of thrombus formation. *New England Journal of Medicine*, 359(9):938–949, 2008.

[126] V. Fuster, L. E. Rydén, D. S. Cannom, H. J. Crijns, A. B. Curtis, K. A. Ellenbogen, J. L. Halperin, J.-Y. L. Heuzey, G. N. Kay, J. E. Lowe, S. B. Olsson, E. N. Prystowsky, J. L. Tamargo, S. Wann, A. T. F. Members, S. C. Smith, A. K. Jacobs, C. D. Adams, J. L. Anderson, E. M. Antman, J. L. Halperin, S. A. Hunt, R. Nishimura, J. P. Ornato, R. L. Page, B. Riegel, E. C. f. P. Guidelines, S. G. Priori, J.-J. Blanc, A. Budaj, A. J. Camm, V. Dean, J. W. Deckers, C. Despres, K. Dickstein, J. Lekakis, K. McGregor, M. Metra, J. Morais, A. Osterspey, J. L. Tamargo, and J. L. Zamorano. ACC/AHA/ESC 2006 Guidelines for the Management of Patients With Atrial Fibrillation: A Report of the American College of Cardiology/American Heart Association Task Force on Practice Guidelines and the European Society of Cardiology Committee for Practice Guidelines (Writing Committee to Revise the 2001 Guidelines for the Management of Patients With Atrial Fibrillation): Developed in Collaboration With the European Heart Rhythm Association and the Heart Rhythm Society. *Circulation*, 114(7):e257–e354, Aug. 2006.

[127] A. Garfinkel, Y.-H. Kim, O. Voroshilovsky, Z. Qu, J. R. Kil, M.-H. Lee, H. S. Karagueuzian, J. N. Weiss, and P.-S. Chen. Preventing ventricular fibrillation by flattening cardiac restitution. *Proceedings of the National Academy of Sciences of the United States of America*, 97(11):6061–6066, May 2000.

[128] M. W. Gee, C. Förster, and W. A. Wall. A computational strategy for prestressing patient-specific biomechanical problems under finite deformation. *International Journal for Numerical Methods in Biomedical Engineering*, 26(1):52–72, Jan. 2010.

[129] C. Geuzaine and J.-F. Remacle. Gmsh: A 3-D finite element mesh generator with built-in pre- and post-processing facilities. *International Journal for Numerical Methods in Engineering*, 79(11):1309–1331, Sept. 2009.

[130] G. Giorgiani, S. Fernández-Méndez, and A. Huerta. Hybridizable discontinuous Galerkin p-adaptivity for wave propagation problems. *International Journal for Numerical Methods in Fluids*, 72(12):1244–1262, Aug. 2013.

[131] S. Göktepe and E. Kuhl. Computational modeling of cardiac electrophysiology: A novel finite element approach. *International Journal for Numerical Methods in Engineering*, 79(2):156–178, July 2009.

[132] P. Gould, D. Ghista, L. Brombolich, and I. Mirsky. In vivo stresses in the human left ventricular wall: Analysis accounting for the irregular 3-dimensional geometry and comparison with idealised geometry analyses. *Journal of Biomechanics*, 5(5):521–539, Sept. 1972.

[133] E. Grandi, S. V. Pandit, N. Voigt, A. J. Workman, D. Dobrev, J. Jalife, and D. M. Bers. Human Atrial Action Potential and Ca2+ Model: Sinus Rhythm and Chronic Atrial Fibrillation. *Circulation Research*, 109(9):1055–1066, Oct. 2011.

[134] E. Grandi, F. S. Pasqualini, and D. M. Bers. A novel computational model of the human ventricular action potential and Ca transient. *Journal of Molecular and Cellular Cardiology*, 48(1):112–121, Jan. 2010.

[135] R. A. Gray and J. Jalife. Ventricular fibrillation and atrial fibrillation are two different beasts. *Chaos: An Interdisciplinary Journal of Nonlinear Science*, 8(1):65–78, Mar. 1998.

[136] J. M. Guccione, K. D. Costa, and A. D. McCulloch. Finite element stress analysis of left ventricular mechanics in the beating dog heart. *Journal of Biomechanics*, 28(10):1167–1177, Oct. 1995.

[137] J. M. Guccione, A. D. McCulloch, and L. K. Waldman. Passive Material Properties of Intact Ventricular Myocardium Determined From a Cylindrical Model. *Journal of Biomechanical Engineering*, 113(1):42–55, Feb. 1991.

[138] F. B. Gul'ko and A. A. Petrov. Mechanism of formation of closed propagation pathways in excitable media. *Biofizika*, 17(2):261–270, 1972 Mar-Apr.

[139] V. Gurev, P. Pathmanathan, J.-L. Fattebert, H.-F. Wen, J. Magerlein, R. A. Gray, D. F. Richards, and J. J. Rice. A high-resolution computational model of the deforming human heart. *Biomechanics and Modeling in Mechanobiology*, 14(4):829–849, Aug. 2015.

[140] M. E. Gurtin. *An Introduction to Continuum Mechanics*. Academic Press, Jan. 1982.

[141] E. Haber and J. Modersitzki. Numerical methods for volume preserving image registration. *Inverse Problems*, 20(5):1621–1638, Oct. 2004.

[142] E. Haber and J. Modersitzki. A Multilevel Method for Image Registration. *SIAM Journal on Scientific Computing*, 27(5):1594–1607, Jan. 2006.

[143] N. Hagiwara, H. Irisawa, and M. Kameyama. Contribution of two types of calcium currents to the pacemaker potentials of rabbit sino-atrial node cells. *The Journal of Physiology*, 395(1):233–253, Jan. 1988.

[144] M. Haissaguerre, M. Hocini, A. Denis, A. J. Shah, Y. Komatsu, S. Yamashita, M. Daly, S. Amraoui, S. Zellerhoff, M.-Q. Picat, A. Quotb, L. Jesel, H. Lim, S. Ploux, P. Bordachar, G. Attuel, V. Meillet, P. Ritter, N. Derval, F. Sacher, O. Bernus, H. Cochet, P. Jais, and R. Dubois. Driver Domains in Persistent Atrial Fibrillation. *Circulation*, 130(7):530–538, Dec. 2014.

[145] M. Haïssaguerre, P. Jaïs, D. C. Shah, A. Takahashi, M. Hocini, G. Quiniou, S. Garrigue, A. Le Mouroux, P. Le Métayer, and J. Clémenty. Spontaneous Initiation of Atrial Fibrillation by Ectopic Beats Originating in the Pulmonary Veins. *New England Journal of Medicine*, 339(10):659–666, Sept. 1998.

[146] J. C. Hancox, H. J. Witchel, and A. Varghese. Alteration of HERG Current Profile during the Cardiac Ventricular Action Potential, Following a Pore Mutation. *Biochemical and Biophysical Research Communications*, 253(3):719–724, Dec. 1998.

[147] D. M. Harrild, R. Penland, and C. S. Henriquez. A flexible method for simulating cardiac conduction in three-dimensional complex geometries. *Journal of Electrocardiology*, 33(3):241–251, July 2000.

[148] J. Heeringa, D. A. M. van der Kuip, A. Hofman, J. A. Kors, G. van Herpen, B. H. C. Stricker, T. Stijnen, G. Y. H. Lip, and J. C. M. Witteman. Prevalence, incidence and lifetime risk of atrial fibrillation: The Rotterdam study. *European Heart Journal*, 27(8):949–953, Apr. 2006.

[149] E. Heidenreich, J. Rodríguez, F. Gaspar, and M. Doblaré. Fourth-order compact schemes with adaptive time step for monodomain reaction–diffusion equations. *Journal of Computational and Applied Mathematics*, 216(1):39–55, June 2008.

[150] P. A. Helm, H.-J. Tseng, L. Younes, E. R. McVeigh, and R. L. Winslow. Ex vivo 3D diffusion tensor imaging and quantification of cardiac laminar structure. *Magnetic Resonance in Medicine*, 54(4):850–859, Oct. 2005.

[151] B. D. F. Hermosillo. Semi-automatic enhancement of atrial models to include atrial architecture and patient specific data: For biophysical simulations. In *2008 Computers in Cardiology*, pages 633–636, Sept. 2008.

[152] T. Hershkovich, T. Shalmon, O. Shitrit, N. Halay, B. H. Menze, I. Dolgopyat, I. Kahn, I. Shelef, and T. Riklin Raviv. Probabilistic model for 3D interactive segmentation. *Computer Vision and Image Understanding*, 151:47–60, Oct. 2016.

[153] J. S. Hesthaven and T. Warburton. *Nodal Discontinuous Galerkin Methods: Algorithms, Analysis, and Applications*. Number 54 in Texts in Applied Mathematics. Springer, New York, 2008.

[154] D. W. Hilgemann and D. Noble. Excitation-contraction coupling and extracellular calcium transients in rabbit atrium: Reconstruction of basic cellular mechanisms. *Proceedings of the Royal Society of London. Series B, Biological Sciences*, 230(1259):163–205, Mar. 1987.

[155] M. Hiraoka, Y. Hirano, S. Kawano, and T. Furukawa. Regulation of Cardiac Ion Channels by Phosphorylation, Ca2+, Cytoskeleton, and Stretch. In N. Sperelakis, Y. Kurachi, A. Terzic, and M. V. Cohen, editors, *Heart Physiology and Pathophysiology (Fourth Edition)*, pages 389–404. Academic Press, San Diego, 2001.

[156] S. Ho and D. Sánchez-Quintana. The importance of atrial structure and fibers. *Clinical Anatomy*, 22(1):52–63, Jan. 2009.

[157] S. Y. Ho. Anatomy and myoarchitecture of the left ventricular wall in normal and in disease. *European Journal of Echocardiography*, 10(8):iii3–iii7, Dec. 2009.

[158] S. Y. Ho. File:Figure 5.jpg - Textbook of Cardiology, 2012.

[159] S. Y. Ho. File:Figure 8.jpg - Textbook of Cardiology, 2012.

[160] S. Y. Ho, R. H. Anderson, and D. Sánchez-Quintana. Atrial structure and fibres: Morphologic bases of atrial conduction. *Cardiovascular research*, 54(2):325–336, May 2002.

[161] S. Y. Ho, J. A. Cabrera, and D. Sanchez-Quintana. Left Atrial Anatomy Revisited. *Circulation: Arrhythmia and Electrophysiology*, 5(1):220–228, Feb. 2012.

[162] S. Y. Ho, K. P. McCarthy, and F. F. Faletra. Anatomy of the left atrium for interventional echocardiography. *European Journal of Echocardiography*, 12(10):i11–i15, Oct. 2011.

[163] S. Y. Ho and P. Nihoyannopoulos. Anatomy, echocardiography, and normal right ventricular dimensions. *Heart*, 92(Suppl 1):i2–i13, Apr. 2006.

[164] S. Y. Ho, D. Sanchez-Quintana, J. A. Cabrera, and R. H. Anderson. Anatomy of the Left Atrium: Implications for Radiofrequency Ablation of Atrial Fibrillation. *Journal of Cardiovascular Electrophysiology*, 10(11):1525–1533, Nov. 1999.

[165] A. L. Hodgkin and A. F. Huxley. A quantitative description of membrane current and its application to conduction and excitation in nerve. *The Journal of Physiology*, 117(4):500–544, Aug. 1952.

[166] J. M. Hoermann, C. Bertoglio, M. Kronbichler, M. R. Pfaller, R. Chabiniok, and W. A. Wall. An adaptive hybridizable discontinuous Galerkin approach for cardiac electrophysiology. *International Journal for Numerical Methods in Biomedical Engineering*, Feb. 2018.

[167] J. M. Hoermann, C. Bertoglio, and W. A. Wall. Discontinuous Approximations for Electrophysiology Problems. In *4th International Conference on Computational & Mathematical Biomedical Engineering*, pages 692–695, 2015.

[168] J. M. Hoermann, M. R. Pfaller, C. Bertoglio, L. Avena, and W. A. Wall. Automatic Mapping of Atrial Fiber Orientations for Patient-Specific Modeling of Cardiac Electromechanics using Image-Registration. *International Journal for Numerical Methods in Biomedical Engineering*, Mar. 2019.

[169] B. F. Hoffman and P. F. Cranefield. The physiological basis of cardiac arrhythmias. *The American journal of medicine*, 37(5):670–684, 1964.

[170] A. V. Holden. Mathematics: The restless heart of a spiral. *Nature*, 387(6634):655, June 1997.

[171] G. A. Holzapfel. *Nonlinear Solid Mechanics: A Continuum Approach for Enineering: A Continuum Approach for Engineering*. Wiley, Chichester ; New York, 1 edition, Mar. 2000.

[172] J. M. Hörmann, C. Bertoglio, A. Nagler, M. R. Pfaller, F. Bourier, M. Hadamitzky, I. Deisenhofer, and W. A. Wall. Multiphysics Modeling of the Atrial Systole under Standard Ablation Strategies. *Cardiovascular Engineering and Technology*, 8(2):205–218, June 2017.

[173] L. V. Hryshko. Membrane Pumps and Exchangers. In D. P. Zipes and J. Jalife, editors, *Cardiac Electrophysiology: Fourth Edition*, pages 42–50. W.B. Saunders, 2004.

[174] E. W. Hsu, A. L. Muzikant, S. A. Matulevicius, R. C. Penland, and C. S. Henriquez. Magnetic resonance myocardial fiber-orientation mapping with direct histological correlation. *American Journal of Physiology - Heart and Circulatory Physiology*, 274(5):H1627–H1634, May 1998.

[175] M. Huemer, A. Wutzler, A. S. Parwani, P. Attanasio, H. Matsuda, F. Blaschke, L.-H. Boldt, and W. Haverkamp. Comparison of the anterior and posterior mitral isthmus ablation lines in patients with perimitral annulus flutter or persistent atrial fibrillation. *Journal of Interventional Cardiac Electrophysiology*, 44(2):119–129, Nov. 2015.

[176] J. D. Humphrey, R. K. Strumpf, and F. C. P. Yin. Determination of a Constitutive Relation for Passive Myocardium: I. A New Functional Form. *Journal of Biomechanical Engineering*, 112(3):333–339, Aug. 1990.

[177] P. Hunter, M. P. Nash, and G. B. Sands. Compuational Electromechanics of the Heart. In *Computational Biology of the Heart*, pages 345–407. John Wiley & Sons Ltd, Chichester, New York, Mar. 1997.

[178] O. F. Hutter and D. Noble. Rectifying Properties of Heart Muscle. *Nature*, 188(4749):495, Nov. 1960.

[179] B. M. C. Inc. Pericardial Sac, 2013.

[180] V. Iyer, R. Mazhari, and R. L. Winslow. A Computational Model of the Human Left-Ventricular Epicardial Myocyte. *Biophysical Journal*, 87(3):1507–1525, Sept. 2004.

[181] V. Jacquemet and C. Henriquez. Finite Volume Stiffness Matrix for Solving Anisotropic Cardiac Propagation in 2-D and 3-D Unstructured Meshes. *IEEE Transactions on Biomedical Engineering*, 52(8):1490–1492, Aug. 2005.

[182] J. Jalife. Ventricular fibrillation: Mechanisms of initiation and maintenance. *Annual review of physiology*, 62(1):25–50, 2000.

[183] R. F. Janz and A. F. Grimm. Deformation of the Diastolic Left Ventricle. *Biophysical Journal*, 13(7):689–704, July 1973.

[184] N. Kawel, E. B. Turkbey, J. J. Carr, J. Eng, A. S. Gomes, W. G. Hundley, C. Johnson, S. C. Masri, M. R. Prince, R. J. van der Geest, J. a. A. C. Lima, and D. A. Bluemke. Normal Left Ventricular Myocardial Thickness for Middle-Aged and Older Subjects With Steady-State Free Precession Cardiac Magnetic Resonance. *Circulation: Cardiovascular Imaging*, 5(4):500–508, July 2012.

[185] J. Keener and J. Sneyd. Biochemical Reactions. In *Mathematical Physiology*, Interdisciplinary Applied Mathematics, pages 1–47. Springer, New York, NY, 2009.

[186] J. Keener and J. Sneyd. Cellular homeostasis. In *Mathematical Physiology*, pages 49–119. Springer, 2009.

[187] J. Keener and J. Sneyd. Excitability. In *Mathematical Physiology*, Interdisciplinary Applied Mathematics, pages 195–228. Springer, New York, NY, 2009.

[188] J. Keener and J. Sneyd. Membrane Ion Channels. In *Mathematical Physiology*, Interdisciplinary Applied Mathematics, pages 121–173. Springer, New York, NY, 2009.

[189] J. Keener and J. Sneyd. Passive Electrical Flow in Neurons. In *Mathematical Physiology*, Interdisciplinary Applied Mathematics, pages 175–194. Springer, New York, NY, 2009.

[190] J. P. Keener and K. Bogar. A numerical method for the solution of the bidomain equations in cardiac tissue. *Chaos: An Interdisciplinary Journal of Nonlinear Science*, 8(1):234–241, Mar. 1998.

[191] R. H. Keldermann, K. H. W. J. ten Tusscher, M. P. Nash, C. P. Bradley, R. Hren, P. Taggart, and A. V. Panfilov. A computational study of mother rotor VF in the human ventricles. *American Journal of Physiology - Heart and Circulatory Physiology*, 296(2):H370–H379, Feb. 2009.

[192] R. H. Keldermann, K. H. W. J. ten Tusscher, M. P. Nash, R. Hren, P. Taggart, and A. V. Panfilov. Effect of heterogeneous APD restitution on VF organization in a model of the human ventricles. *American Journal of Physiology - Heart and Circulatory Physiology*, 294(2):H764–H774, Feb. 2008.

[193] I. Kholová and J. Kautzner. Morphology of Atrial Myocardial Extensions Into Human Caval Veins: A Postmortem Study in Patients With and Without Atrial Fibrillation. *Circulation*, 110(5):483–488, Aug. 2004.

[194] P. Kirchhof and H. Calkins. Catheter ablation in patients with persistent atrial fibrillation. *European Heart Journal*, 38(1):20–26, Jan. 2017.

[195] R. Klabunde. *Cardiovascular Physiology Concepts*. Lippincott Williams & Wilkins, Nov. 2011.

[196] A. G. Kléber and Y. Rudy. Basic Mechanisms of Cardiac Impulse Propagation and Associated Arrhythmias. *Physiological Reviews*, 84(2):431–488, Apr. 2004.

[197] B. M. Koeppen and B. A. Stanton. *Berne & Levy Physiology, 6th Edition*. Mosby, Philadelphia, PA, 6th edition edition, Jan. 2010.

[198] P. Kohl. Cardiac Stretch–Activated Channels and Mechano-Electric Coupling. In D. P. Zipes and J. Jalife, editors, *Cardiac Electrophysiology: From Cell to Bedside (Sixth Edition)*, pages 139–149. W.B. Saunders, Philadelphia, 2014.

[199] P. Kohl, D. Noble, R. L. Winslow, and P. J. Hunter. Computational Modelling of Biological Systems: Tools and Visions. *Philosophical Transactions: Mathematical, Physical and Engineering Sciences*, 358(1766):579–610, 2000.

[200] J. T. Koivumäki, T. Korhonen, and P. Tavi. Impact of Sarcoplasmic Reticulum Calcium Release on Calcium Dynamics and Action Potential Morphology in Human Atrial Myocytes: A Computational Study. *PLOS Computational Biology*, 7(1):e1001067, Jan. 2011.

[201] E. Konukoglu, J. Relan, U. Cilingir, B. H. Menze, P. Chinchapatnam, A. Jadidi, H. Cochet, M. Hocini, H. Delingette, P. Jaïs, M. Haïssaguerre, N. Ayache, and M. Sermesant. Efficient probabilistic model personalization integrating uncertainty on data and parameters: Application to Eikonal-Diffusion models in cardiac electrophysiology. *Progress in Biophysics and Molecular Biology*, 107(1):134–146, Oct. 2011.

[202] A. D. Krahn, J. Manfreda, R. B. Tate, F. A. L. Mathewson, and T. E. Cuddy. The natural history of atrial fibrillation: Incidence, risk factors, and prognosis in the manitoba follow-up study. *The American Journal of Medicine*, 98(5):476–484, May 1995.

[203] S. Krishnamoorthi, M. Sarkar, and W. S. Klug. Numerical quadrature and operator splitting in finite element methods for cardiac electrophysiology. *International Journal for Numerical Methods in Biomedical Engineering*, 29(11):1243–1266, Nov. 2013.

[204] T. Krogh-Madsen, G. W. Abbott, and D. J. Christini. Effects of Electrical and Structural Remodeling on Atrial Fibrillation Maintenance: A Simulation Study. *PLOS Computational Biology*, 8(2):e1002390, Feb. 2012.

[205] M. W. Krueger, V. Schmidt, C. Tobón, F. M. Weber, C. Lorenz, D. U. J. Keller, H. Barschdorf, M. Burdumy, P. Neher, G. Plank, K. Rhode, G. Seemann, D. Sanchez-Quintana, J. Saiz, R. Razavi, and O. Dössel. Modeling Atrial Fiber Orientation in Patient-Specific Geometries: A Semi-automatic Rule-Based Approach. In *Functional Imaging and Modeling of the Heart*, Lecture Notes in Computer Science, pages 223–232. Springer, Berlin, Heidelberg, May 2011.

[206] M. W. Krueger, W. H. W. Schulze, K. S. Rhode, R. Razavi, G. Seemann, and O. Dössel. Towards personalized clinical in-silico modeling of atrial anatomy and electrophysiology. *Medical & Biological Engineering & Computing*, 51(11):1251–1260, Nov. 2013.

[207] M. W. Krueger, G. Seemann, K. Rhode, D. U. J. Keller, C. Schilling, A. Arujuna, J. Gill, M. D. O'Neill, R. Razavi, and O. Dossel. Personalization of Atrial Anatomy and Electrophysiology as a Basis for Clinical Modeling of Radio-Frequency Ablation of Atrial Fibrillation. *IEEE Transactions on Medical Imaging*, 32(1):73–84, Jan. 2013.

[208] W. M. Lai, D. Rubin, and E. Krempl. *Introduction to Continuum Mechanics, Fourth Edition*. Elsevier, Amsterdam ; Boston, 4 edition edition, Sept. 2009.

[209] B. Lambermont, P. Gérard, O. Detry, P. Kolh, P. Potty, J.-O. Defraigne, V. D'Orio, and R. Marcelle. Comparison between three-and four-element windkessel models to characterize vascular properties of pulmonary circulation. *Archives of physiology and biochemistry*, 105(7):625–632, 1997.

[210] T. G. Laske, M. Shrivastav, and P. A. Iaizzo. The Cardiac Conduction System. In *Handbook of Cardiac Anatomy, Physiology, and Devices*, pages 215–233. Springer, Cham, 2015.

[211] R. Lemery, L. Soucie, B. Martin, A. S. L. Tang, M. Green, and J. Healey. Human Study of Biatrial Electrical Coupling. Determinants of Endocardial Septal Activation and Conduction Over Interatrial Connections. *Circulation*, Oct. 2004.

[212] C. Lenk, F. M. Weber, M. Bauer, M. Einax, P. Maass, and G. Seeman. Initiation of atrial fibrillation by interaction of pacemakers with geometrical constraints. *Journal of Theoretical Biology*, 366:13–23, Feb. 2015.

[213] H. Lester and S. R. Arridge. A survey of hierarchical non-linear medical image registration. *Pattern Recognition*, 32(1):129–149, Jan. 1999.

[214] L. S. Lilly and H. M. School, editors. *Pathophysiology of Heart Disease: A Collaborative Project of Medical Students and Faculty*. Wolters Kluwer, Philadelphia, edition 6 edition, 2016.

[215] D. S. Lindblad, C. R. Murphey, J. W. Clark, and W. R. Giles. A model of the action potential and underlying membrane currents in a rabbit atrial cell. *American Journal of Physiology - Heart and Circulatory Physiology*, 271(4):H1666–H1696, Oct. 1996.

[216] T. Lindeberg. Scale-space theory: A basic tool for analyzing structures at different scales. *Journal of Applied Statistics*, 21(1-2):225–270, Jan. 1994.

[217] G. T. Lines, P. Grottum, and A. Tveito. Modeling the electrical activity of the heart: A Bidomain Model of the ventricles embedded in a torso. *Computing and Visualization in Science*, 5(4):195–213, July 2002.

[218] S. Linge, J. Sundnes, M. Hanslien, G. Lines, and A. Tveito. Numerical solution of the bidomain equations. *Philosophical Transactions of the Royal Society A: Mathematical, Physical and Engineering Sciences*, 367(1895):1931–1950, May 2009.

[219] D. C. Liu and J. Nocedal. On the limited memory BFGS method for large scale optimization. *Mathematical Programming*, 45(1-3):503–528, Aug. 1989.

[220] D. W. Liu, G. A. Gintant, and C. Antzelevitch. Ionic bases for electrophysiological distinctions among epicardial, midmyocardial, and endocardial myocytes from the free wall of the canine left ventricle. *Circulation Research*, 72(3):671–687, Mar. 1993.

[221] A. N. Lopatin and J. M. B. Anumonwo. Structural and Molecular Bases of Cardiac Inward Rectifier Potassium Channel Function. In D. P. Zipes and J. Jalife, editors, *Cardiac Electrophysiology: From Cell to Bedside (Sixth Edition)*, pages 33–41. W.B. Saunders, Philadelphia, 2014.

[222] C.-h. Luo and Y. Rudy. A model of the ventricular cardiac action potential. Depolarization, repolarization, and their interaction. *Circulation research*, 68(6):1501–1526, June 1991.

[223] C. H. Luo and Y. Rudy. A dynamic model of the cardiac ventricular action potential. I. Simulations of ionic currents and concentration changes. *Circulation Research*, 74(6):1071–1096, June 1994.

[224] C. H. Luo and Y. Rudy. A dynamic model of the cardiac ventricular action potential. II. Afterdepolarizations, triggered activity, and potentiation. *Circulation Research*, 74(6):1097–1113, June 1994.

[225] M. Mangoni, B. Couette, L. Marger, E. Bourinet, J. Striessnig, and J. Nargeot. Voltage-dependent calcium channels and cardiac pacemaker activity: From ionic currents to genes. *Progress in Biophysics and Molecular Biology*, 90(1-3):38–63, Jan. 2006.

[226] V. Markides, R. J. Schilling, S. Y. Ho, A. W. C. Chow, D. W. Davies, and N. S. Peters. Characterization of Left Atrial Activation in the Intact Human Heart. *Circulation*, 107(5):733–739, Feb. 2003.

[227] A. R. Marks. Calcium and the heart: A question of life and death. *Journal of Clinical Investigation*, 111(5):597–600, Mar. 2003.

[228] G. G. Matthews. Derivation of the Nernst Equation. In *Cellular Physiology of Nerve and Muscle*, pages 208–211. Blackwell Publishing Ltd., 2002.

[229] R. E. McAllister, D. Noble, and R. W. Tsien. Reconstruction of the electrical activity of cardiac Purkinje fibres. *The Journal of Physiology*, 251(1):1–59, Sept. 1975.

[230] K. S. McDowell, F. Vadakkumpadan, R. Blake, J. Blauer, G. Plank, R. S. MacLeod, and N. A. Trayanova. Methodology for patient-specific modeling of atrial fibrosis as a substrate for atrial fibrillation. *Journal of Electrocardiology*, 45(6):640–645, Nov. 2012.

[231] B. H. Menze, K. V. Leemput, A. Honkela, E. Konukoglu, M.-A. Weber, N. Ayache, and P. Golland. A Generative Approach for Image-Based Modeling of Tumor Growth. In *Information Processing in Medical Imaging*, Lecture Notes in Computer Science, pages 735–747. Springer, Berlin, Heidelberg, July 2011.

[232] B. H. Menze, E. Stretton, E. Konukoglu, and N. Ayache. Image-based modeling of tumor growth in patients with glioma. In C. Garbe, R. Rannacher, U. Platt, and T. Wagner, editors, *Optimal control in image processing*. Springer Heidelberg, 2011.

[233] J. Modersitzki. *Numerical Methods for Image Registration*. OUP Oxford, 2004.

[234] P. Moireau, C. Bertoglio, N. Xiao, C. A. Figueroa, C. A. Taylor, D. Chapelle, and J.-F. Gerbeau. Sequential identification of boundary support parameters in a fluid-structure vascular model using patient image data. *Biomechanics and Modeling in Mechanobiology*, 12(3):475–496, July 2012.

[235] J. B. Moubarak, J. V. Rozwadowski, C. T. Strzalka, W. R. Buck, W. S. Tan, G. F. Kish, T. Kisiel, H. C. Fronc, and J. D. Maloney. Pulmonary Veins-Left Atrial Junction: Anatomic and Histological Study. *Pacing and Clinical Electrophysiology*, 23(11P2):1836–1838, Nov. 2000.

[236] B. J. M. Mulder and E. E. van der Wall. Size and function of the atria. *The International Journal of Cardiovascular Imaging*, 24(7):713–716, Oct. 2008.

[237] M. Murillo and X.-C. Cai. A fully implicit parallel algorithm for simulating the non-linear electrical activity of the heart. *Numerical Linear Algebra with Applications*, 11(2-3):261–277, Mar. 2004.

[238] E. Mutschler, H.-G. Schaible, and P. Vaupel. *Anatomie, Physiologie, Pathophysiologie des Menschen*. Wissenschaftliche Verlagsgesellschaft, Stuttgart, 6 edition, May 2007.

[239] A. Nagler, C. Bertoglio, M. Gee, and W. Wall. Personalization of cardiac fiber orientations from image data using the unscented kalman filter. In *Functional Imaging and Modeling of the Heart*, pages 132–140. Springer, 2013.

[240] A. Nagler, C. Bertoglio, C. T. Stoeck, S. Kozerke, and W. A. Wall. Cardiac Fibers Estimation from Arbitrarily Spaced Diffusion Weighted MRI. In *Functional Imaging and Modeling of the Heart*, Lecture Notes in Computer Science, pages 198–206. Springer, Cham, June 2015.

[241] A. Nagler, C. Bertoglio, C. T. Stoeck, S. Kozerke, and W. A. Wall. Maximum likelihood estimation of cardiac fiber bundle orientation from arbitrarily spaced diffusion weighted images. *Medical Image Analysis*, 39:56–77, July 2017.

[242] J. Nagumo, S. Arimoto, and S. Yoshizawa. An Active Pulse Transmission Line Simulating Nerve Axon. *Proceedings of the IRE*, 50(10):2061–2070, Oct. 1962.

[243] M. P. Nash and A. V. Panfilov. Electromechanical model of excitable tissue to study reentrant cardiac arrhythmias. *Progress in Biophysics and Molecular Biology*, 85(2-3):501–522, June 2004.

[244] S. Nattel. New ideas about atrial fibrillation 50 years on. *Nature*, 415:219, Jan. 2002.

[245] S. Nattel and M. Harada. Atrial Remodeling and Atrial Fibrillation: Recent Advances and Translational Perspectives. *Journal of the American College of Cardiology*, 63(22):2335–2345, June 2014.

[246] J. M. Nerbonne. Voltage-Regulated Potassium Channels. In D. P. Zipes and J. Jalife, editors, *Cardiac Electrophysiology: From Cell to Bedside (Sixth Edition)*, pages 23–32. W.B. Saunders, Philadelphia, 2014.

[247] N. Nguyen, J. Peraire, and B. Cockburn. An implicit high-order hybridizable discontinuous Galerkin method for linear convection–diffusion equations. *Journal of Computational Physics*, 228(9):3232–3254, May 2009.

[248] S. A. Niederer, E. Kerfoot, A. P. Benson, M. O. Bernabeu, O. Bernus, C. Bradley, E. M. Cherry, R. Clayton, F. H. Fenton, A. Garny, E. Heidenreich, S. Land, M. Maleckar, P. Pathmanathan, G. Plank, J. F. Rodriguez, I. Roy, F. B. Sachse, G. Seemann, O. Skavhaug, and N. P. Smith. Verification of cardiac tissue electrophysiology simulators using an N-version benchmark. *Philosophical Transactions of the Royal Society A: Mathematical, Physical and Engineering Sciences*, 369(1954):4331–4351, Nov. 2011.

[249] S. A. Niederer and N. P. Smith. The Role of the Frank–Starling Law in the Transduction of Cellular Work to Whole Organ Pump Function: A Computational Modeling Analysis. *PLOS Computational Biology*, 5(4):e1000371, Apr. 2009.

[250] P. M. Nielsen, I. J. Le Grice, B. H. Smaill, and P. J. Hunter. Mathematical model of geometry and fibrous structure of the heart. *American Journal of Physiology-Heart and Circulatory Physiology*, 260(4):H1365–H1378, 1991.

[251] A. Nikou, R. C. Gorman, and J. F. Wenk. Sensitivity of left ventricular mechanics to myofiber architecture: A finite element study. *Proceedings of the Institution of Mechanical Engineers, Part H: Journal of Engineering in Medicine*, 230(6):594–598, June 2016.

[252] D. Noble. Cardiac Action and Pacemaker Potentials based on the Hodgkin-Huxley Equations. *Nature*, 188(4749):495, Nov. 1960.

[253] D. Noble. A modification of the Hodgkin—Huxley equations applicable to Purkinje fibre action and pacemaker potentials. *The Journal of Physiology*, 160(2):317–352, Feb. 1962.

[254] D. Noble and S. J. Noble. A model of sino-atrial node electrical activity based on a modification of the DiFrancesco-Noble (1984) equations. *Proceedings of the Royal Society of London. Series B, Biological Sciences*, 222(1228):295–304, Sept. 1984.

[255] D. Noble and Y. Rudy. Models of Cardiac Ventricular Action Potentials: Iterative Interaction between Experiment and Simulation. *Philosophical Transactions: Mathematical, Physical and Engineering Sciences*, 359(1783):1127–1142, 2001.

[256] D. Noble and R. W. Tsien. The kinetics and rectifier properties of the slow potassium current in cardiac Purkinje fibres. *The Journal of Physiology*, 195(1):185–214, Mar. 1968.

[257] D. Noble and R. W. Tsien. Outward membrane currents activated in the plateau range of potentials in cardiac Purkinje fibres. *The Journal of Physiology*, 200(1):205–231, Jan. 1969.

[258] D. Noble and A. Varghese. Modelling of sodium-overload arrhythmias and their suppression. *The Canadian journal of cardiology*, 14(1):97–100, Jan. 1998.

[259] J. Nocedal and S. J. Wright. *Numerical Optimization*. Springer Series in Operations Research and Financial Engineering. Springer New York, 2006.

[260] D. A. Nordsletten, S. A. Niederer, M. P. Nash, P. J. Hunter, and N. P. Smith. Coupling multi-physics models to cardiac mechanics. *Progress in Biophysics and Molecular Biology*, 104(1):77–88, Jan. 2011.

[261] H. B. Nuss and S. R. Houser. T-type Ca2+ current is expressed in hypertrophied adult feline left ventricular myocytes. *Circulation research*, 73(4):777–782, 1993.

[262] A. Nygren, C. Fiset, L. Firek, J. W. Clark, D. S. Lindblad, R. B. Clark, and W. R. Giles. Mathematical Model of an Adult Human Atrial Cell: The Role of K+ Currents in Repolarization. *Circulation Research*, 82(1):63–81, Jan. 1998.

[263] A. Nygren, L. J. Leon, and W. R. Giles. Simulations of the human atrial action potential. *Philosophical Transactions of the Royal Society of London A: Mathematical, Physical and Engineering Sciences*, 359(1783):1111–1125, June 2001.

[264] J. O-Uchi, B. S. Jhun, and S.-S. Sheu. Structural and Molecular Bases of Mitochondrial Ion Channel Function. In D. P. Zipes and J. Jalife, editors, *Cardiac Electrophysiology: From Cell to Bedside (Sixth Edition)*, pages 71–84. W.B. Saunders, Philadelphia, 2014.

[265] R. W. Ogden. *Non-Linear Elastic Deformations*. Courier Corporation, 1997.

[266] T. O'Hara, L. Virág, A. Varró, and Y. Rudy. Simulation of the Undiseased Human Cardiac Ventricular Action Potential: Model Formulation and Experimental Validation. *PLOS Computational Biology*, 7(5):e1002061, May 2011.

[267] M. S. Olufsen, A. Nadim, and others. On deriving lumped models for blood flow and pressure in the systemic arteries. *Math Biosci Eng*, 1(1):61–80, 2004.

[268] M. S. Olufsen, C. S. Peskin, W. Y. Kim, E. M. Pedersen, A. Nadim, and J. Larsen. Numerical simulation and experimental validation of blood flow in arteries with structured-tree outflow conditions. *Annals of biomedical engineering*, 28(11):1281–1299, 2000.

[269] OpenStax. Anatomy & Physiology. OpenStax CNX. Aug 1, 2017 http://cnx.org/contents/14fb4ad7-39a1-4eee-ab6e-3ef2482e3e22@8.108.

[270] OpenStax. Blood Flow, Blood Pressure, and Resistance. OpenStax CNX. Feb 6, 2017 http://cnx.org/contents/03841c4c-9e9a-4822-95b2-12273c843a4e@4.

[271] OpenStax. Cardiac Muscle and Electrical Activity. OpenStax CNX. Feb 6, 2017 http://cnx.org/contents/302812e9-2d2d-4e44-8075-4bb75db53f36@4.

[272] OpenStax. Cardiac Cycle. OpenStax CNX. Jun 19, 2013 http://cnx.org/contents/22c3f969-ab9d-4df0-8baf-5b1a99372fac@3, 2013.

[273] T. Otani, A. Al-Issa, A. Pourmorteza, E. R. McVeigh, S. Wada, and H. Ashikaga. A Computational Framework for Personalized Blood Flow Analysis in the Human Left Atrium. *Annals of Biomedical Engineering*, 44(11):3284–3294, Nov. 2016.

[274] S. C. Panda and R. Natarajan. Finite-element method of stress analysis in the human left ventricular layered wall structure. *Medical and Biological Engineering and Computing*, 15(1):67–71, Jan. 1977.

[275] A. Panfilov and J. P. Keener. Re-entry in an anatomical model of the heart. *Chaos, Solitons & Fractals*, 5(3):681–689, Mar. 1995.

[276] A. V. Panfilov. Spiral breakup as a model of ventricular fibrillation. *Chaos: An Interdisciplinary Journal of Nonlinear Science*, 8(1):57–64, Mar. 1998.

[277] A. V. Panfilov and A. V. Holden. Computer Simulation of Re-entry Sources in Myocardium in Two and Three Dimensions. *Journal of Theoretical Biology*, 161(3):271–285, Apr. 1993.

[278] F. Pashakhanloo, D. A. Herzka, H. Ashikaga, S. Mori, N. Gai, D. A. Bluemke, N. A. Trayanova, and E. R. McVeigh. Myofiber architecture of the human atria as revealed by submillimeter diffusion tensor imaging. *Circulation: Arrhythmia and Electrophysiology*, 9(4):e004133, 2016.

[279] A. S. Patelli, L. Dedè, T. Lassila, A. Bartezzaghi, and A. Quarteroni. Isogeometric approximation of cardiac electrophysiology models on surfaces: An accuracy study with application to the human left atrium. *Computer Methods in Applied Mechanics and Engineering*, 317:248–273, Apr. 2017.

[280] P. Pathmanathan, G. R. Mirams, J. Southern, and J. P. Whiteley. The significant effect of the choice of ionic current integration method in cardiac electro-physiological simulations. *International Journal for Numerical Methods in Biomedical Engineering*, 27(11):1751–1770, Nov. 2011.

[281] M. Pavelka and J. Roth. Myofibrils, Intercalated Disk. In *Functional Ultrastructure*, pages 310–311. Springer, Vienna, 2010.

[282] R. C. Penland, D. M. Harrild, and C. S. Henriquez. Modeling impulse propagation and extracellular potential distributions in anisotropic cardiac tissue using a finite volume element discretization. *Computing and Visualization in Science*, 4(4):215–226, July 2002.

[283] J. M. Peyrat, M. Sermesant, X. Pennec, H. Delingette, C. Xu, E. R. McVeigh, and N. Ayache. A Computational Framework for the Statistical Analysis of Cardiac Diffusion Tensors: Application to a Small Database of Canine Hearts. *IEEE Transactions on Medical Imaging*, 26(11):1500–1514, Nov. 2007.

[284] S. Pezzuto, J. Hake, and J. Sundnes. Space-discretization error analysis and stabilization schemes for conduction velocity in cardiac electrophysiology. *International Journal for Numerical Methods in Biomedical Engineering*, 32(10), Oct. 2016.

[285] M. R. Pfaller, J. M. Hoermann, M. Weigl, A. Nagler, R. Chabiniok, C. Bertoglio, and W. A. Wall. The importance of the pericardium for cardiac biomechanics: From physiology to computational modeling. *Biomechanics and Modeling in Mechanobiology*, Apr. 2019.

[286] T. Pochet, P. Gérard, J. M. Marnette, V. D'Orio, R. Marcelle, M. Fatemi, A. Fossion, and J. Juchmes. Identification of Three-Element Windkessel Model: Comparison of Time and Frequency Domain Techniques. *Archives Internationales de Physiologie, de Biochimie et de Biophysique*, 100(3), 1992.

[287] A. Prakosa, P. Malamas, S. Zhang, F. Pashakhanloo, H. Arevalo, D. A. Herzka, A. Lardo, H. Halperin, E. McVeigh, N. Trayanova, and F. Vadakkumpadan. Methodology for Image-Based Reconstruction of Ventricular Geometry for Patient-Specific Modeling of Cardiac Electrophysiology. *Progress in biophysics and molecular biology*, 115(0):226–234, Aug. 2014.

[288] L. Priebe and D. J. Beuckelmann. Simulation Study of Cellular Electric Properties in Heart Failure. *Circulation Research*, 82(11):1206–1223, June 1998.

[289] F. W. Prinzen, K. Vernooy, and A. Auricchio. Cardiac Resynchronization Therapy: State-of-the-Art of Current Applications, Guidelines, Ongoing Trials, and Areas of Controversy. *Circulation*, 128(22):2407–2418, Nov. 2013.

[290] Z. Qu, G. Hu, A. Garfinkel, and J. N. Weiss. Nonlinear and stochastic dynamics in the heart. *Physics Reports*, May 2014.

[291] W. Quan, S. J. Evans, and H. M. Hastings. Efficient integration of a realistic two-dimensional cardiac tissue model by domain decomposition. *IEEE Transactions on Biomedical Engineering*, 45(3):372–385, 1998.

[292] C. Ramanathan, P. Jia, R. Ghanem, K. Ryu, and Y. Rudy. Activation and repolarization of the normal human heart under complete physiological conditions. *Proceedings of the National Academy of Sciences of the United States of America*, 103(16):6309–6314, Apr. 2006.

[293] R. J. Ramirez, S. Nattel, and M. Courtemanche. Mathematical analysis of canine atrial action potentials: Rate, regional factors, and electrical remodeling. *American Journal of Physiology - Heart and Circulatory Physiology*, 279(4):H1767–H1785, Oct. 2000.

[294] J. Relan, P. Chinchapatnam, M. Sermesant, K. Rhode, M. Ginks, H. Delingette, C. A. Rinaldi, R. Razavi, and N. Ayache. Coupled personalization of cardiac electrophysiology models for prediction of ischaemic ventricular tachycardia. *Interface Focus*, 1(3):396–407, June 2011.

[295] M. Reumann, J. Bohnert, G. Seemann, B. Osswald, and O. Dossel. Preventive Ablation Strategies in a Biophysical Model of Atrial Fibrillation Based on Realistic Anatomical Data. *IEEE Transactions on Biomedical Engineering*, 55(2):399–406, Feb. 2008.

[296] H. Reuter. The dependence of slow inward current in Purkinje fibres on the extracellular calcium-concentration. *The Journal of Physiology*, 192(2):479–492, Sept. 1967.

[297] J. J. Rice, R. L. Winslow, and W. C. Hunter. Comparison of putative cooperative mechanisms in cardiac muscle: Length dependence and dynamic responses. *American Journal of Physiology - Heart and Circulatory Physiology*, 276(5):H1734–H1754, May 1999.

[298] E. S. Richardson, A. J. Hill, N. D. Skadsberg, M. Ujhelyi, Y.-F. Xiao, and P. A. Iaizzo. The Pericardium. In *Handbook of Cardiac Anatomy, Physiology, and Devices*, pages 125–136. Humana Press, 2009.

[299] J. M. Rogers and A. D. McCulloch. A collocation-Galerkin finite element model of cardiac action potential propagation. *IEEE Transactions on Biomedical Engineering*, 41(8):743–757, Aug. 1994.

[300] D. Romero, O. Camara, F. Sachse, and R. Sebastian. Analysis of Microstructure of the Cardiac Conduction System Based on Three-Dimensional Confocal Microscopy. *PLOS ONE*, 11(10):e0164093, Oct. 2016.

[301] R. A. Rose and P. H. Backx. Calcium Channels in the Heart. In D. P. Zipes and J. Jalife, editors, *Cardiac Electrophysiology: From Cell to Bedside (Sixth Edition)*, pages 13–22. W.B. Saunders, Philadelphia, 2014.

[302] M. Rotter, L. Dang, V. Jacquemet, N. Virag, L. Kappenberger, and M. Haissaguerre. Impact of Varying Ablation Patterns in a Simulation Model of Persistent Atrial Fibrillation. *Pacing and Clinical Electrophysiology*, 30(3):314–321, 2007.

[303] P. Ruchat, L. Dang, J. Schlaepfer, N. Virag, L. K. von Segesser, and L. Kappenberger. Use of a biophysical model of atrial fibrillation in the interpretation of the outcome of surgical ablation procedures☆. *European Journal of Cardio-Thoracic Surgery*, 32(1):90–95, July 2007.

[304] P. Ruchat, N. Virag, L. Dang, J. Schlaepfer, E. Pruvot, and L. Kappenberger. A biophysical model of atrial fibrillation ablation: What can a surgeon learn from a computer model? *Europace: European Pacing, Arrhythmias, and Cardiac Electrophysiology: Journal of the*

Working Groups on Cardiac Pacing, Arrhythmias, and Cardiac Cellular Electrophysiology of the European Society of Cardiology, 9 Suppl 6:vi71–76, Nov. 2007.

[305] M. Ruiz. Diagram showing a cell union called gap junction, June 2006.

[306] F. B. Sachse. 6. Cardiac Anatomy. In *Computational Cardiology*, Lecture Notes in Computer Science, pages 119–155. Springer, Berlin, Heidelberg, 2004.

[307] F. B. Sachse. 7. Cardiac Electrophysiology. In *Computational Cardiology*, Lecture Notes in Computer Science, pages 157–219. Springer, Berlin, Heidelberg, 2004.

[308] F. B. Sachse, R. Frech, C. D. Werner, and O. Dossel. A model based approach to assignment of myocardial fibre orientation. In *Computers in Cardiology, 1999*, pages 145–148. IEEE, 1999.

[309] H. I. Saleheen and K. T. Ng. A new three-dimensional finite-difference bidomain formulation for inhomogeneous anisotropic cardiac tissues. *IEEE Transactions on Biomedical engineering*, 45(1):15–25, 1998.

[310] F. H. Samie, O. Berenfeld, J. Anumonwo, S. F. Mironov, S. Udassi, J. Beaumont, S. Taffet, A. M. Pertsov, and J. Jalife. Rectification of the Background Potassium Current: A Determinant of Rotor Dynamics in Ventricular Fibrillation. *Circulation Research*, 89(12):1216–1223, Dec. 2001.

[311] D. Sánchez-Quintana, R. H. Anderson, J. A. Cabrera, V. Climent, R. Martin, J. Farré, and S. Y. Ho. The terminal crest: Morphological features relevant to electrophysiology. *Heart*, 88(4):406–411, Oct. 2002.

[312] P. Sanders, P. Jaïs, M. Hocini, L. F. Hsu, C. Scavée, F. Sacher, M. Rotter, Y. Takahashi, J. L. Pasquié, D. C. Shah, S. Garrigue, J. Clémenty, and M. Haïssaguerre. Electrophysiologic and clinical consequences of linear catheter ablation to transect the anterior left atrium in patients with atrial fibrillation. *Heart rhythm*, 1(2):176–184, July 2004.

[313] U. Schotten, S. Verheule, P. Kirchhof, and A. Goette. Pathophysiological Mechanisms of Atrial Fibrillation: A Translational Appraisal. *Physiological Reviews*, 91(1):265–325, Jan. 2011.

[314] H. W. Schuchlenz, G. Saurer, W. Weihs, and P. Rehak. Persisting eustachian valve in adults: Relation to patent foramen ovale and cerebrovascular events. *Journal of the American Society of Echocardiography*, 17(3):231–233, Mar. 2004.

[315] D. R. L. Scriven, P. Dan, and E. D. W. Moore. Distribution of Proteins Implicated in Excitation-Contraction Coupling in Rat Ventricular Myocytes. *Biophysical Journal*, 79(5):2682–2691, Nov. 2000.

[316] G. Seemann, C. Höper, F. B. Sachse, O. Dössel, A. V. Holden, and H. Zhang. Heterogeneous three-dimensional anatomical and electrophysiological model of human atria. *Philosophical Transactions of the Royal Society of London A: Mathematical, Physical and Engineering Sciences*, 364(1843):1465–1481, June 2006.

[317] R. Sevilla, O. Hassan, and K. Morgan. An analysis of the performance of a high-order stabilised finite element method for simulating compressible flows. *Computer Methods in Applied Mechanics and Engineering*, 253:15–27, Jan. 2013.

[318] A. J. Shah, M. Hocini, O. Xhaet, P. Pascale, L. Roten, S. B. Wilton, N. Linton, D. Scherr, S. Miyazaki, A. S. Jadidi, X. Liu, A. Forclaz, I. Nault, L. Rivard, M. E. F. Pedersen, N. Derval, F. Sacher, S. Knecht, P. Jais, R. Dubois, S. Eliautou, R. Bokan, M. Strom, C. Ramanathan, I. Cakulev, J. Sahadevan, B. Lindsay, A. L. Waldo, and M. Haissaguerre. Validation of Novel 3-Dimensional Electrocardiographic Mapping of Atrial Tachycardias by Invasive Mapping and Ablation: A Multicenter Study. *Journal of the American College of Cardiology*, 62(10):889–897, Sept. 2013.

[319] Y. Shi, P. Lawford, and R. Hose. Review of Zero-D and 1-D Models of Blood Flow in the Cardiovascular System. *BioMedical Engineering OnLine*, 10:33, Apr. 2011.

[320] R. J. Solaro. Mechanisms Regulating Cardiac Myofilament Response to Calcium. In N. Sperelakis, Y. Kurachi, A. Terzic, and M. V. Cohen, editors, *Heart Physiology and Pathophysiology (Fourth Edition)*, pages 519–526. Academic Press, San Diego, 2001.

[321] O. Sorkine. Least-squares rigid motion using svd. *Technical notes*, 120(3):52, 2009.

[322] D. E. Sosnovik, R. Wang, G. Dai, T. G. Reese, and V. J. Wedeen. Diffusion MR tractography of the heart. *Journal of Cardiovascular Magnetic Resonance*, 11(1):47, Nov. 2009.

[323] P. B. Sparks, H. G. Mond, J. K. Vohra, S. Jayaprakash, and J. M. Kalman. Electrical Remodeling of the Atria Following Loss of Atrioventricular Synchrony: A Long-Term Study in Humans. *Circulation*, 100(18):1894–1900, Nov. 1999.

[324] P. B. Sparks, H. G. Mond, J. K. Vohra, A. G. Yapanis, L. E. Grigg, and J. M. Kalman. Mechanical Remodeling of the Left Atrium After Loss of Atrioventricular Synchrony: A Long-Term Study in Humans. *Circulation*, 100(16):1714–1721, Oct. 1999.

[325] Spjkrul. File:Conductionsystem.svg - Textbook of Cardiology. https://www.textbookofcardiology.org/wiki/File:Conductionsystem.svg, 2011.

[326] D. H. Spodick. *The Pericardium: A Comprehensive Textbook*. CRC Press, New York, 1 edition edition, Oct. 1996.

[327] N. Stergiopulos, B. E. Westerhof, and N. Westerhof. Total arterial inertance as the fourth element of the windkessel model. *American Journal of Physiology - Heart and Circulatory Physiology*, 276(1):H81–H88, Jan. 1999.

[328] M. F. Stoddard, P. R. Dawkins, C. R. Prince, and N. M. Ammash. Left atrial appendage thrombus is not uncommon in patients with acute atrial fibrillation and a recent embolic event: A transesophageal echocardiographics tudy. *Journal of the American College of Cardiology*, 25(2):452–459, Feb. 1995.

[329] C. T. Stoeck, C. von Deuster, M. Genet, D. Atkinson, and S. Kozerke. Second-order motion-compensated spin echo diffusion tensor imaging of the human heart. *Magnetic Resonance in Medicine*, 75(4):1669–1676, Apr. 2016.

[330] C. Stöllberger, G. Ernst, E. Bonner, J. Finsterer, and J. Slany. Left atrial appendage morphology: Comparison of transesophageal images and postmortem casts. *Zeitschrift für Kardiologie*, 92(4):303–308, Apr. 2003.

[331] D. D. Streeter and D. L. Bassett. An engineering analysis of myocardial fiber orientation in pig's left ventricle in systole. *The Anatomical Record*, 155(4):503–511, Aug. 1966.

[332] D. D. Streeter, H. M. Spotnitz, D. P. Patel, J. Ross, and E. H. Sonnenblick. Fiber orientation in the canine left ventricle during diastole and systole. *Circulation research*, 24(3):339–347, 1969.

[333] K. H. W. J. Ten Tusscher, A. Mourad, M. P. Nash, R. H. Clayton, C. P. Bradley, D. J. Paterson, R. Hren, M. Hayward, A. V. Panfilov, and P. Taggart. Organization of ventricular fibrillation in the human heart: Experiments and models. *Experimental Physiology*, 94(5):553–562, May 2009.

[334] K. H. W. J. ten Tusscher, D. Noble, P. J. Noble, and A. V. Panfilov. A model for human ventricular tissue. *American Journal of Physiology - Heart and Circulatory Physiology*, 286(4):H1573–H1589, Apr. 2004.

[335] K. H. W. J. ten Tusscher and A. V. Panfilov. Alternans and spiral breakup in a human ventricular tissue model. *American Journal of Physiology - Heart and Circulatory Physiology*, 291(3):H1088–H1100, Sept. 2006.

[336] C. Tobón, C. Ruiz, J. Rodríguez, F. Hornero, J. Ferrero, and J. Sáiz. A biophysical model of atrial fibrillation to simulate the Maze III ablation pattern. In *2010 Computing in Cardiology*, pages 621–624, Sept. 2010.

[337] N. Toussaint, C. T. Stoeck, T. Schaeffter, S. Kozerke, M. Sermesant, and P. G. Batchelor. In vivo human cardiac fibre architecture estimation using shape-based diffusion tensor processing. *Medical Image Analysis*, 17(8):1243–1255, Dec. 2013.

[338] J. A. Trangenstein and C. Kim. Operator splitting and adaptive mesh refinement for the Luo–Rudy I model. *Journal of Computational Physics*, 196(2):645–679, May 2004.

[339] N. A. Trayanova. Whole Heart Modeling: Applications to Cardiac Electrophysiology and Electromechanics. *Circulation research*, 108(1):113–128, Jan. 2011.

[340] N. A. Trayanova and J. J. Rice. Cardiac Electromechanical Models: From Cell to Organ. *Frontiers in Physiology*, 2, Aug. 2011.

[341] M. Trew, I. Le Grice, B. Smaill, and A. Pullan. A Finite Volume Method for Modeling Discontinuous Electrical Activation in Cardiac Tissue. *Annals of Biomedical Engineering*, 33(5):590–602, May 2005.

[342] M. L. Trew, B. H. Smaill, D. P. Bullivant, P. J. Hunter, and A. J. Pullan. A generalized finite difference method for modeling cardiac electrical activation on arbitrary, irregular computational meshes. *Mathematical Biosciences*, 198(2):169–189, Dec. 2005.

[343] K. H. W. J. T. Tusscher, R. Hren, and A. V. Panfilov. Organization of Ventricular Fibrillation in the Human Heart. *Circulation Research*, 100(12):e87–e101, June 2007.

[344] K. H. W. J. T. Tusscher and A. V. Panfilov. Reentry in heterogeneous cardiac tissue described by the Luo-Rudy ventricular action potential model. *American Journal of Physiology - Heart and Circulatory Physiology*, 284(2):H542–H548, Feb. 2003.

[345] E. Ukwatta, H. Arevalo, M. Rajchl, J. White, F. Pashakhanloo, A. Prakosa, D. A. Herzka, E. McVeigh, A. C. Lardo, N. A. Trayanova, and F. Vadakkumpadan. Image-based reconstruction of three-dimensional myocardial infarct geometry for patient-specific modeling of cardiac electrophysiology. *Medical Physics*, 42(8):4579–4590, Aug. 2015.

[346] S. Uribe, T. Tangchaoren, V. Parish, I. Wolf, R. Razavi, G. Greil, and T. Schaeffter. Volumetric Cardiac Quantification by Using 3D Dual-Phase Whole-Heart MR Imaging. *Radiology*, 248(2):606–614, Aug. 2008.

[347] F. Vadakkumpadan, H. Arevalo, C. Ceritoglu, M. Miller, and N. Trayanova. Image-Based Estimation of Ventricular Fiber Orientations for Personalized Modeling of Cardiac Electrophysiology. *IEEE Transactions on Medical Imaging*, 31(5):1051–1060, May 2012.

[348] F. Vadakkumpadan, L. J. Rantner, B. Tice, P. Boyle, A. J. Prassl, E. Vigmond, G. Plank, and N. Trayanova. Image-based models of cardiac structure with applications in arrhythmia and defibrillation studies. *Journal of electrocardiology*, 42(2):157.e1, 2009.

[349] H. H. Valdivia. Structural and Molecular Bases of Sarcoplasmic Reticulum Ion Channel Function. In D. P. Zipes and J. Jalife, editors, *Cardiac Electrophysiology: From Cell to Bedside (Sixth Edition)*, pages 55–69. W.B. Saunders, Philadelphia, 2014.

[350] F. J. van Capelle and D. Durrer. Computer simulation of arrhythmias in a network of coupled excitable elements. *Circulation Research*, 47(3):454–466, Sept. 1980.

[351] J. P. Veinot, P. J. Harrity, F. Gentile, B. K. Khandheria, K. R. Bailey, J. T. Eickholt, J. B. Seward, A. J. Tajik, and W. D. Edwards. Anatomy of the Normal Left Atrial Appendage: A Quantitative Study of Age-Related Changes in 500 Autopsy Hearts: Implications for Echocardiographic Examination. *Circulation*, 96(9):3112–3115, Nov. 1997.

[352] A. Verma, C.-y. Jiang, T. R. Betts, J. Chen, I. Deisenhofer, R. Mantovan, L. Macle, C. A. Morillo, W. Haverkamp, R. Weerasooriya, J.-P. Albenque, S. Nardi, E. Menardi, P. Novak, and P. Sanders. Approaches to Catheter Ablation for Persistent Atrial Fibrillation. *New England Journal of Medicine*, 372(19):1812–1822, May 2015.

[353] F. J. Vetter and A. D. McCulloch. Three-dimensional stress and strain in passive rabbit left ventricle: A model study. *Annals of Biomedical Engineering*, 28(7):781–792, July 2000.

[354] M. Viceconti, S. Olsen, L.-P. Nolte, and K. Burton. Extracting clinically relevant data from finite element simulations. *Clinical Biomechanics*, 20(5):451–454, June 2005.

[355] E. Vigmond, F. Aguel, and N. Trayanova. Computational techniques for solving the bidomain equations in three dimensions. *IEEE Transactions on Biomedical Engineering*, 49(11):1260–1269, Nov. 2002.

[356] N. Virag, O. Blanc, O. Eick, J. Vesin, and L. Kappenberger. A computer model to test therapeutic interventions for atrial fibrillation. *Computer Simulation and Experimental Assessment of Cardiac Electrophysiology*, pages pp 139–144, 2001.

[357] G. M. Wahler. Cardiac Action Potentials. In N. Sperelakis, Y. Kurachi, A. Terzic, and M. V. Cohen, editors, *Heart Physiology and Pathophysiology (Fourth Edition)*, pages 199–211. Academic Press, San Diego, 2001.

[358] F. M. Weber, S. Lurz, D. U. J. Keller, D. L. Weiss, G. Seemann, C. Lorenz, and O. Dossel. Adaptation of a minimal four-state cell model for reproducing atrial excitation properties. In *2008 Computers in Cardiology*, pages 61–64, Sept. 2008.

[359] A. J. Weinhaus. Anatomy of the Human Heart. In *Handbook of Cardiac Anatomy, Physiology, and Devices*, pages 61–88. Springer, Cham, 2015.

[360] A. J. Weinhaus and K. P. Roberts. Anatomy of the Human Heart. In *Handbook of Cardiac Anatomy, Physiology, and Devices*, pages 59–85. Humana Press, 2009.

[361] N. Westerhof, F. Bosman, C. J. D. Vries, and A. Noordergraaf. Analog studies of the human systemic arterial tree. *Journal of Biomechanics*, 2(2):IN3, May 1969.

[362] N. Westerhof, G. Elzinga, and P. Sipkema. An artificial arterial system for pumping hearts. *Journal of Applied Physiology*, 31(5):776–781, Nov. 1971.

[363] J. P. Whiteley. An Efficient Numerical Technique for the Solution of the Monodomain and Bidomain Equations. *IEEE Transactions on Biomedical Engineering*, 53(11):2139–2147, Nov. 2006.

[364] J. P. Whiteley. Physiology Driven Adaptivity for the Numerical Solution of the Bidomain Equations. *Annals of Biomedical Engineering*, 35(9):1510–1520, Aug. 2007.

[365] M. Wilhelms, H. Hettmann, M. M. Maleckar, J. T. Koivumäki, O. Dössel, and G. Seemann. Benchmarking electrophysiological models of human atrial myocytes. *Frontiers in Physiology*, 3, 2013.

[366] R. L. Winslow, P. Helm, W. Baumgartner, S. Peddi, T. Ratnanather, E. McVeigh, and M. I. Miller. Imaging-Based Integrative Models of the Heart: Closing the Loop between Experiment and Simulation. In *'In Silico' Simulation of Biological Processes*, pages 129–143. Wiley-Blackwell, Oct. 2008.

[367] R. L. Winslow, A. L. Kimball, A. Varghese, and D. Noble. Simulating cardiac sinus and atrial network dynamics on the connection machine. *Physica D: Nonlinear Phenomena*, 64(1):281–298, Apr. 1993.

[368] R. L. Winslow, D. F. Scollan, A. Holmes, C. K. Yung, J. Zhang, and M. S. Jafri. Electrophysiological Modeling of Cardiac Ventricular Function: From Cell to Organ. *Annual review of biomedical engineering*, 2:119–155, 2000.

[369] A. L. Wit and M. R. Rosen. Pathophysiologic mechanisms of cardiac arrhythmias. *American Heart Journal*, 106(4, Part 2):798–811, Oct. 1983.

[370] P. A. Wolf, R. D. Abbott, and W. B. Kannel. Atrial fibrillation as an independent risk factor for stroke: The Framingham Study. *Stroke*, 22(8):983–988, Jan. 1991.

[371] A. Y. K. Wong and P. M. Rautaharju. Stress distribution within the left ventricular wall approximated as a thick ellipsoidal shell. *American Heart Journal*, 75(5):649–662, May 1968.

[372] J. Wong and E. Kuhl. Generating fiber orientation maps in human heart models using Poisson interpolation. *Computer methods in biomechanics and biomedical engineering*, 17(11):1217–1226, Aug. 2014.

[373] F. Xie, Z. Qu, J. Yang, A. Baher, J. N. Weiss, and A. Garfinkel. A simulation study of the effects of cardiac anatomy in ventricular fibrillation. *Journal of Clinical Investigation*, 113(5):686–693, Mar. 2004.

[374] M. Yamamoto, Y. Seo, N. Kawamatsu, K. Sato, A. Sugano, T. Machino-Ohtsuka, R. Kawamura, H. Nakajima, M. Igarashi, Y. Sekiguchi, T. Ishizu, and K. Aonuma. Complex Left Atrial Appendage Morphology and Left Atrial Appendage Thrombus Formation in Patients With Atrial Fibrillation. *Circulation: Cardiovascular Imaging*, page CIRCIMAGING.113.001317, Feb. 2014.

[375] K. Yanagihara, A. Noma, and H. Irisawa. Reconstruction of sino-atrial node pacemaker potential based on the voltage clamp experiments. *The Japanese journal of physiology*, 30(6):841–857, 1980.

[376] L. Yue, J. Xie, and S. Nattel. Molecular determinants of cardiac fibroblast electrical function and therapeutic implications for atrial fibrillation. *Cardiovascular Research*, 89(4):744–753, Mar. 2011.

[377] H. Zhang and N. Patel. Spiral wave breakdown in an excitable medium model of cardiac tissue. *Chaos, Solitons & Fractals*, 5(3):635–643, Mar. 1995.

[378] J. Zhao, T. D. Butters, H. Zhang, A. J. Pullan, I. J. LeGrice, G. B. Sands, and B. H. Smaill. An Image-Based Model of Atrial Muscular Architecture. *Circulation: Arrhythmia and Electrophysiology*, 5(2):361–370, Apr. 2012.

[379] S. Zozor, O. Blanc, V. Jacquemet, N. Virag, J.-M. Vesin, E. Pruvot, L. Kappenberger, and C. Henriquez. A numerical scheme for modeling wavefront propagation on a monolayer of arbitrary geometry. *IEEE Transactions on Biomedical Engineering*, 50(4):412–420, Apr. 2003.